Reservoir Characterization with Limited Sample Data using Geostatistics

By:

Sayyed Mojtaba Ghoraishy

Submitted to the Department of Chemical and Petroleum Engineering and the Faculty of the Graduate School at The University of Kansas in Partial Fulfillment of the Requirements for the Degree of Doctor of Philosophy

Chairperson: Dr. G.P. Willhite

Dissertation Committee:

Dr. Jenn-Tai Liang

Dr. Shapour Vossoughi

Dr. Anthony W. Walton

Dr. Jyun Syung Tsau

Dr. Don Green

Date Defended: October 13, 2008

The dissertation committee for Sayyed Mojtaba Ghoraishy certifies

that this is the approved version of the following dissertation:

Reservoir Characterization with Limited Sample Data using Geostatistics

Chairperson: Dr. G.P. Willhite

Dissertation Committee:

Dr. Jenn-Tai Liang

Dr. Shapour Vossoughi

Dr. Anthony W. Walton

Dr. Jyun Syung Tsau

Dr. Don Green

Date Approved: December 10, 2008

Acknowledgments

The author wishes to extent his sincere gratitude to all the members of his committee Dr. G. Paul Willhite, Dr. Green, Dr Jen Tai Liang, Dr. Jyung-Syung Tsau, Dr. Shapour Vossoughi, and Dr. Tony Walton.

I would like to thank my fellow graduate students and officemates who made my graduate life more fun.

The financial support of the Tertiary Oil recovery Project (TORP) is appreciated.

Lastly, and most importantly, I have to thank my wife, Leila, my son Mohammad and my daughter Minoo for the love, encouragement, care, and support they have given me all the way.

To my wife Leila, my son Mohammad and my daughter Minoo

Abstract

The primary objective of this dissertation was to develop a systematic method to characterize the reservoir with the limited available data. The motivation behind the study was characterization of CO_2 pilot area in the Hall Gurney Field, Lansing Kansas City Formation. The main tool of the study was geostatistics, since only geostatistics can incorporate data from variety of sources to estimate reservoir properties. Three different subjects in geostatistical methods were studied, analyzed and improved.

The first part investigates the accuracy of different geostatistical methods as a function of the available sample data. The effect of number and type of samples on conventional and stochastical methods was studied using a synthetic reservoir. The second part of the research focuses on developing a systematic geostatistical method to characterize a reservoir in the case of very limited sample data. The objective in this part was the use of dynamic data, such as data from pressure transient analysis, in geostatistical methods. In the literature review of this part emphasis is given to those works involving the incorporation of well-test data and the use of simulated annealing to incorporate different type of static and dynamic data. The second part outlines a systematic procedure to estimate the reservoir properties for a CO2 pilot area in the Lansing Kansas City formation. The third part of the thesis discusses the multiple-point geostatistics and presents an improvement in reservoir characterization using training image construction. Similarity distance function is used to find the most consistent and similar pattern for to the existing data. This part of thesis presents a mathematical improvement to the existing similarity functions.

TABLE OF CONTENTS

List of Figures

List of Tables

Chapter 1- Overview

The primary objective of this study was to develop a systematic method to characterize the reservoir with the limited available data. The motivation behind the study was characterization of CO_2 pilot area in the Hall Gurney Field, Lansing Kansas City Formation. The main tool of the study was geostatistics, since only geostatistics can incorporate data from variety of sources to estimate reservoir properties. First step of the study was to compare the different geostatistical methods and the effect of availability of the data on the accuracy of the estimation. The second step was to propose a procedure to estimate the reservoir properties for a CO_2 pilot area in the Lansing Kansas City formation. The proposed procedure incorporates available dynamic data to geostatistical analysis to reduce the uncertainty. In final step, the application of multiple-point geostatistics was studied and in the process an improvement made to reservoir characterization using training image construction.

Reservoir modeling is a crucial step in the development and management of petroleum reservoirs. Field development decisions made during the life of a reservoir such as depletion strategy, number and location of production/injection wells, reservoir pressure maintenance schemes, etc. require an accurate model of reservoir heterogeneities and topology. Furthermore, accurate prediction of reservoir performance requires a reservoir model that not only honors all available data but also accounts for the scale and precision at which they are available. The data available to model a reservoir is scarce

due to high acquisition costs; hence the challenge is to extract the maximum possible reservoir information from the available data.

The data obtained from the field can be classified as static or dynamic. The static data do not vary over time generally and are related to the intrinsic characteristics of the rock through simple linear relationships, such as well logs, core measurements and seismic amplitude. The dynamic data, on the other hand, do vary with time. Dynamic data are related to the intrinsic characteristics of the rock generally through a complex, non-linear transfer function. These include field measurements that are made regularly throughout the life of the reservoir. Examples of this type are well-bore flowing pressures, fluid production rates, pressure transients, fractional flow data and time-lapse seismic data.

Geostatistics has been extensively used in reservoir characterization for a variety reasons including its ability to successfully analyze and integrate different types of data, provide meaningful results for model building, and quantitatively evaluate uncertainty for risk management. Geostatistical techniques are statistical methods that develop the spatial relationship between the sample data to model the possible values of random variables at unsampled locations. Since its introduction to the petroleum industry almost four decades ago, geostatistics has been increasingly used for the characterization of reservoir properties. The most important advantage of geostatistics, that makes it attractive for reservoir characterization, is that geostatistical techniques are numerically based. The

final product of a geostatistical method is a volume of key petrophysical properties honoring the well and seismic data.

Geostatistical methods are the focus of this thesis. Three different subjects in geostatistical methods were studied, analyzed and improved. These subjects, although appear unrelated in the first glance, are part of geostatistical application in reservoir characterization. Following paragraphs briefly introduce three topic of this thesis.

The first part investigates the accuracy of different geostatistical methods as a function of the available sample data. The effect of number and type of samples on conventional and stochastical methods was studied using a synthetic reservoir. The topics comes in Chapter 2 that also presents a literature review of the basic concepts of geostatistics and different geostatistical techniques used in subsurface modeling.

The second part of the research focuses on developing a systematic geostatistical method to characterize a reservoir in the case of very limited sample data. The objective in this part was the use of dynamic data, such as data from pressure transient analysis, in geostatistical methods. In the literature review of this part emphasis is given to those works involving the incorporation of well-test data and the use of simulated annealing to incorporate different type of static and dynamic data. The second section includes the chapter 6 which also outlines a systematic procedure to estimate the reservoir properties for a CO2 pilot area in the Lansing Kansas City formation.

The third part of the thesis discusses the multiple-point geostatistics and presents an improvement in reservoir characterization using training image construction. The multiple-point geostatistics use the concept of training image for the purpose of subsurface modeling. The image construction, in turn, relies on the concept of similarity of available data and the patterns of a training image. Similarity distance function is used to find the most consistent and similar pattern to the existing data. This part of thesis presents a mathematical improvement to the existing similarity functions. Then using examples shows its advantages to the other methods.

Part I

Chapter 2

Review of the Geostatistical Reservoir Characterization

2.1. Introduction

Proper characterization of reservoir heterogeneity is a crucial requirement for accurate prediction of reservoir performance. One of the most valuable tools for characterization is geostatistics. Geostatistics applies statistical concepts to geological-based phenomena and improve the modeling of the reservoir. The basis for all the geostatistical prediction is available sample data from the reservoir. Thus it is expected that the availability of data have effect on the accuracy of the predictions. For instance, permeability is a key parameter to any reservoir study since it defines flow paths within the reservoir. In a permeability characterization study, it is vital to characterize and preserve in the model the values and their spatial patterns. The available permeability data come from core measurements, which always represent a small proportion of the total heterogeneity of the reservoir. Therefore, to build a reservoir geostatistical model for permeability, it is necessary to have enough core samples to represent the real heterogeneity of the subsurface reservoir. The objective of this part of dissertation is to investigate the effect of the quantity of available sample data on the accuracy of conventional and stochastic geostatistical methods in predicting the permeability distribution.

In this chapter, a brief review of basic geostatistical concepts and methods is presented. The methods is based on all theories, equations and ideas in the existing

literature [11,18,34,37]. In chapter three, four geostatistical methods (selected based on performance and ease of implementation), were applied to investigate the effect of number of the available data on the accuracy of prediction.

2.2. Background

This section briefly reviews the fundamentals of geostatistics that are essential in understanding this study. For the deeper understanding of subject matter and the mathematics behind it, however, readers are referred to existing literature[11,18,34,37].

2.2.1. Random Variables

A random variable is a variable with values that are randomly generated according to a probabilistic mechanism. The throwing of a die, for instance, produces random values from the set {1, 2, 3, 4, 5, 6}.

Random variables are seen in a wide variety of scientific and engineering disciplines. In meteorology, for example, temperature and pressure that are collected at some stations are used to model the weather pattern. In this case, temperature and pressure can be regarded as random variables. In geology and petroleum engineering, the estimate of variation of subsurface properties such as formation thickness, permeability, and porosity are regarded as random variables.

Mathematically, a numeric sequence is said to be statistically random when it contains no recognizable patterns or regularities; sequences such as the results of an ideal

die roll. Some, such as the annual amount of rainfall, are time dependent; others, such as the thickness of geological formation are invariant at the human scale of the time. The accurate characterization of a random variable is an expensive and time-consuming problem. Commonly, random variables are known only through a scattered set of observations (table function). In statistical jargon, the selected observation is called *samples*.

Random variables at specific location or time have a degree of uncertainty, even if the observations have been carefully taken to minimize measurement error. The value of a random variable at unsampled locations is uncertain, and no method has been devised yet to yield error-free estimates. Figure 2.1 is a cross-section based on two sample elements at locations A and B, where the random variable is known. Here, any surface is a possible description of the real random variable at the unsampled locations. The four alternatives presented in Figure 2.1 are a small subset of all possible answers. For some arbitrary location, such as C, a table can be prepared containing all the estimated values at that location. The minimum and maximum values in the table define the interval which encloses all likely answers to the value of the parameter at location C. A tabulation of events and their associated probability of occurrence corresponds to the statistical concept of a probability density function. Figure 2.2 represents a hypothetical probability density function for all likely values of spatial function at some arbitrary unsampled location. Based on the probability density function at location C, one value of the random variable in Figure 2.1 is more probable than the other values.

In general, the variation in the outcomes of a random variable is presented by an informative short description rather than listing all its possible outcomes. The average of all possible outcomes of a random variable weighted by their probability of occurrence is the mean of sample. The mean is the central value of all outcomes. The weighted average of the squares of the differences between the outcomes and the mean is the variance. The variance becomes larger when the differences increase. The standard deviation is the square root of the variance. Thus, variance and the standard deviation are measures of the dispersion of the outcomes relative to the mean value. The standard deviation of Figure 2.2 is a measure of the uncertainty as the true value of the random variable at point C in Figure 2.1. A small standard deviation indicates the outcomes are clustered tightly around the central value (mean) over relatively narrow range of possibilities.

Throughout this dissertation, the uppercase letters, such as Z, denote a random variable while the lower case letters, such as z, denote the outcome values. Also, the set of possible outcomes that a random variable might take is denoted by $z(1),..., z(n)$ and the outcomes that are actually observed are denoted by $z_1,..., z_n$.

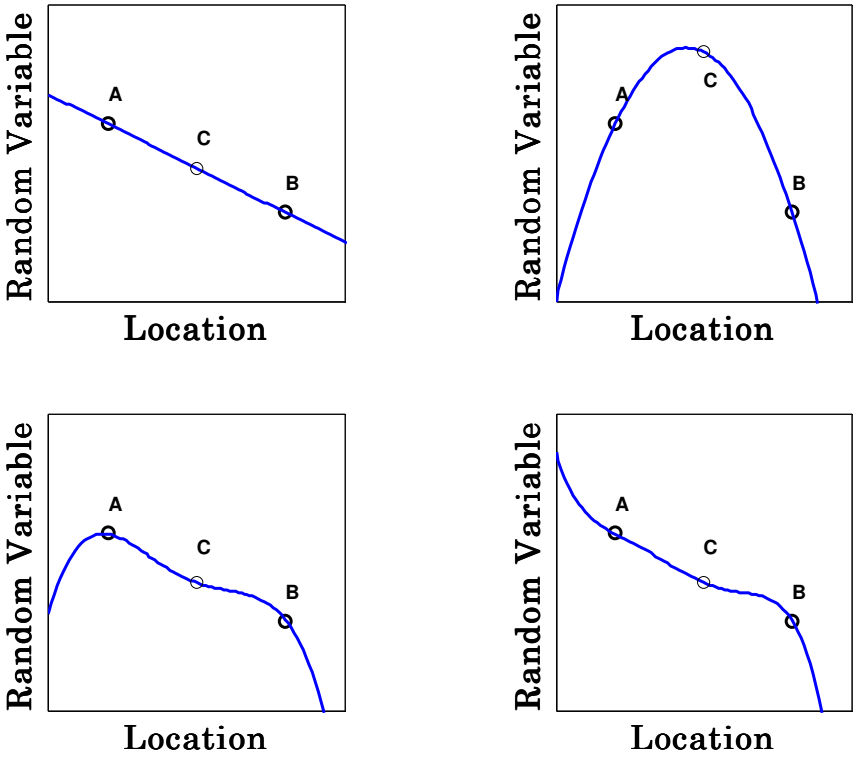

Figure 2.1. Cross-sectional view of a random variable. The random variable is known at locations A and B, but is not known at other locations, such as C.

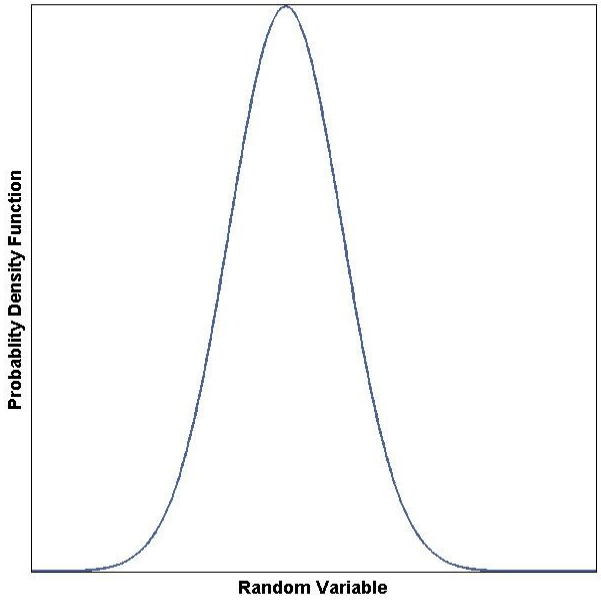

Figure 2.2 Probability density function of a random variable at a location not considered in the sampling process, such as location C in Figure 2.1

2.2.2. The Random Function Concept

A random function is a function that its independent variables are random variables. In other words a random function performs a set of mathematical operation on the random variables.

For instance, in the throwing a single die example, a random function can be defined as the set of values generated by throwing a die and doubling the outcomes. If the random variable (RV) at location **u** is denoted by Z(**u**), a random function (RF) is a set of RV's defined over some field such as porosity and formation thickness. Just as a random variable Z(**u**) is characterized by its conditional distribution function (cdf), a RF

is characterized by the set of all its *N*-variate cdfs for any number *N* and any choice of the *N* locations $\mathbf{u_i}$, i=1,…,*N* within the study area A:

$$F(\mathbf{u}_1,...,\mathbf{u}_n;z_1,...,z_n) = \text{Prob}\{Z(\mathbf{u}_1) \le z_1,...,Z(\mathbf{u}_N) \le z_N\} \quad (2.1)$$

Similar to the univariate cdf of the RV $Z(\mathbf{u})$, that is used to characterize uncertainty about the value $z(\mathbf{u})$, the multivariate cdf in Eq.(2.1) is used to characterize joint uncertainty about the *N* values $z(\mathbf{u}_1),\ldots, z(\mathbf{u}_N)$. Particularly, this is important when using the bivariate (*N*=2) cdf of any two RVs $Z(\mathbf{u_1})$, $Z(\mathbf{u_2})$. In fact, conventional geostatistical procedures are restricted to univariate ($F(\mathbf{u},z)$) and bivariate distributions defined as:

$$F(\mathbf{u}_1,\mathbf{u}_2;z_1,z_2) = \text{Prob}\{Z(\mathbf{u}_1) \le z_1, Z(\mathbf{u}_2) \le z_2\} \quad (2.2)$$

2.2.3. Stationary Constraints

The assumption of stationarity is an essential assumption in geostatistical analysis. Stationarity means that a random function has certain properties such as mean or covariance that are constant everywhere in the region of interest. The decision of the stationarity, in other words, is the decision of which data should be picked up from region of interest for the analysis. Stationarity is divided into categories; the first order and the second order.

Mathematically, the first order of stationarity can be written as

$$f[Z(\vec{u})] = f[Z(\vec{u}+\vec{L})] \quad (2.3)$$

Where $f[]$ is any function of a random variable, $(\vec{u})$ and $(\vec{u}+\vec{L})$ define the two locations of the random variable. The most commonly used random function in Eq.(2.3) is the expected value. The expected value of the variable itself is an arithmetic mean. That

means that arithmetic means of random variables across the region are the same. Using expected value, Eq.(2.3) is written as:

$$E[Z(\vec{u})] = E[Z(\vec{u} + \vec{L})] \tag{2.4}$$

That is, the expected value of a random variable at $(\vec{u})$ is the same as the expected value of a random variable $\vec{L}$ lag distance away. The value of $\vec{L}$ can vary from zero to the maximum distance between variables within the region of interest. If the region of interest divided into small subregions, and within each subregions the mean or expected value of samples are calculated (assuming that adequate numbers of samples are present within each subregion), those means should remain fairly close to each other assuming first order of stationarity. If the means vary significantly, the assumption of stationarity may not hold. Also the first order of stationarity may not hold if the sampled data have a strong trend.

The second order of stationarity can be mathematically defined as:

$$f[Z(\vec{u}_1), Z(\vec{u}_1 + \vec{L})] = f[Z(\vec{u}_2), Z(\vec{u}_2 + \vec{L})] \tag{2.5}$$

This relationship indicates that any function of two random variables located *L* distance apart is independent of the location and is a function of only the distance and the direction between the two locations. The arrows over the *u* and *L* indicate that locations can be treated in terms of vectors rather than distances.

In practice, covariance can be used as one of the functions that relate two variables located a certain distance and direction apart. In other words,

$$C[Z(\vec{u}_1), Z(\vec{u}_1 + \vec{L})] = C[Z(\vec{u}_2), Z(\vec{u}_2 + \vec{L})] \tag{2.6}$$

That is, the covariance within the region of stationarity is function of only the vector *L*, not the variable itself. This is an important assumption that implies by knowing the distance and direction between any two points, the covariance between the random variables at these two points can be estimated without knowing the actual random variable at those locations.

2.2.4. Covariance Function

Computational procedures used to present the statistics of a single random variable can be extended to calculate the joint variability of pair random variables. In bivariate statistics, the covariance function is a tool that is employed to present the joint statistics of two RVs. For two random variables $Z_1(\mathbf{u}), Z_2(\mathbf{u})$, the covariance function at two locations $\mathbf{u_1}$ and $\mathbf{u_2}$ is defined as:

$$C(\mathbf{u_1}, \mathbf{u}_2) = E[\{Z(\mathbf{u_1}) - \mu(\mathbf{u_1})\}\{Z(\mathbf{u}_2) - \mu(\mathbf{u}_2)\}] \tag{2.7}$$

where *E* is the expected value or mean of the expression, $\mu(\mathbf{u}_1)\ and\ \mu(\mathbf{u}_2)$ are the means of *Z* at $\mathbf{u_1}$ and $\mathbf{u_2}$ respectively. Assuming first order stationarity that the mean of the random variable is constant everywhere, Eq.(2.7) can be rewritten as:

$$C(\mathbf{u_1}, \mathbf{u}_2) = E[\{Z(\mathbf{u_1})Z(\mathbf{u}_2)\} - \mu^2] \tag{2.8}$$

Experimental covariance can be calculated as:

$$c(\vec{L}) = \frac{1}{n(\vec{L})}\sum_{i=1}^{n(\vec{L})} z(\vec{u}_i)z(\vec{u}_i + \vec{L}_i) - \left[\frac{1}{n}\sum_{i=1}^{n(\vec{L})} z(\vec{u}_i)\right]^2 \tag{2.9}$$

Where $n(\vec{L})$ is the number of pairs at vector distance *L*; $z(\vec{u}_i)$ and $z(\vec{u}_i+\vec{L})$ are values of the variable at locations $\vec{u}_i$ and $\vec{u}_i+\vec{L}$ respectively, and *n* is the total number of sample

points. The second term in Eq.(2.9) represents the arithmetic mean of all the data points. As a special case, the definition at $\vec{L}=0$ is $c(0)=\frac{1}{n}\sum_{i=1}^{n} z(\vec{u}_i)z(\vec{u}_i)-\bar{x}^2$. This is the definition of variance. The covariance decreases from variance at the origin and often reaches zero at a certain distance r termed the range or correlation length. In other words, when the covariance is zero, there is no relationship between the two random variables. A typical covariance for a random variable is shown in Figure 2.3 in which *Co* and *r* represents variance and range of the sample data.

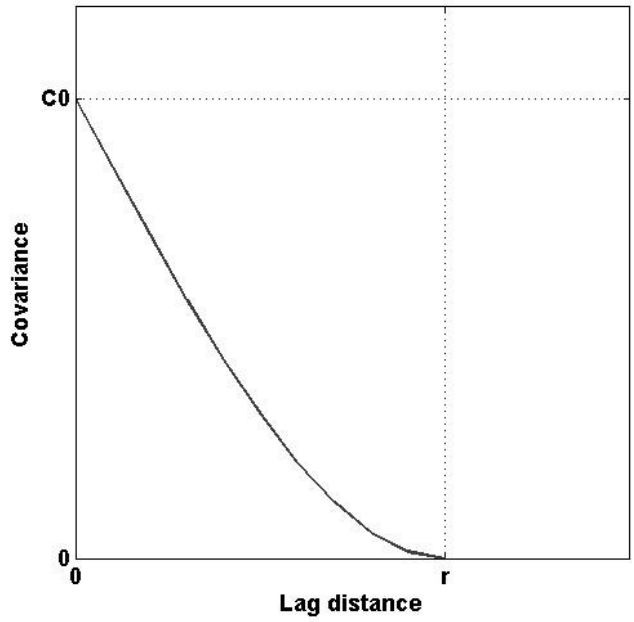

Figure 2.3. A typical covariance function for a random variable

2.2.5. Semivariograms

The semivariogram is the most commonly used geostatistical technique for describing the spatial relationship of random variables. Mathematically, semivariogram is defined as:

$$\gamma(\vec{L}) = \frac{1}{2}\sigma^2\left[Z(\mathbf{u}+\vec{L}) - Z(\mathbf{u})\right] = \frac{1}{2}\left(\mathrm{E}\left\{\left[\mathrm{Z}(\mathbf{u}) - \mathrm{Z}(\mathbf{u}+\vec{\mathrm{L}})\right]^2\right\}\right) - \left(\mathrm{E}\left\{\left[\mathrm{Z}(\mathbf{u}) - \mathrm{Z}(\mathbf{u}+\vec{\mathrm{L}})\right]\right\}^2\right) \tag{2.10}$$

It is half of the variance of the difference between the two values of a random variable located L distance apart. Assuming the first order stationarity the second term on the right side of Eq.(2.10) is equal zero. As a result, the semivariogram is rewritten as:

$$\gamma(\vec{L}) = \frac{1}{2}E[\{Z(\mathbf{u}+\vec{L}) - Z(\mathbf{u})\}^2] \tag{2.11}$$

Under the decision of stationarity the covariance and semivariogram functions are related tools for characterizing two-point correlation:

$$C(\vec{L}) = C(0) - \gamma(\vec{L}) \tag{2.12}$$

where $C(0)$ is the covariance function at L=0. Eq.(2.12) indicates that the difference between the two function increases as the distance increases. Experimentally, the semivariogram for lag distance $\vec{L}$ is defined as the average squared difference of values separated approximately by $\vec{L}$:

$$\gamma(\vec{L}) = \frac{1}{n(\vec{L})}\sum_{i=1}^{n(\vec{L})}[z(\vec{\mathbf{u}}+\vec{L}) - z(\vec{\mathbf{u}})]^2 \tag{2.13}$$

where $n(\vec{L})$ is the number of pairs at vector distance $\vec{L}$; $z(\mathbf{u})$ and $z(\mathbf{u}+\vec{L})$ are the data values for the ith pair located $\vec{L}$ lag distance apart. Semivariogram can be calculated for several directions in 3D space. The semivariogram increases from zero at the origin and

often reaches a plateau at a certain distance, which is termed the range or correlation length. The plateau is termed the sill and corresponds to the statistical variance of the sample data set. There is no correlation between the random variables beyond the range of the semivariogram. Figure 2.4 represents a typical semivariogram for a random variable.

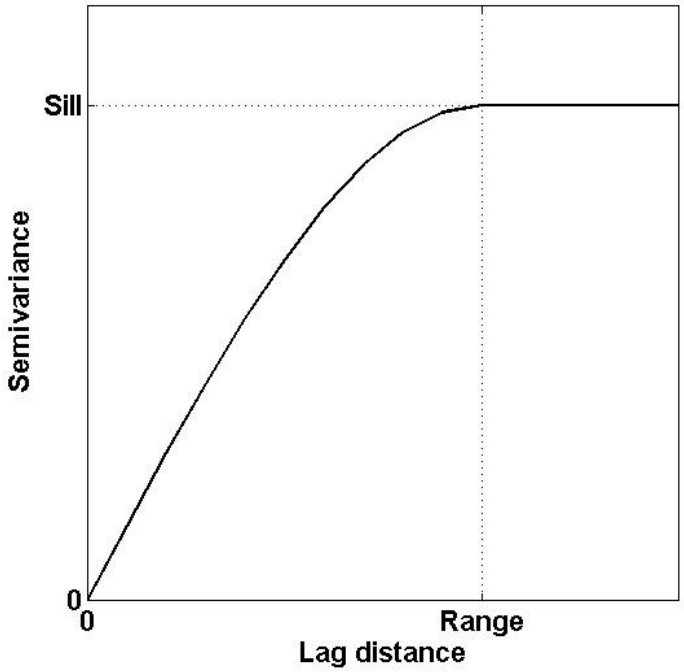

Figure 2.4. A typical semivariogram function for a random variable

2.2.6. Cross-variograms

Cross-variogram and the corresponding cross-covariance represent the spatial relationship between two random variables located a certain lag distance apart. Considering permeability and porosity as two random variables, for instance, a cross variogram can be applied to determine whether these two variables are spatially related at different lag distances apart. If such a relationship exists, it is possible to improve the

estimation of a random variable at the unsampled location. Mathematically, the cross variogram is defined as:

$$\gamma_c(\vec{L}) = \frac{1}{2} E[\{Z_1(\mathbf{u}) - Z_1(\mathbf{u}+\vec{L})\}\{Z_2(\mathbf{u}) - Z_2(\mathbf{u}+\vec{L})\}] \tag{2.14}$$

where E is the expected value, and Z_1, Z_2 are *RVs* representing the permeability and porosity respectively. Experimentally, the cross-variogram is estimates as:

$$\gamma_c(\vec{L}) = \frac{1}{2n(\vec{L})} \sum_{i=1}^{n(\vec{L})} [z_1(\mathbf{u}) - z_1(\mathbf{u}+\vec{L})][z_2(\mathbf{u}) - z_2(\mathbf{u}+\vec{L})] \tag{2.15}$$

Where $n(\vec{L})$ is the number of pairs at vector distance $\vec{L}$; and z_1, z_2 are the values of two properties at locations that are $\vec{L}$ distance apart. Obviously, the estimation of cross experimental cross variogram requires that both variable values be available at different locations.

2.2.7. Mathematical Modeling of a Spatial Function

The primary purpose in estimating a semivariogram or covariance is to use them to estimate values of the random variable at unsampled locations. However, these spatial functions are only available at limited lag distances. There are desired lag-distances for which the corresponding semivariogram value is not available. Hence, it is necessary to develop a mathematical model that could be used for any lag distance in the estimation process. Such a mathematical model must match closely with the estimated semivariogram at available lag distances.

For the mathematical modeling of an experimental semivariogram, two requirements must be considered. The first is to use of the minimum number of

parameters in the mathematical model to make it simple. In other words, the most important features of an estimated variogram must be captured with as a few parameters as possible. That means the model does not need to pass through every estimated semivariogram value. The second requirement is the condition of positive definiteness [34]. In other words, Any model used to match the experimental semivariogram or covariance data should satisfy this requirement which ensures a unique solution for the estimation procedure.

There are several models in the literature that satisfy the above requirement. Figure 2.5 represents three transitions semivariogram models. The choice of mathematical models for a matching process depends on the behavior of the experimental data near the origin. For instance, if the underlying phenomenon is continuous, the estimated spatial function will likely show a parabolic behavior near the origin, and the Gaussian semivariogram model will usually provide the best fit for this case. When there is discontinuity among the estimated semivariogram values near the origin, a nugget model is considered for matching process. The nugget model indicates total lack of information with respect to the spatial relationship.

Nugget signifies the lack of quantitative information about the random variable under the study. There are two reasons for observing nugget effect discontinuity. First, the shortest distance at which the sample pairs are available may be greater than the range of the variogram. The second is the measurement errors that add uncertainty in the

estimation process. Figure 2.5 indicates a Nugget model. In the figure, the abrupt increase of semivariogram values from 0 to C_0 shows the nugget effect.

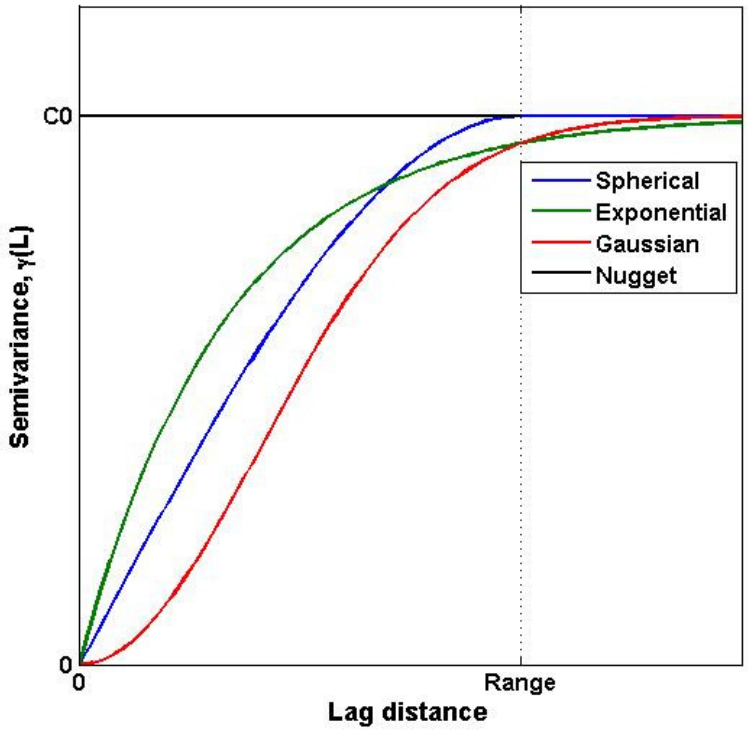

Figure 2.5. Basics semivariogram models with sill

In addition, a linear combination of any of the four semivariogram mathematical models described above could be used to match a given experimental semivariogram. Mathematically, these combinations are shown as follows:

$$\gamma(\vec{L}) = a_0 + \sum_{i}^{N} a_i \gamma_i(\vec{L}) \tag{2.16}$$

where a_0 represents the nugget effect and $a_i's$ show the contribution of other semivariogram model.

2.3. Conventional Estimation Techniques

In principle, all estimation techniques assume that the value at the unsampled location is estimated by

$$Z^*(\vec{u}_0) = \sum_{i=1}^{n} \lambda_i Z(\vec{u}_i) \tag{2.17}$$

Where $Z^*(\vec{u}_0)$ is the estimated value at the unsampled location, $Z(\vec{u}_i)$ is the value at neighboring location $\vec{u}_i$, and λ_i is the weight assigned to any neighboring value $Z(\vec{u}_i)$. That is to say the estimated value is a weighted average of the neighboring values. The goal in the estimation procedure is to calculate the weights assigned to the individual neighboring points.

Different techniques have been proposed for the estimation based on finding the weights to the points in the neighborhood region [17,21,34,35,46]. The neighborhood region defines the neighboring sample points used in estimating values at the unsampled location. In the following sections some of these methods will be reviewed.

2.3.1. Cell De-clustering

In practice, sample data are rarely collected to represent statistical properties. For instance, wells are often drilled in areas with greater probability of good reservoir quality not with purpose of finding the permeability at the location. This is the same for core measurements. In this situation, the sample data are clustered in some area.

In the cell de-clustering approach, the entire area is divided into rectangular regions called cells. Each sample receives a weight inversely proportional to the number of samples that fall within the same cell. As a result, the clustered samples generally receive lower weights. This is because the cells in which they are located also contain several other samples. Figure 2.6 shows a grid of cells superimposed on a number of clustered samples. The dashed lines show the boundaries of cells. The two cells in the north contain only one sample; so both of these samples receive a weight of one. On the other hand, the southwestern cell contains two samples, both of which receive a weight of 1/2. Also, the southeastern cell contains eight samples that receive a weight of 1/8. The cell de-clustering method can be viewed as a two-step procedure. In the first step, sample data are used to calculate the mean value within the cells, and then the mean of these samples is used for calculation at unsampled locations.

2.3.2. Inverse Distance Method

Inverse distance methods estimate the value of the random variable at an unsampled location by assigning a larger weight to closest sample and a smaller weight to the farthest one. This is possible by weighting each sample in a data set inversely proportional to its distance from unsampled locations. Mathematically, it is defined as follows:

$$Z^*(\vec{u}_0) = \frac{\sum_{i=1}^{n} \frac{1}{d_i^{\,p}} Z(\vec{u}_i)}{\sum_{1}^{n} \frac{1}{d_i^{\,p}}} \tag{2.18}$$

where d_i is the distances from each of the n sample locations to the point being estimated and p is an arbitrary constant. Traditionally, the most common choice for p is 2 since it results in fewer calculations.

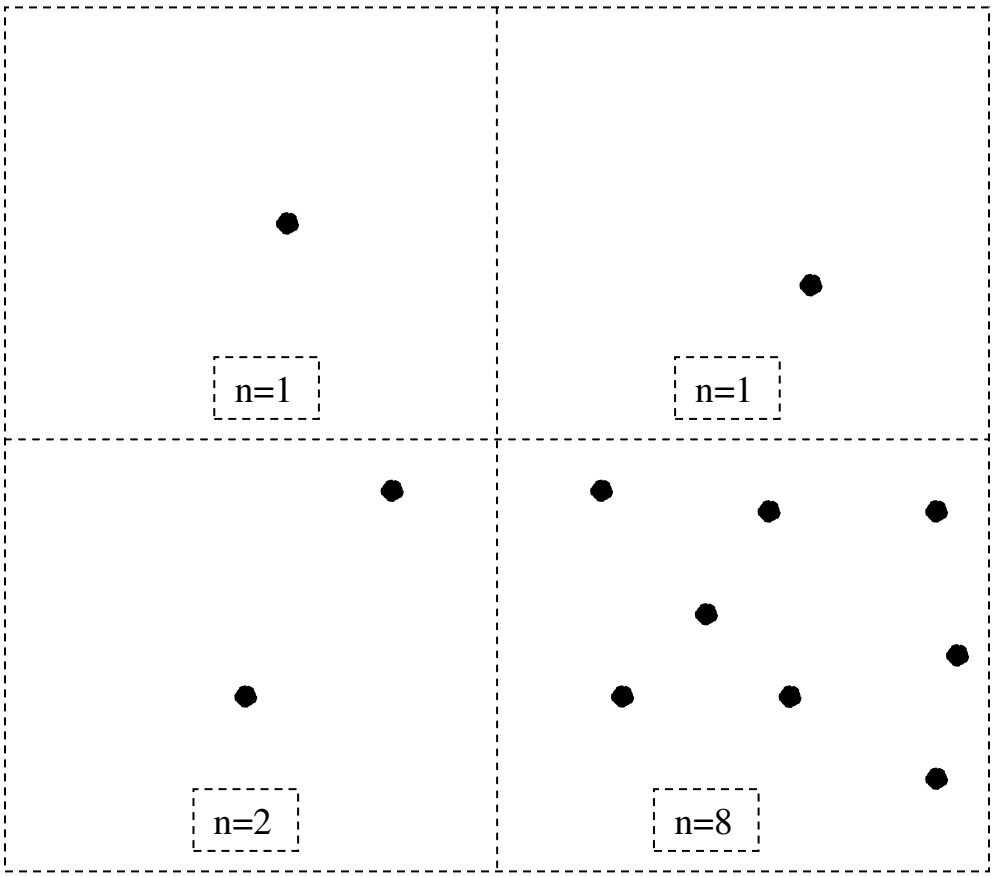

Figure 2.6. An example of cell declustering

2.3.3. Simple Kriging

Simple kriging starts with assumption that the value of a random variable at an unsampled location could be estimated as follows:

$$Z^*(\vec{u}_0) = \lambda_0 + \sum_{i=1}^{n} \lambda_i Z(\vec{u}_i) \tag{2.19}$$

The value of λ_i is estimated by using MUVE (Minimum Variance Unbiased Estimate) criterion. An unbiased condition requires that:

$$E(Z^*(\vec{u}_0) - Z(\vec{u}_0)) = 0 \tag{2.20}$$

Substituting $Z^*(\vec{u}_0)$ from Eq.(2.19),

$$\lambda_0 + \sum_{i=1}^{n} \lambda_i E[Z(\vec{u}_i)] = E[Z(\vec{u}_0)] \tag{2.21}$$

By assuming first order stationarity condition, $E[Z(\vec{u}_i)] = E[Z(\vec{u}_0)]$ it can be written

$$\lambda_0 = m(1 - \sum_{1}^{n} \lambda_i) \tag{2.22}$$

In addition to unbiased criterion in Eq.(2.20), the condition of minimum variance must also be satisfied. Mathematically, weights (λ_i) are chosen in a manner that $\sigma^2[Z^*(\vec{u}_0) - Z(\vec{u}_0)]$ is minimized. The result of this condition is as follows:

$$\sum_{i}^{n} \lambda_i C(\vec{u}_i, \vec{u}_j) = C(\vec{u}_i, \vec{u}_0) \;\; for\, i, j = 1,...,n \tag{2.23}$$

Where $C(\vec{u}_i, \vec{u}_j)$ is the covariance value between points located at $\vec{u}_i$ and $\vec{u}_j$ respectively, and $C(\vec{u}_i, \vec{u}_0)$ is the covariance between the sampled location, $\vec{u}_i$, and the unsampled location $\vec{u}_0$. The covariance values are obtained based on the spatial model. In matrix form, Eq.(2.23) can be written as

$$\begin{bmatrix} C(u_1,u_1) & . & . & . & C(u_1,u_{1n}) \\ . & & & & . \\ . & & & & . \\ . & & & & . \\ C(u_n,u_1) & . & . & . & C(u_n,u_n) \end{bmatrix} \begin{bmatrix} \lambda_1 \\ . \\ . \\ . \\ \lambda_n \end{bmatrix} = \begin{bmatrix} C(u_1,u_0) \\ . \\ . \\ . \\ C(u_n,u_0) \end{bmatrix} \tag{2.24}$$

Rearranging the above equation in compact matrix, the weight matrix is calculated as follows:

$$|\Lambda| = |C|^{-1}|c| \tag{2.25}$$

Eq.(2.25) states that the weights assigned to the samples are directly proportional to $|c|$ and inversely proportional to $|C|$, where $|c|$ represents the covariance between the sample point and the unsampled location. The stronger the spatial relationship between the sample point and the unsampled location, the larger is the value of $C(\vec{u}_i, \vec{u}_0)$. As a result, the weight assigned to the sample point at $\vec{u}_i$ is greater. On the other hand, $|C|$ represents the covariance among the sampled points. If a particular sample point at u_i is very close to the surrounding sample points (i.e. clustered sampled), $|C|$ will be large and $|C|^{-1}$ will be small, and as a result the weight assigned to sample point will be reduced. If sample points are clustered together, they do not receive large weights because they do not provide independent information on an individual basis.

In summary, the weight assigned to an individual sample is dependent on two factors. One is its spatial relationship to the unsampled location. The stronger the relationship, the larger is the assigned value. The second factor is the sample point's spatial relationship to other sample point. The stronger the relationship, the less independent information that point can provide. In addition to the estimation, error variance associated with the estimation can be calculated as follows:

$$\hat{\sigma}^2{}_E = C(\vec{u}_0, \vec{u}_0) - \sum_1^n \lambda_i C(\vec{u}_i, \vec{u}_0) \tag{2.26}$$

By examining Eq.(2.26) it is observed that the maximum value of the error variance is $C(\vec{u}_0, \vec{u}_0)$ (data variance). It means that in the absence of spatial information, uncertainty with respect to estimation is represented by the variance of the data. As spatial relationship information becomes available, error variance is reduced.

2.3.4. Ordinary Kriging

In the simple kriging procedure, it is assumed that the mean value *m(u)* is known. In practice, however, the true global mean is rarely known unless it is assumed that the sample mean is the same as global mean. Besides, the local mean within the search neighborhood may vary over the region of interest. As a result, the assumption of first order stationarity may not be strictly valid for the estimation process. The ordinary kriging method was developed to overcome this problem by redefining the estimation equation.

Considering Eq.(2.20), and $E[Z(\vec{u}_i)] = E[Z(\vec{u}_0)] = m(\vec{u}_0)$, where $m(\vec{u}_0)$ represents the mean within the search neighborhood of location $\vec{u}_0$, then Eq.(2.22) could be written in the following form:

$$\lambda_0 = m(\vec{u}_0)(1 - \sum_{1}^{n} \lambda_i) \tag{2.27}$$

It is possible to force λ_0 to be zero by assuming,

$$\sum_{1}^{n} \lambda_i = 1 \tag{2.28}$$

Then, the estimation equation is written as:

$$Z^*(\vec{u}_0) = \sum_{i=1}^{n} \lambda_i Z(\vec{u}_i) \tag{2.29}$$

The necessity of having the mean value is also eliminated by forcing λ_0 to be zero. Furthermore, using this constraint in Eq.(2.28) (the minimum variance criterion) results in:

$$\sum_{i}^{n} \lambda_i C(\vec{u}_i, \vec{u}_j) + \mu = C(\vec{u}_i, \vec{u}_0) \quad for\ i, j = 1,...,n \tag{2.30}$$

Where μ is called a Lagrange parameter, and C represents the covariance. In matrix form, Eq.(2.30) is written as:

$$\begin{bmatrix} C(u_1,u_1) & . & . & . & C(u_1,u_n) \\ . & & & & . \\ . & & & & . \\ C(u_n,u_1) & & & & C(u_n,u_n) \\ 1 & 1 & . & 1 & 0 \end{bmatrix} \begin{bmatrix} \lambda_1 \\ . \\ . \\ \lambda_n \\ \mu \end{bmatrix} = \begin{bmatrix} C(u_1,u_0) \\ . \\ . \\ C(u_n,u_0) \\ 1 \end{bmatrix} \tag{2.31}$$

Once λ_i is calculated, the error variance can be estimated by

$$\hat{\sigma}^2{}_E = C(\vec{u}_0, \vec{u}_0) - \sum_{1}^{n} \lambda_i C(\vec{u}_i, \vec{u}_0) - \mu \tag{2.32}$$

2.3.5 Indicator Kriging

The main idea behind the indicator kriging is to code all of the data in a common format as probability values. The main advantage of this approach is simplified data integration due to the common probability coding. The comparative performance of indicator methods has been studied extensively by Goovarets [33].

An indicator variable is essentially a binary variable which takes the values 1 and 0 only. Typically such variable denotes presence or absence of a property. For a continuous variable, the equation for an indicator transform is written as:

$$I(\vec{u}_j, z_t) = \begin{cases} 1 \; if \;\; Z(\vec{u}_j) \le z_t \\ 0 \; if \;\; Z(\vec{u}_j) > z_t \end{cases} \tag{2.33}$$

Where $I(\vec{u}_j, z_t)$ is the indicator value, $Z(\vec{u}_j)$ is the value of the random variable at $\vec{u}_j$, and z_t is the threshold value. Depending on the value of $Z(\vec{u}_j)$ the indicator value could take either a value of one or zero. Similar to a continuous variable, an equation for a discrete variable is written as:

$$I(\vec{u}_j, K_t) = \begin{cases} 1 \; if \;\; K(\vec{u}_j) = K_t \\ 0 \; if \;\; K(\vec{u}_j) \ne K_t \end{cases} \tag{2.34}$$

K_t represents a threshold value. Depending on whether the sample value is equal or not equal to the threshold value, the indicator variable can take either a value of zero or one.

For both continuous and discrete variables it is helpful to understand the indicator variable in terms of the confidence in a sample value. If there is 100% confidence about a sample, indicator values are defined in terms of zero or one. On the other hand, a value between zero and one represents the uncertainty in the sampled value. This provides flexibility in assigning probability values when information about particular sample point is incomplete.

The goal of indicator kriging is to directly estimate the distribution of uncertainty $F_z(\boldsymbol{u})$ at unsampled location $\boldsymbol{u}$. The cumulative distribution function is estimated at a

series of threshold values: $z_k, k=1,\ldots,K$. For instance, Figure 2.7 shows probability values at five threshold ($K=5$) values that provide a distribution of uncertainty at unsampled location **u**. The probability values are evaluated by coding the data as indicator value or probability values. The correct selection of the threshold values z_k for the indicator kriging is important. Selection of too many threshold values makes the inference and computation needlessly tedious and expensive. On the other hand, with too few thresholds the distribution details are lost.

After selecting the threshold values, the indicator variogram is calculated and fitted by a mathematical model for each threshold value. Once the indicator values at each threshold are defined, the next step is to estimate the spatial relationships or semivariograms. The number of semivariograms depends on the number of thresholds. For a continuous variable, such as permeability, if high permeability values exhibit different continuity than low permeability values, indicator approach provides the flexibility to model different levels of permeability with different semivariograms.

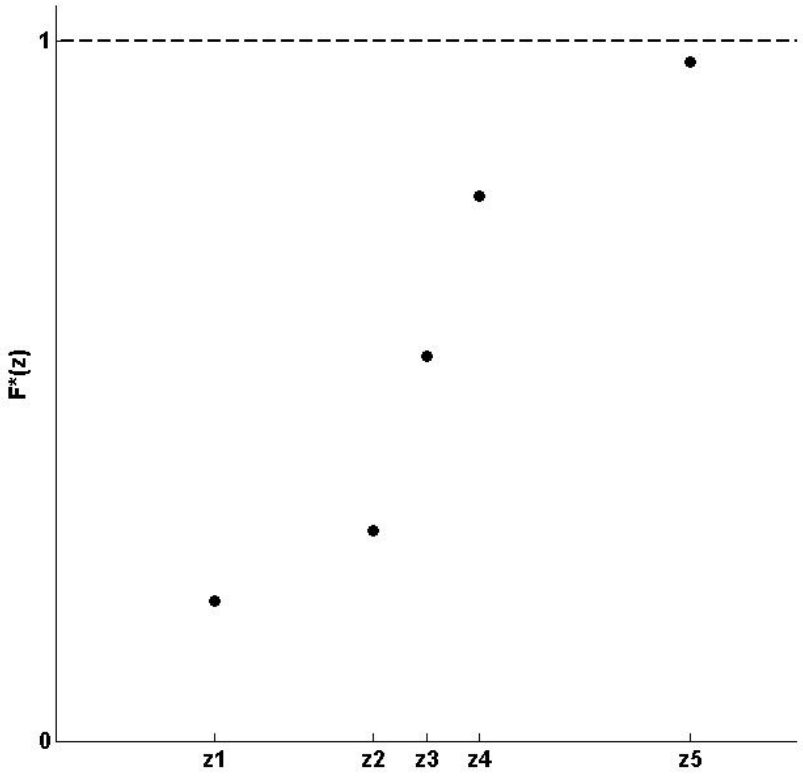

Figure 2.7. Schematic illustration of probability distribution *F(z)* at a series of five threshold values, z_k, $k=1,...,5$ [35]

The final step is to estimate an indicator value at unsampled locations. The approach is the same as the one for conventional kriging, except the kriging procedure is repeated at each threshold. For ordinary kriging the equation is:

$$I^*(\vec{u}_0, z_t) = \lambda_0 + \sum_{j=1}^{n} \lambda_j I(\vec{u}_j, z_t) \tag{2.35}$$

And for simple kriging the equation is:

$$I^*(\vec{u}_0, z_t) = \sum_{j=1}^{n} \lambda_j I(\vec{u}_j, z_t) \tag{2.36}$$

Because the weights assigned to sample points fall between zero and one, and the indicator values are between zero and one, the estimate from both equation fall between zero and one. After all unsampled points are visited; the indicator value for each threshold at each location is available. The estimate depends on whether indicator kriging used for continuous or discrete variables. Figure 2.8 represents possible estimates that could be obtained for continuous variables. For example, location (a) for continuous variable indicates that there is 20% probability that the value at that location is less than the first threshold.

A similar explanation could be given for the other thresholds. By examining the probabilities for the location (b) in Figure 2.8, the probability of a sample value occurring between the second and third thresholds is 0.9-0.2=0.7. This high probability shows that the value falls within that interval.

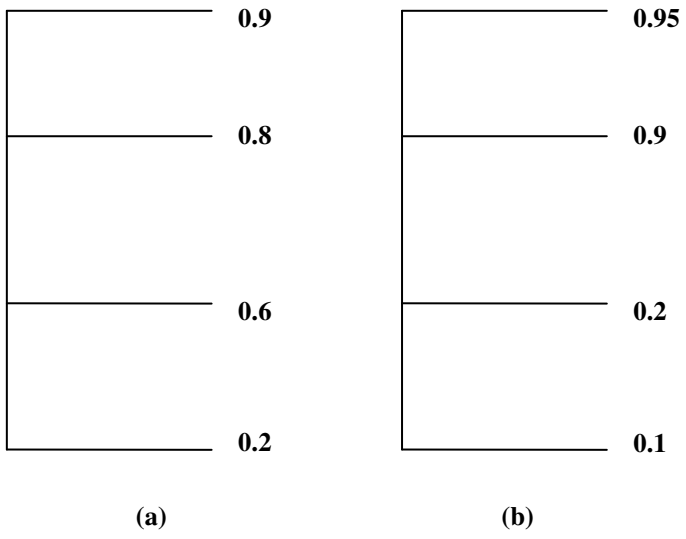

Figure 2.8. Uncertainty estimation in indicator kriging

2.3.6. Co-kriging

The term co-kriging is reserved for linear regression that correlates data that is defined with different attributes. Basically, the goal in co-kriging is to improve the estimate and reduce the uncertainty in the kriging estimation with the help of spatial information available from other variables. The implicit assumption in the process is the variable of interest and the other variables are spatially related to each other. For instance, to improve reservoir description, permeability can be estimated by using porosity data. This could be beneficial to permeability estimation since typically, a few wells are cored but almost all wells are logged. By establishing a spatial relationship between porosity and permeability data, the estimation of permeability at unsampled location could be improved by the surrounding porosity data.

The limitation of co-kriging is that the variables must be linearly related to each other. Therefore, it is critical to check the relationship between the variable of interest (principle variable) and the supporting variables (covariables). Furthermore, the application of co-kriging requires a substantial spatial modeling and additional computational effort compared to an ordinary kriging system.

Mathematically, if *n* and *m* are the number of samples of the principal variables and covariable *Y* respectively, then

$$Z^*(\vec{u}_0) = \sum_{i=1}^{n} \lambda^*_{z_i} Z(\vec{u}_i) + \sum_{k=1}^{m} \lambda^*_{Y_k} Y(\vec{u}_{Y_k}) \tag{2.37}$$

Where $\lambda^*_{z_i}$ is the weight assigned to the sample $Z(\vec{u}_i)$ and $\lambda^*_{Y_k}$ is the weight assigned to the sample $Y(\vec{u}_{Y_k})$.

From Eq.(2.37) and the unbiased condition, $E(Z^*(\vec{u}_0) - Z(\vec{u}_0)) = 0$ we can write

$$m_x \sum_{i=1}^{n} \lambda_{Z_i} + m_Y \sum_{k=1}^{n} \lambda_{Y_k} - m_z = 0 \tag{2.38}$$

Where m_z and m_Y are the expected values of the *Z* and *Y* variables, respectively.

The following equations are written to satisfy the unbiased condition,

$$\sum_{i=1}^{n} \lambda_{Z_i} = 1 \qquad \sum_{i=1}^{n} \lambda_{Y_i} = 1 \tag{2.39}$$

Finally, by minimizing the variance, the following equation in matrix form can be solved to calculate the weights, λ_i

$$\begin{bmatrix}
C_Z(\vec{u}_{Z_1},\vec{u}_{Z_1}) & ... & C_Z(\vec{u}_{Z_1},\vec{u}_{Z_n}) & C_C(\vec{u}_{Z_1},\vec{u}_{Y_1}) & ... & C_C(\vec{u}_{Z_1},\vec{u}_{Y_m}) & 1 & 0 \\
. & ... & & ... & ... & ... & ... & ... \\
C_Z(\vec{u}_{Z_1},\vec{u}_{X_n}) & ... & C_Z(\vec{u}_{Z_n},\vec{u}_{Z_n}) & C_C(\vec{u}_{Z_n},\vec{u}_{Y_1}) & ... & C_C(\vec{u}_{Z_n},\vec{u}_{Y_m}) & 1 & 0 \\
C_C(\vec{u}_{Z_1},\vec{u}_{Y_1}) & ... & C_C(\vec{u}_{Z_n},\vec{u}_{Y_1}) & C_Y(\vec{u}_{Y_1},\vec{u}_{Y_1}) & ... & C_Y(\vec{u}_{Y_1},\vec{u}_{Ym}) & 0 & 1 \\
... & ... & ... & ... & ... & ... & ... & ... \\
C_C(\vec{u}_{Z_1},\vec{u}_{Y_m}) & ... & C_C(\vec{u}_{Zn},\vec{u}_{Y_m}) & C_Y(\vec{u}_{Y_1},\vec{u}_{Y_1}) & ... & C_Y(\vec{u}_{Y_1m},\vec{u}_{Ym}) & 0 & 1 \\
1 & ... & 1 & 0 & ... & 0 & 0 & 0 \\
0 & ... & 0 & 1 & ... & 1 & 0 & 0
\end{bmatrix} \tag{2.40}$$

$$\begin{bmatrix}
\lambda_{Z_1} \\
. \\
\lambda_{Zn} \\
\lambda_{Y_1} \\
. \\
\lambda_{Yn} \\
\mu_Z \\
\mu_Y
\end{bmatrix} =
\begin{bmatrix}
C_Z(\vec{u}_{0,}\vec{u}_{Z_1}) \\
.. \\
C_Z(\vec{u}_{0,}\vec{u}_{Z_n}) \\
C_C(\vec{u}_{0,}\vec{u}_{Y_1}) \\
... \\
C_C(\vec{u}_{0,}\vec{u}_{Y_n}) \\
1 \\
0
\end{bmatrix}$$

Where C_Z and C_Y are the covariance for the Z and Y variables, C_C is the cross covariance, and μ_Z and μ_Y are the Lagrange parameters. It is clear that the matrix size in co-kriging technique is much bigger than ordinary kriging.

The expression for error variance, which is an indication of relative sample variogram, is as follows:

$$\hat{\sigma}^2{}_E = C(\vec{u}_0,\vec{u}_0) - \sum_1^n \lambda_{Z_i} C(\vec{u}_{Zi},\vec{u}_0) - \sum_1^n \lambda_{Y_k} C(\vec{u}_{Y_k},\vec{u}_0) - \mu_Z \qquad (2.41)$$

One of the difficulties existed in co-kriging method is that sometimes the estimate of principle variable at unsampled location is overwhelmed by the covariable samples in search neighborhood. To avoid such conditions, different search neighborhoods are defined for principle variables and covariables.

2.3.7. Monte-Carlo simulation techniques

An estimation technique such as kriging uses the assumed spatial relationship (the geological continuity model) between the data and the unknown to produce a single best guess of the unknown. When kriging is applied to a grid of unsampled values, for instance Figure 2.9, the resulting estimates shows a clear deviation from actual geological phenomena.

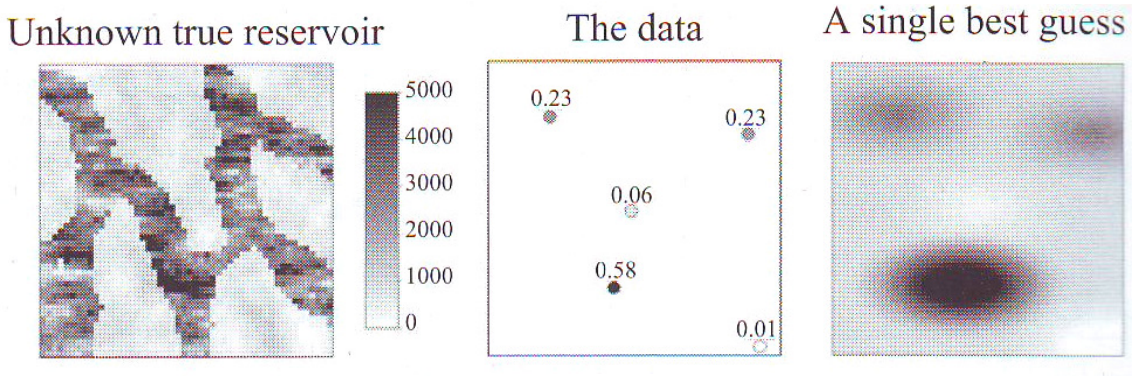

Figure 2.9. Lack of true geological continuity in kriging estimation [36]

The kriging results cannot be identical to the actual phenomenon simply because of limited sample data. It is also important to note that the spatial continuity displayed by a map of kriged estimates is smoother than that of the true unknown. This observation is true for any other spatial estimation or interpolation technique. The reason is that kriging and other interpolation techniques attempt to produce a best estimate at each unsampled location. A conservative estimate is required to obtain an estimate that is as close as possible to the true value at each location. Eq.(2.27) defines a measure of conservatism. Because kriging is inherently conservative and the estimates cannot be too extreme at the risk of being too far off the true value. Consequently, estimation models are said to be locally accurate in that they seek to minimize local errors independently of what the global map of estimates may look like.

Accurate prediction of fluid flow in a subsurface formation depends on how well the data reflect the overall geological continuity in terms of permeability. Such an accurate prediction requires the use of a model that provides an accurate global representation of the subsurface heterogeneity. Stochastic simulation is a geostatistical

tool for generating numerical models that aim to honor the more realistic global representation of the subsurface heterogeneity. Stochastic simulation (or conditional simulation) technique is a procedure that simulates various attributes at unsampled locations and is conditioned by prior information. The main idea in simulation techniques is that attributes are simulated rather than estimated. In other words, the overall goal of simulation techniques is to simulate a reality rather than to obtain a picture of the reservoir which minimizes error variance. These techniques constitute a part of a broader class of simulation techniques and are called Monte Carlo simulations. In the following, some of the more common simulation techniques that are used to generate a stochastic random field are reviewed.

2.4. Review of Sequential Simulation

Sequential Simulation [37], and more specifically sequential Gaussian simulation (SGSIM [5]), was introduced as a solution to the smoothing problem of kriging. Sequential simulation algorithms are 'globally' correct in that they reproduce a global structured statistics such as a variogram model, whereas kriging is 'locally' accurate in that it provides at each location a best estimate in a minimum error variance sense, regardless of estimates made at other locations. Since flow in a reservoir is controlled by the spatial disposition of permeability values in the reservoir, sequential simulation algorithms provide more relevant reservoir models that honor the global structure specified by the variogram.

The implementation of sequential simulation consists of reproducing the desired spatial properties through the sequential use of conditional distributions. Consider a set of N random variables $Z(u_\alpha), \alpha = 1,..., N$ defined at N locations u_α. The aim is to generate L joint realizations $z^l(u_\alpha), \alpha = 1,..., N$ with $l = 1, \ldots, L$ of the N random variables, conditional to n available data and then reproducing the properties of a given multivariate distribution. To achieve this goal, the *N-point* multivariate distribution is decomposed into a set of N univariate distributions (conditional cumulative distribution functions or *ccdfs*):

$$\begin{aligned} &F(\mathbf{u}_1,\ldots,\mathbf{u}_N; z_1,\ldots,z_N|(n)) = \\ &\quad F(\mathbf{u}_N; z_N|(n+N-1)) \ \times \\ &F(\mathbf{u}_{N-1}; z_{N-1}|(n+N-2)) \times \ldots \times \\ &F(\mathbf{u}_2; z_2|(n+1)) \ \times \ F(\mathbf{u}_1; z_1|(n)) \end{aligned} \tag{2.42}$$

where $F(\mathbf{u}_N; z_N|(n+N-1)) = \Pr ob\{ Z(\mathbf{u}_N) \le z_{N-1}|(n+N-1)\}$ is the conditional cumulative distribution function (*ccdf*) of $Z(\mathbf{u}_N)$ given the set of n original data values and *(N-1)* realizations $z^l(u_\alpha), \alpha = 1,..., N-1$ of the previously simulated values. The decomposition allows generating a realization by sequentially visiting each node on the simulation grid. In theory, the approach requires a full analytical expression for the *ccdf* at each step. In the following, the two main variogram-based algorithms, sequential Gaussian simulation (SGSIM) and sequential indicator simulation (SISIM), are presented.

2.4.1. Sequential Gaussian Simulation (SGS)

The most straightforward algorithm for generating realizations of a multivariate Gaussian field is provided by the sequential principle described above. Each variable is simulated sequentially according to its normal *ccdf* fully characterized through a simple kriging system of Eq.(2.28). The conditioning data consist of all original data and all previously simulated values found within a neighborhood of the location being simulated. The conditional simulation of a continuous variable $z(\boldsymbol{u})$ modeled by a Gaussian related stationary random function (RF) $Z(u)$ proceeds as follows:

1. Determine the univariate cumulative distribution function ($F_Z(z)$), representative of the entire study area and not only the available z-data. The mean and standard deviation of $F_Z(z)$ is calculated from sample data. Declustering may be needed if the z-data are preferentially located [5], [39].
2. Perform the normal score transform of the *z-data*, with the $F_Z(z)$, into *y-data* with a standard normal *cdf* [5], [37]. This step may be skipped for a random variable such as porosity showing a normal distribution.
3. Although not a part of the algorithm, it is good practice to check for bivariate normality of the normal score *y-data* by comparing the experimental indicator semivariogram to the ones expected from multi-Gaussian theory [5], [40]. If the data do not show a bivariate Gaussian behavior, then alternate models such as an indicator-based approach should be considered.
4. If a multivariate Gaussian RF model is adopted for the y-variable then proceed with sequential simulation, i.e. :

1) Define a random path that visits each node of the grid once. The path should not necessarily be regular. At each node u, retain a specified number of the original and the previously simulated y-data. These data are called neighboring hard conditioning data.
2) Use simple kriging estimation to determine the parameters (mean and variance) of the *ccdf* of the random function $Y(\boldsymbol{u})$ at location **u**.
3) Draw a simulated value $y^{(l)}(\boldsymbol{u})$ from that *ccdf*. $y^{(l)}(\boldsymbol{u})$ is the simulated normal score of $z(u)$ for the realization (1).
4) Add the simulated value $y^{(l)}(\boldsymbol{u})$ to the data set.
5) Proceed to the next node, and loop until all nodes are simulated.
6) Back-transform the simulated normal values $\{y^{(l)}(\mathbf{u}), \mathbf{u} \in A\}$ into simulated values for the original variable $\{z^{(l)}(\mathbf{u}) = \varphi^{-1}(y^{(l)}(\mathbf{u})), \mathbf{u} \in A\}$. Often, it is necessary to perform interpolations and tail extrapolations. See Deutsch and Journel[5] for details.
7) If multiple realizations are desired, the previous algorithm is repeated L times with a different random path for each realization. The prior decision of stationarity requires that simple kriging (SK) with zero mean (for $Y(\boldsymbol{u})$) to be used in step 4 of the SGS algorithm. However, if there are enough data to indicate that a non-stationary RF model would be more appropriate, one may split the area into distinct sub-zones and consider for each sub-zone a different RF model. This implies inference of a different normal score covariance for each sub-zone.

There are a number of implementations of the sequential Gaussian simulation (SGS) algorithms presented in literatures. The program gsim3d.c written by Isaaks [41] and the **sgsim** program of **GSLIB** [5] are two examples.

2.4.2. Sequential Indicator Simulation (SIS)

It is not always necessary to use a parametrical multi-Gaussian random function. Non-parametric indicator Kriging technique can also be implemented in sequential Gaussian simulation. In this approach the conditional probability of the data are directly estimated, using indicator kriging that is applied to binary indicator transforms of the data. If the indicator variable being kriged arises from a categorical variable, i.e., $i(\mathbf{u})$ set to 1 if the location u belongs to category k, to zero otherwise, then:

$$\Pr ob\{i(\mathbf{u}) = 1 | (n)\} = E\{i(\mathbf{u}) | (n)\} \tag{2.43}$$

If the variable $z(\mathbf{u})$ to be simulated is continuous, its ccdf can also be written as an indicator conditional expectation:

$$\Pr ob\{Z(\mathbf{u}) \le z | (n)\} = E\{i(\mathbf{u}; z) | (n)\} \tag{2.44}$$

with $i(\mathbf{u}; z) = 1 if\ Z(\mathbf{u}) \le z, = 0$ otherwise.

In both cases, the problem of evaluating the conditional probability is converted into that of evaluating the conditional expectation of a specific indicator random variable. The evaluation of a conditional expectation calls for well-established regression theory, i.e., kriging (see section 1.3.2).The sequential simulation algorithm proceeds somewhat differently for categorical and continuous variables:

2.4.2.1. Categorical (Discrete) Variables

1. At each node $\boldsymbol{u}$ along the random path, indicator kriging followed by order relation corrections[1] provides K estimated probabilities $p_k^*(\mathbf{u}|(.)$. The conditioning information $(.)$ consists of both the original i_k-data and the previously simulated i_k-values for category k.
2. Define any ordering of the K categories like $1,2,\ldots,K$. This ordering defines a cdf-type scaling of the probability interval [0, 1] with K intervals.
3. Draw a random number p that is uniformly distributed in [0, 1]. The interval contains p determines the simulated category at location $\boldsymbol{u}$.
4. Update all K indicator data sets with this new simulated information, and proceed to the next location $\boldsymbol{u}$ along the random path. The arbitrary ordering of the K probabilities $p_k^*(\mathbf{u}|(.)$ does not affect which category is drawn or the spatial distribution of categories [42].

2.4.2.2. Continuous Variables

The continuous variable $z(u)$ discretized into K mutually exclusive classes k: $(z_{k-1}, z_k], k = 1,\ldots,K$. $z(u)$ can be interpreted and simulated as the spatial distribution of K class indicators. One advantage of discretizing the continuous variable $z(u)$ into K classes is the flexibility to model the spatial distribution of each class by a different indicator semivariograms [5].

[1] Order relation corrections apply to ensuring that the estimated distribution follows the axioms of a probability distribution: a cdf is never less than 0, greater than 1, and must be non-decreasing. The probabilities of a pdf must all be greater (or equal to) zero and sum to one.

At each node u that is to be simulated along the random path, indicator kriging (Simple or Ordinary kriging) provides a *ccdf* through *K* probability estimates:

$$F^*(\mathbf{u}; z_k|(n)) = \Pr ob^*(Z(\mathbf{u}) \le z|(n)\}, k = 1,..., K \quad (2.45)$$

Interpolation provides the continuum for all threshold values $(z \in [z_{\min}, z_{\max}]$ [5]. Monte-Carlo simulation of a realization $z^{(l)}(\mathbf{u})$ is obtained by drawing a uniform random number $p^{(l)} \in [0,1]$ and retrieving the ccdf $p^{(l)}$-quantile $z^{(l)}(\mathbf{u}) = F^{*-1}(\mathbf{u}; p^{(l)}(n))$ such that $F^*(\mathbf{u}; z^{(l)}(\mathbf{u})|n) = p^{(l)}$.

The indicator data set (for all thresholds z_k) is updated with the simulated value $z^{(l)}(\boldsymbol{u})$ and indicator kriging is performed at the next location $\boldsymbol{u}$ along the random path. Once all locations u have been simulated, a stochastic image $\{z^{(l)}(\mathbf{u}), \mathbf{u} \in A\}$ is obtained. The entire sequential simulation process with a new random path can be repeated to obtain another independent realization $\{z^{(l')}(\mathbf{u}), \mathbf{u} \in A\}, l' \neq l$.

Unlike SGSIM, SISIM permits the use of different indicator semivariograms to model the relations of each of the *K* thresholds, i.e. one can account for category-specific patterns of spatial continuity. Thus, correlating and connecting the extreme values of a reservoir, as different from median values, becomes a possibility. SISIM added more variogram flexibility to reservoir modeling but it was quickly recognized that the limitation in reproducing curvilinear geological shapes such as meandering channels, is in the variogram itself, not in the use of indicators. In general, as a two-point statistics, the

semivariogram (no matter how many) cannot capture complex curvilinear shapes [1]. For more details and the theoretical development of the sequential indicator simulation methodology, see Deutsch and Journel [5].

Chapter 3

Effect of Quantity of Samples on Geostatistical Methods

3.1. Introduction

All geostatistical methods require a minimum number of the sample data to build a subsurface model. In petroleum engineering, these data are frequently available at the production or exploration wells. At times there appears to be a lot of sample data such as core, well logs, seismic, and production data. Even in this ideal situation, however, there is always uncertainty in the assignment of reservoir properties at unsampled locations.

Permeability is one of the most complex data among the various types of sample data to be obtained at wells. It can be obtained from the number of sources such as well logs, cores and well testing. Permeability is also a key parameter to any reservoir study since it defines the extreme behavior of flow paths. Thus, it is crucial to characterize and preserve in a model the extreme values of permeability and their spatial patterns. The range of variability for reservoir permeability is usually higher than the other reservoir properties.

Because of the scale of variability for permeability and complexity of porous media, the data sets sampled from a hydrocarbon field are often inadequate to represent the real heterogeneity of the reservoir. This is especially true for permeability. However, collecting more sample data from a reservoir can help in two ways. First, they help constraining the geostatistical interpolation methods by providing more points where the

parameters are known. Second, the quantity of data sets can improve the inference governing spatial correlations between the random variables.

The effect of quantity of sample data on the accuracy of various geostatistical methods has not received a deserved attention in petroleum engineering literature. The primary objective of this work is to examine the effect of the amount of sample data on the estimation of random properties of the reservoir at unsampled locations using geostatistics. The accuracy of geostatistical methods is investigated by comparing the statistical analysis of the random properties from the obtained realizations to the properties of a reference reservoir. The comparison was not limited to the reservoir properties, the dynamic data of the realization and the reference reservoir were also compared. For comparing the dynamic data, the realizations generated by geostatistical methods are considered to represent actual random properties of a reservoir and used as an input data in flow simulations. For instance, porosity and permeability are random variables whose values are estimated by geostatistics. The results of flow simulation or dynamic data are affected directly by the accuracy of the realizations, which in turn could be the function of the quantity of data sets. Investigating the effect of quantity of sample data on the outcome of flow simulations or dynamic data is another important objective of this work.

3.2. Case Study

For the purpose of the study a hypothetical 2D reservoir was put together using data that was prepared and provided by Stanford University [5]. The properties of this reservoir, that considered 'true' or 'reference' data, were used to demonstrate and study the accuracy of the various geostatistical algorithms. The dimension of this hypothetical reservoir is 2500 ft by 2500 ft that is divided into 50 by 50 grids. It has a single layer of constant 30ft vertical thickness.

The permeability of the reservoir, reference permeability, was obtained by Computer Tomography (CT). CT measurement consists of generating a beam of high energy photons through the object and recording them on an array of detectors placed diametrically opposite the source. The resultant photon intensity at the detectors is used to reconstruct the CT characteristics of the object. The scanned cross section is discretized into voxels and a CT number is attributed to each voxel. The CT number is proportional to the density of material within the scan plane. For the purpose of this research, the CT values were rescaled to obtain the histogram of the actual permeability values that derived from well-log of a deep water turbiditic reservoir [43]. The porosity map was derived from well-log data. The resultant permeability and porosity maps and corresponding histograms are given in Figures 3.1 and 3.2 respectively. The permeability distribution of the reservoir results in Dykstra-Parson coefficient of about 0.75 which implies that the reservoir is quite heterogeneous.

3.3. Sample Data Sets

In a real reservoir, samples are taken from well locations that are typically drilled in patterns. As for the hypothetical reservoir in this study, the sample data are taken in a way that replicates the typical well spacing used in the petroleum engineering literature. Therefore, two sets of sample were taken from well locations that drilled in two types of well spacing: 10 and 40 acre well-spacing. From 10 acre well-spacing forty one samples and from 40 acre, sixteen samples were taken. Figures 3.3 and 3.4 display the location of the data sets on the reference case study. Throughout this dissertation, the 10 and 40 acre well spacing samples are labeled as data sets A (10 Acre) and B (40 Acre).

The accuracy of the dynamic response as a function of the number of samples was examined in a five-spot 40-Acre pattern (Figure 3.5). Well I at the center of the five-spot is an injection well. There are four production wells at the corners. The wells are drilled exactly at the locations where samples have been taken. In other words, the properties of the reservoir, permeability and porosity, are only known at the well locations. That is because there is no other way to compare the outcomes of flow simulations or dynamic data as a function of the number of samples.

3.4. Flow Simulator

Flow simulations in this research were performed using ECLIPSE100© Black Oil simulator (ECLIPSE-100© Reference Manual and Technical description, 2005A, Schlumberger [32]). The relative permeabilities used for the oil-water system is given in

Figure 3.6**.** Additional information pertaining to the 2-D reservoir model used for this research is given in Table 3.1**.**

Table 3.1. Model specifications for flow simulator

Reservoir Dimension	50 x 50
Dimension of each cell	50ft x 50 ft
Thickness of reservoir	30 ft
Fluid Viscosities	Oil(0.7 cp) Water(1 cp)
Water Density	69.26 lb/ft^3
Oil Density	51.26 lb/ft^3
Rock Compressibility	$6x10^{-6}$/psi
Equilibrium conditions	1000psi@4500 ft
Constant initial water saturation	0.25

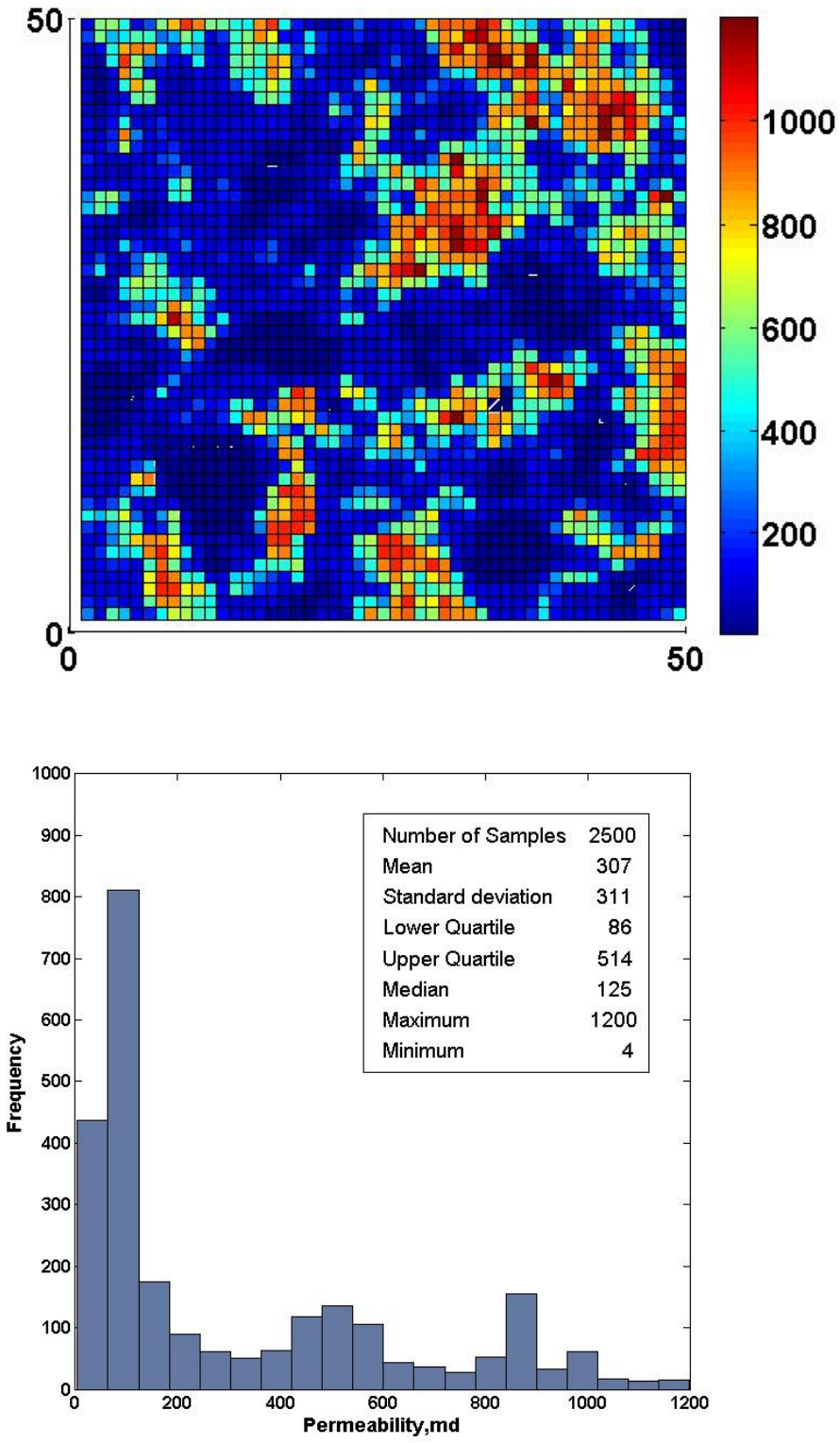

Figure 3.1. Permeability map of the reference reservoir and the corresponding histogram

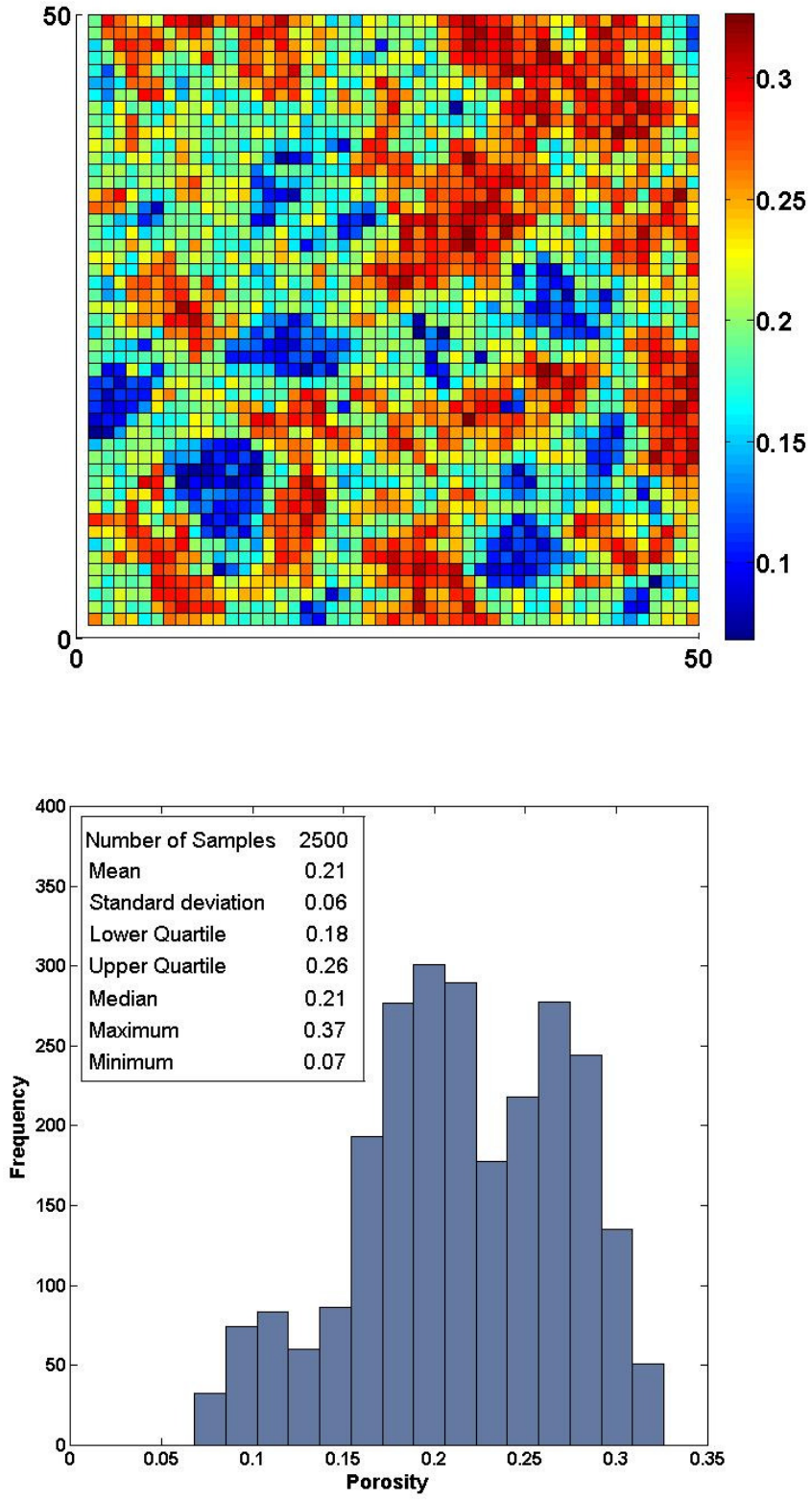

Figure 3.2. Porosity map of the reference reservoir and the corresponding histogram

A five spot pattern, shown in Figure 3.5**,** is considered to examine the dynamic performance of the outcome realizations. The injection well I at the center was shut-in and all the production wells P's at the corner produced at 400 psi which is higher than oil bubble point pressure. The reason for constraining the pressure at production well is to ensure the elimination of gas in the course of the simulation. Therefore, the oil production in this condition is governed by the total compressibility of the reservoir. The simulation was terminated after 120 days when the oil production for all wells fell down to almost zero after this period.

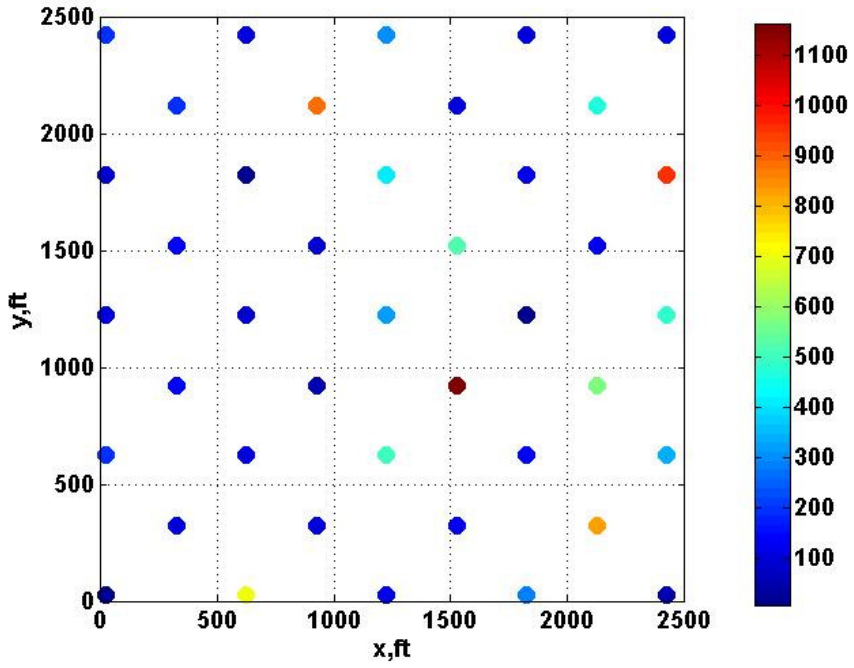

Figure 3.3. Location of sample in 10 Acre well spacing data set.

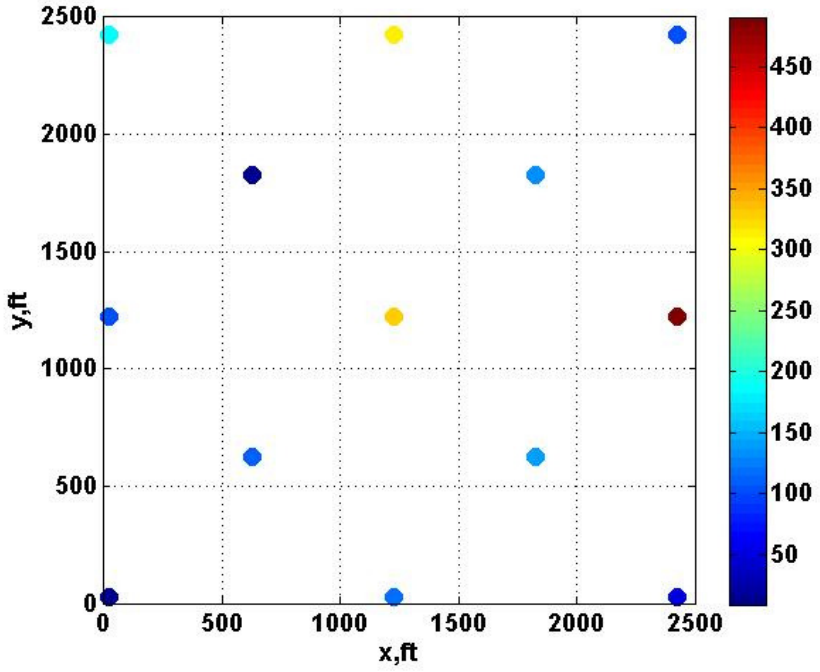

Figure 3.4. Location of sample in 40 Acre well spacing data set.

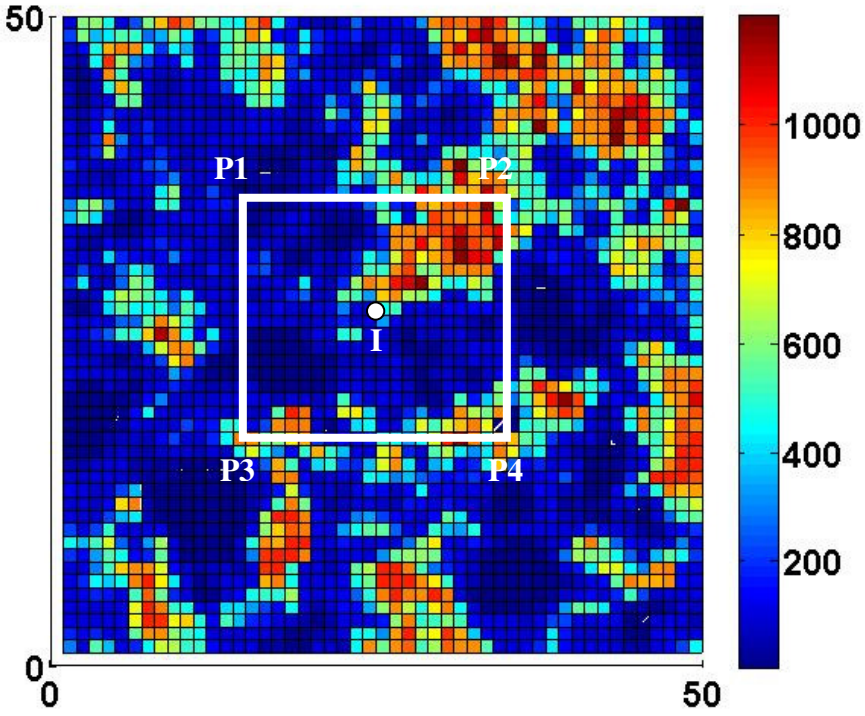

Figure 3.5. Location of a five-spot pattern on the reference reservoir (2500 points)

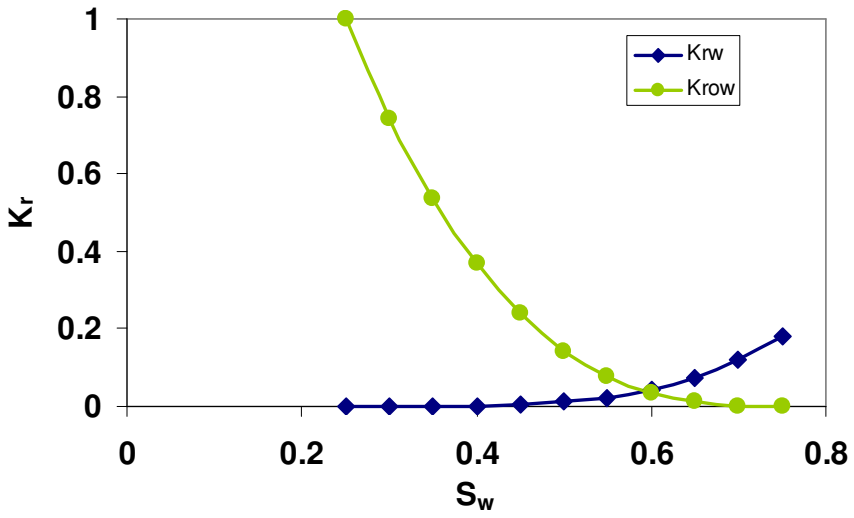

Figure 3.6. Oil-water relative permeability data set used in the flow simulator

3.5. Methodology

Four geostatistical techniques were considered to used to assign permeability to the grid blocks described in the previous section. The techniques were:

- Ordinary Kriging (OK)
- Indicator Kriging (IK)
- Sequential Gaussian Simulation (SGS)
- Sequential Indicator Simulation (SIS)

The techniques were applied to estimate the properties of the reservoir at unsampled locations. The first two methods, ordinary and indicator kriging, are classified as conventional estimation techniques. On the other hand, both SGS and SIS are considered Monte Carlo simulation routines.

The four methods were used to estimate the permeability at unsampled locations using two different data sets explained in the previous section**.** The initial step in most geostatistical techniques is to estimate the experimental semivariogram using available sample data. For the data sets of this study the experimental semivariograms of logarithm of permeability (LogPerm) were calculated and are shown in Figure 3.7. In addition**,** the semivariogram for all 2500 exhaustive sample data of the reference reservoir is shown the figure. Figure 3.7 indicates the variance of both data sets (sill of the semivariograms) is smaller than that of the variance of the reference data set. None of the data sets represent the heterogeneity of the reference reservoir. All adjacent data are beyond the range of the reference semivariogram for the two sample data sets (closest distance

between wells in 10 acre is 667 ft). Therefore, there appear to be no correlation between data for the reduced sample sets.

The reference reservoir is a heterogeneous reservoir (Dykstra-Parson coefficient 0.75). As a result it is difficult to take samples from the reservoir that could represent such heterogeneity. Consequently, it was decided to use the experimental semivariogram of 2500 LogPerm of the reference reservoir instead of semivariograms of the two other data sets A and B.

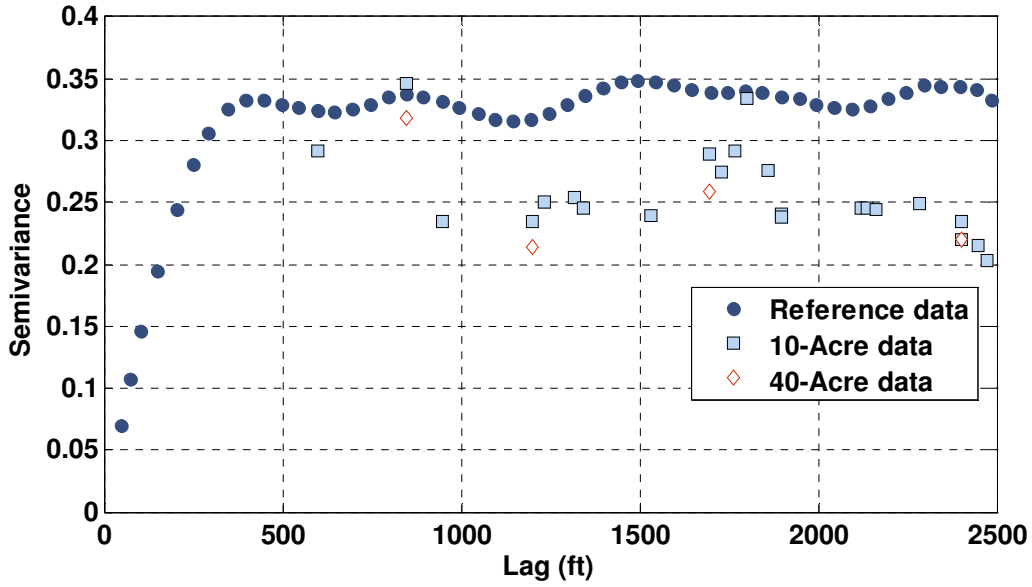

Figure 3.7. The experimental semivariograms for the two data sets and the reference reservoir

3.5.1. Semivariogram Modeling

The semivariogram of the LogPerm of the reference reservoir was estimated in different directions in order to investigate anisotropy of permeability. For the purpose of orientation, 0° corresponds to the east direction and 90° correspond to the north direction. The directional tolerance used is ±30°. All geostatistical routines in this work were performed by GSLIB (Geostatistical Software Library) developed at Stanford University.

Figure 3.8 presents the experimental semivariograms in four directions: 0, 45, 90, and 135°. The sill and range of semivariograms are approximately the same in different directions. Thus, there is no clear indication of anisotropy of LogPerm for the reference reservoir. Semivariogram in east direction was assumed to be the reference semivariogram of LogPerm for the rest of the study.

The next step is to fit an analytical model that is defined by a few parameters to the experimental semivariograms. This procedure ensures that semivariogram values for any possible lag distances used in the kriging matrices can be computed. The experimental semivariogram data were fit to the basic mathematical semivariogram models explained in section 1.2.7. The results of the regression showed that a spherical semivariogram model with sill of 0.33 and range of 450 ft fit the semivariogram data better than other models. Figure 3.9 presents the analytical model fitted to the semivariogram of LogPerm for the reference reservoir. This semivariogram model was used to calculate the LogPerm at unsampled location in ordinary kriging method.

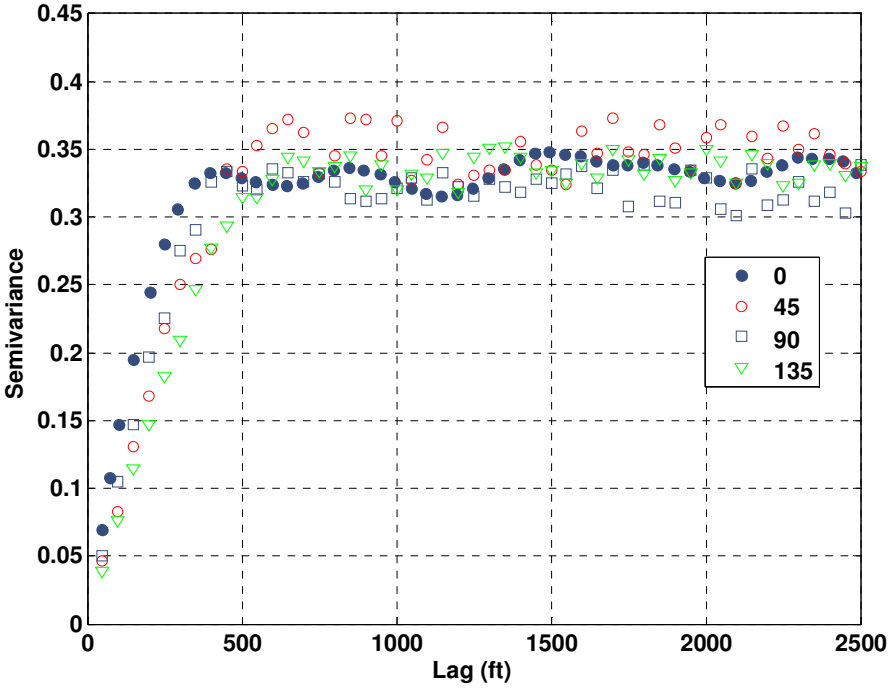

Figure 3.8. Experimental semivariogram of LogPerm in different directions of the reference reservoir

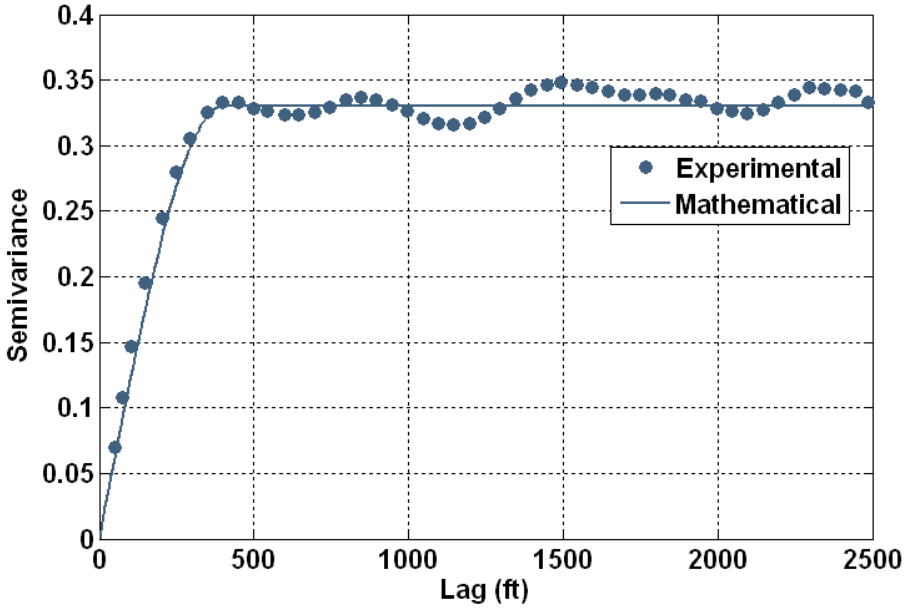

Figure 3.9. Experimental and mathematical model of semivariogram for LogPerm

For indicator kriging and sequential indicator simulation (SIS) methods, as it was explained in section 2.4.2, the first step is to select the number of thresholds used to transform the continuous variables to indicator values. First, a sensitivity analysis was carried out to select the number of thresholds. Then, the lower and upper quartile and median of LogPerm were selected to transform the data into indicator values. For each threshold, the estimated semivariogram was calculated for LogPerm and fitted by a basic analytical model. A spherical model was used to fit the estimated semivariograms for the lower quartile threshold; while an exponential model was used to fit the estimated semivariograms for the median and upper thresholds. Figures 3.10 through 3.12 represent the estimated and analytical semivariograms of LogPerm indicator values for the three thresholds.

In the sequential Gaussian simulation, the data set is transformed with a normal score transformation. As for the original LogPerm data, they were first transformed into normal score using mean and standard deviation of the exhaustive data set. Then, the semivariogram was estimated for the normal score transformation of the original data. Similar to the other techniques, the last step is to fit a mathematical model to the estimated semivariogram. Examining the fit of the basic model suggested a Gaussian semivariogram model with a range of 450 ft to fit the data. Figure 3.13 presents the estimated and mathematical semivariogram model for the normal score of LogPerm data.

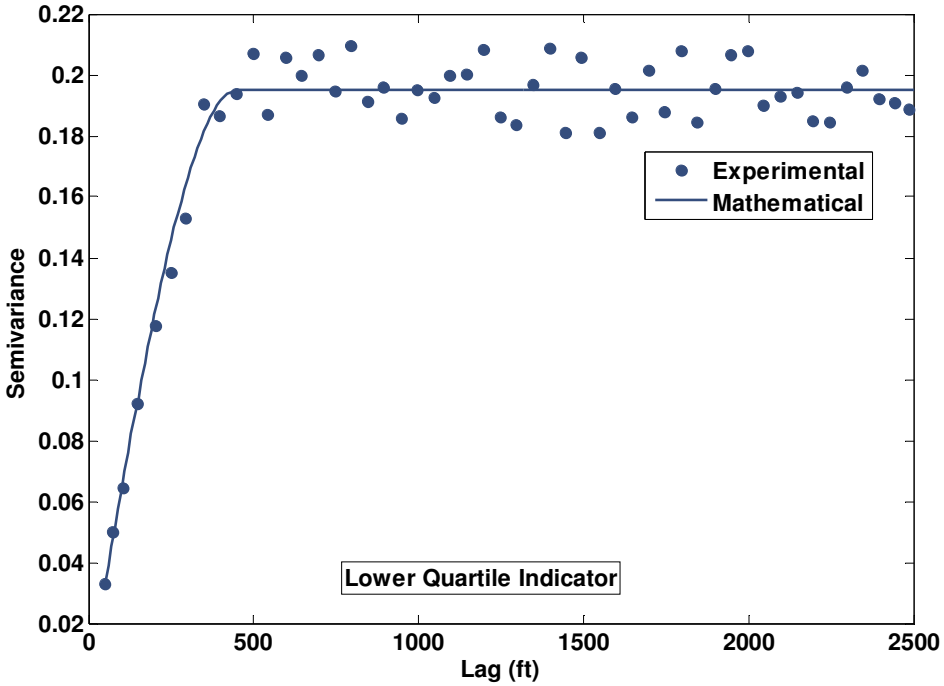

Figure 3.10. Experimental and mathematical semivariogram for lower quartile threshold

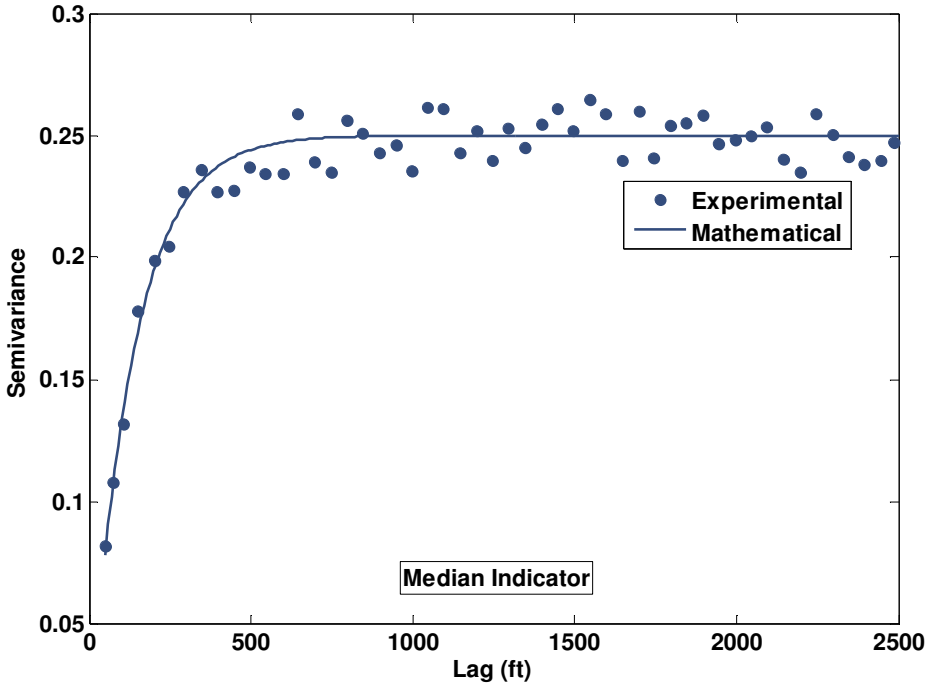

Figure 3.11. Experimental and mathematical semivariogram for median threshold

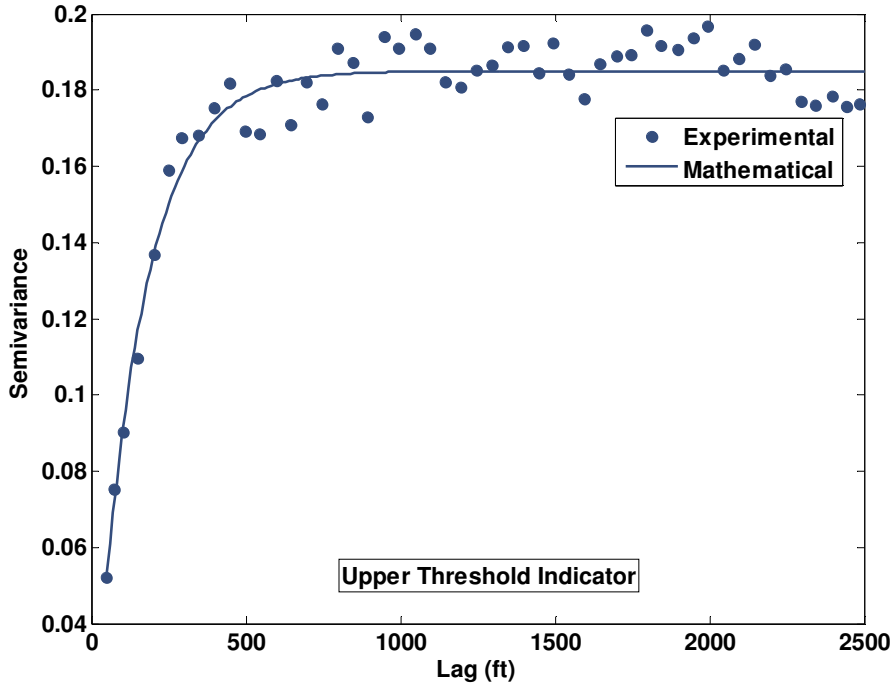

Figure 3.12. Experimental and mathematical semivariogram for upper quartile threshold

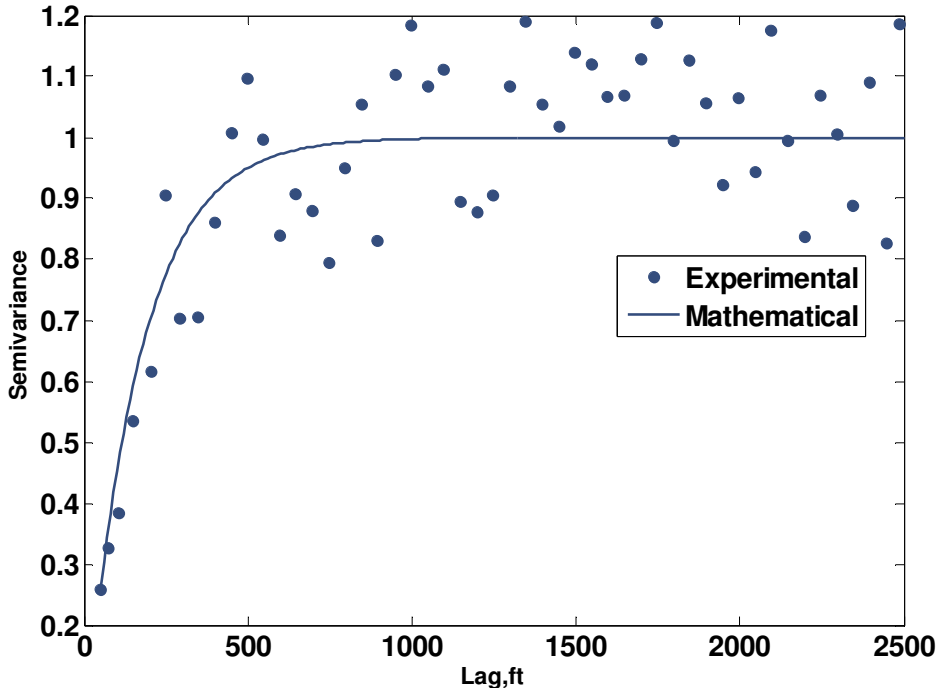

Figure 3.13. Experimental and mathematical semivariogram of the LogPerm normal score

3.5.2 Ordinary Kriging

Ordinary kriging implemented in the GSLIB program kb2d was employed to generate LogPerm values at unsampled locations. This program computes a local estimate of the mean of the kriged variable at every grid point. The search radius of 4000 ft was estimated from the distribution of well locations in the location maps in Figures 3.3 and 3.4. The radius was chosen in a manner to encompass the minimum number of data points (3) at any unsampled grids. Using a smaller radius (smaller than 4000 ft) would result in search failures at some of the unsampled grid nodes. This is reasonable because it prevents the procedure extrapolating too far from the well control. The minimum and maximum number of points used in the estimation procedure was three and eight respectively. The analytical semivariogram of the exhaustive data set shown in Figure 3.9 was used for this technique. Data sets A and B described in Section 3.3 set aside as hard control data for estimation the LogPerm at unsampled grids. After calculation at the unsampled grid cells, LogPerm was transformed to permeability using antilogarithm transformation. The permeability maps generated with ordinary kriging using two data sets A and B are compared against the reference permeability map in Figure 3.14. The maps generated by ordinary kriging are smooth which is typical for the kriging estimation. The ordinary kriging variance maps are shown in Figure 3.15 for data set B. The figure indicates that the estimation variance is small in grid blocks close to the conditioning hard data, and it becomes large in areas far from the hard data. The histograms of the permeability data for maps generated by ordinary kriging are shown in Figure 3.16.

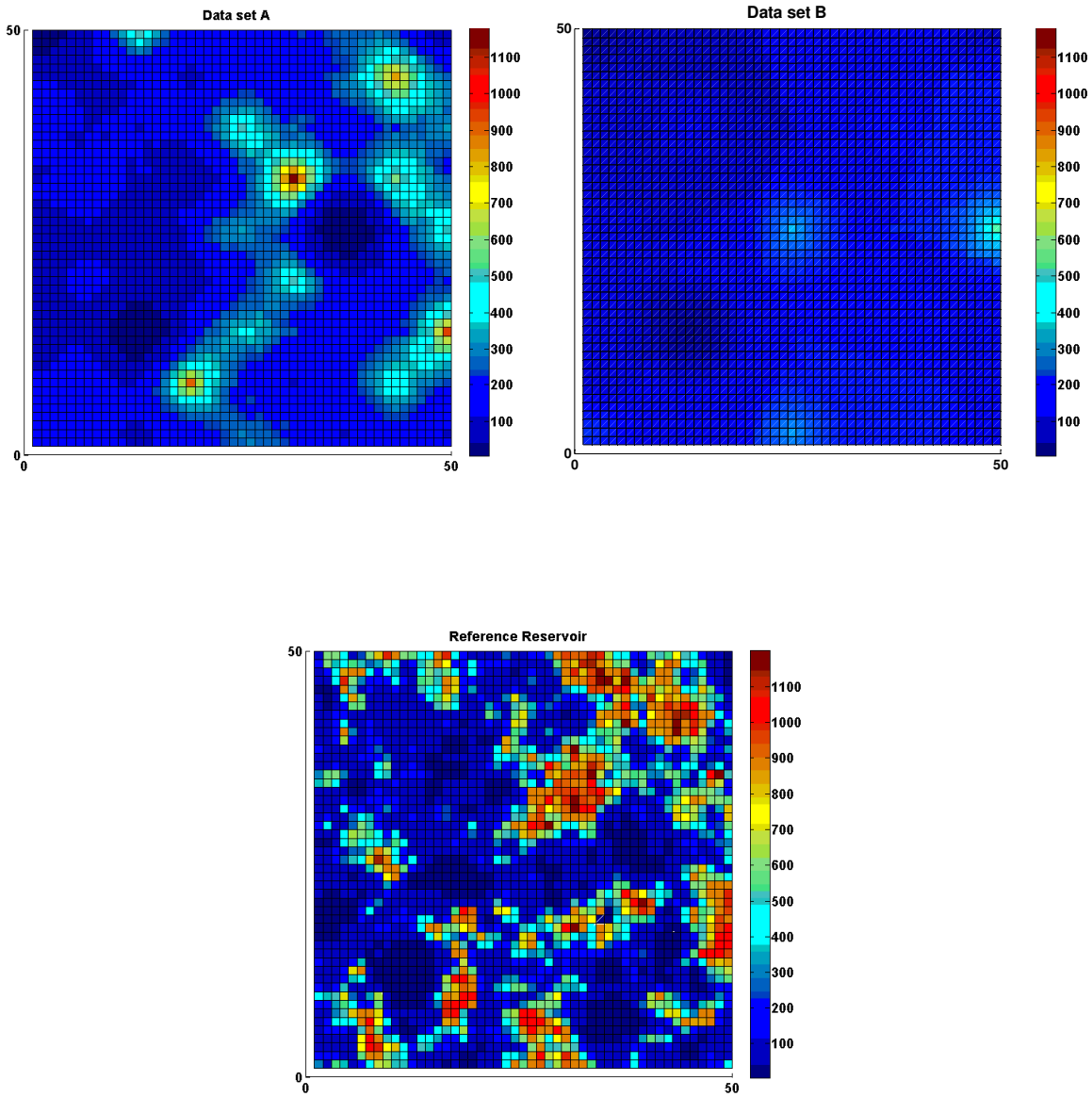

Figure 3.14. Comparison of the permeability maps generated by ordinary kriging and the reference reservoir

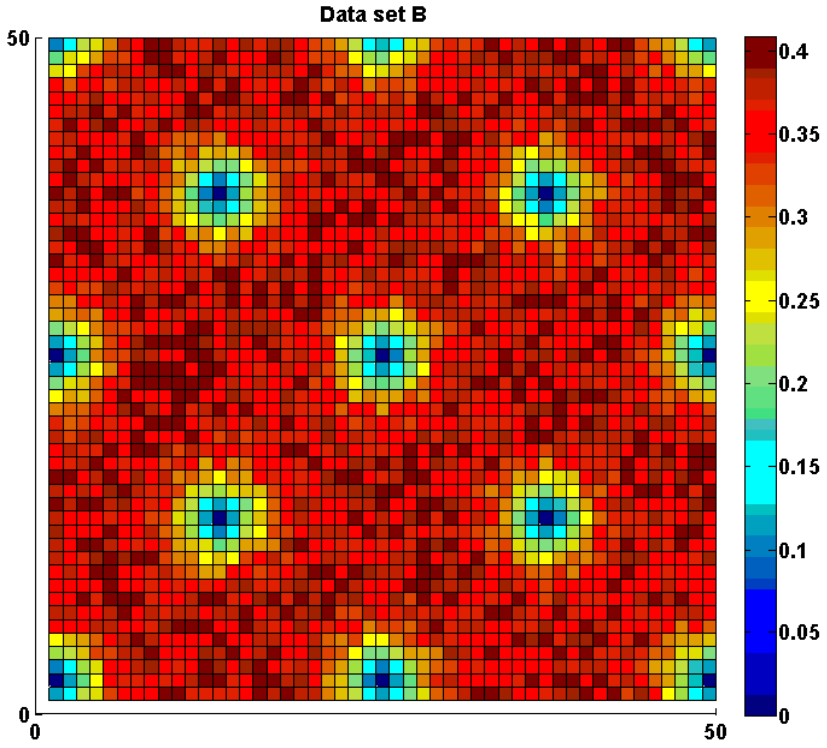

Figure 3.15. Variance map of ordinary kriging for estimation of the permeability

Figure 3.16 shows that the mean of the kriging estimates are close to that of conditioning hard data (224 md and 128 md are the average permeability of two data sets A & B, respectively). Also, the histograms are narrower than the reference data histogram. The mean of the permeability data generated by ordinary kriging was 200 and 115 md respectively, while it was 307 md for the reference data set. In general, Ordinary kriging does not reproduce extreme values of permeability which is not observed in the conditioning hard data.

Kriging honors data values at data locations, However, values are assigned the mean of the sample data beyond the range of the semivariogram. In other words, beyond

the range of a semivariogram the variance of estimation is maximum value (sill) indicating the maximum uncertainty of estimated values at the unsampled locations. This is considered to be a drawback for this type of estimation.

Kriging procedure estimates the permeability of the unsampled locations equal to sample mean beyond the range of semivariograms. Figure 3.17 shows the sample locations enclosed by a circle with semivariogram radius (450 ft) for the 40 acre data set. Estimated LogPerm using kriging were subtracted from the LogPerm mean of the 40 acre data set. Figure 3.18 shows the results of such calculation. Figure 3.18 indicates the difference between the kriged values and the mean of samples is zero beyond the range of the semivariogram shown by a circle around each sample. This shows that the kriged estimates becomes smoother and smoother when approaching the semivariogram range. The smoothing of kriging is directly proportional to the kriging variance. There is no smoothing at data locations where the kriging variance is zero (Figure 3.15). The estimate is completely smooth beyond the range where all estimates are equal to the mean and kriging variance is the variance of the sample data (sill).

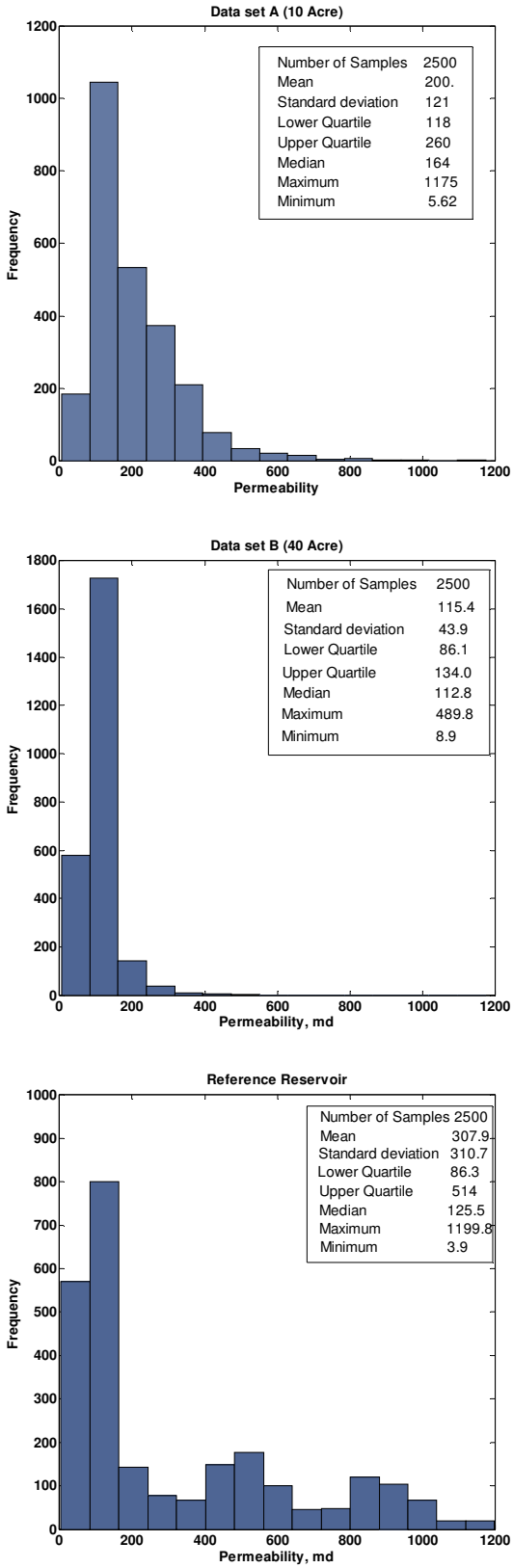

Figure 3.16. Histogram of permeability maps generated by ordinary kriging

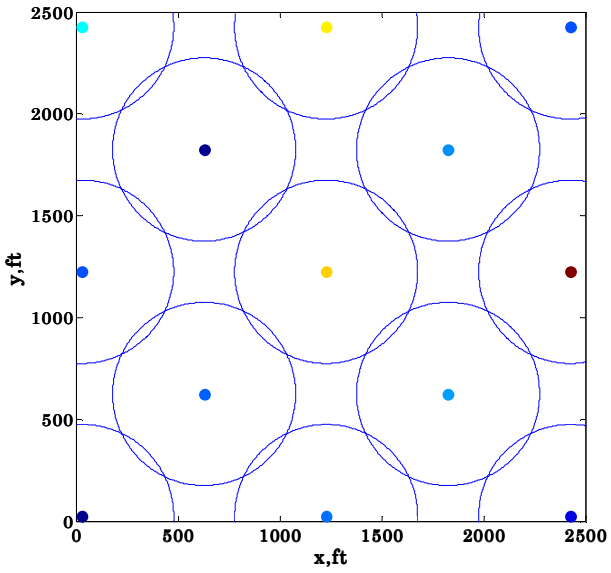

Figure 3.17. Location of sample data in the 40 Acre data set.

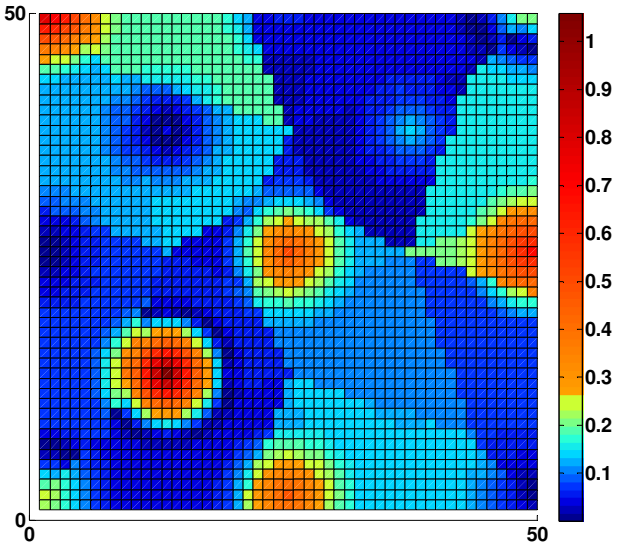

Figure 3.18. The difference between LogPerm kriged and sample mean of the 40 Acre data

3.5.3. Indicator Kriging

LogPerm values were estimated at all grid blocks were obtained using indicator kriging (GSLIB program ik3d). For the purpose of the estimation, the hard control permeability data were transformed into indicators with three specified thresholds (first and third quartile and median). These thresholds were selected to avoid excessive semivariogram modeling and computational effort. Similar to ordinary kriging, the search radius was assigned to 4000 ft to assure covering minimum data for the computation process. The minimum and maximum numbers of points were also the same as the ordinary kriging described in the previous section.

The estimated of semivariogram for three thresholds of the reference permeability data set were utilized. In general, the approach is the same as conventional ordinary kriging, except the routine must be repeated at each threshold. Unlike ordinary kriging whose outcome is a single map, indicator kriging generates one map for each threshold. These maps represent the probability of exceeding threshold values. In addition, at each threshold, these maps are used to estimate the local conditional probability distribution.

The indicator maps corresponding to three thresholds are shown in Figure 3.19 for the data set A**.** The figures show the probability of the event when LogPerm value is less than the threshold. For instance, the map for the lower quartile threshold shows that most areas have low probabilities of having LogPerm less than 1.94. Similarly, the upper quartile map shows the areas of the east part have the highest probability of high LogPerm values.

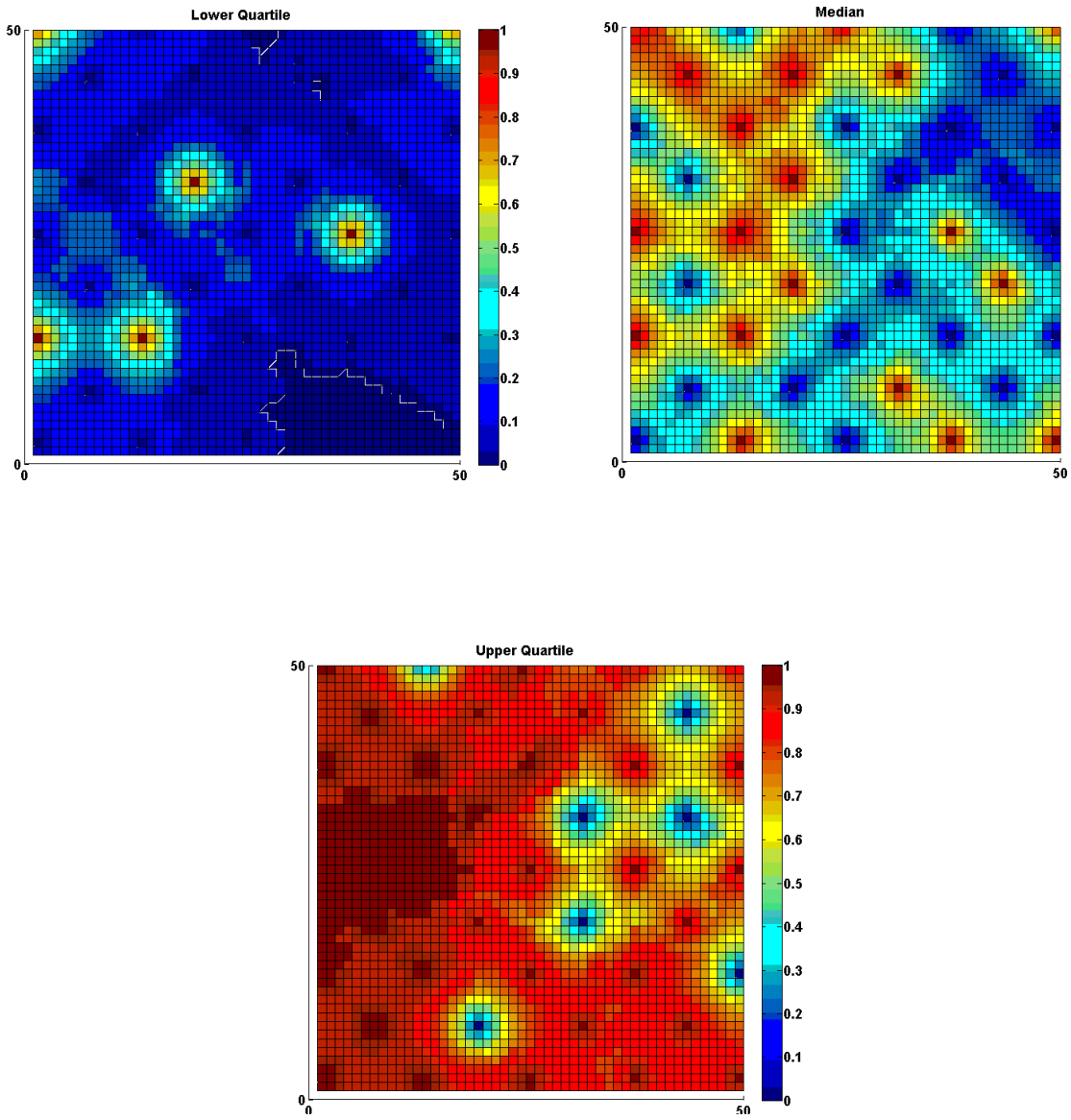

Figure 3.19. Indicator maps of the three thresholds used in IK

These indicator values at different thresholds together describe the conditional probability distribution at each grid block.

Histograms of the indicator maps for the 10-Acre spacing data set are shown in Figure 3.20. The mean of the estimates increases as thresholds increases, because indicator values present cumulative probability. In other words, the shape of histograms shifts from values close to zero for the lower threshold to values to close one for the upper threshold. Finally, the E-type estimate and mean value of the conditional distribution (that derived from the indicator) were computed by post-processing program in GSLIB called *postik*. Using *postik*, the permeability for each grid cell was assigned based on the mean value of conditional probability at all unsampled locations. Figure 3.21 illustrates the final permeability distribution generated by indicator kriging that uses two data sets for conditioning hard data. Figure 3.22 shows the histogram of the permeability data created by indicator krigging. Generally, the permeability maps shown in Figure 3.21 have a smooth appearance like ordinary kriging technique. The histogram of the permeability values generated by data set A are wider that the one generated by data set B. This could be explained by the fact that the range of the samples data in data set A is larger than B. This shows one of the effects of the number of the available sample data.

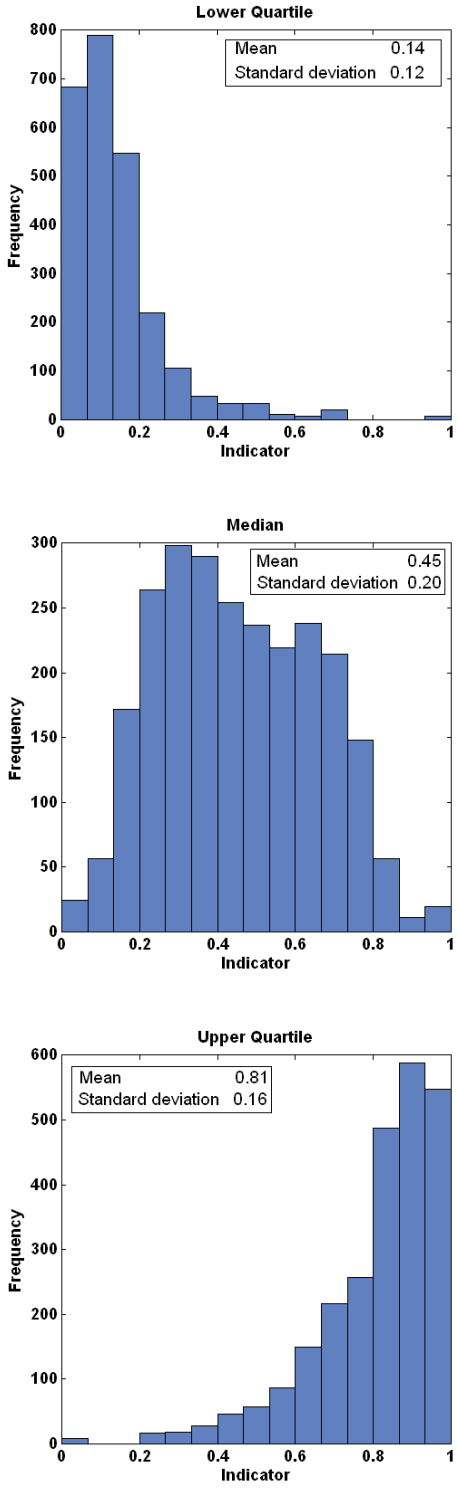

Figure 3.20. Histograms of indicator maps for three thresholds

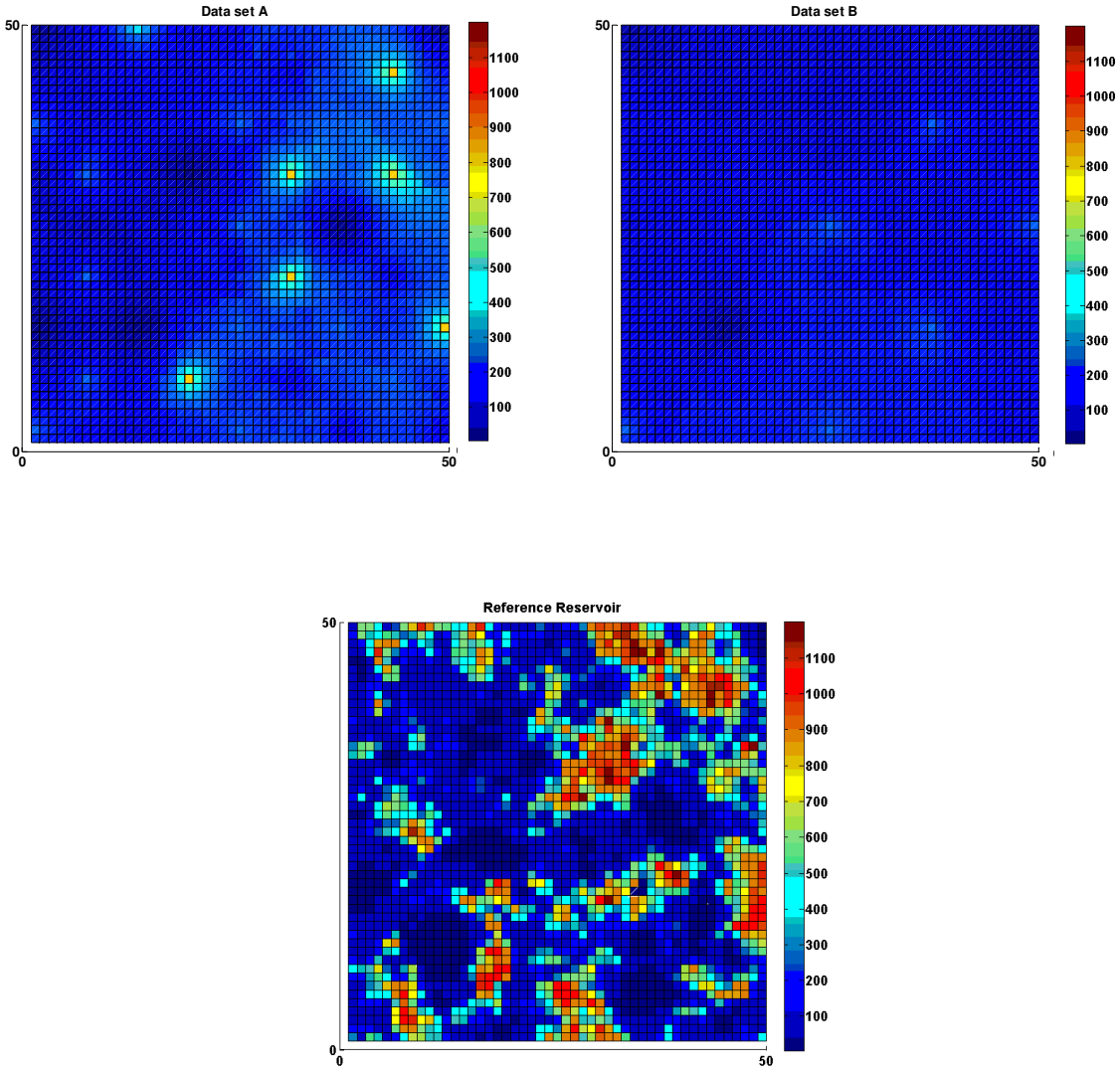

Figure 3.21. Permeability maps generated by indicator kriging

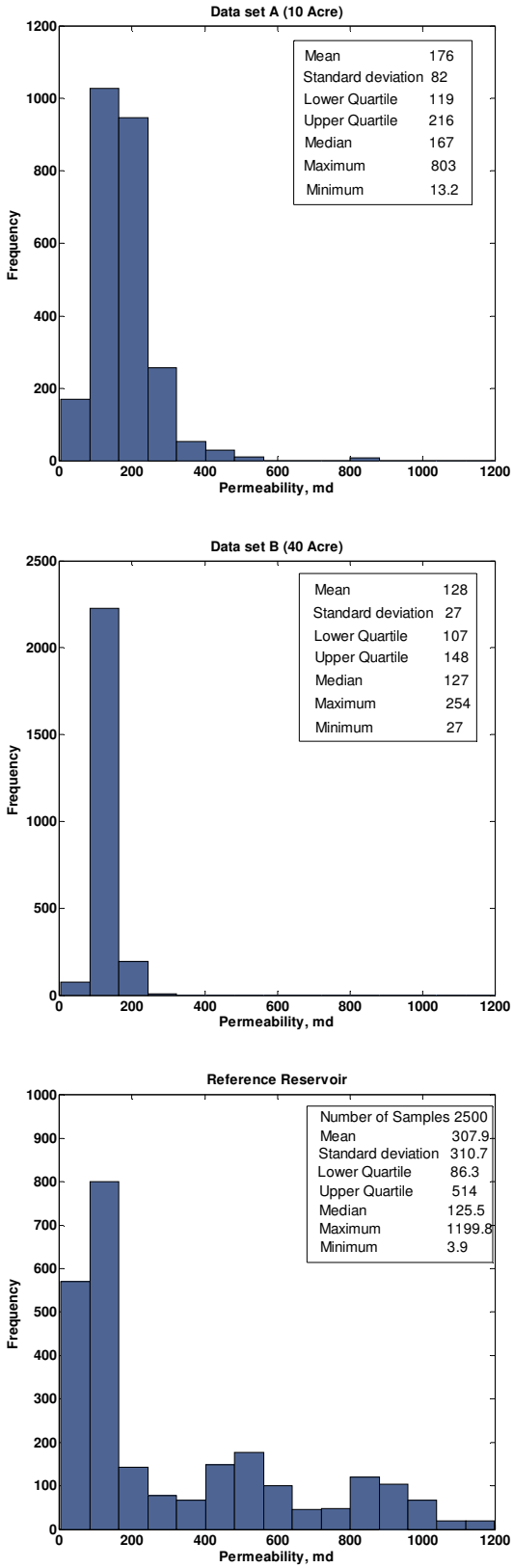

Figure 3.22. Histogram of permeability maps generated by indicator kriging

3.5.4. Sequential Gaussian Simulation

GSLIB program, *sgsim,* was used to generate fifty realizations of the permeability using sequential Gaussian simulation. In order to generate the realizations, the LogPerm values of the two sample data sets were transformed into normal score prior to simulation using mean and standard deviation of the samples. Next, the semivariogram for these normal scores was computed and fitted to an analytical model as described in detail in the previous section. Other parameters such as search radius and minimum and maximum data that are required for the simulation are the same as those used in the ordinary kriging estimation. It should be noted that simulations included a feature called *multiple grid search*. This feature, first performs the simulation on a fairly coarse grid in order to reproduce larger scale structures; then fills in a sequence of finer grids until the grid resolution that is specified by the user in the program is reached.

Once the semivariograms of data were estimated and modeled, the realizations of normal scores were created for all grid blocks. The normal scores values then were back transformed into LogPerm using interpolation models available in GSLIB. Figure 3.23 shows the estimated semivariograms obtained from the fifty realizations (solid gray line) using two data sets A and B. This estimated semivariogram is compared to the estimated semivariogram of the reference case (Solid Black Line). Figure 3.23 shows that the semivariogram of the reference case lie within the range of all the semivariograms that are estimated from realizations generated using data set A. That indicates the acceptable accuracy of the results that come from data set A. Furthermore, the results in Figure 3.23

show better precision for data set A, since the estimated semivariogram lie in a narrower band. This again reflects the effect of number of available sample data.

Figure 3.24 shows two permeability realizations generated with SGS using samples in data set A. The difference between these two realizations generated using the same data set, is mostly clear at locations where there is no conditioning data set. This validates the claim that the conditional simulation quantifies the uncertainty at locations away from the conditioning data set. The difference between the permeability values of the reference reservoir and ten realizations generated by SGS using 10 Acre data set was calculated. Figures 3.25 and 3.26 shows the difference between the permeability values of the reference and four SGS realizations. These figures indicate that SGS provides poor estimates for both high and low permeability regions of the reference reservoir. This is clearer for the high permeability areas in the reference reservoir where SGS underestimate the permeability. From reservoir engineering standpoint, it is crucial to characterize and preserve in the model these extreme values of permeability that control the fluid flow in the porous media. This is also true for the SGS realization generated by 40 Acre data set. Figure 3.27 displays the permeability realization generated by the two data sets compared against the permeability distribution of the reference case. Figure 3.28 compares the histogram realizations in Figure 3.27 with the reference data. The mean and standard deviation of the realization generated by data set A (303 and 296 md) is very close to that of the reference data (308 and 311 md), while this is not true for the realization generated by data set B. This once more suggests the effect of quantity of

available sample data on the accuracy of stochastic geostatistical methods in predicting the permeability distribution.

Sequential Gaussian simulation was introduced as a solution to the smoothing problem of kriging for the locations beyond the range. At the unsampled locations, SGS honors the spatial relationship between the unsampled locations and the previously estimated values are considered during the course of simulation. This is one reason that SGS is able to reproduce the input semivariogram and adequate heterogeneity beyond the range. The LogPerm values of a realization simulated using the 40 Acre data set were subtracted from the LogPerm mean of the 40 Acre data set. Figure 3.29 shows the results of this analysis. This figure indicates the limitations of sequential simulation to estimate values different than mean beyond the range of the semivariogram.

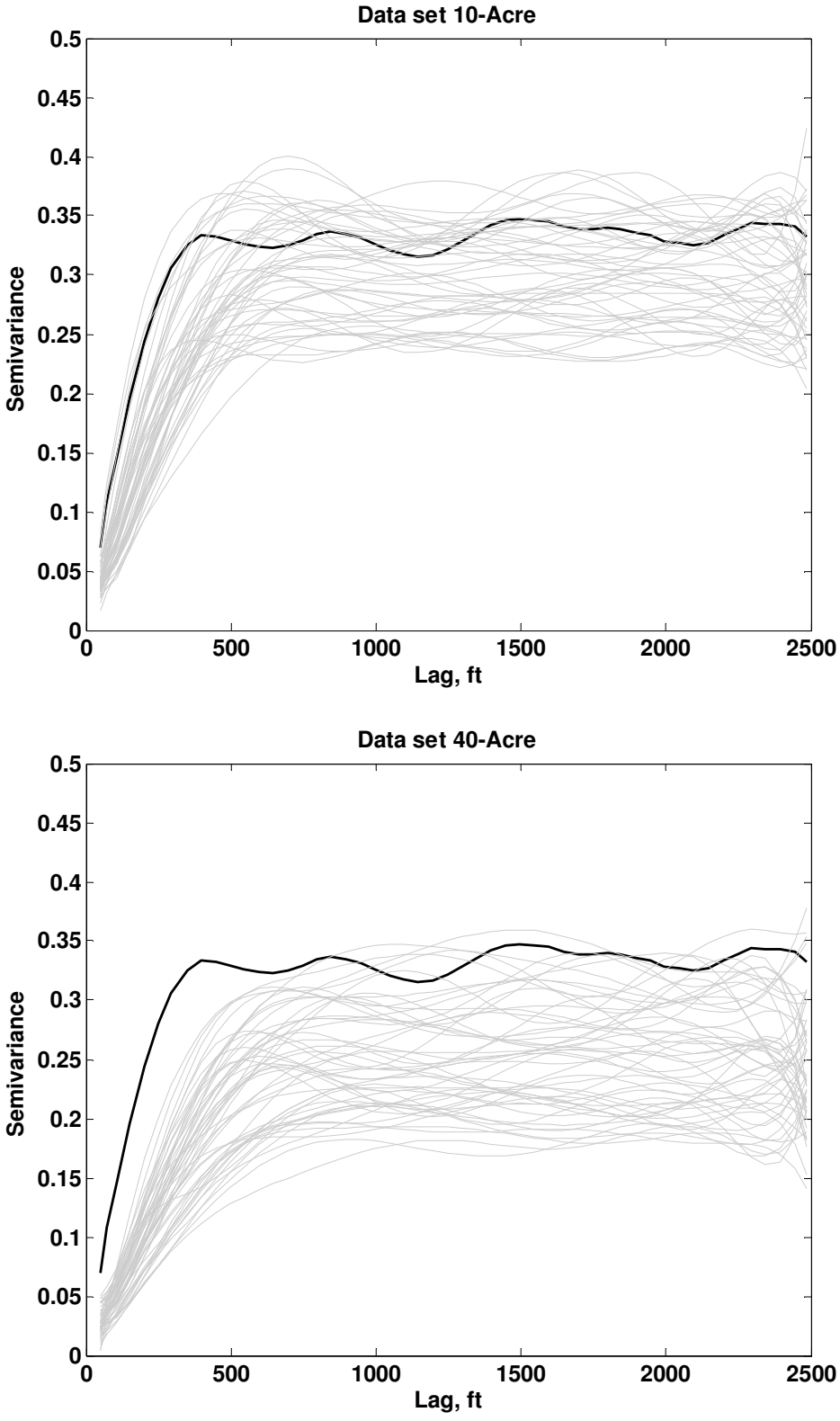

Figure 3.23. Comparison between semivariograms of the permeability realizations for two data sets and the reference reservoir

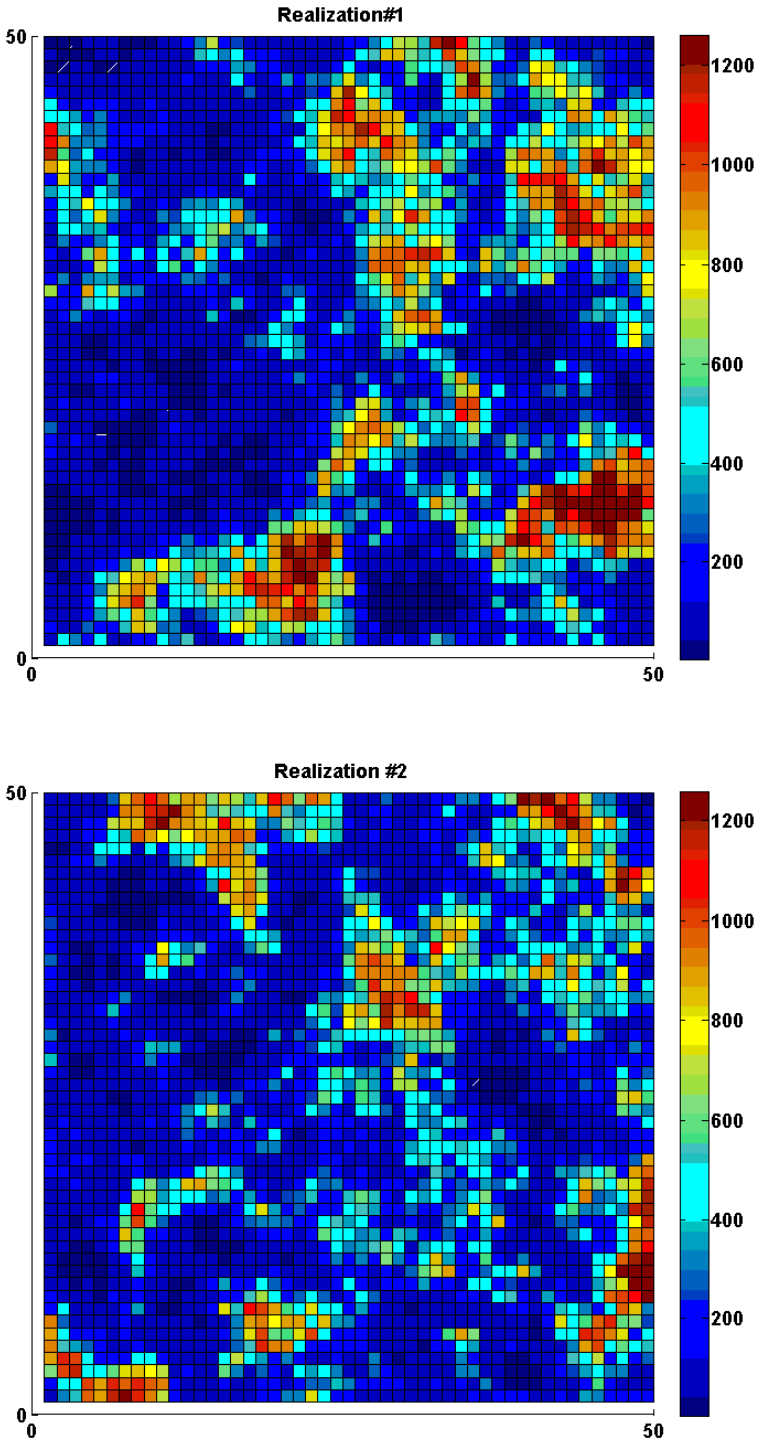

Figure 3.24. SGS Permeability realizations using data set 10-Acre

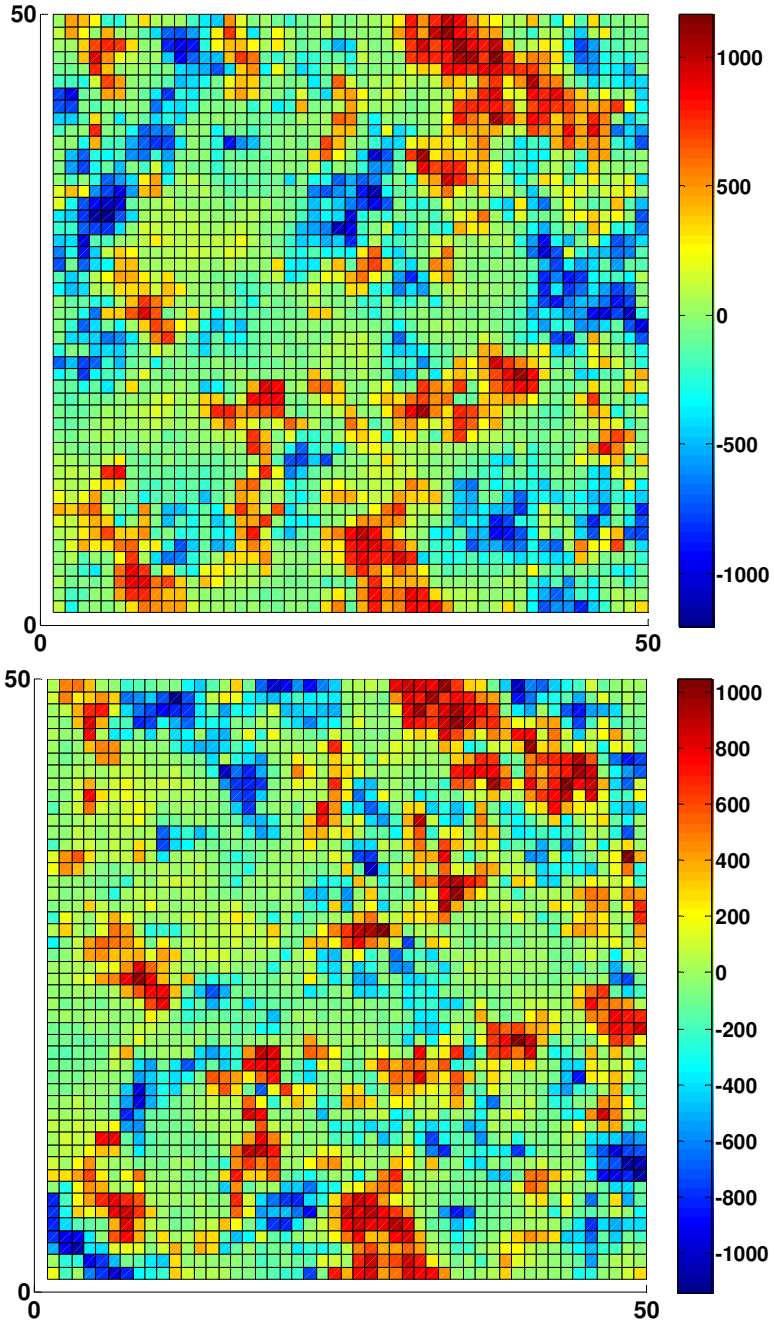

Figure 3.25. The difference between the permeability values of the reference reservoir and four SGS realizations

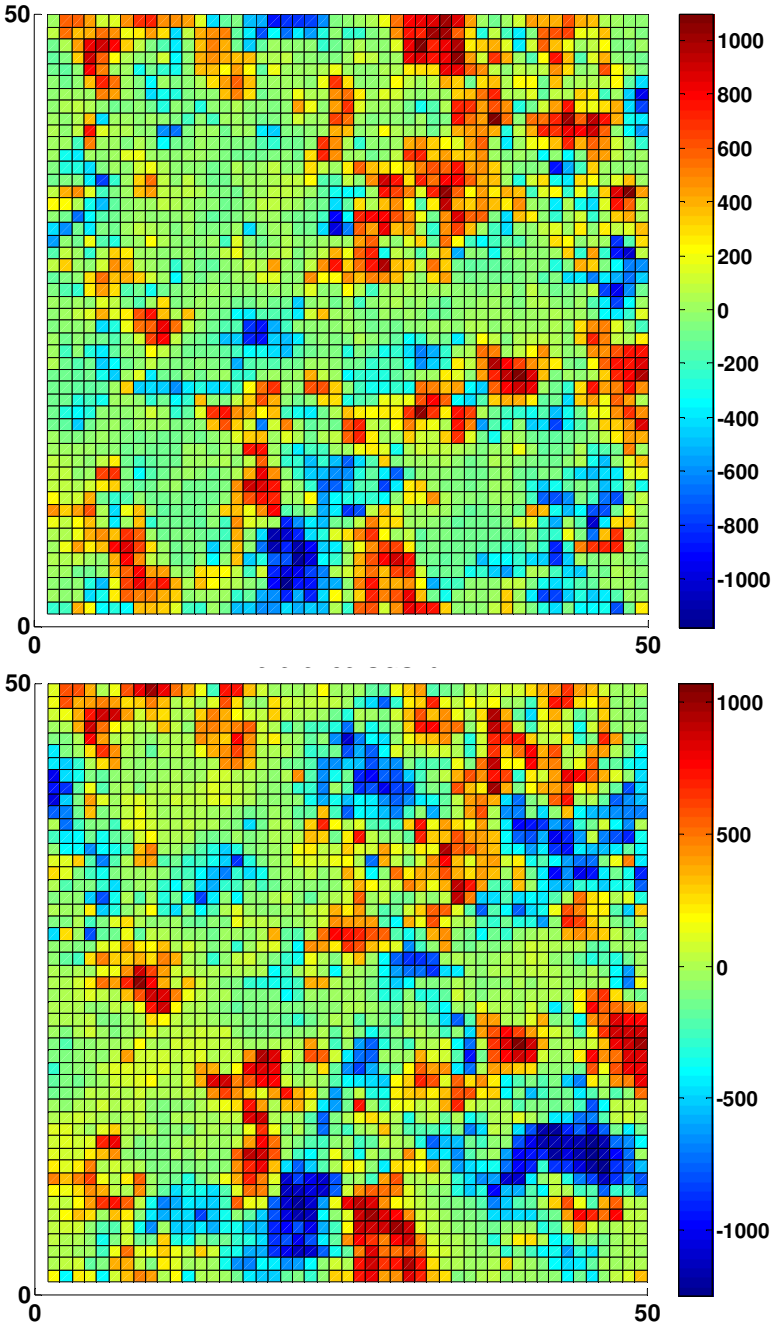

Figure 3.26. The difference between the permeability values of the reference reservoir and four SGS realizations

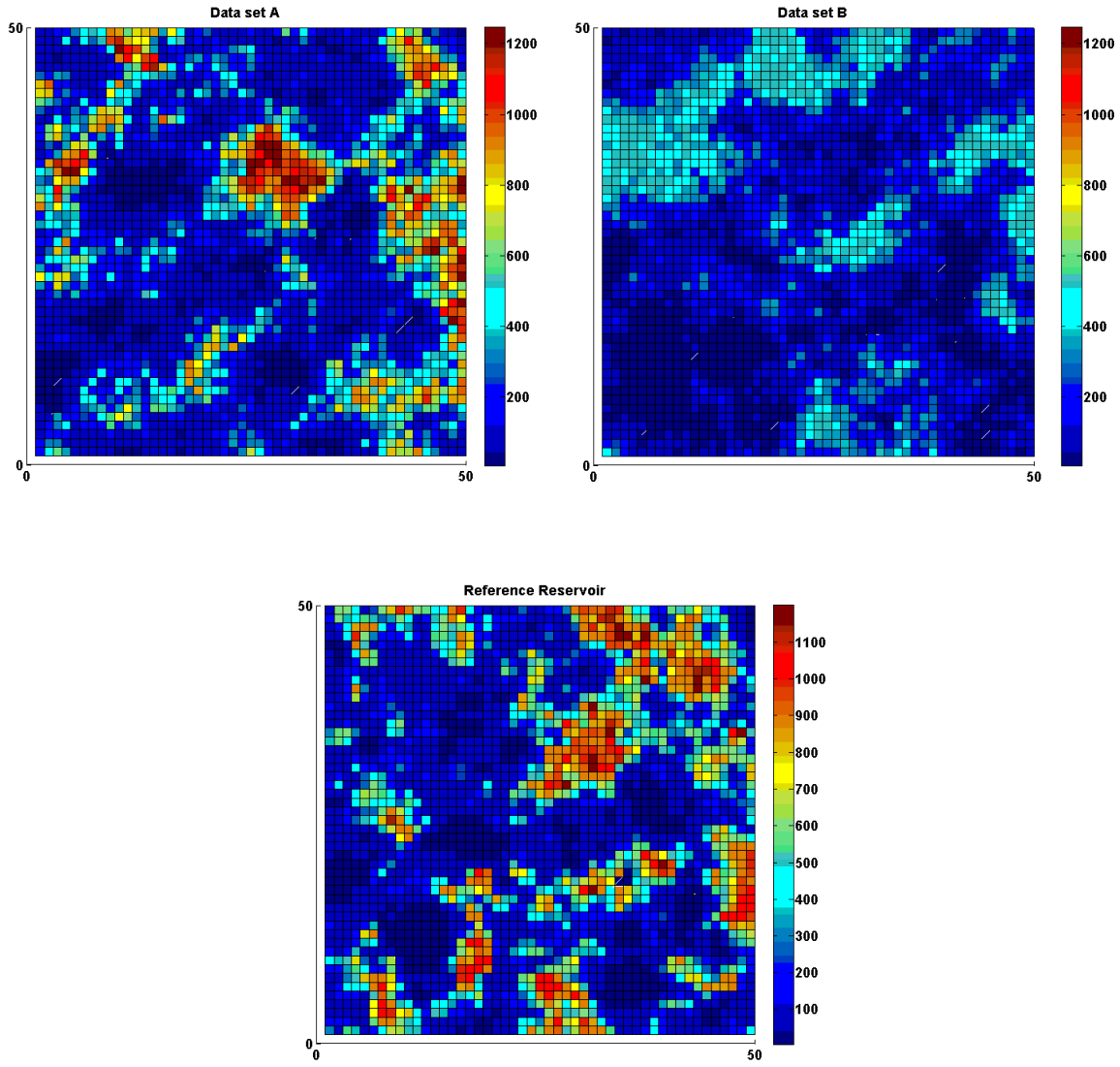

Figure 3.27. Comparison of the permeability maps generated by SGS using two data sets

10-Acre & 40-Acre and the reference reservoir

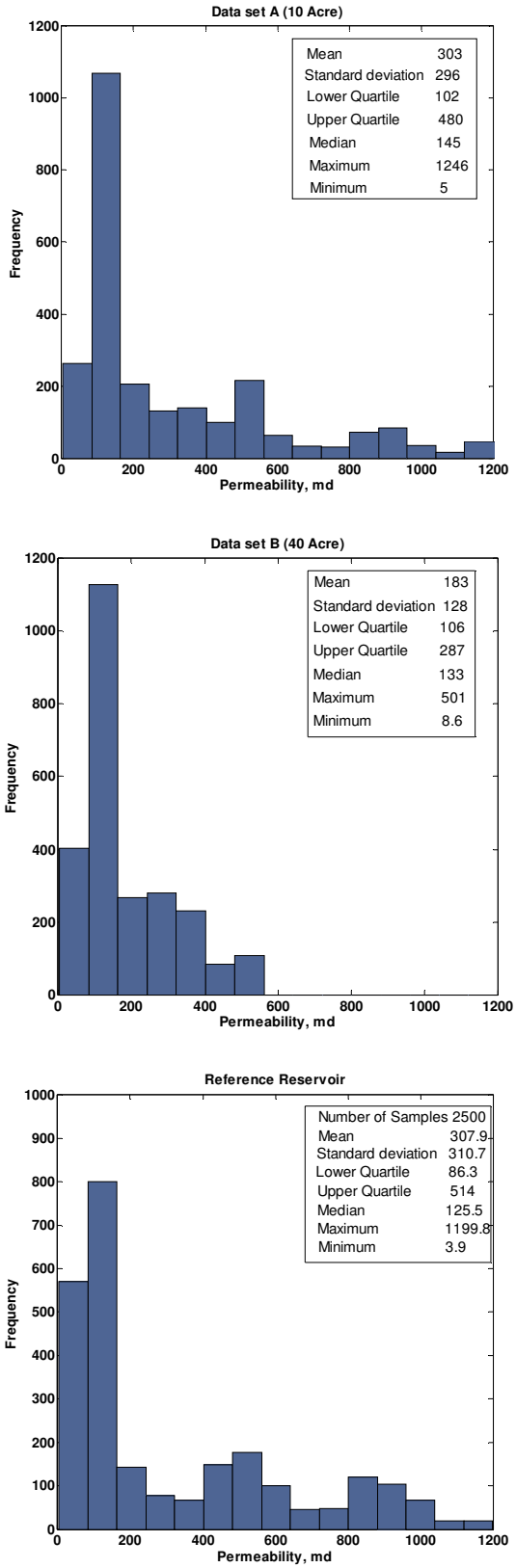

Figure 3.28. Histograms of permeability maps shown in Figure 3.26

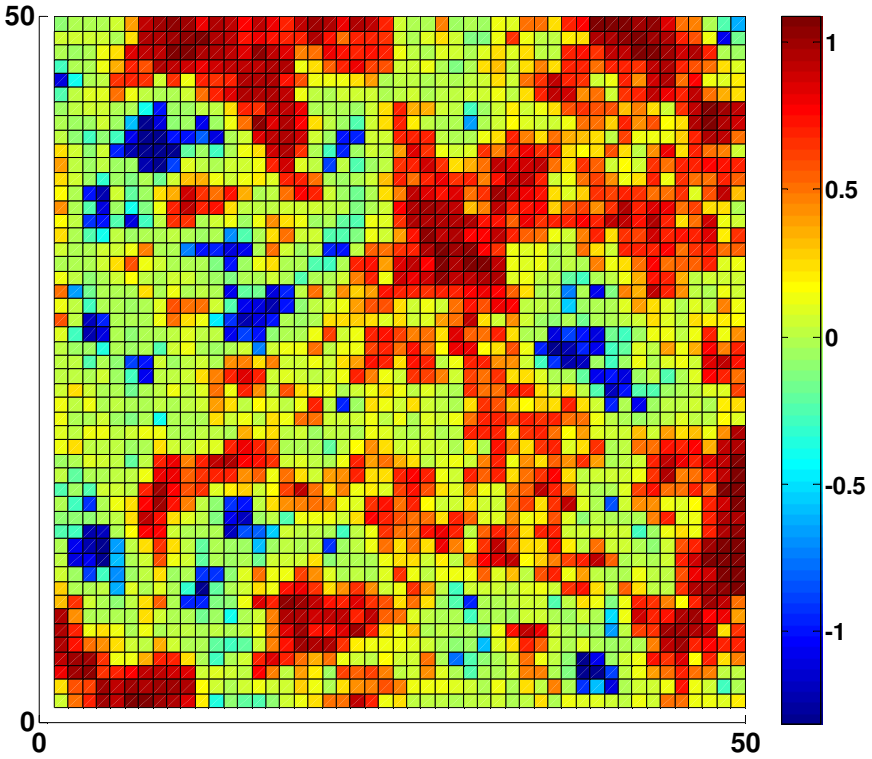

Figure 3.29. The difference between LogPerm sample mean and SGS simulated values for the 40 Acre data set

3.5.5. Sequential Indicator Kriging

Sequential indicator simulation (SIS) in GSLIB for both continuous and discrete variables is implemented in a program called *sisim*. One of the features of the program is the ability of using a combination of simple and ordinary kriging. Fifty realizations of permeability (using both data set A and B) were generated by *sisim.* The first step in generating the realizations was to transform the conditioning hard data into indicator values by means of a specified number of thresholds. Similar to the indicator kriging method described in Section 2.5.3, three thresholds (the lower quartile, median and upper quartile) were selected after the sensitivity analysis. All other parameters including the search radius, the minimum and maximum number of points and the number of previously simulated data is the same as in the indicator kriging provided in Section 2.5.3. Furthermore, the analytical models of semivariograms are the same as the one that was developed in Section 2.5.1.

sisim program provides local conditional distribution at each unsampled location using kriging estimation of indicator values that are resulted from different threshold. Once all unsampled locations are visited and values in the transformed domain are estimated with their local uncertainties, the simulated values into original domain were back transformed by an interpolation routine implemented in *sisim*.

After permeability realizations generated with *sisim*, the experimental semivariogram was calculated for each realization to examine the capability of sequential indicator kriging to reproduce the continuity that exists in the reference data set. Figure

3.30 represents the estimated semivariograms of fifty permeability realizations (Solid gray line) using data sets A & B compared against the semivariogram of the reference permeability data set (Solid black line). It should be noted that, the semivariograms of the realizations in both figures do not include the semivariogram of the reference permeability data. This implies the inaccuracy of the sequential indicator simulation in generating permeability realizations when using the two sample data sets. Furthermore, the semivariograms of the realizations for both sample data sets lie in the same range of uncertainty indicating that SIS is not sensitive to the quantity of samples as described above. Also, Figure 3.30 shows that the permeability realizations generated with SIS for both data sets are less precise in comparison to the realizations created by SGS using data set A (Figure 3.23).

Figure 3.31 displays two permeability realizations generated with SIS using 10-Acre spacing sample data. At each unsampled location, indicator values are randomly drawn from local conditional distribution. That is why most dissimilarity occurs at these locations. Figure 3.32 compares the permeability realizations created by SIS to the permeability of the reference reservoir. Figure 3.33 show the univariate statistics of the permeability realizations in Figure 3.32 and the reference case. The mean and standard deviation of the realization generated using hard conditioning data in data set A (352 md, 330 md) is close to the statistics of the reference data(308 md and 310 md). However, the statistics of the other permeability realization (Data set B) indicate that SIS does not reproduce the shape of the reference permeability histogram. In fact, the mean and standard deviation of this realization is far from that of the original data.

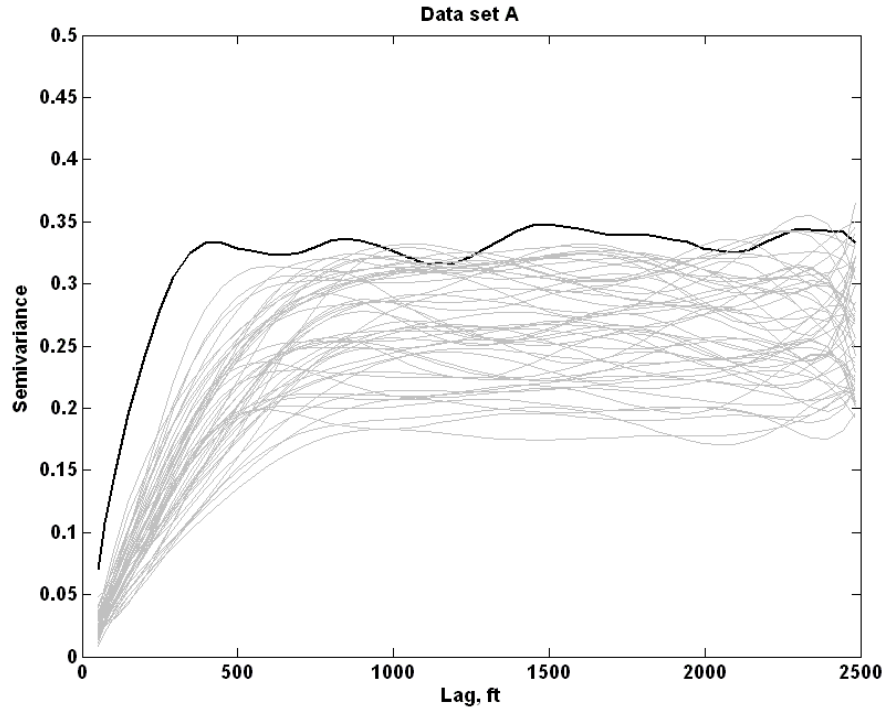

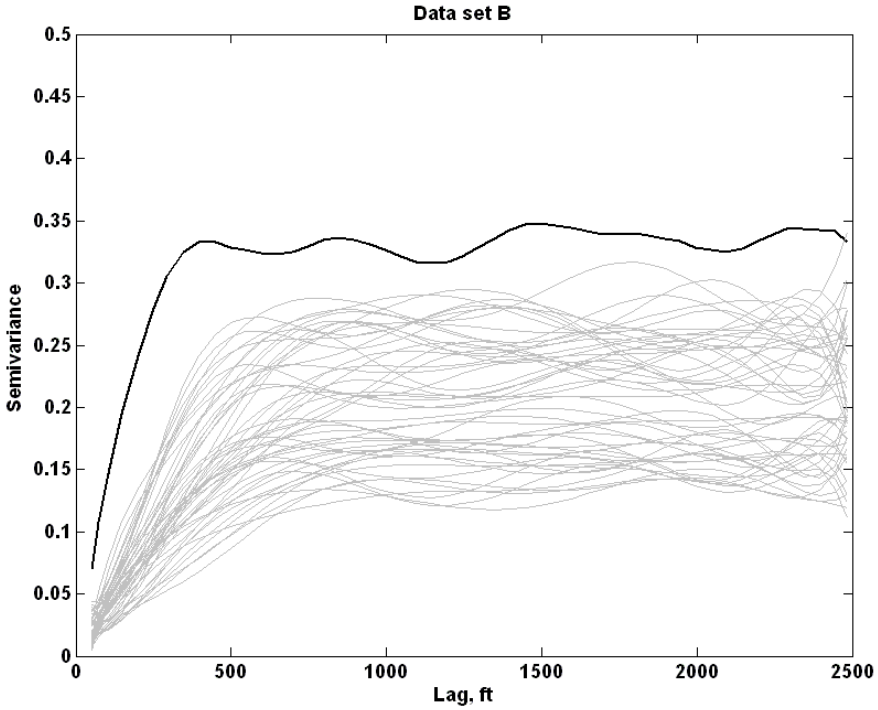

Figure 3.30 Comparison between semivariograms of the permeability realizations generated by SIS using two data sets and the reference reservoir

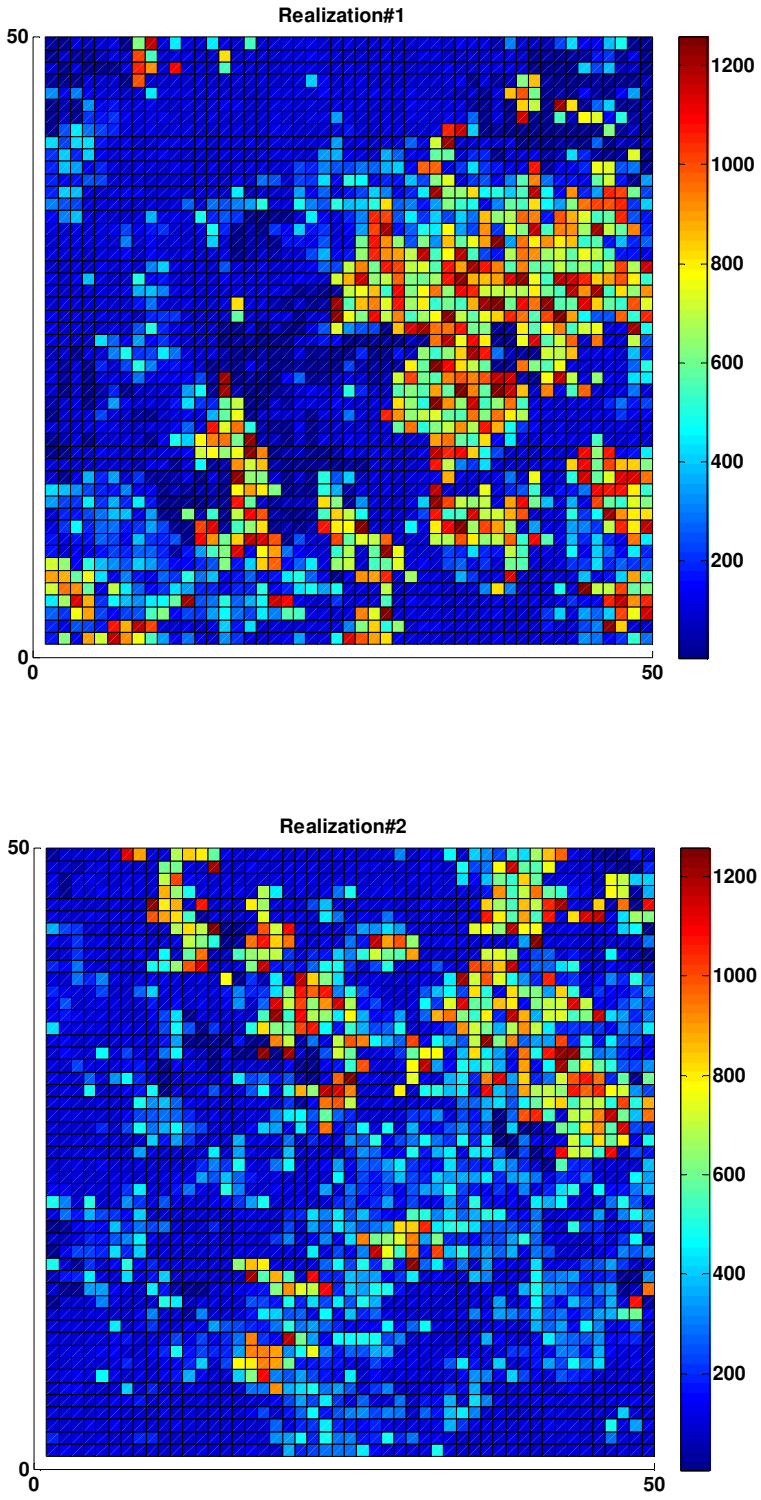

Figure 3.31. SIS Permeability realizations using data set A.

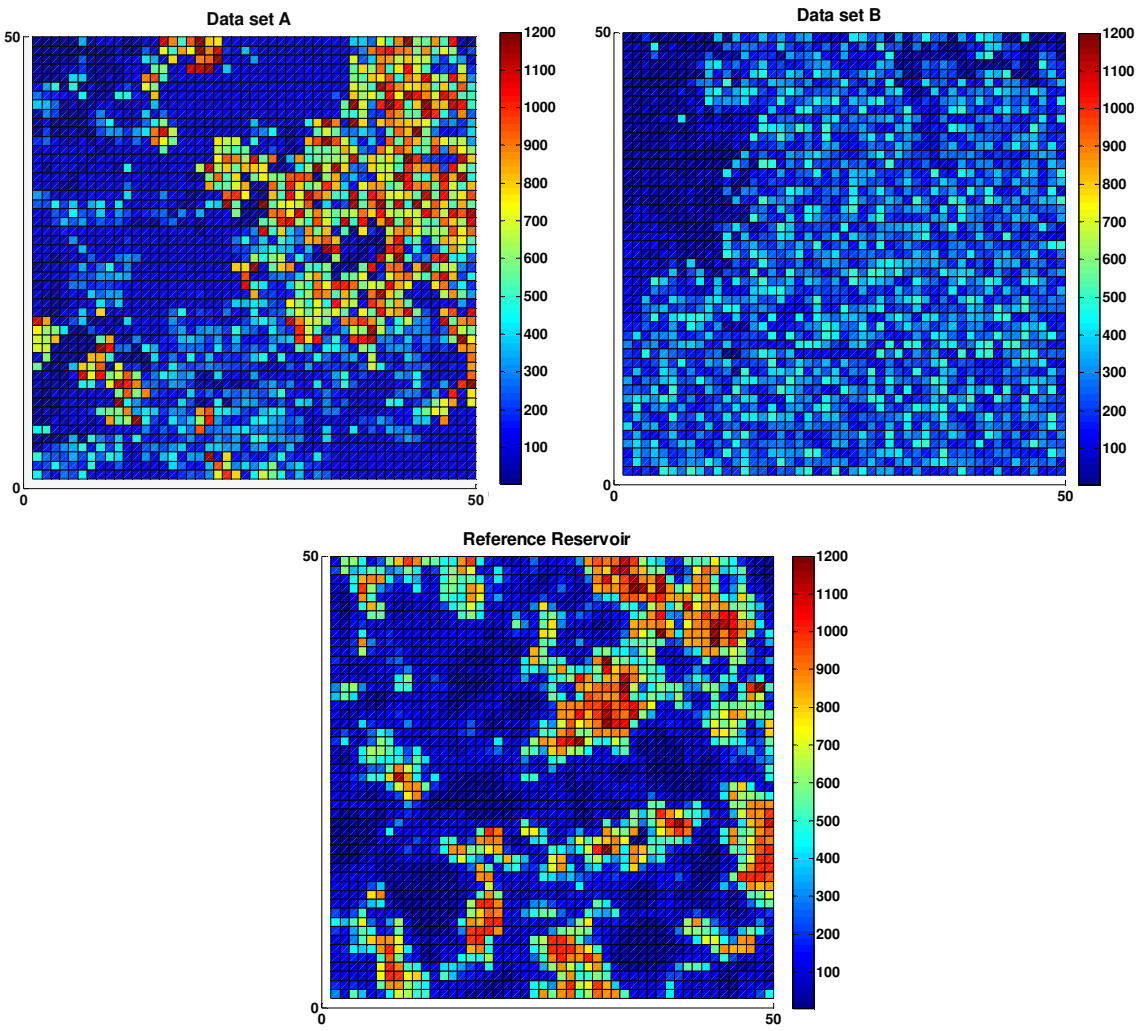

Figure 3.32. Comparison of the permeability maps generated by SIS using two data sets A & B and the reference reservoir

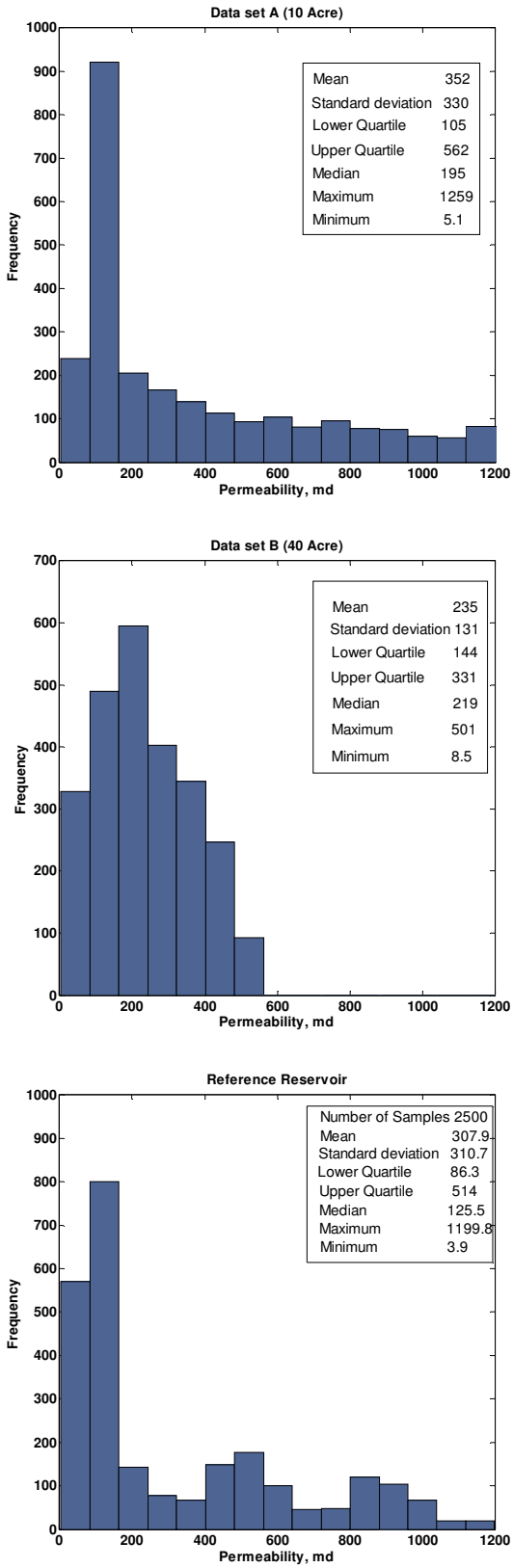

Figure 3.33. Histograms of permeability maps shown in Figure 3.32

This statistics indicates that the available samples in this data set do not represent the real heterogeneity of the reference field.

3.6. The Effect of Second Variable (Porosity)

All the estimation methods that are discussed in sections 3.1-3.5 use the sample values of one variable which is the permeability in this work. However, a data set often contains not only the primary variable of interest, but also one or more secondary variables. These secondary variables may be spatially cross-correlated with primary variables as discussed in Section 2.3.5. The secondary variable becomes even more valuable when the primary variable of interest is under-sampled. For example, in the petroleum industry permeability values are available at cored wells; while wells have well-log data including porosity values. In such cases, a cross correlation between permeability and porosity is one method to estimate permeability at unsampled locations. This section presents two methods to consider the effect of porosity on estimation of permeability.

3.6.1. Exponential Models (Crossplot)

Porosity and permeability relationship traditionally have been modeled with exponential functions of the form:

$$k = \alpha e^{\beta \Phi} \tag{3.1}$$

or equivalently,

$$\ln(k) = \ln(\alpha) + \beta \Phi \tag{3.2}$$

where k is the permeability, Φ is porosity, and α and β are constants. These models offer the advantages of simplicity and convenience since they fit the data into a straight line on semi-logarithmic plot. However, they unrealistically predict nonzero permeabilities when the porosity is zero.

In one approach, the porosity samples were taken from well locations in the 10 Acre and 40 Acre patterns (Data sets A and B) of the hypothetical Stanford Reservoir. Then the porosity distribution was estimated by ordinary kriging using two data sets A & B. Figure 3.34 shows the porosity maps generated by ordinary kriging (sample A and B) and the porosity distribution of the real reservoir. Then, the exponential model was applied for both data sets to find the relationship between porosity and permeability. Figures 3.35 and 3.36 represent the crossplot of permeability-porosity for both cases. The R-square indicates the proportion of the variability captured by the model. For both cases, R-square is close to one, which indicates a linear relationship between LogPerm and porosity samples.

In the next step, the permeability values at all unsampled locations were estimated by means of the exponential model and the porosity values. Figure 3.37 compares the permeability distributions estimated by this method to the permeability distribution of the reference reservoir. The figure shows that the maps generated by this method display smooth distribution. This could be explained by the fact that the corresponding porosity maps used to generate permeability maps were estimated by ordinary kriging. The

univariate statistics and histogram of both permeability maps are compared to the permeability of the reference reservoir and is shown in Figure 3.38.

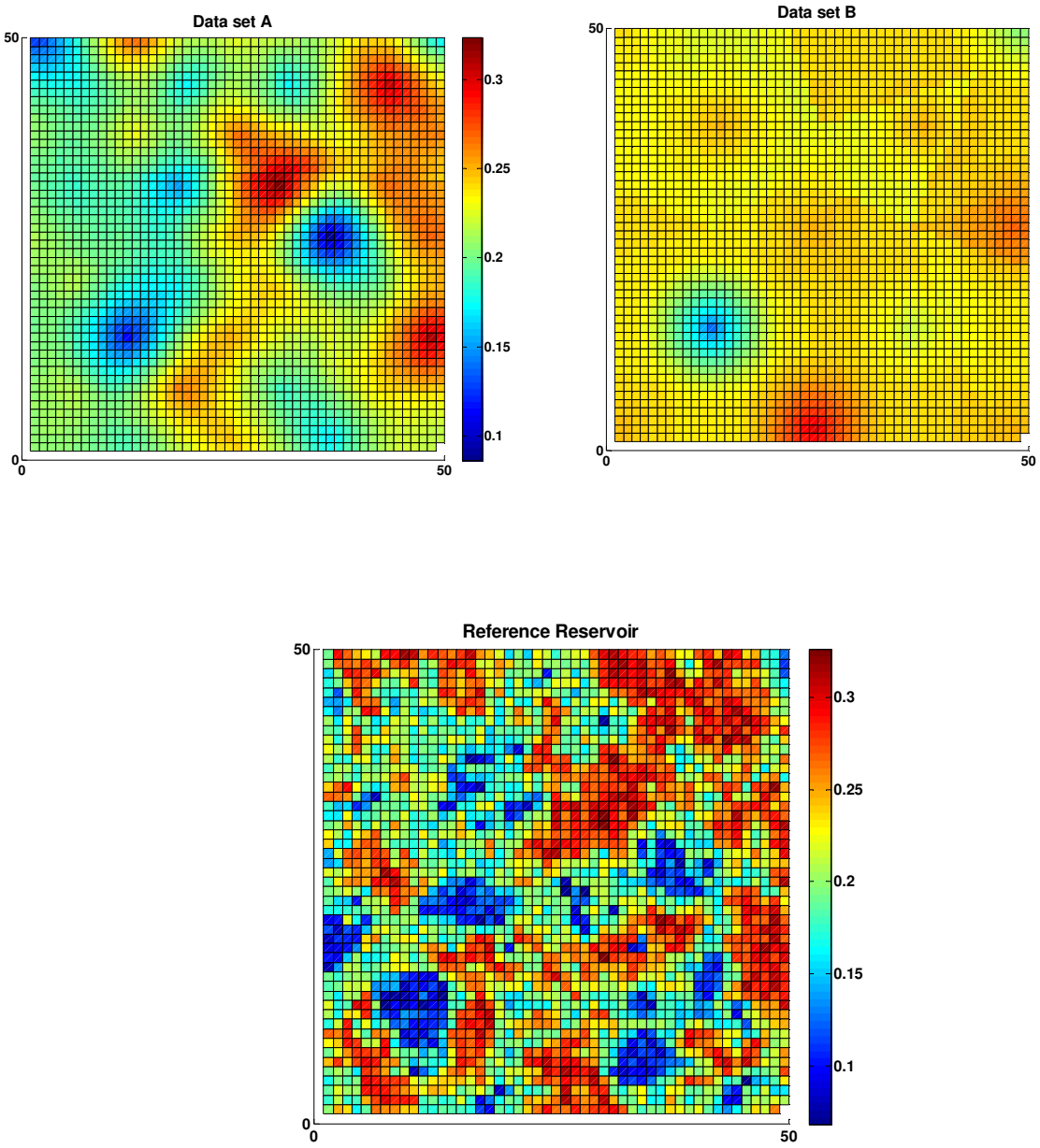

Figure 3.34. Comparison of the porosity maps generated by ordinary kriging using two data sets A & B and the reference reservoir

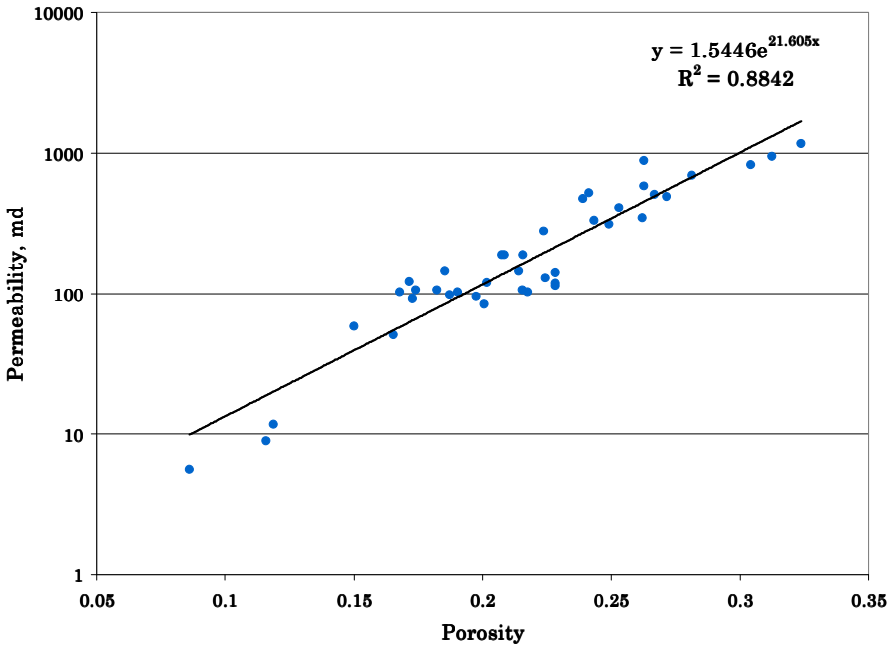

Figure 3.35. Crossplot of permeability and porosity for data set A

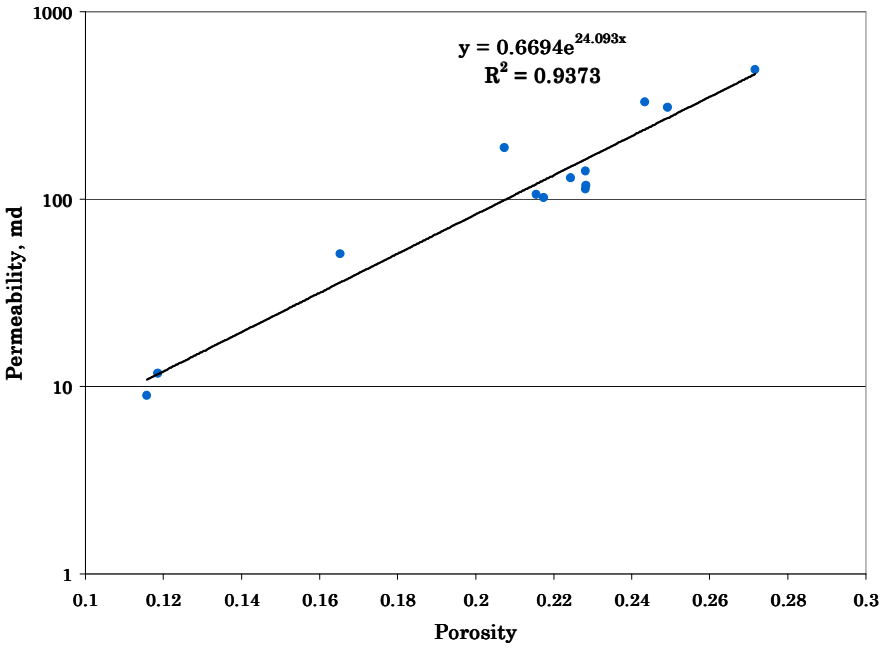

Figure 3.36. Crossplot of permeability and porosity for data set B

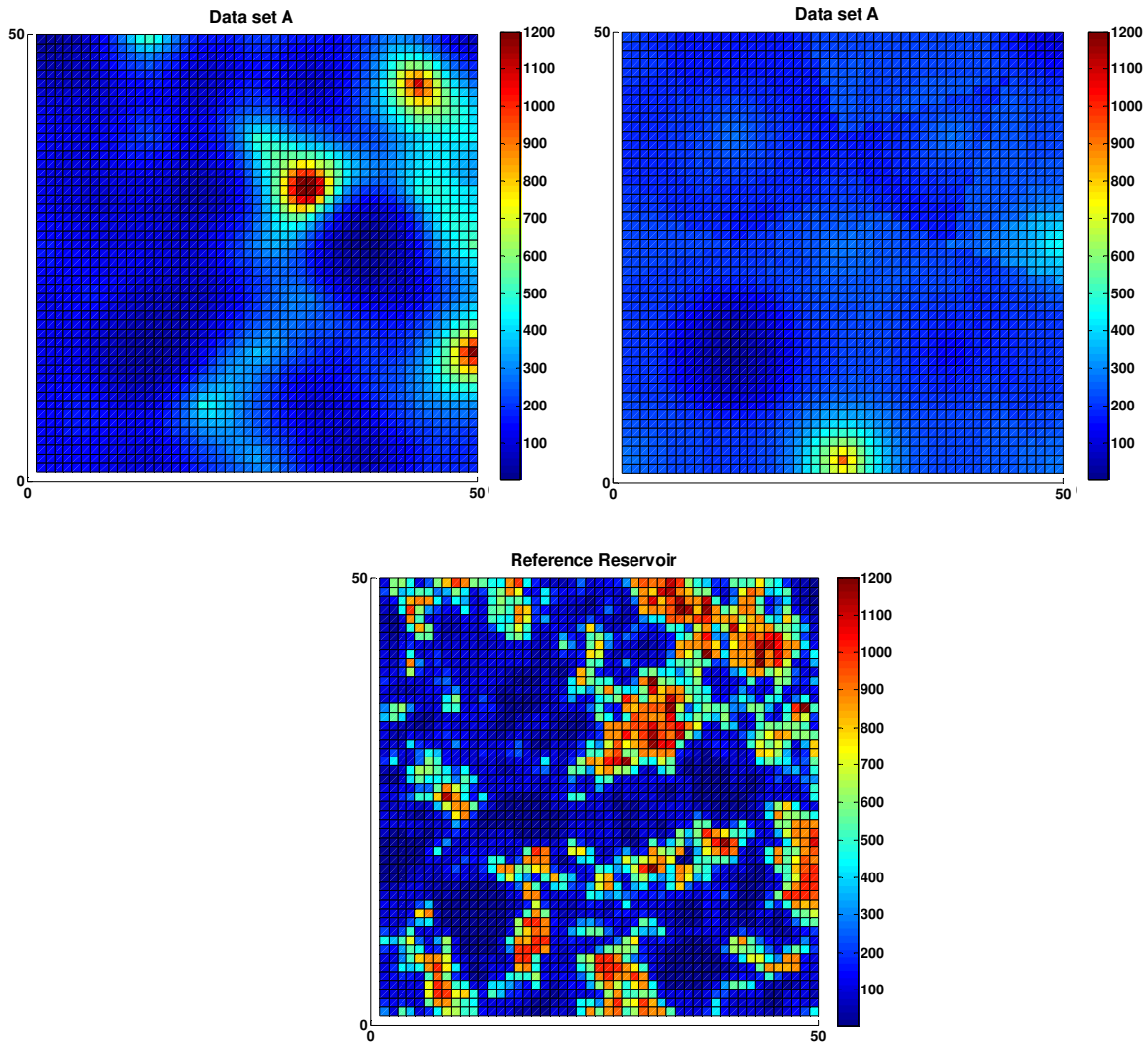

Figure 3.37. Comparison of the permeability maps generated by exponential model using data sets A & B

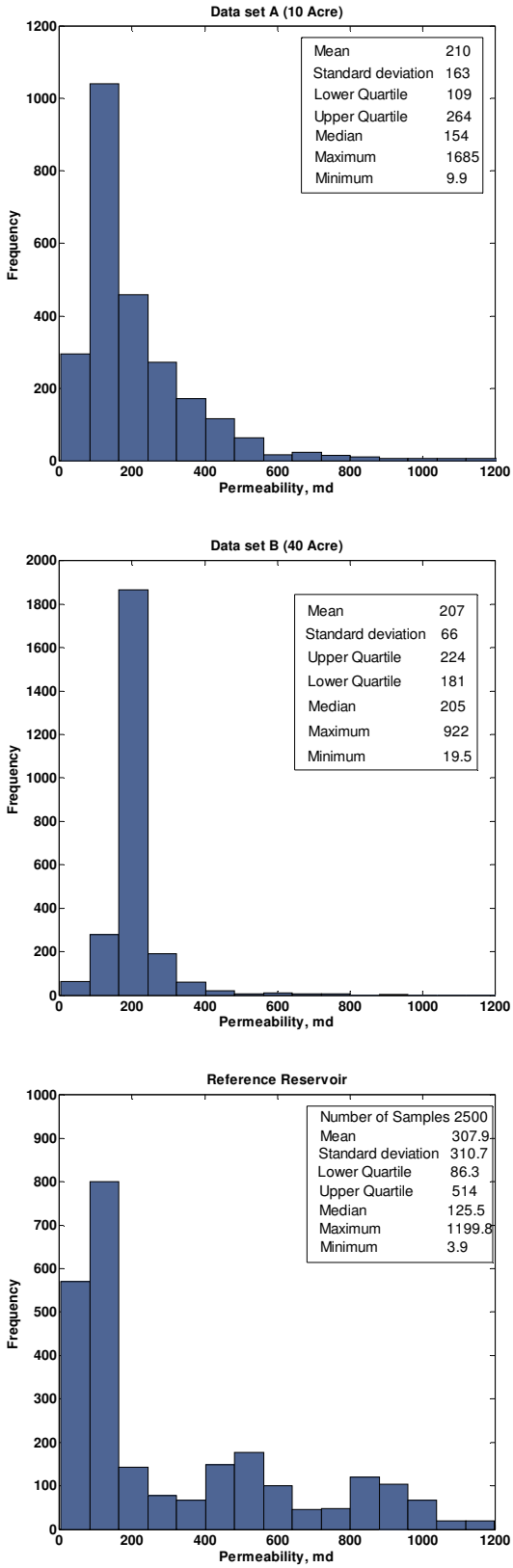

Figure 3.38. Histograms of permeability maps in Figure 3.37

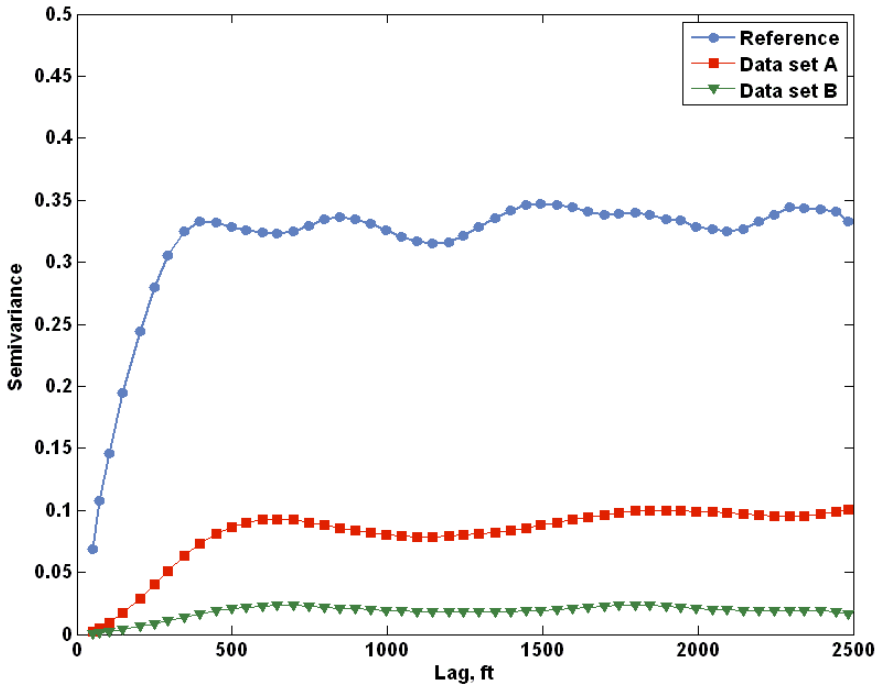

Figure 3.39. Comparison between experimental semivariogram of permeability estimated by exponential model and the reference reservoir

The histogram of permeability map generated using data set A is wider in comparison with that of the map generated by the data set B. A wider range of permeability values was generated once more sample data were taken from the data set A (41 samples). However, the heterogeneity of these maps is not close to the real heterogeneity of the reference reservoir. This is illustrated by Figure 3.39 in which the experimental semivariograms of these permeability maps are compared to that of reference reservoir. The sill of the LogPerm semivariograms, which shows the variance of the data, in both realizations are much smaller than that of the reference reservoir. From above comparisons, one can conclude the method presented here can not capture the real heterogeneity of the reservoir.

3.6.2. Co-kriging

GSLIB program cokb3d was used to generate the permeability distribution by co-kriging method using two sample data sets A and B. The required input parameters such as the search radius, the minimum and maximum number of points are the same as ordinary kriging. The permeability and porosity data was considered as primary and secondary variables respectively. Porosity values at unsampled locations were estimated with ordinary kriging using the hard conditioning data sets. The strong positive correlation between porosity and logarithm of permeability (LogPerm) for the samples of the two data sets is shown in Figures 3.35 and 3.36. The abundance of porosity data and positive correlation with the LogPerm makes porosity a good candidate for a secondary variable in co-kriging.

The following steps were taken to estimate the permeability with co-kriging method. First, the experimental cross variogram of porosity and LogPerm were estimated and matched with a mathematical model (Figure 3.40). Then, the permeability distribution was generated using the samples of the two data sets A & B. Figure 3.41 indicates the comparison between permeability maps generated by co-kriging and the reference permeability distribution. Figure 3.42 shows the histogram of the permeability data created by co-kriging. The permeability map generated by the data set A contains a larger range of permeability in comparison to the one generated with data set B. This is related to difference in the number of available samples in data set A and B. The ability of co-kriging to reproduce the heterogeneity of the reference reservoir is illustrated in Figure 3.43. In this figure, the experimental semivariograms of the co-kriged

permeability maps generated by two data sets are compared to that of the reference reservoir. The variances of the permeability values in both maps are much smaller than that of the reference reservoir indicating the smoothing nature of co-kriging technique.

Figure 3.44 compares the permeability values of ordinary kriging and co-kriging estimation. The co-kriging and ordinary kriging estimates differ significantly as shown in this figure. Figure 3.45 shows that the co-kriging error variance is smaller than the error variance estimated with ordinary kriging. This shows that additional information used in co-kriging reduces the error variance in estimate.

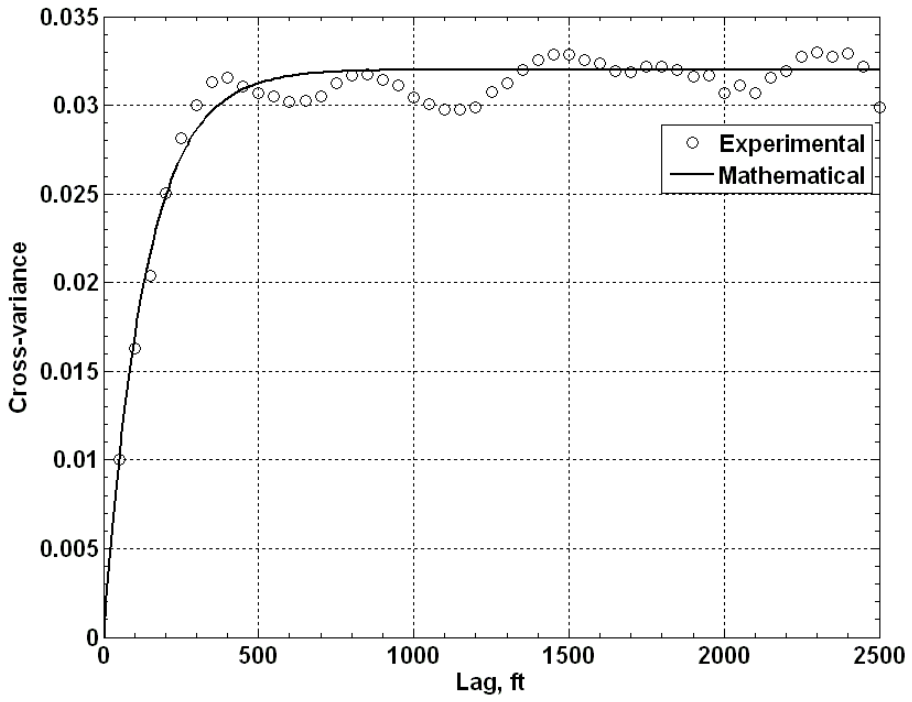

Figure 3.40. Experimental and mathematical cross-variogram of porosity and LogPerm for the reference reservoir

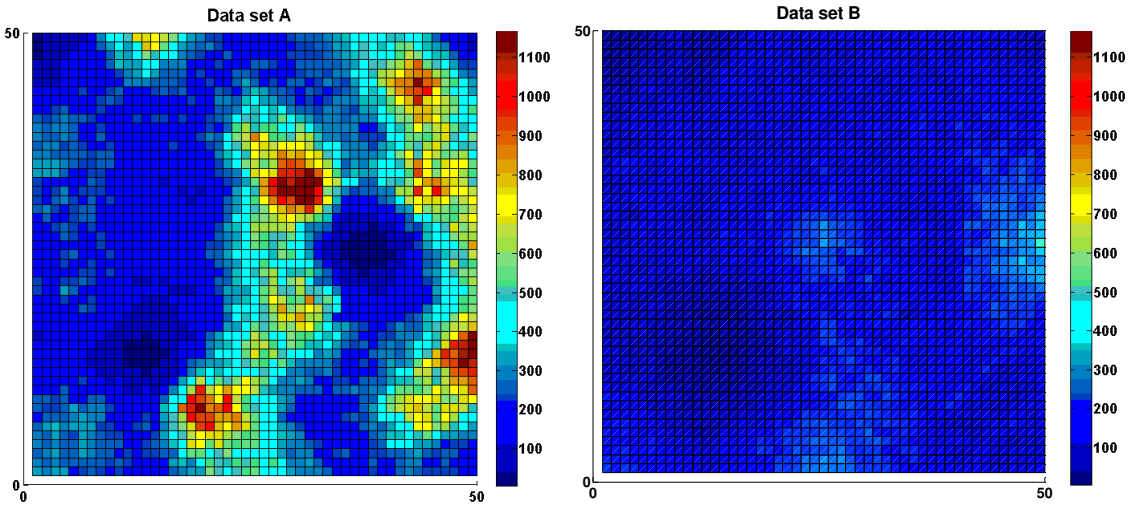

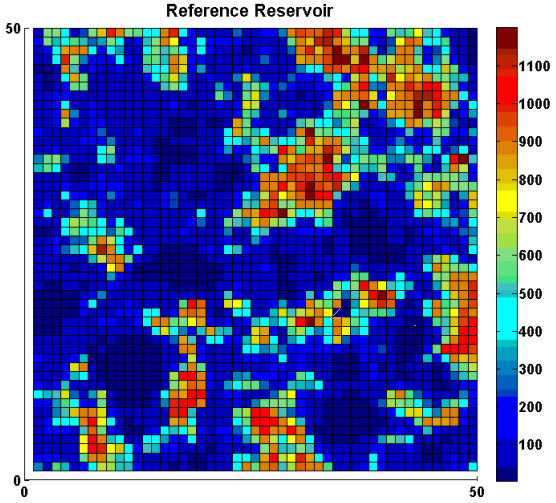

Figure 3.41. Comparison of the permeability maps generated by co-kriging model using data sets A & B and the reference reservoir

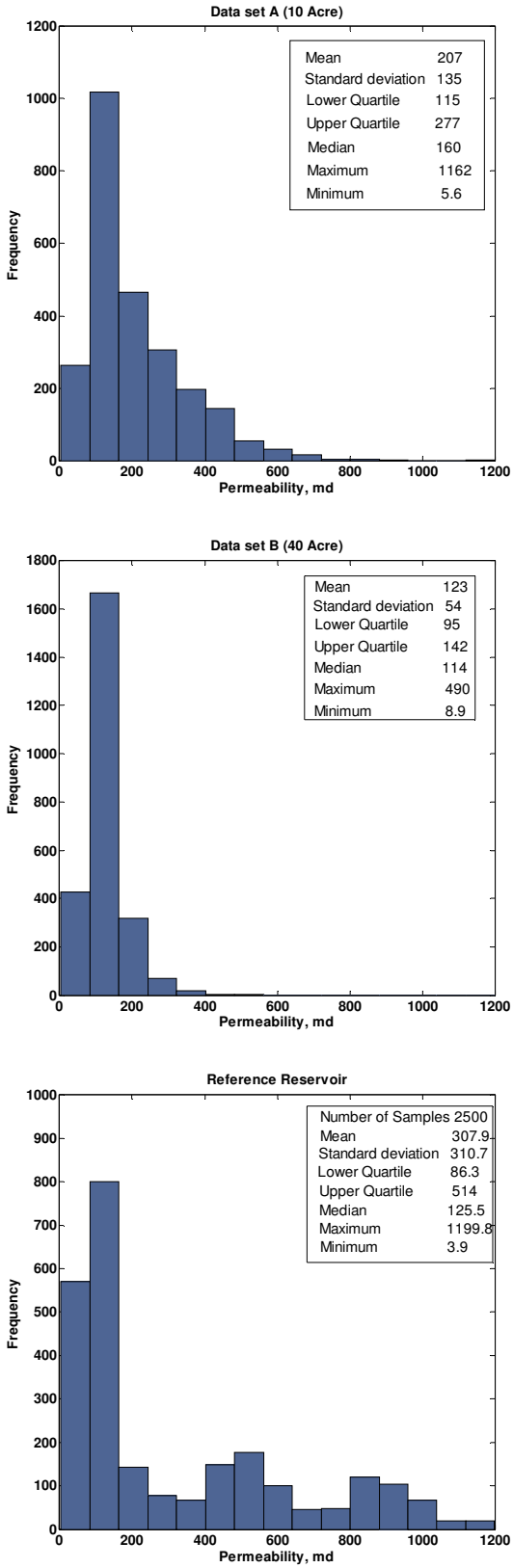

Figure 3.42. Histograms of permeability maps in Figure 3.41

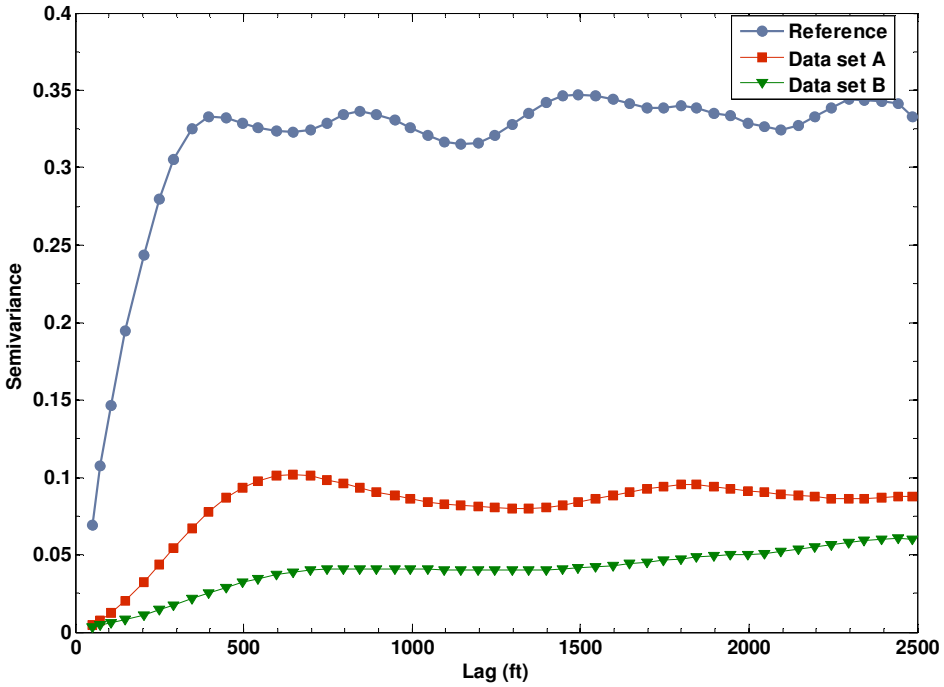

Figure 3.43. Comparison between experimental semivariogram of permeability estimated by co-kriging and the reference reservoir

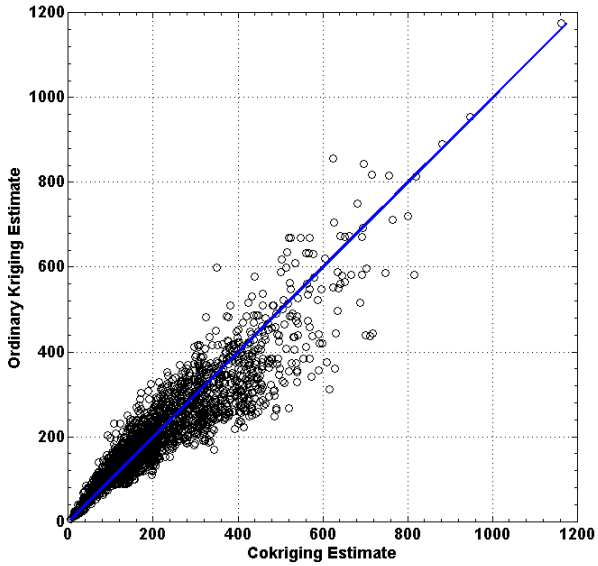

Figure 3.44. Comparison between ordinary kriging and co-kriging estimation

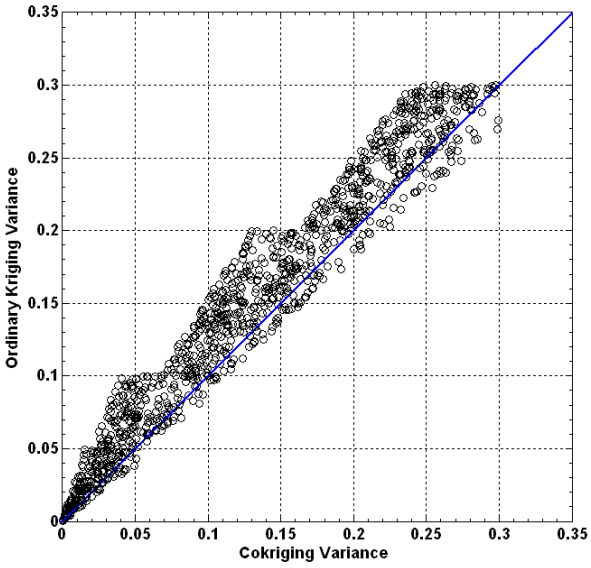

Figure 3.45. Comparison between ordinary kriging and co-kriging estimation error variance

3.7. The Effect of Quantity of Sample Data on Dynamic Data

The effect of quantity of sample data was studied with flow simulations. The permeability distribution was estimated from data set A or data set B. As mentioned earlier, the difference between the data sets is in the number of sample data in each set. In order to estimate the permeability from the data set, geostatistical methods discussed earlier in this chapter were employed.

The flow simulator used in the study was ECLIPSE100© Black Oil simulator (Section 3.4). The parameters of the simulated reservoir are listed in Table 1. For the base case, a simulation was run using these parameters and the base case permeability distribution. The results of this simulation in terms of cumulative oil production and oil rate for production wells P1, P2, P3, and P4 in Figure 3.5 are regarded as the base case. The permeability distribution that was estimated from data set A (10 Acre), and data set B (40 Acre) from each of the described geostatistical methods was used as input for the simulation, leaving the other parameters unchanged. The results of each of these simulations were compared to the base case results in Figures 3.46 through 3.57. It should be noted that in case of sequential Gaussian (SGS) and indicator simulation (SIS) the permeability realizations generated by the average semivariogram (Figures 3.21 and 3.25) was taken as the input to simulations.

For the Monte Carlo techniques such as SIS and SGS, the simulation was carried out for all fifty permeability realizations. Figures 3.58 through 3.61 present the cumulative oil production of each well for all fifty SGS and SIS stochastic permeability

realizations (solid blue line) generated by data sets A and B compared against the base case (filled black circle). The cumulative production after fifty days was selected to quantify the accuracy and precision of the Monte Carlo techniques (SGS & SIS) for the two data sets A and B. Figures 3.62 through 3.65 show the histogram of cumulative oil production for each well after fifty days resulting from SGS and SIS permeability realizations generated by data sets A and B respectively. The true values are shown in the histograms as black solid circles. The mean of frequency distribution for the histograms corresponding to data set A (more available samples) is closer to the true value when compared against the mean value of histograms corresponding to data set B. The lower standard deviation of the histograms obtained using data set A indicates better precision of the corresponding permeability realizations.

In order to quantify the goodness of fit of the simulation results of the realization to that of the reference cases an objective function is used. The objective function, f, is a modified form of the simple sum of the squares. This function is defined as follows:

$$f = \frac{\alpha}{2} r^T r \tag{3.3}$$

where α is the overall weight for the production, r is the vector of residuals for the observed production data, and T is the transpose of a matrix. Each element, r_i, in the vector of residuals for the observed production data is the normalized and weighted difference between an observed production value and the corresponding simulated value. These elements are defined as:

$$r_i = w_i \frac{(O_i - C_i)}{\sigma_d} \tag{3.4}$$

where σ_d is measurement error for any production set, O_i and C_i are observed and calculated (simulated) production values, and w_i is the overall weighting of a data set respectively. Also,

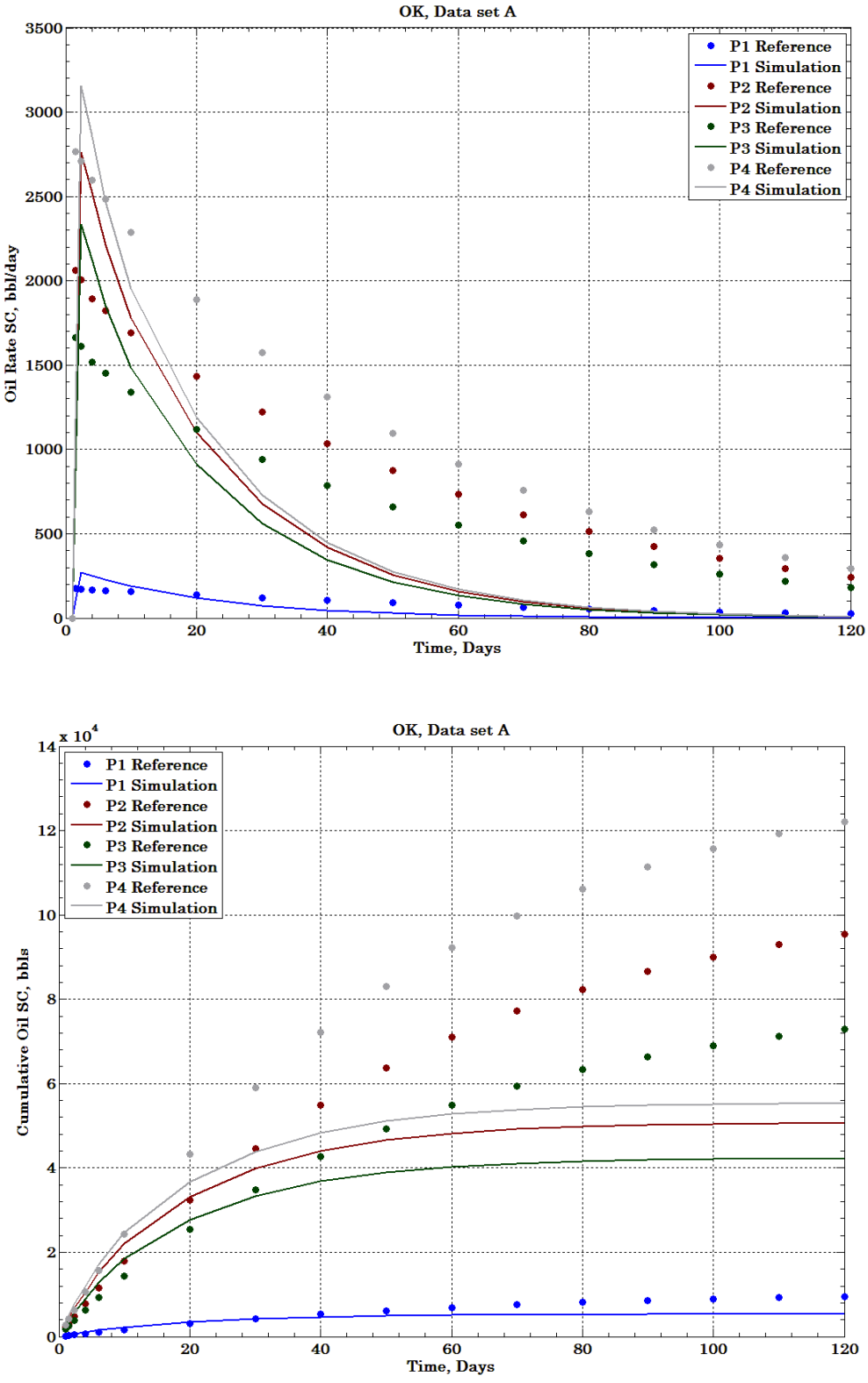

Figure 3.46. Comparison of dynamic data for ordinary kriging method using data set A

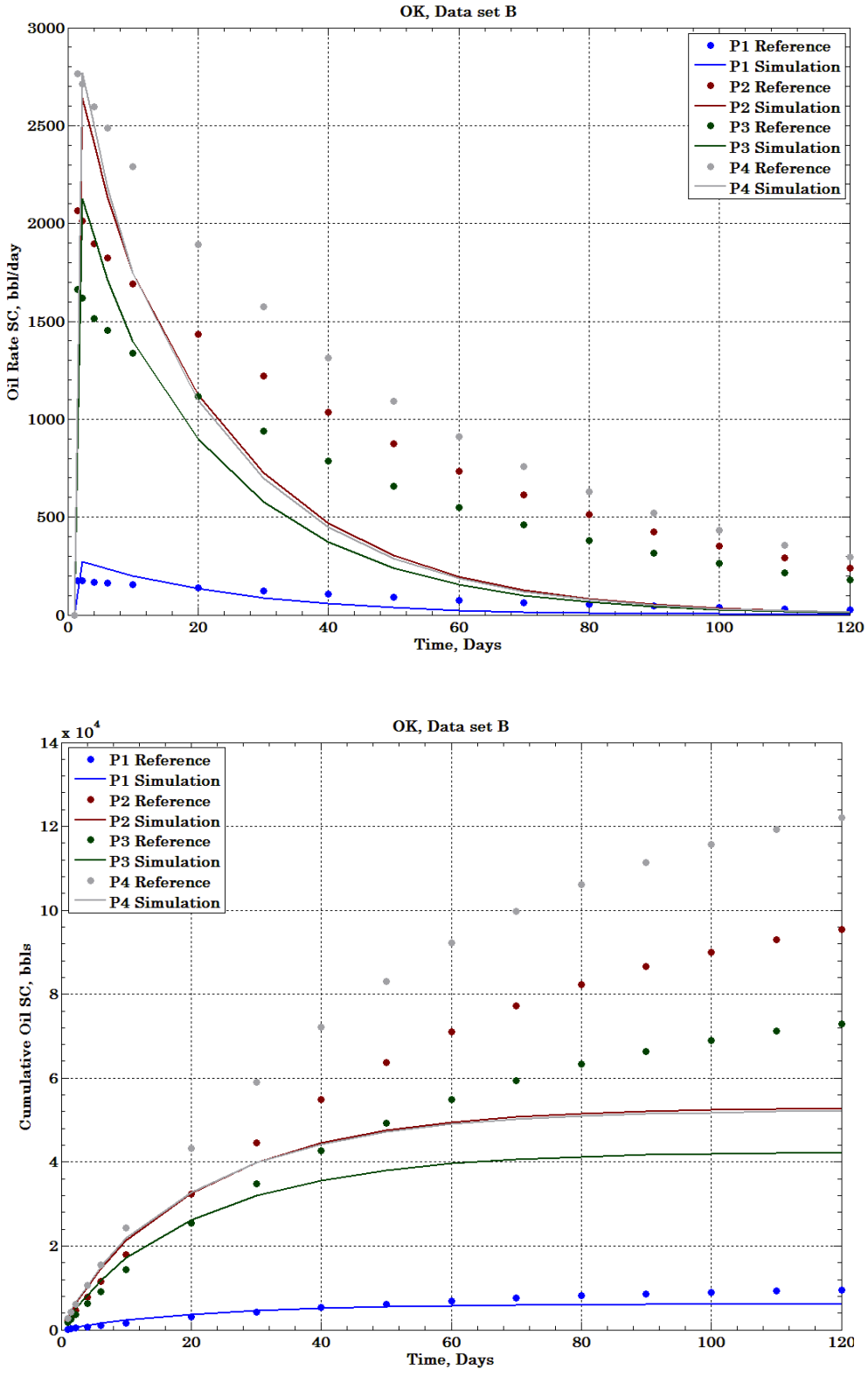

Figure 3.47. Comparison of dynamic data for ordinary kriging method using data set B

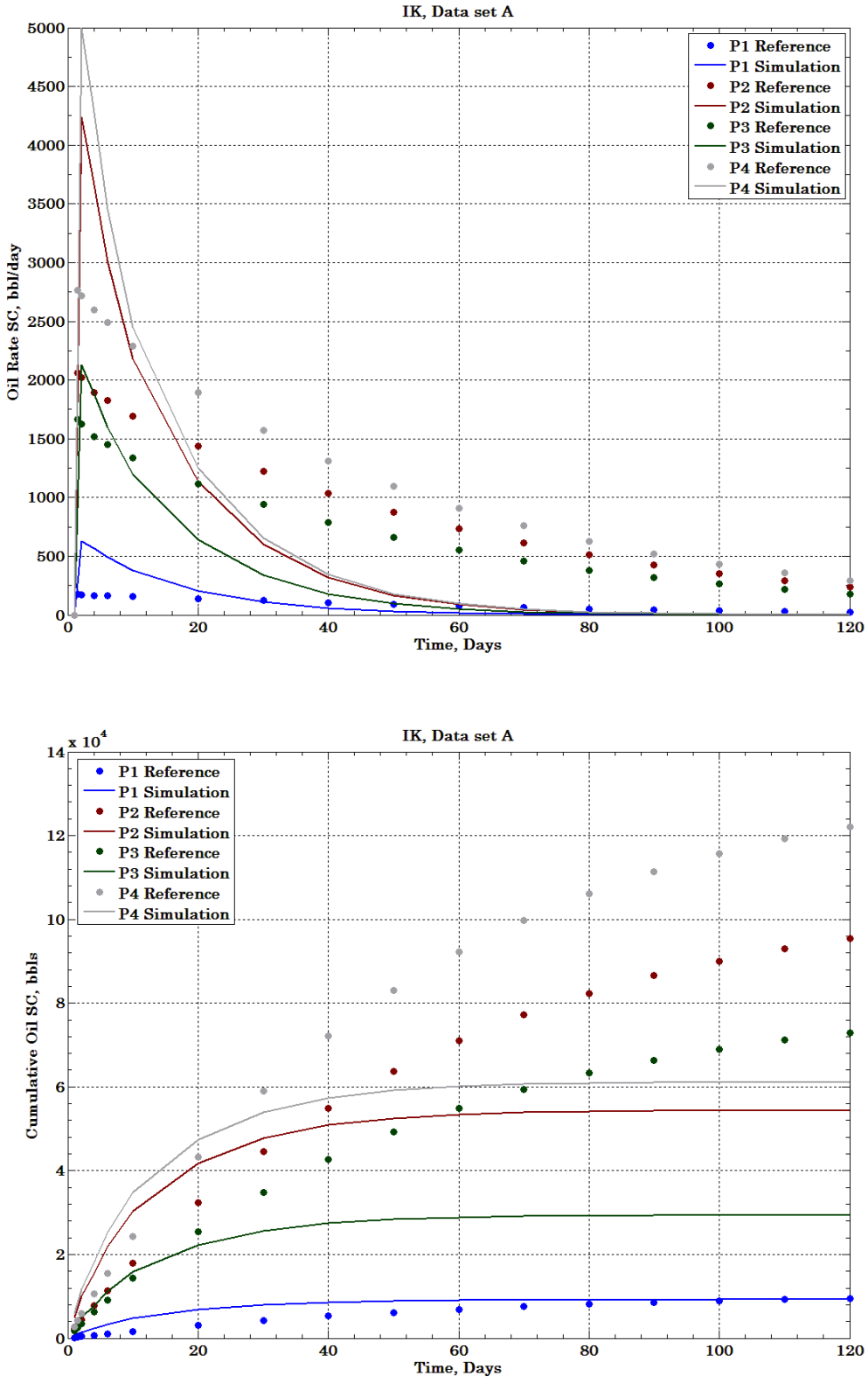

Figure 3.48. Comparison of dynamic data for indicator kriging method using data set A

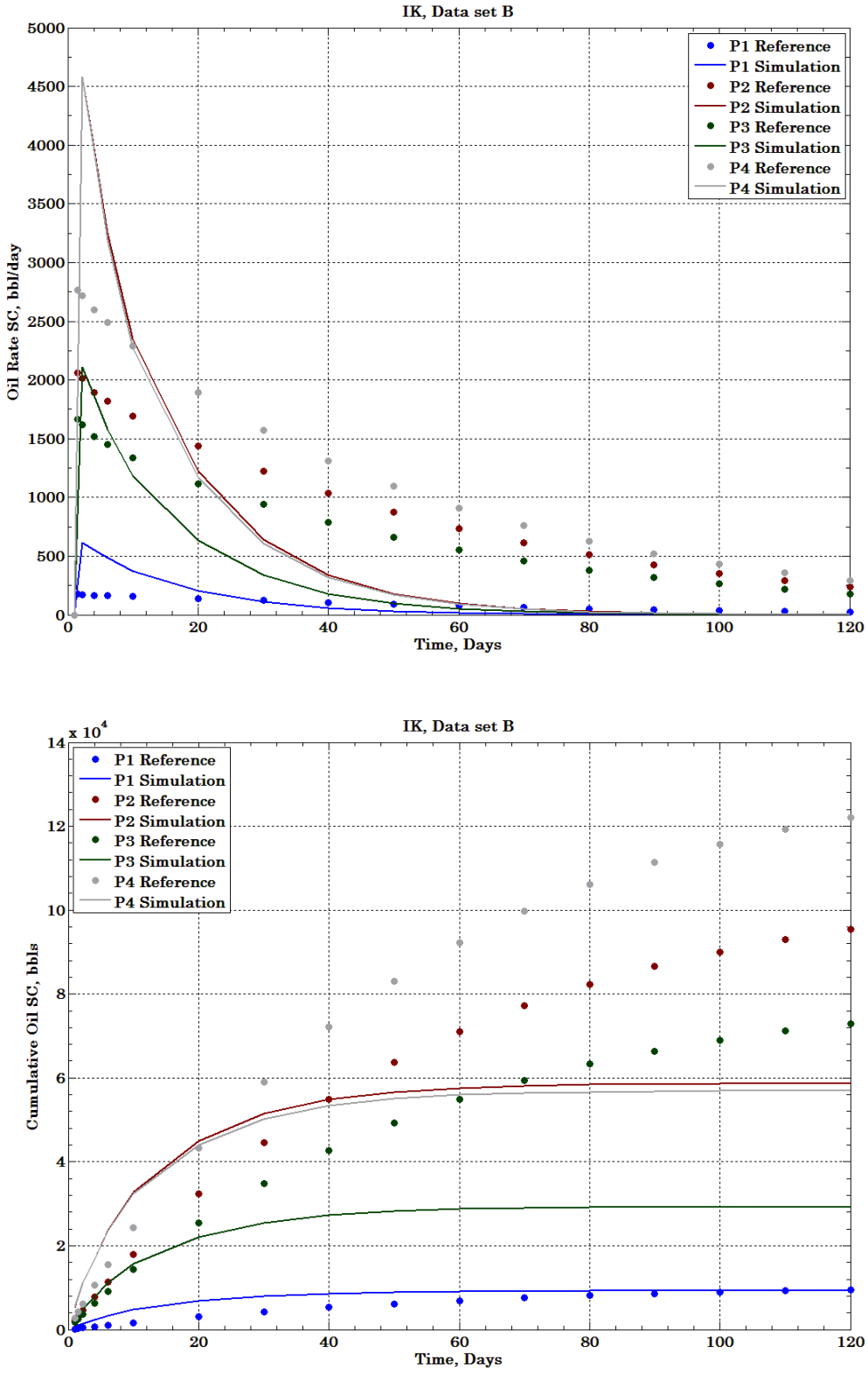

Figure 3.49. Comparison of dynamic data for indicator kriging method using data set B

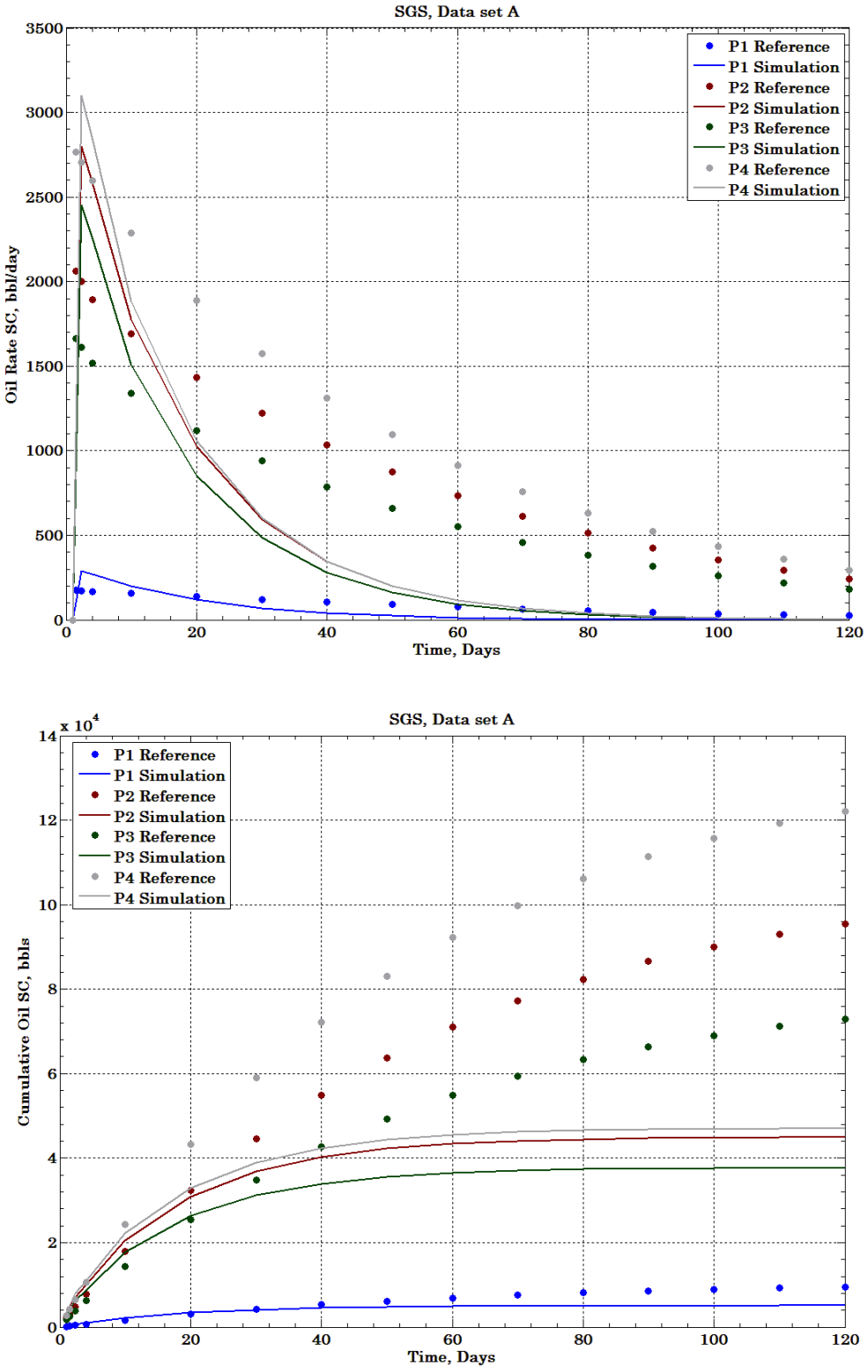

Figure 3.50. Comparison of dynamic data for SGS method using data set A

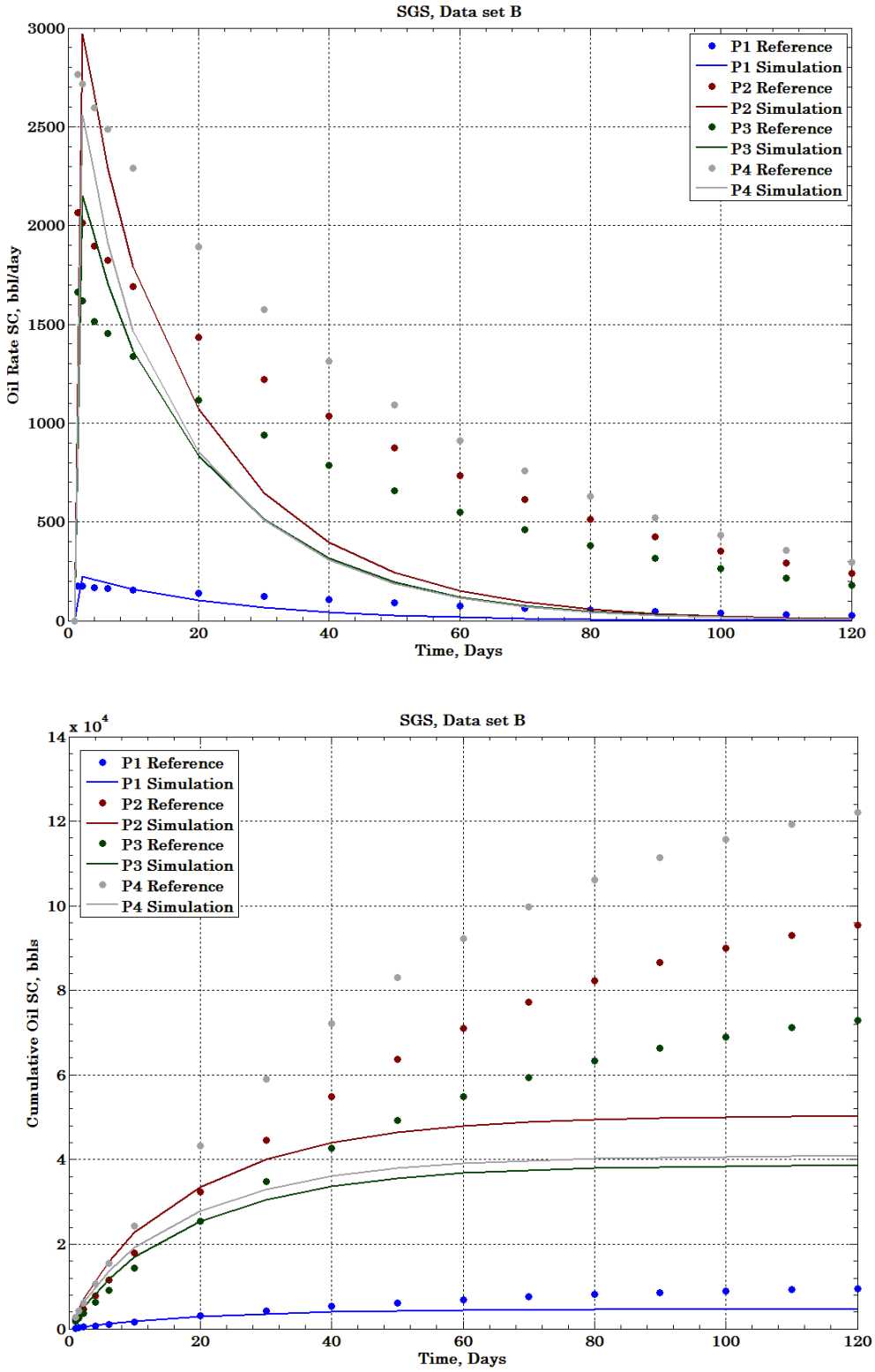

Figure 3.51. Comparison of dynamic data for SGS method using data set B

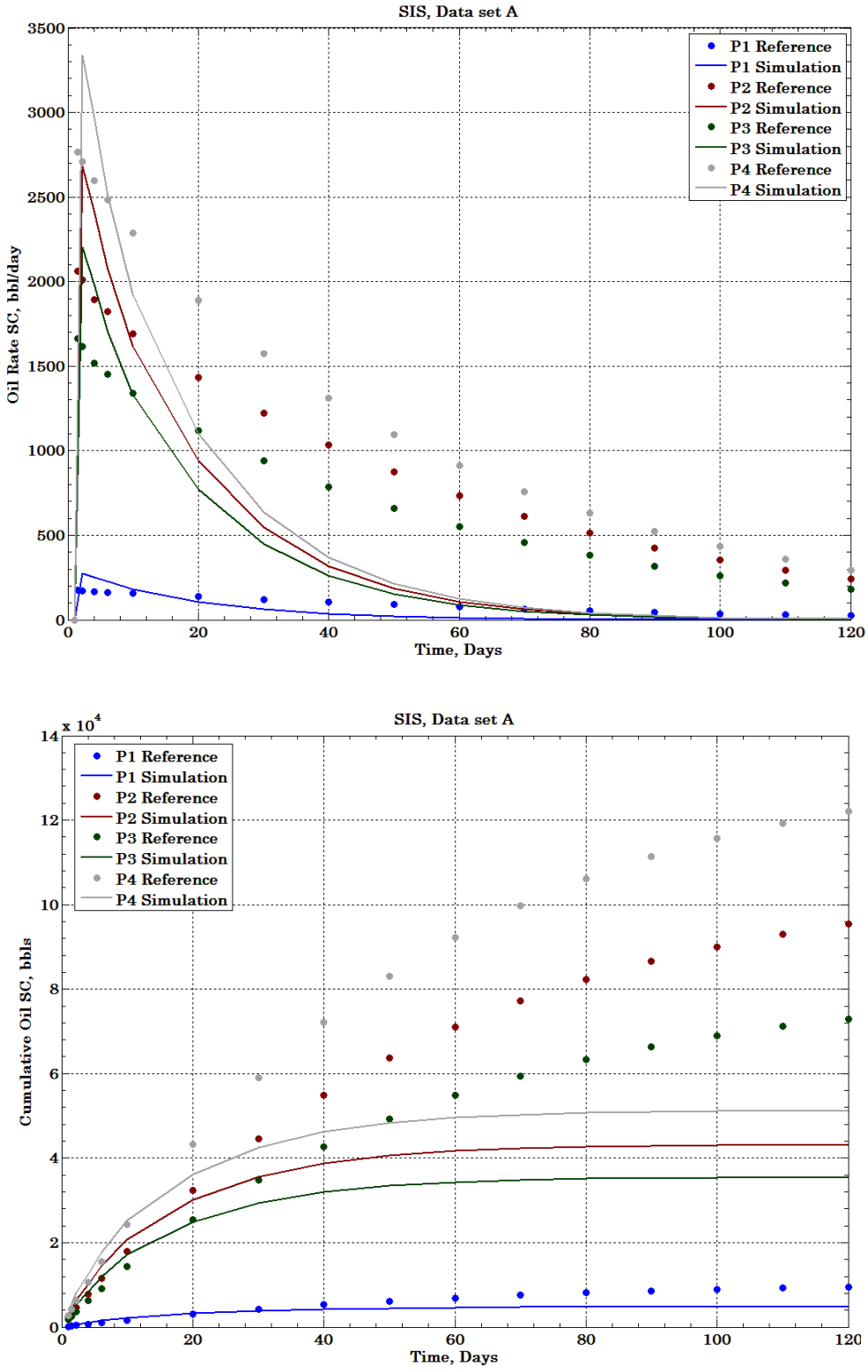

Figure 3.52. Comparison of dynamic data for SIS method using data set A

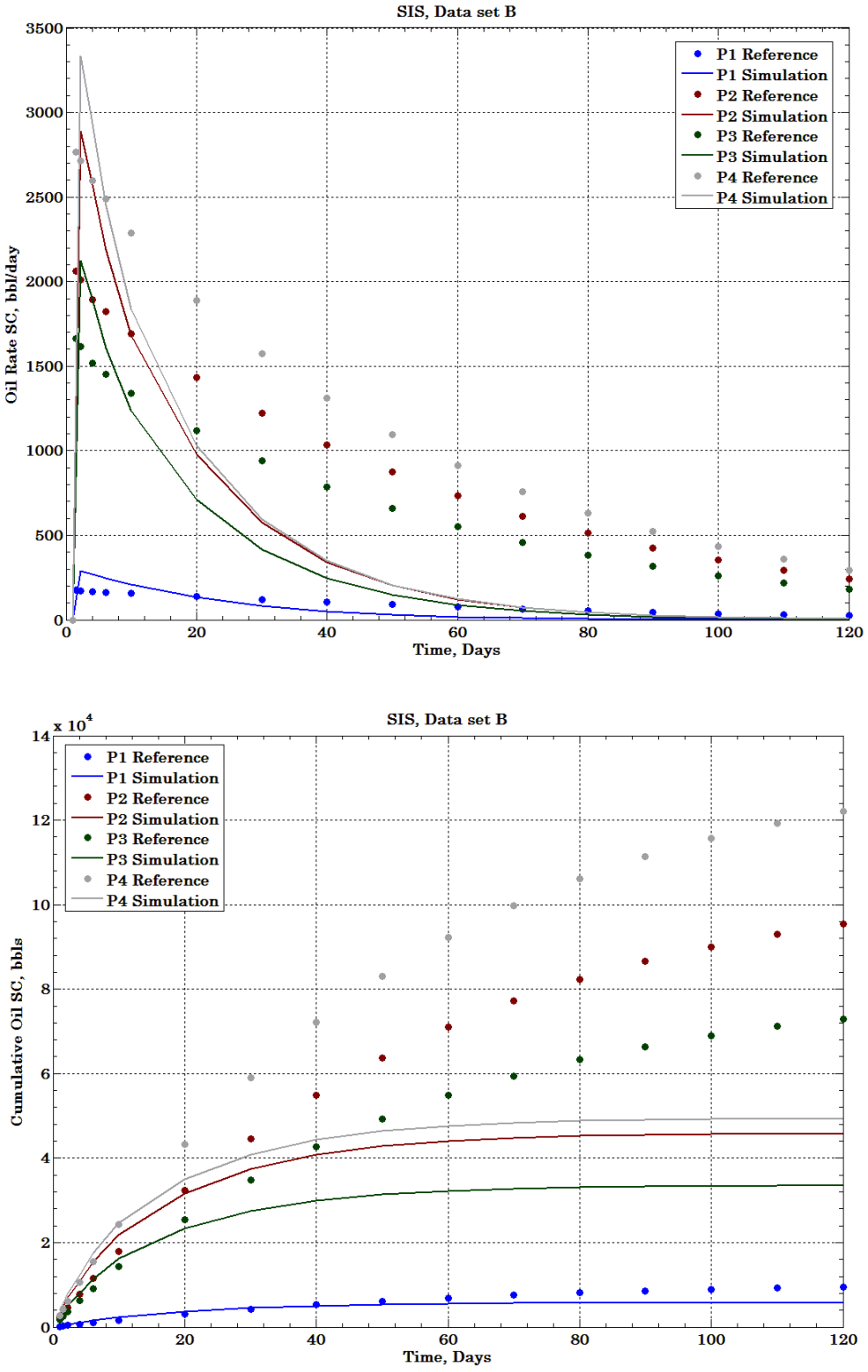

Figure 3.53. Comparison of dynamic data for SIS method using data set B

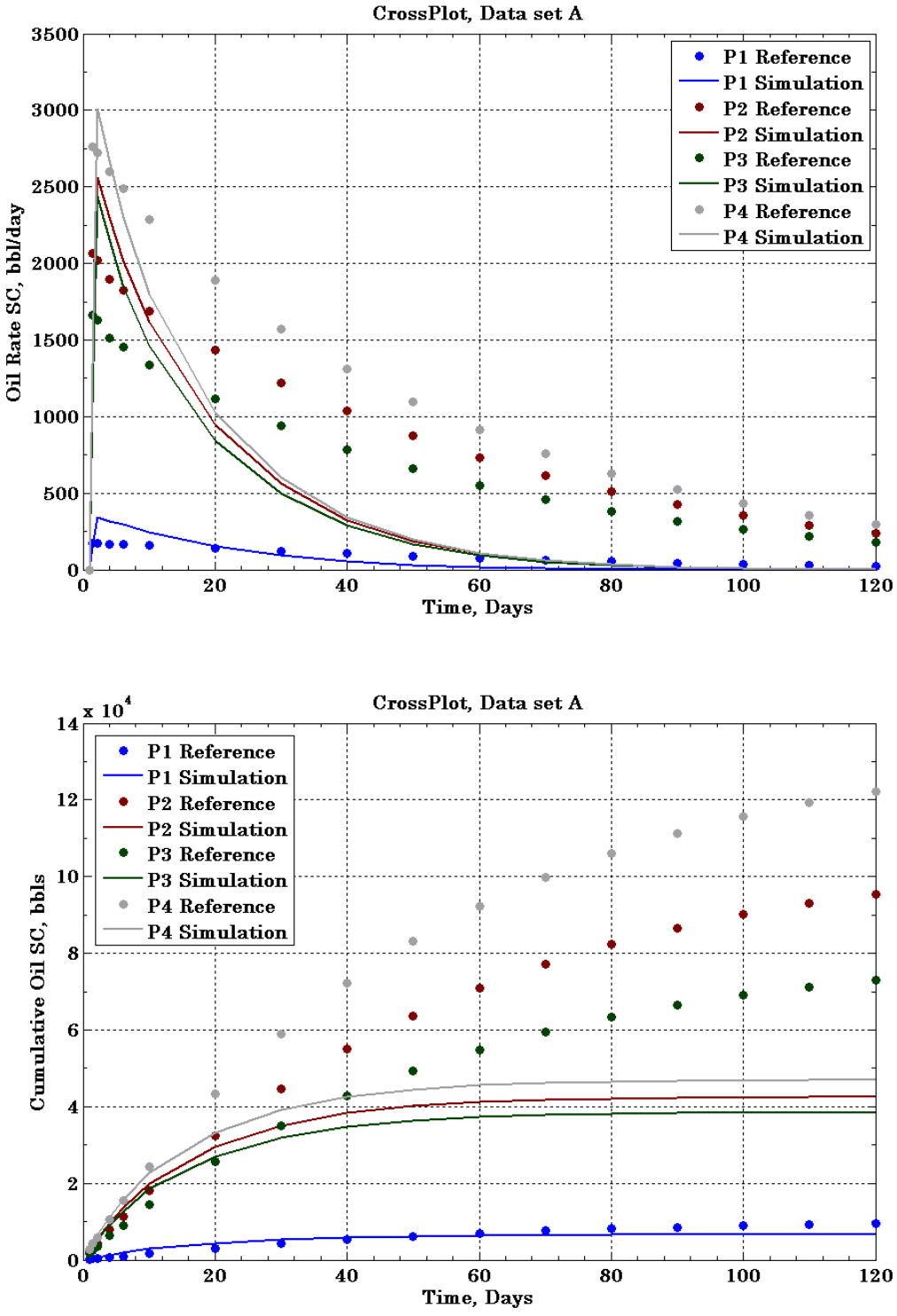

Figure 3.54. Comparison of dynamic data for Crossplot method using data set A

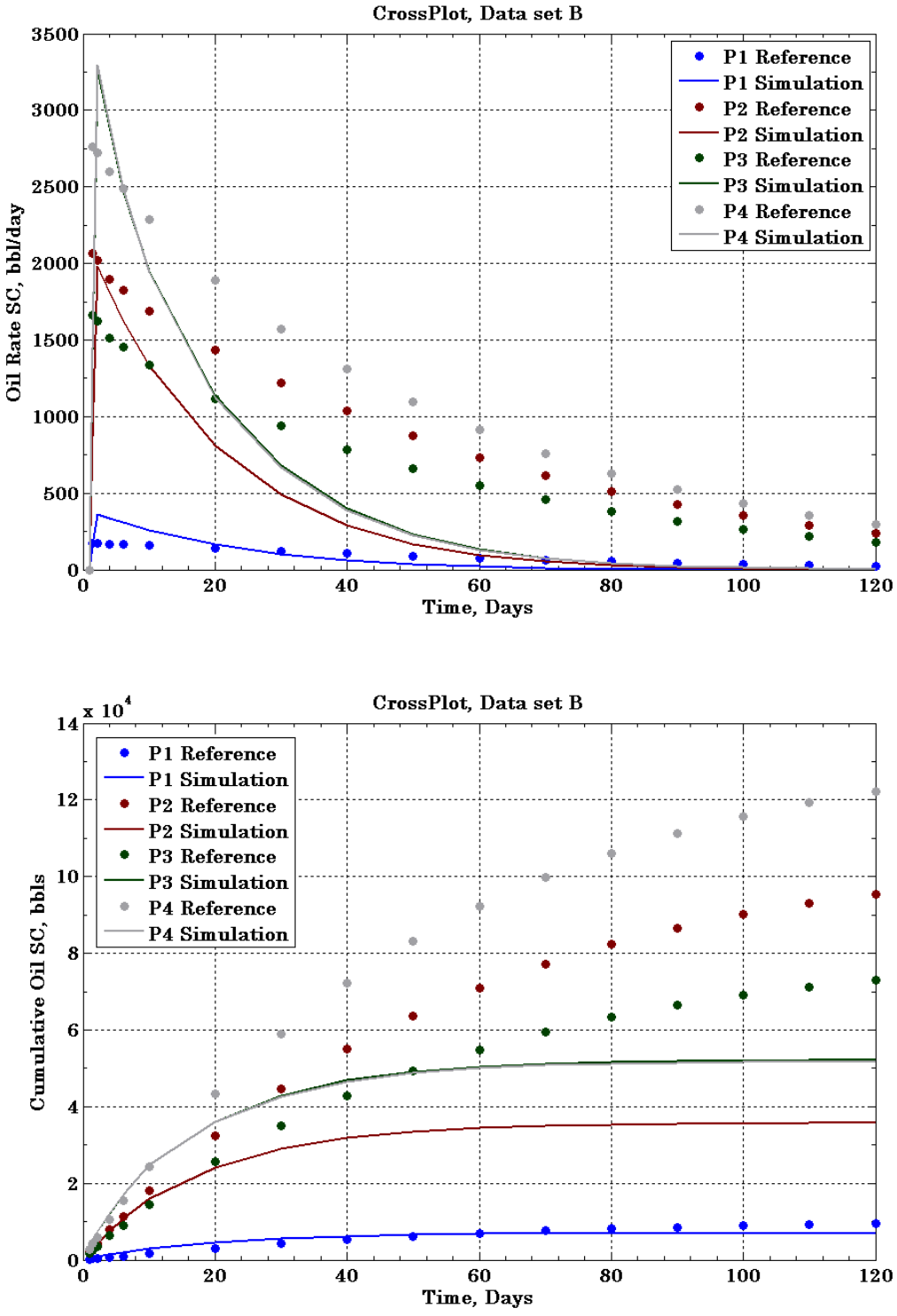

Figure 3.55. Comparison of dynamic data for Crossplot method using data set B

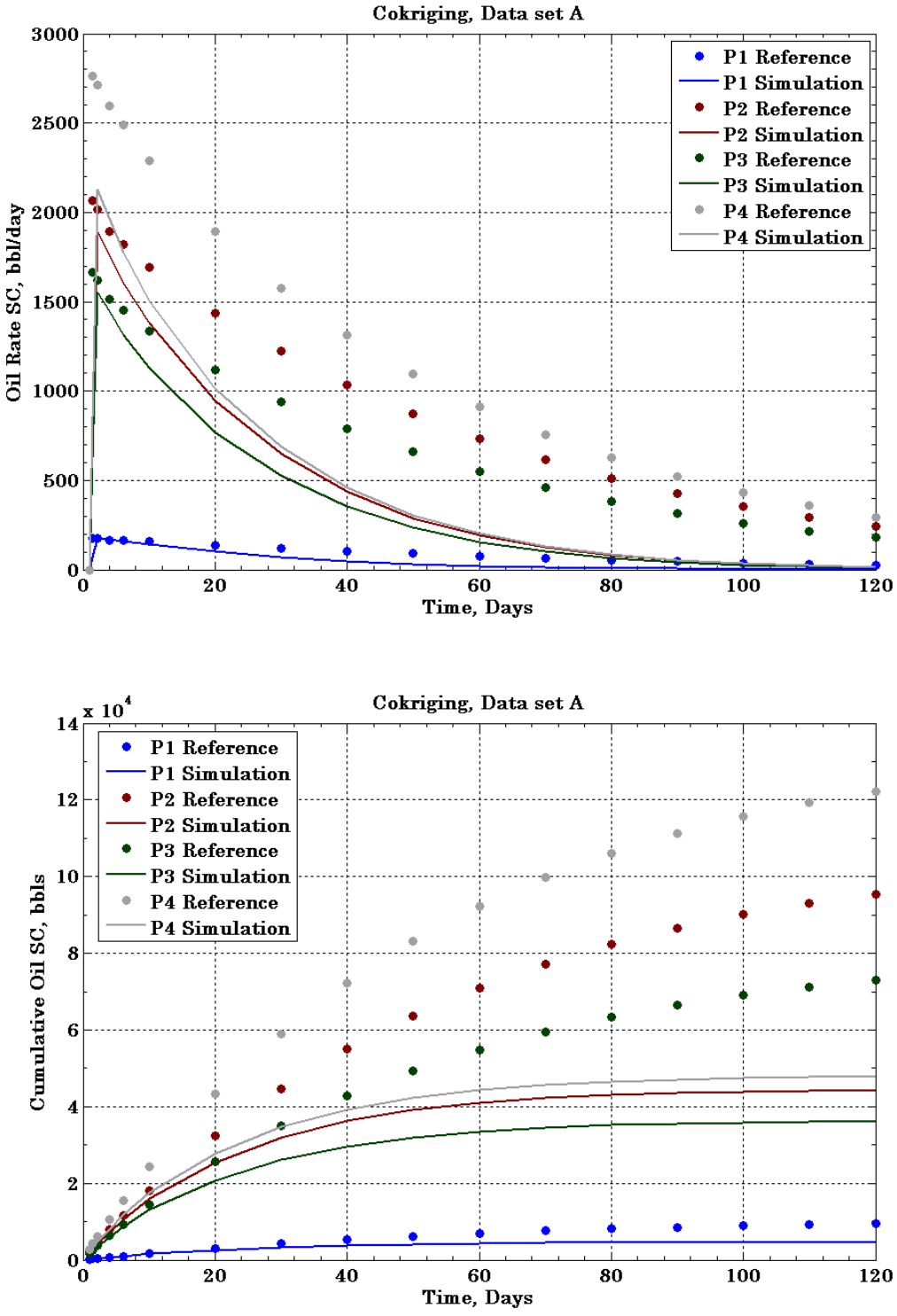

Figure 3.56. Comparison of dynamic data for co-kriging method using data set A

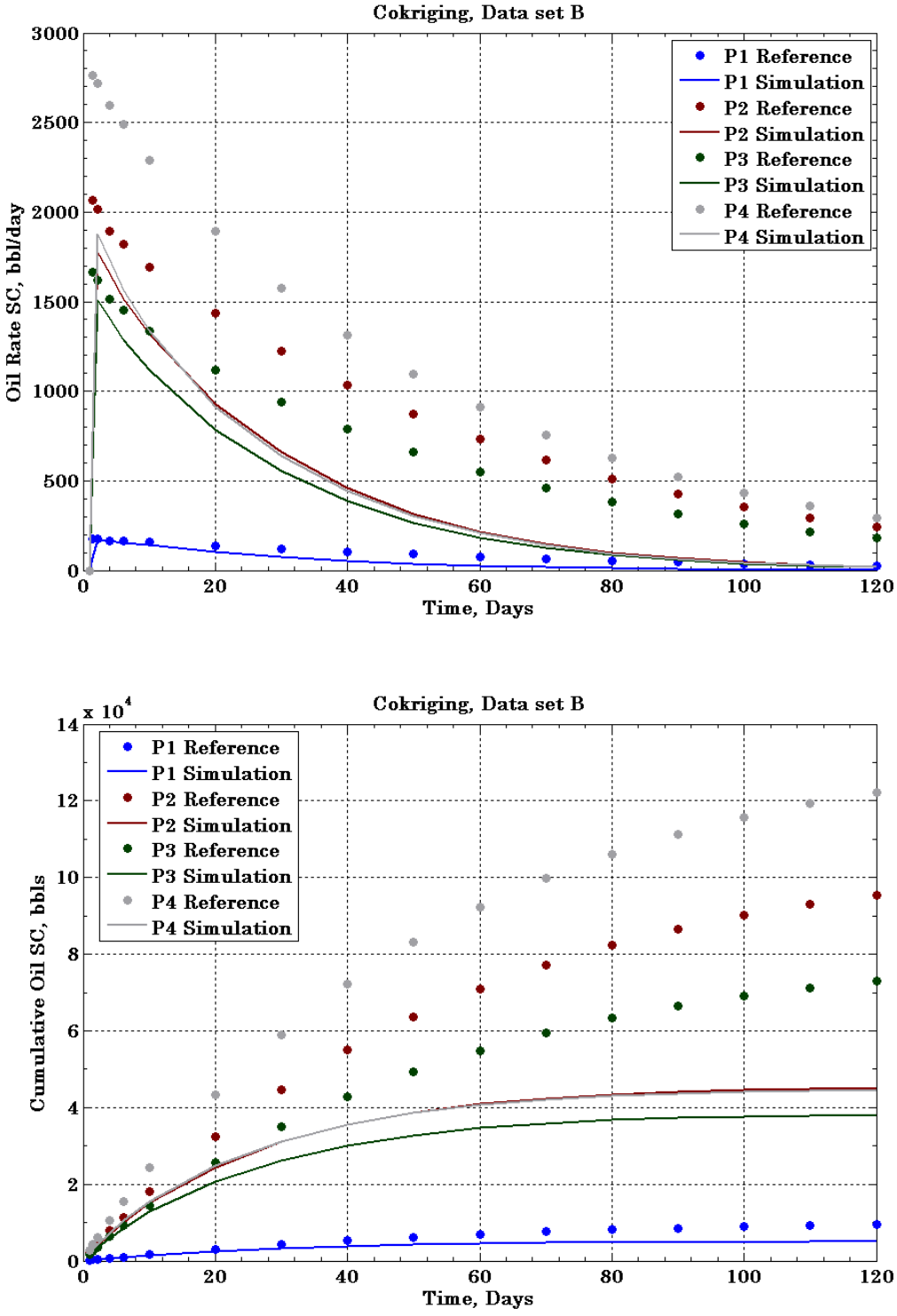

Figure 3.57. Comparison of dynamic data for co-kriging method using data set B

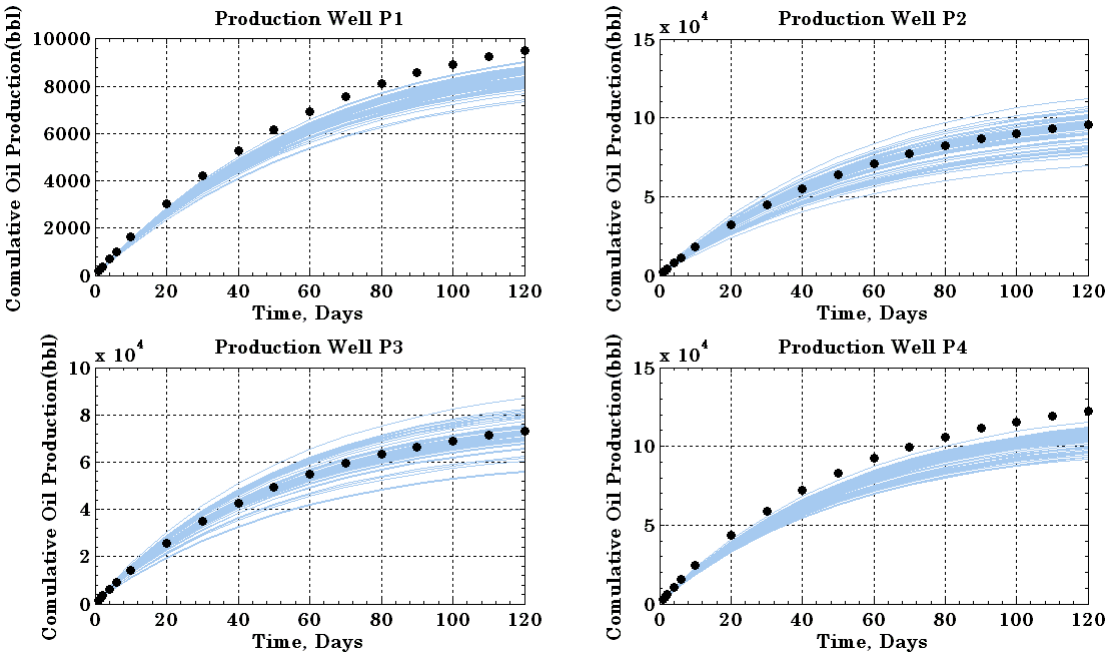

Figure 3.58. Cumulative oil production of SGS realizations generated by data set A

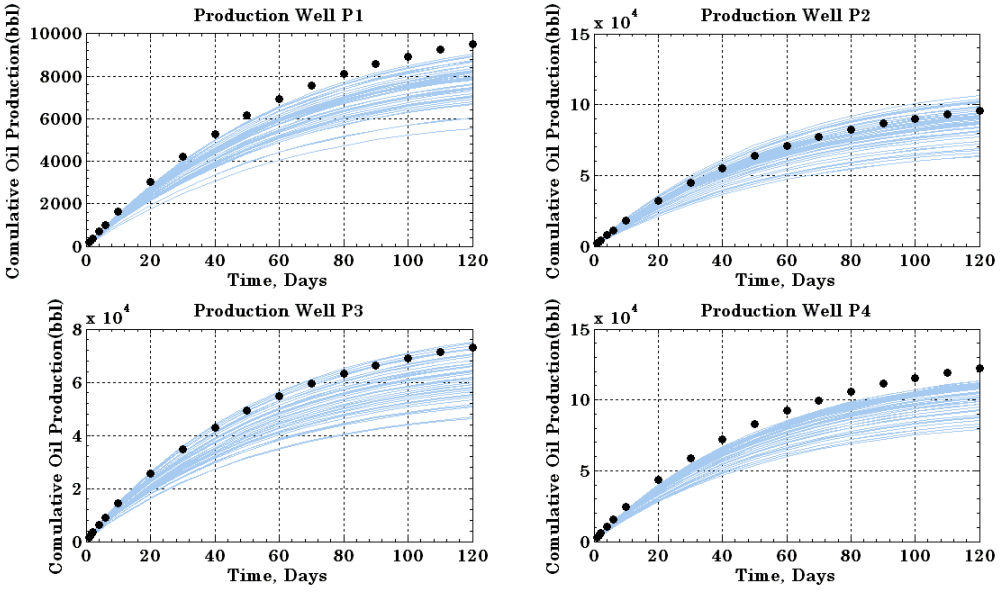

Figure 3.59. Cumulative oil production of SGS realizations generated by data set A

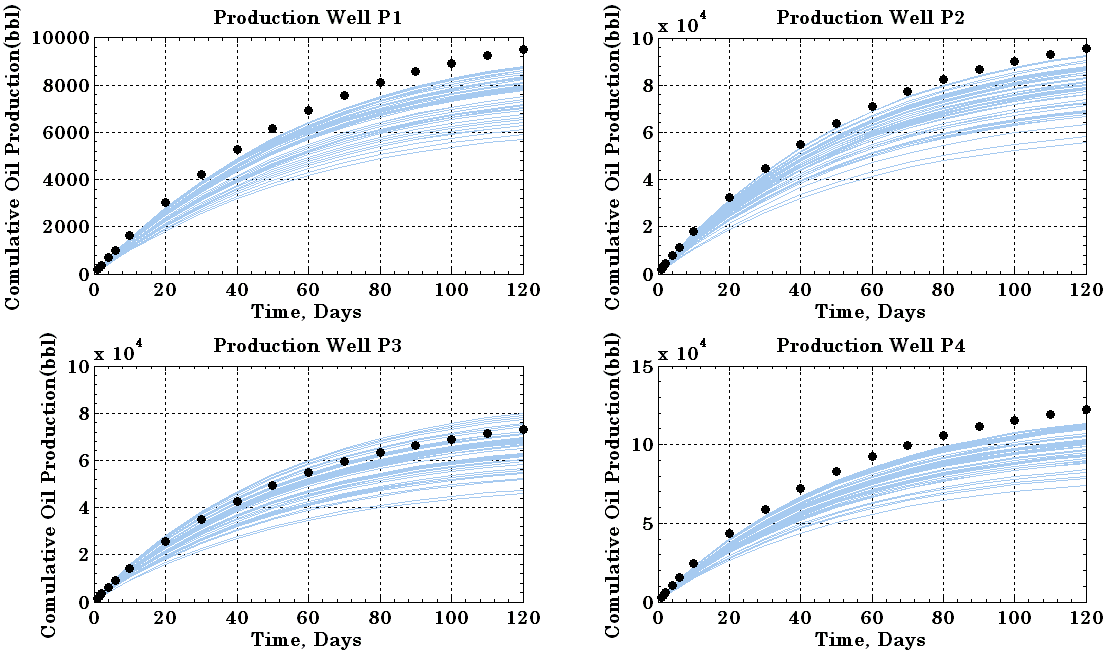

Figure 3.60. Cumulative oil production of SIS realizations generated by data set A

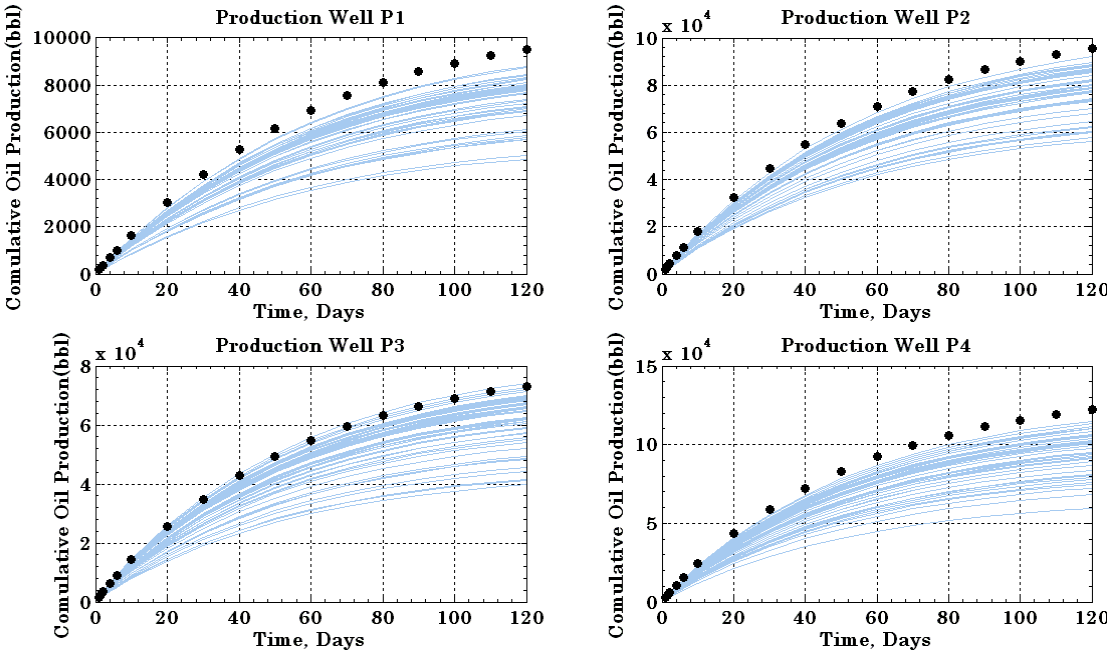

Figure 3.61. Cumulative oil production of SIS realizations generated by data set B

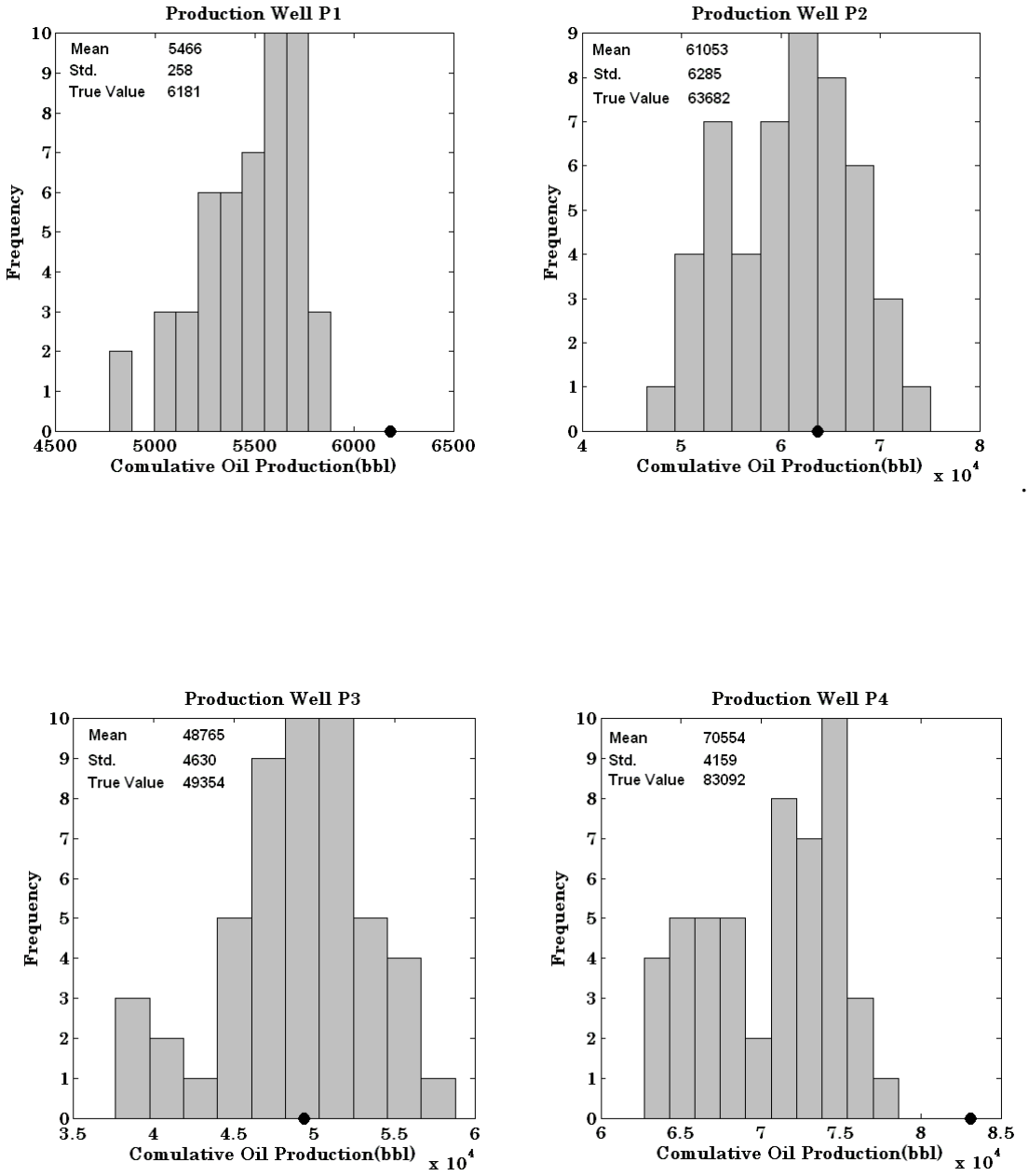

Figure 3.62. Histogram of **c**umulative oil production after fifty days for SGS realizations generated by data set A

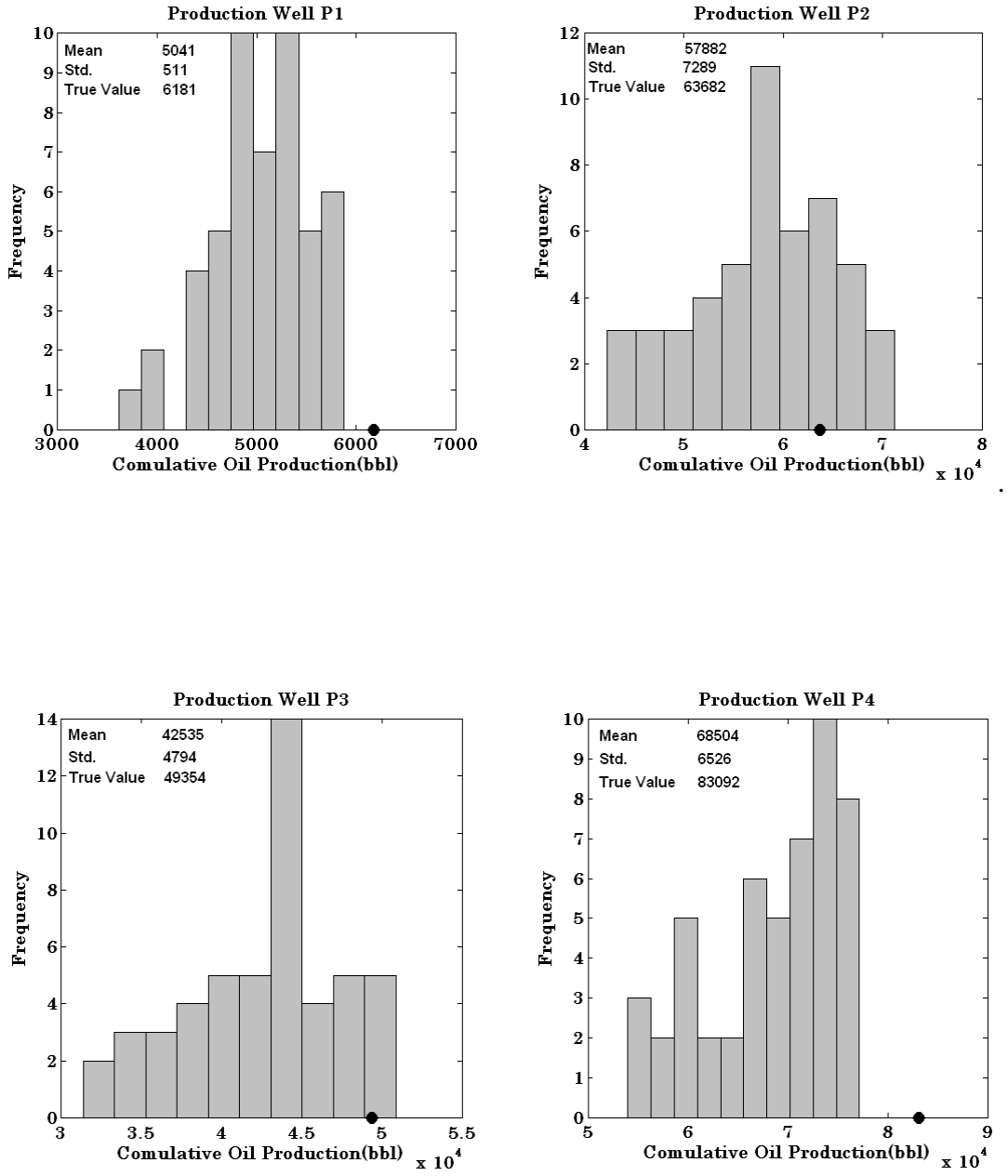

Figure 3.63. Histogram of **c**umulative oil production after fifty days for SGS realizations generated by data set B

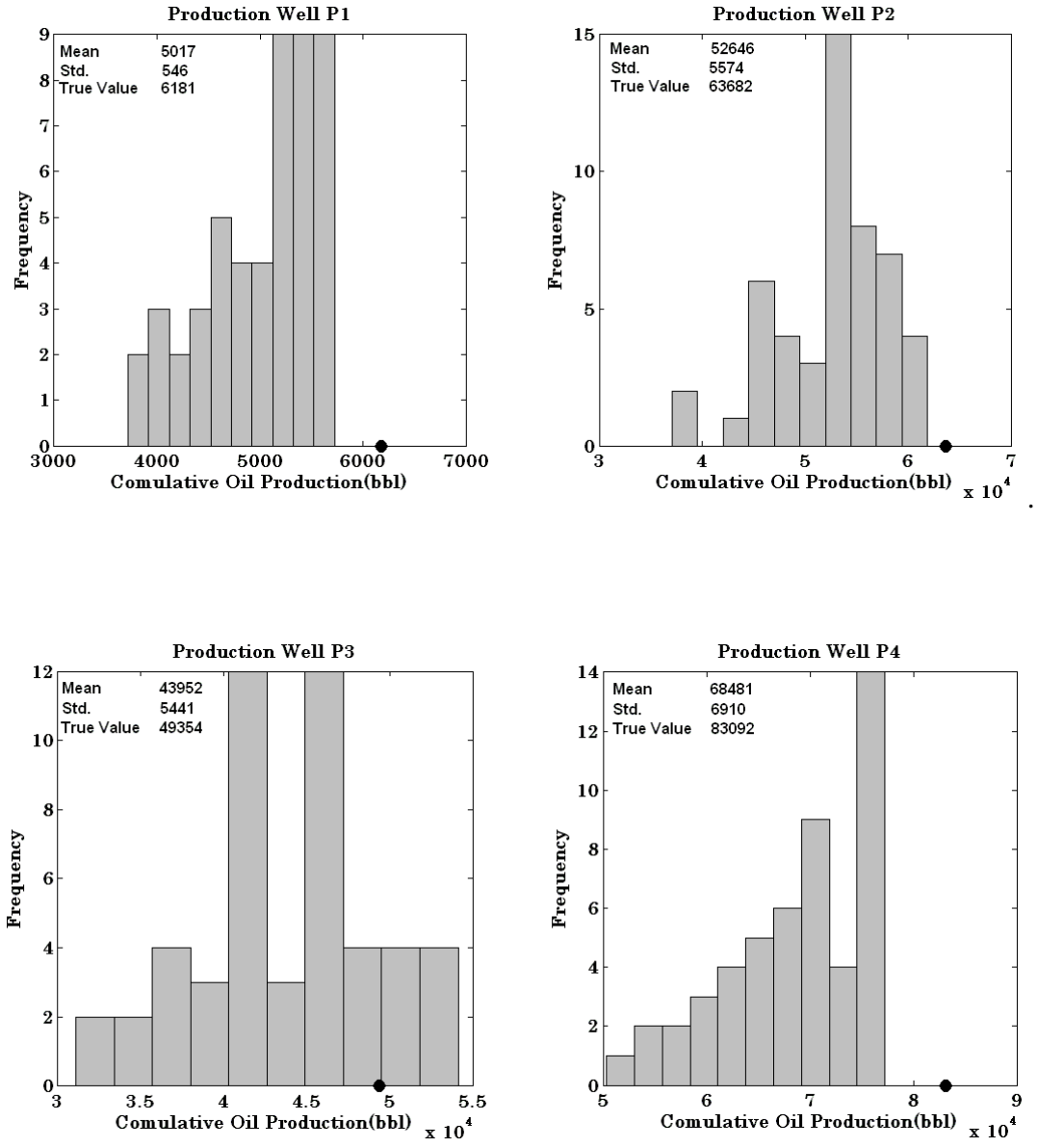

Figure 3.64. Histogram of **c**umulative oil production after fifty days for SIS realizations generated by data set A.

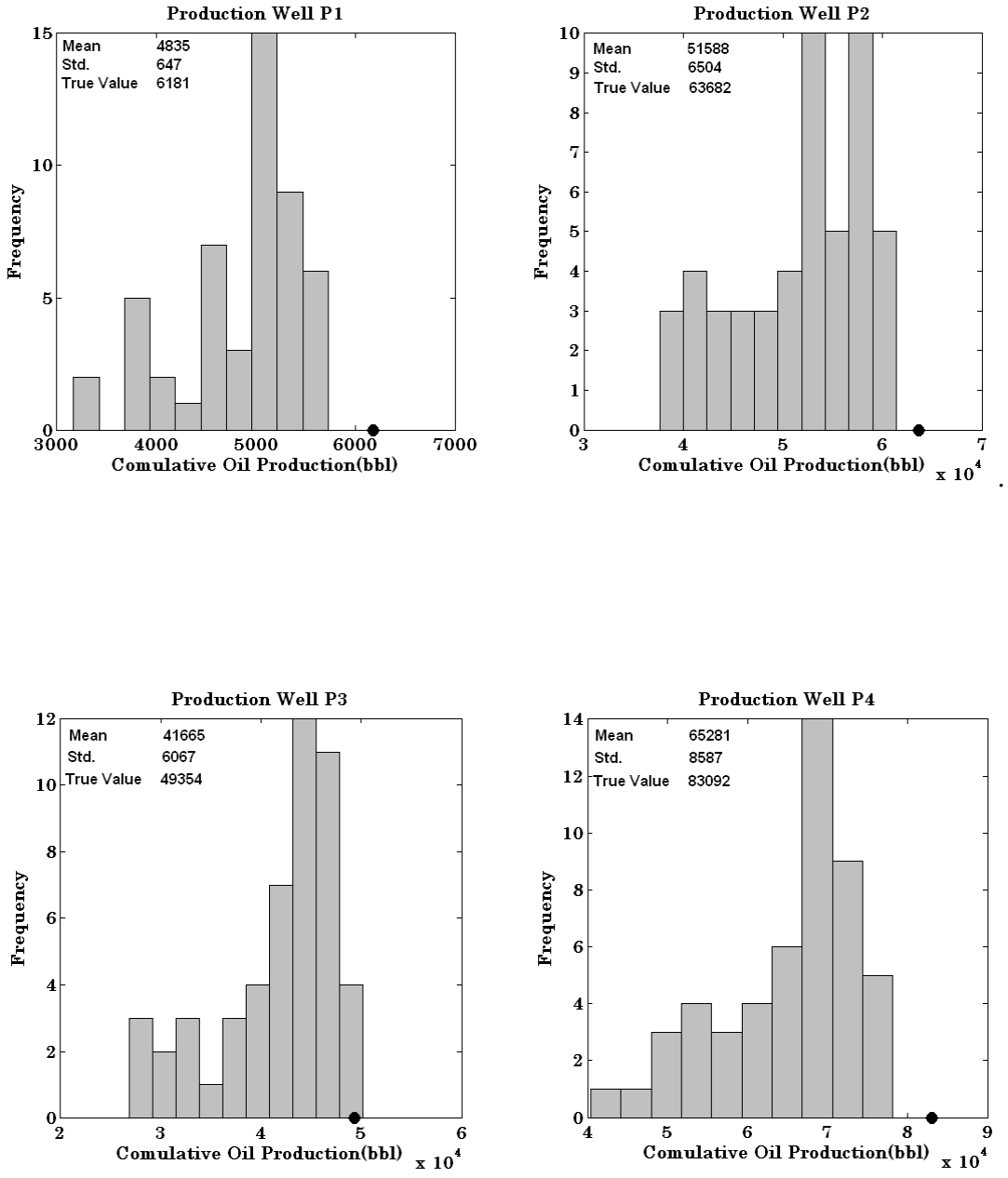

Figure 3.65. Histogram of **c**umulative oil production after fifty days for SIS realizations generated by data set B.

The overall measure of the goodness of a match is defined by *RMS* index defied by following equation:

$$RMS = \sqrt{\frac{2f}{m}} \tag{3.5}$$

where m is the total number of observations over which the index is formed, and f is the objective function. This *RMS* index provides an average value of the deviation between simulated and observed data.

The *RMS* index of the simulation results coming from six different geostatistical techniques for two data sets A and B were calculated. The oil production rates shown in Figures 3.46 through 3.57 were used in the RMS index calculation. The RMS index of each well in the five-spot pattern (described in Section 3.4) was calculated. The total RMS of the five-spot pattern was also calculated. Table 3.2 summarizes the results of these calculations. The results of this analysis reveal that the total RMS index is not sensitive to the data sets for the geostatistical methods applied in this research. In other words, the total RMS index does not significantly change with the number of samples in the data sets. As a result, the simulated dynamic data obtained from the different geostatistical realizations in this study is not a function of the quantity of sample data. Furthermore, the analysis shows that the total RMS index, except for indicator kriging (IK), does not significantly change with all geostatistical techniques. This can be explained by heterogeneity of the reference reservoir and the nature of the geostatistical methods used in this study. All geostatistical techniques used in this study rely on a semivariogram. Semivariograms are based on two-point correlation within the data set. However, the level of heterogeneity of the reference reservoir in this study demands a

technique that uses multiple-point statistics that correlate more than two points at the same time. It should be noted that the range of semivariograms in this study is almost the same for all the geostatistical methods used in this study. Beyond the range of semivariogram the results of geostatistical methods would suffer from significant uncertainty.

Table 3.2 RMS index for each well and the five-spot pattern.

Method	Data Set	Well P1	Well P2	Well P3	Well P4	Total
Ordinary Kriging	**A**	5.6	53.3	42.7	68.1	48.3
	B	5.4	49.1	37.7	69.7	46.7
Indicator Kriging	**A**	18.6	89	44	95.6	69.5
	B	18.1	100.5	44.3	87.1	70.7
Gaussian Simulation(SGS)	**A**	6.1	58.1	47.6	75.7	53.4
	B	4.9	55.7	39.7	80.0	52.7
Indicator Simulation(SIS)	**A**	5.9	55.2	42.6	71.0	49.8
	B	6.0	56.3	42.0	71.9	50.3
Crossplot *Log(k) vs. Φ*	**A**	7.8	52.1	43.7	70.4	49.1
	B	8.5	55.7	66.6	67.9	55.3
Co-kriging	**A**	4.6	51.4	38.6	79.7	51.2
	B	4.3	52.1	37.7	87.0	54.1

Chapter 4
Conclusions

1. The permeability distribution estimated by conventional geostatistical techniques (Ordinary and Indicator Kriging) using more samples provide wider range of permeability at unsampled locations. However, both data sets (A & B) result in a smooth permeability map, which is the nature of these types of method.

2. Monte Carlo techniques such as SGS and SIS reproduce the basic univariate statistics of the reference reservoir. The result of this study shows the permeability realizations generated with SGS using more samples are more precise and accurate to capture the semivariogram of the reference reservoir.

3. The SIS permeability realizations generated with two data sets did not reproduce the semivariogram of the synthetic reference reservoir in this study.

4. The univariate statistics of the SGS permeability realizations generated with data set A (10-Acre) are closer to that of the reference reservoir in comparison to the other geostatistical techniques used in this research.

5. The effect of second variable (porosity) on the estimation of permeability distribution was investigated using two techniques, exponential model and co-kriging. The permeability realizations estimated by these techniques are very smooth compared to the permeability of the reference reservoir. However, the

results show that co-kriging techniques improve the ordinary kriging estimation by lowering the error variance at most of the unsampled locations.

6. The results of this analysis reveal that the total RMS index is not sensitive to the data sets for the geostatistical methods applied in this research. In other words, the total RMS index does not significantly change with the number of samples in the data sets. As a result, the simulated dynamic data obtained from different geostatistical realizations in this study is not a function of the quantity of samples.

7. The analysis shows that the total RMS index, except indicator kriging (IK), does not significantly change with all geostatistical techniques. This could be explained by the fact that the range of semivariograms in this study is almost the same for all the geostatistical methods used in this study. Beyond the range of semivariogram the results of geostatistical methods would suffer from significant uncertainty.

Part II

Chapter 5

Introduction

The Hall-Gurney Lansing –Kansas City reservoir has limited geologic data, fluid property information, and field pressure information. Fluid production history was restricted to oil sales data commingled from various formations on a lease wide basis. Individual well oil and water production rates were available only in 1980 near the end of waterflood. This lack of data in fact was motivation for the objective of this study: characterize a reservoir using limited available geologic and production data.

The main tool of the study was geostatistics. Geostatistics provides a framework for integrating diverse types of data in order to generate multiple realizations of the reservoir. The data obtained from the field can be classified as static or dynamic. The static data do not vary over time generally and are related to the intrinsic characteristics of the rock through simple linear relationships, such as well logs, core measurements and seismic amplitude. The dynamic data, on the other hand, do vary with time. Dynamic data are related to the intrinsic characteristics of the rock generally through a complex, non-linear transfer function. These include field measurements that are made regularly throughout the life of the reservoir. Examples of this type are well-bore flowing pressures, fluid production rates, pressure transients, fractional flow data and time-lapse seismic data. An essential difference among the various forms of dynamic data is that

these data are at vastly different scales and it is wrong to ignore the scale difference when constructing a geostatistical model.

Dynamic data contains tremendous amount of information about the reservoir connectivity. For example, the wellbore flowing pressure is an indication of the connectivity in the near wellbore region at early times and of reservoir scale connectivity at later times. The rate of pressure decline provides valuable information regarding the extent of communication between the well and the reservoir. This information cannot be obtained from the static data alone.

Since static data such as core and well log data are only representative at a specific volume, integration of such data into reservoir models is fairly straightforward and several algorithms are available to condition reservoir models to such data. However, conditioning the reservoir models to dynamic data is a complex procedure mainly because of the non-linear relationship between the input model parameters (spatially varying petrophysical properties) and the output dynamic response of a reservoir (e.g. well pressure as a function of time). In addition, fluid flow through porous medium depends on other factors such as fluid properties, fluid distribution, boundary conditions and rock-fluid interactions which influence relationship between dynamic and static data.

Reservoir models that are only conditioned to static data generally exhibit simulated flow response that deviate from the true field response. These models then are manually adjusted to reproduce the historic data (history-matched) which is a tedious and time-consuming process. In the process of history matching, the spatial covariance model

that reflects the geological structure may be lost. As a result, although the adjusted reservoir models may match the historical production records, they may yield erroneous future prediction of reservoir performance.

The ability to forecast future production scenarios accurately is the ultimate objective of any reservoir simulation. Historical dynamic data are integrated into the reservoir model construction step such that the final model is conditioned to all the available static and dynamic data. Accurate and efficient reservoir modeling thus requires an understanding of the complex relationship between reservoir geology and the flow of fluids through the reservoir. This part of the dissertation focuses on complex relationship between reservoir geology and the flow of fluids through the reservoir. The main focus of this part of dissertation is to investigate the integration of dynamic data such as well test data into reservoir models.

Chapter 6 reviews the relevant literature and discusses the advantages and drawbacks of the current methods. Chapter 7 introduces the case study which is a CO_2 Pilot area in Lansing Kansas City formation. Chapter 7, also, presents details of proposed methodology to integrate the dynamic well test data into reservoir models using different crossplots of permeability-porosity. Chapter 8 demonstrates the results of applications of the proposed technique on the CO_2 case study. Finally, the last chapter summarizes the conclusions of the investigation.

Chapter 6

Literature Review and Background

The objective of this chapter was to develop a methodology to improve the reservoir description using well test data. The topic of reservoir characterization conditioning to dynamic data was extensively reviewed in the literature. Chapter 6 summarizes a literature review of the conditioning reservoir models to dynamic data

The subject of conditioning reservoir models to reservoir flow response has been actively investigated by numerous researchers [15,17,38,49]. Most of the algorithms for conditioning the dynamic data were developed by hydrogeologists to address groundwater flow problems [53,55]. The flow of groundwater through an aquifer is physically similar to the flow of petroleum fluids through a reservoir. Statistical characterization of aquifer heterogeneity is crucial for predicting the aquifer performance when subjected to different external stresses such as pumping of water and transport of contaminants. In groundwater flow models, transmissivity (which is directly related to permeability) is measured at a few locations in a groundwater aquifer [55]. In addition, piezometric head measurements are available at numerous boreholes located throughout the aquifer. The objective for hydrogeologists is to model the variations in the transmissivity field given the hard measurements at a few locations and the more prevalent head data.

An important difference between a groundwater aquifer and petroleum reservoir modeling is the relative availability of flow response data for groundwater aquifers. Well test data, in the case of petroleum reservoirs, is available only at a few producers that are drilled to take advantage of the oil reserves profitably. In comparison, piezometric data are more abundant because the cost of drilling boreholes is much less than that of oil reservoirs. This renders many of the algorithms for dynamic data integration proposed in ground water literature to be not useful for petroleum reservoir modeling. Nevertheless, this section attempts to introduce all the methodologies suggested to solve the problem irrespective of the field of application.

The problem of determining permeability fields from dynamic data collected at wells is a classical inverse problem and is typically ill-posed. In the mathematical sense, a well-posed problem refers to one that has a unique solution which depends continuously on the data. Mathematically, history matching has been posed in an optimization context. This means the minimization of a complex least squares objective function in a parameter space populated by multiple local minima. The objective of the optimization procedure is to update the prior permeability model ℓ generated by any geostatistics method such that application of a flow simulator on the final optimized model yields a response $d^{\ell}(\mathbf{u},t)$ which is close to the target response $d(\mathbf{u},t)$. The target response model is defined the true dynamic reservoir response (field data) at location **u** and time *t*. Several techniques utilizing this principle are reviewed.

The optimization algorithm for iteratively updating a prior permeability model using the flow response data typically utilizes a perturbation scheme on the permeability field. This perturbation process is guided by the computation of sensitivity coefficients of the model parameters on the flow response. The sensitivity coefficients are the gradients of the flow response variable taken with respect to the model parameters. If f is defined as a reservoir flow simulation response such as flowing wellbore pressure and well water-cut and the parameter being modeled is permeability $k(\mathbf{u})$; then for every location in the reservoir the sensitivity coefficient is defined as

$$\frac{\partial f}{\partial k(\mathbf{u})} \quad \forall \mathbf{u} \in \textit{Reservoir} \tag{6.1}$$

The use of sensitivity coefficients was first proposed by Jacquard et al. [44]. This was one of the first attempts to automate the process of history matching within a deterministic framework. They developed a methodology to condition a permeability and porosity model to pressure data measured at wells in a two-dimensional reservoir. In their study, they considered single-phase flow in a reservoir, which was partitioned into different permeability zones. The objective function was defined as a squared mismatch between well flowing pressures. This objective function measures the proximity of the generated model to the target model. The basis of the method was validated using the simplistic language of an electric analyzer. The purpose was to minimize the potential measurements at points in an electrical circuit with adjustment made to the contained resistance. The computed gradients are the change in potential at individual nodes with respect to a perturbation at individual resistances. The process of resistance modification is continued iteratively until a convergence criterion was met that is when the mean square deviation between the model and the actual system becomes negligible. They

applied the same principles to history match the reservoir by adjusting the average permeability within the multiple reservoir zones (defined by the partitions). The obtained results were satisfying mainly due to reduced dimensionality of the problem and simplicity of the case studied. The work by Jacquard et al. [44] introduced the concept of Automatic History Matching.

With advancements in computational techniques, the flow simulations became more and more complex in order to realistically represent flow processes in the reservoir. However, the increased complexities of the reservoir simulations also caused the history matching of reservoir models became more and more difficult. Several algorithms were introduced to automate the history matching process by intelligently formulating and solving a mathematical minimizations problem. These algorithms are described in the following sections.

Reservoir history matching problems are generally characterized by a very large number of unknown parameters. Consequently the efficiency of the numerical minimization algorithm is a key concern. Most of the early history matching algorithms were not suitable for applications involving large numbers of unknown parameters. The evaluation of the sensitivity coefficients was too expensive due to the large dimensionality of the problem. Hence different multivariate optimization techniques were introduced to reduce the computational time required for the operation. The following is a discussion of these approaches.

6.1. Optimization-Based Methods

In an automatic history matching, unknown parameters are determined by minimizing a performance index *J*:

$$\min J(x) = \left\| f_{target}(x,t) - f^{*}(x,t) \right\|^{2} \tag{6.2}$$

where x is the vector of parameters to be estimated, $f_{target}(x,t)$ is the target response function and $f^{*}(x,t)$ is the response function corresponding to the current realization model. A least squares performance index such as the function given above is usually applied in an optimization procedure. Iterative numerical methods are used to solve the above minimization problem. This is done by sequentially updating the reservoir parameters estimates by the following equation:

$$\mathbf{x}_{k+1} = \mathbf{x}_{k} + \alpha_{k} p_{k} \tag{6.3}$$

The sensitivity coefficient defined in Eq.(6.1) was used to find the search direction p_k and the step length α_k, and continually perturb the vector **x** such that the performance index is minimized. This mathematical formulation leads us to the gradient based optimization methods.

In a gradient method the sensitivity coefficients were computed with respect to the model parameters. There are several gradient-based optimization methods discussed in literature. All of these optimization-based methods are reviewed in the following paragraphs.

Gill et al. [45] used Taylor Series expansion for the linear approximation of the performance index J in Eq.(6.2) as follows:

$$J(x_k + p_k) = J(x_k) + \frac{\partial J^T}{\partial x_k} p_k \tag{6.4}$$

Where J and T are the performance index and transpose of a matrix respectively. The necessary condition in Eq.(6.4) to approach toward the minimum is that the directional derivative must be negative. That is:

$$\frac{\partial J^T}{\partial x_k} p_k < 0 \tag{6.5}$$

Based on the linear approximation, the search direction that minimizes $\frac{\partial J^T}{\partial x_k} p_k$ is the negative gradient,

$$p_k = -\frac{\partial J}{\partial x_k} \tag{6.6}$$

which is called the steepest descent direction. The steepest direction method usually works well when the gradient is large, or when the estimation point is far away from the minimum. However it progresses very slowly in the vicinity of the minimum. In fact, it has been shown that the rate of convergence for the steepest descent method is linear at best. A better rate of convergence to the minimum can be obtained by choosing the search direction based on the second order approximation to the performance index,

$$J(x_k + p_k) = J(x_k) + \frac{\partial J^T}{\partial x_k} p_k + \frac{1}{2} p_k{}^T \frac{\partial^2 J^T}{\partial x_k{}^2} p_k \tag{6.7}$$

where $\frac{\partial^2 J^T}{\partial x_k{}^2}$ is the Hessian matrix of the performance index.

$$p_k = -\frac{\partial^2 J^{-1}}{\partial x_k{}^2} \frac{\partial J}{\partial x_k} \tag{6.8}$$

which yield to solve Eq. (6.8) by the Newton's method. The rate of convergence for Newton's method is quadratic. This means the convergence mimics the steepest gradient in regions far from the optimum but close to the minimum the convergence is more quadratic in nature.

Anterion et al. [47] introduced one of the earliest methods in petroleum engineering field. This method was earlier implemented in groundwater hydrology applications [48]. In the model, the sensitivity of pressure and fluid saturations to model parameters were computed at the end of each simulator time step by solving a set of linear system of equations. The linear equations were obtained by differentiating the matrix form of the flow equations with respect to model parameters such as gridblock value of porosity and permeability. Once these sensitivity coefficients were calculated, the sensitivity of wellbore pressure and water-cut to permeability were derived. Anterion et al. [47] concluded that the rate of convergence can be improved by using the curvature information provided by the Hessian matrix. However, computation of the Hessian matrix is very expensive for reservoir history matching problems.

Killough et al. [46] proposed a new method to speed up the iterative procedure of the gradient simulator. They concluded that the effort required for sensitivity with respect to a single parameter is still of the order of 10% of a forward simulation. Landa et al. [49] attempted to reduce the runtime simulation of gradient method using some form of zonation according to Jacquard et al. [44]. They increased the computational efficiency of the gradient simulator method by computing the performance index only at the wells. Wu

et al. [50] suggested discrete adjoint methods for calculating the sensitivity coefficient. With their procedure they were able to directly generate the sensitivity of well bore pressures and water-oil ratios to the model parameters without having to calculate the same for all grid blocks in the model. This method requires one basic reservoir simulation run to calculate the grid block pressures and saturations and the solution of linear adjoint systems backward in time with multiple right-hand side vectors.

The advantage of the gradient simulator method is that sensitivity coefficients are computed with the same coefficient matrix used to solve for pressure and saturations in the flow simulator. Also the coefficient matrix does not depend on the model parameters. This means that only the right hand side of the matrix equation depends on model parameters. Thus, the problem reduces to solving a matrix problem with multiple right-hand side vectors, i.e. one right side vector for each model parameter. This procedure is specially difficult and time-consuming when realizations of permeability and porosity are constructed at several thousands gridblocks.

In general, the major drawback of all gradient based optimization methods is that they do not take into account for a spatial covariance model displayed by permeability values of a reservoir. It is crucial that the final reservoir model for any history matching process is not only conditioned to the available production data, but at the same time honors the spatial semivariogram model $\gamma(\mathbf{h})$ and the hard data values at their respective locations.

6.2. Pilot Point Method

de Marsily et al. [53] proposed the Pilot Point methodology to reduce the computational cost associated with the calculation of the sensitivity coefficients at every location in the reservoir. This method was first established in groundwater literature [52-53] and later was applied to history match petroleum reservoirs by Bissell et al. [54] and Xue et al. [51]. The methodology was developed in order to quantify the uncertainty in prediction of groundwater flow and contaminant transport through groundwater aquifers. The essential objective of the method is to generate a realization of the reservoir permeability field that honors dynamic data, a prior structural model $\gamma(\mathbf{h})$ and the conditioning data at known locations within the reservoir.

The first step is to generate a conditional realization of the permeability distribution $(k(\mathbf{u})|, \forall \mathbf{u} \in \text{Reservoir})$ using a specified variogram model $\gamma(\mathbf{h})$. Then, a group of points are selected that are called pilot points. There are arbitrary gridblock at which the property value is perturbed within prescribed geostatistical limits to minimize the deviation from historic production data. The range of variations permitted at pilot points is determined by the uncertainty associated with the property value in a given region. The initial value for the property at the pilot points given by the prior geostatistical realization conditioned to the variogram and fixed-point values (hard data). The next step is to run the flow simulator with initial reservoir model (base model) to simulate the production data. In this step, sensitivity coefficients are calculated for all of the output variables such as pressures and water-cuts only with respect to the property values at the pilot point locations. The reduced number of parameters (pilot point

locations) at which the sensitivity coefficients are calculated yields a considerable saving of CPU effort. The subsequent step is to calculate the objective function (square deviation from historic data) and on that basis, perturb the property values at pilot points using an optimization algorithm. The last step is to propagate the perturbation at the pilot point gridblocks to all other gridblocks in the reservoir model using a spatial interpolation scheme such as kriging.

Xue et al. [51] provided a discussion of the pilot point methodology when implemented for a field permeability inversion. Their method was evaluated on a 25x25 test case by using 1) full field perturbation inversion; 2) pilot point inversion including a) with 15% of the gridblocks and b) with 7.5% of the gridblocks. The comparison of the computational efficiency for the 3 schemes shows that the overall performance for the second case (15% grids - pilot points) is about 4.5 times faster in comparison to the full perturbation scheme, the first case. This result demonstrates the advantage of the pilot point methodology for field scale inversions consisting of large number of gridblocks. Xue et al. [51] also showed that computational time for the third case (7.5% gridblocks - pilot points) was higher than that for the second case. This indicates that using fewer points does not necessarily guarantee better computational efficiency because sometimes additional number of iterations is required to reach the acceptable misfit criterion. In addition, they investigated the convergence properties of the objective function. The research of Xue et al. [51] concluded that the pilot point scheme can be viewed as a subspace optimization procedure. When it is coupled with Kriging updating scheme, the pilot point method tends to results in perturbations that are too high compared to full field

perturbation schemes. The effect of this over perturbation is visualized as oscillations in objective function as the iterations proceed.

The pilot point methodology is highly affected by the number and location of pilot points. The selection of these parameters remains inherently empirical. It is suggested that the number and locations of these pilot points should be selected based on the complexity of the reservoir under study [49]. It is also recommended that the correlation length and the sill (variance) of the reservoir could be used as a guide for selecting the optimal number of pilot points. Also, they suggested that the sensitivity coefficient values could be used as a guideline for locating the pilot points within the reservoir under study. However, in general, the lack of specific guidelines for determining the number and location of pilot points is one of the major drawbacks of this method.

6.3. Sequential Self-Calibration Method

Gomez-Hernandez et al. [55] first developed the Sequential Self-Calibration (SSC) method for aquifer modeling. This method is similar to the Pilot Point methodology. The main difference is that in SSC method, the pilot (master) points are located randomly. Hence, the user only has to provide the number of master points to be perturbed. The perturbation at the entire master points is initiated jointly using optimization technique and the perturbations are then spread to all other reservoir nodes by kriging estimation. The optimal perturbation at master points is determined by the gradient based optimization method obtained from simulation.

The method was first adapted for petroleum engineering application by Wen et al. [57]. They used the SSC method to integrate single-phase well transient pressure and rate data in a two-stage approach. In their procedure, first, spatial constraints on large-scale permeability trends were set up. Then, multiple realizations of the reservoir at a coarse-scale were generated. The small-scale geostatistical models were generated subject to spatial constraints imposed by the simulation results and the available static data. Also, the coarse-scaled reservoir models were downscaled using other techniques such as Simulated Annealing (SA) and sequential Gaussian simulation incorporating Bayesian updating [56].

Wen et al. [58] showed that the SSC procedure could be also applied for lithofacies simulation where the permeability distribution controlled by multiple lithofacies or channel objects. Tarn et al. [56] proposed a hybrid method using streamlines to improve the computational time of the SSC method. In this method, the coarse scale inversion was created by a semi-analytic method using streamlines. The coarse model is then downscaled by geostatistical procedure. They demonstrated that the use of a semi-analytical streamline model instead of numerically derived model for calculating the sensitivity coefficient, leads to a substantial saving in CPU time. The inverted model is then downscaled to the scale of the hard data using Bayesian updating or block kriging.

6.4. Markov Chain Monte Carlo Method

Markov Chain Monte Carlo (MCMC) methods have been applied for construction of models in different field of studies such as financial, business and social science involving uncertain future events. This method was investigated in earth science by a number of people [59] [60] [61].

Basically, MCMC is an iterative method in which a Markov chain forward in time is generated. The Markov chain eventually converges to the desired stationary probability distribution. Each iterative step of this method consists of a proposal and an acceptance step. In the context of reservoir characterization, permeability realizations could be considered as a Markov chain if the probability of generating a particular realization only depends on the preceding realization in the sequence. If a particular stochastic realization of permeability is denoted by $k^i(\mathbf{u})$, where i represents the i^{th} step of the Markov chain, then each possible permeability realization has an associated probability π_i with $k^i(\mathbf{u})$. The objective is to proceed with every step in the chain towards a realization that matches the dynamic data more closely than the pervious realization. This progression of realizations towards a history match goal is accomplished by carefully specifying the transition probability from state i to state j, p_{ij}. Mathematically, the probability associated with state $j(\pi_j)$ is defined as the sum of the products of transition probability p_{ij} and the probability of being in state $i(\pi_i)$:

$$\pi_j = \sum \pi_i p_{ij} \tag{6.9}$$

There are some conditions for determining a permissible transition matrix. These conditions must be satisfied to make the Markov chain stationary [62]. The first condition is that the transition matrix should satisfy a reversibility condition:

$$\pi_i p_{ij} = \pi_j p_{ji} \tag{6.10}$$

The second condition is that the transition matrix is written as a product of two components:

$$p_{ij} = \alpha_{ij} q_{ij} \tag{6.11}$$

where q_{ij} is the probability of proposing a transition from sate i to state j and α_{ij} is the probability of accepting the transition. Hasting [63] proposed that the form of the acceptance probability should be given as:

$$\alpha_{ij} = \min\left\{1, \frac{\pi_i q_{ij}}{\pi_j q_{ji}}\right\} \tag{6.12}$$

Hence, if the proposed transitions are symmetric, then the decision of whether to accept a transition or not is based only on the ratio of the probability of being in the two states. If the proposed transition is rejected, the old state is repeated in the chain.

Srinivasan [66] implemented MCMC method in his study on reservoir characterization as follows:

- Define the state i of the model by an array of initial values:

$$k^i(\mathbf{u}) = (k(\mathbf{u}_1), k(\mathbf{u}_2), ..., k(\mathbf{u}_M))^T \tag{6.13}$$

T is the transpose of a matrix.

- Transition to a new state j is proposed, for which every element of the array is re-sampled from the normal distribution:

$$k^{j}(\mathbf{u}) = (k'(\mathbf{u}_1), k'(\mathbf{u}_2), ..., k'(\mathbf{u}_M))^T \tag{6.14}$$

- The probability of transitioning from state i to state j is computed by perturbation a grid cell at a time. At each step, a single gridblock $k(\mathbf{u})$ is selected randomly from *n* total gridblocks. The probability to pick the grid cell is $\frac{1}{n}$. Next, a new value $k'(\mathbf{u})$ is proposed for that gridblock by random drawing from a univariate normal distribution. This probability is known to be $f(k'(\mathbf{u}))$. Hence, the probability of proposal is the product of these two probabilities,

$$q_{ij} = \frac{1}{n} f(k'(\mathbf{u})) \tag{6.15}$$

- The acceptance probability is calculated using the Metropolis-Hasting criterion as:

$$\alpha_{ij} = \min\left\{1, \frac{f(k'(\mathbf{u})) \times q_{ij}}{f(k(\mathbf{u})) \times q_{ji}}\right\} \tag{6.16}$$

- The proposal probability is then tested against the acceptance criterion by drawing u~ U[0,1]. If $u < \alpha_{ij}$, the perturbation is accepted, otherwise, it is rejected and the old value $k(\mathbf{u})$ is retained at the gridblocks.

The expressions described above are applicable for generating realizations that are conditioned to the hard data at their locations and at the same time honor the spatial covariance model being used. For conditioning the reservoir model to production data,

only the acceptance probability term is rewritten to account for the conditional probability based on the production data. The expression for this acceptance probability ratio is written using Bayes' relationship. The expression involves the likelihood function that is the probability of observing the dynamic data given a particular permeability field. The evaluation of this likelihood term necessitates running a flow simulation after each perturbation made in the reservoir model. Srinivasan et al. [66] showed that it is possible to reduce these extra computations required for evaluating the likelihood functions using a multipoint proxy function. This multipoint proxy captures the underlying non-linear relationship between the input permeability field and the output response variables using neural network theory.

In summary, the introduction of the multipoint proxy function does significantly reduce the computational effort. However the Markov Chain Monte Carlo method itself requires large number of iterations to converge to a stationary distribution. This is mainly because of low acceptance ratios for transitions to a new state when the number of parameters in a model is large.

6.5. Gradual Deformation Method

The gradual deformation method was first introduced in reservoir modeling applications by Roggero et al. [65]. The method approaches the history matching problem from a different prospective in comparison to the other methods described in the previous sections. The basic principle of the gradual deformation method is to generate realizations that evolve smoothly at each step to honor specific constraints such as prior

structural model, seismic and production data. A sequence of realizations of the reservoir are generated and combined following a prescribed rule. Consider two random vectors Y_1 and Y_2 whose components are standard normal and mutually independent. A new random vector from these vectors can be constructed as follows:

$$Y = \alpha_1 Y_1 + \alpha_2 Y_2 \tag{6.17}$$

For Y to also be standard normal, the following condition has to be satisfied:

$$\alpha_1^{\,2} + \alpha_2^{\,2} = 1 \tag{6.18}$$

The parameters α_i*'s* are determined by performing a 1-D optimization for multiple flow simulations. The space of possible realizations is controlled by the initial realizations Y_1 and Y_2, where α varies between -1 and 1. New realizations evolve as the deformation parameter α is continuously changed. The gradual deformation process can be generalized as:

$$Y = \sum_{i=1}^{n} \alpha_i Y_i \tag{6.19}$$

where $\{\alpha_1, \alpha_2, ..., \alpha_n\}$ are real coefficients between -1 and 1. The multi-Gaussianity property of the model is preserved by applying the following constraint:

$$\sum_{i=1}^{n} \alpha_i^{\,2} = 1 \tag{6.20}$$

The additional parameters α_i assist in constraining the models to other types of data.

In dealing with large geostatistical models, which may be too expensive to run in a flow simulator directly, Mezghani et al. [64] suggested a hybrid method. In summary, the method involves upscaling the geostatistical fine model and then performing a history

match on the coarse scale model. The coarse scaled model is then downscaled using a traditional geostatistical approach such as block kriging. The major problem with the hybrid method is the assumption of a multi-Gaussian permeability field.

Assuming the multi-Gaussian random fields preserves the first and second order moments of the resultant reservoir models by placing constraints on the deformation parameters $\sum_{i=1}^{n} \alpha_i^2 = 1$.

6.6. Simulated Annealing

Simulated annealing (SA) was established based on the physical process of cooling molten metal. In cooling a molten metal, the rate of cooling affects the quality of the frozen metal. Slower cooling yields a better quality, while faster cooling process results in a more defective quality. The reason for this difference could be explained by thermodynamics principles. According to thermodynamics, molten metal tends to achieve the most stable state corresponding to the lowest energy.

Shannon [67] was the first to observe the similarity between annealing and optimization problems. However, it took thirty five years before SA to be applied and developed in practical problems mainly due to computational limitations. Kirkpatrick et al. [70], Siarry et al. [68] proposed an annealing-based procedure with Metropolis algorithm [68] to escape from local minima. The major steps of the SA algorithm are briefly described below.

First, a starting guess model $\mathbf{m} = \{m_1, m_1, ..., m_N\}$ is generated. The model parameters m_i's can be randomly generated from a known cumulative density function. Then, an initial energy or objective function is calculated as:

$$E = \sum_{i=1}^{M} \sum_{j=1}^{J} \omega_{i,j} \left[V_{actual}^{i}(j) - V_{\text{model}}^{i}(j) \right]^2 \tag{6.21}$$

where M and J are respectively the type and the number of constraints. $\omega_{i,j}$ is the weighting factor of the i^{th} constraint with respect the j^{th} constraint type, and $V_{actual}^{i}(j)$ and $V_{\text{model}}^{i}(j)$ are the actual and model values of the i^{th} constraint related to j^{th} constraint type. All variables in Eq.(6.21) are known a *priori* except for $V_{actual}^{i}(j)$ which is calculated using a mathematical function for each constraint type. For instance, if a production forecast is the constraint to be satisfied, a flow simulation provides the values for $V_{actual}^{i}(j)$. The objective function is analogous to the energy of the system. The objective function must be lowered during the annealing process until a minimum energy state is reached.

The next step is to randomly modify the initial model and recalculate Eq. (6.21) for the new model. The difference between the energies of the new and old models is then given by $\Delta E = E_{new} - E_{old}$. If $\Delta E < 0$ then the new model is accepted and the old one is disregarded. If $\Delta E > 0$ whether the new model is accepted depends on Metropolis condition. This condition sets up an acceptance probability based on the Gibbs-Boltzmann probability distribution function as:

$$P(\Delta E) = \exp\left[-\frac{\Delta E}{\theta}\right] \tag{6.22}$$

where θ is the annealing temperature for the current energy state. A random number R, drawn from a uniform distribution between 0 and 1, is compared with $P(\Delta E)$. If $P(\Delta E) < R$, the new model is rejected; otherwise, the new model is accepted, even though the energy of the system is increased. The acceptance of new model in the case of higher energy allows the algorithm to escape from local minima.

Next, the above procedure is repeated for a sequence of decreasing temperatures θ according a cooling schedule given by $\theta_{new} = \alpha\theta_{old}$ where α is a reduction factor ($\alpha < 1$). The system has to be allowed to reach thermal equilibrium after every temperature reduction. Therefore, a certain number of model acceptances (in the order of the number of model parameters) should be performed for each temperature. The abrupt changes of temperature cause discontinuities in the energy function because the acceptable probability is suddenly lowered. The algorithm converges if ΔE is below some given tolerance or the energy remains unchanged for a sufficiently large number of iterations. Additional examples of this procedure can be found elsewhere [34, 35].

Farmer [13] presented the first application of SA in reservoir characterization problems. In his study, synthetic fields were generated constrained to two-point histograms and correlations. Perez [72] used SA to obtain fields constrained to semivariograms. His study showed that the quality of the SA generated descriptions was similar or even superior to that of the other conditional simulation methods. However, SA

demands, in general, more computational work. Deutsch [38] added well test permeability data as one of the constraints. The objective function was given by:

$$E = \omega_1 \sum_{l=1}^{L} \left| \gamma_{actual}(\mathbf{h}_l) - \gamma_{\text{model}}(\mathbf{h}_l) \right| + \omega_2 \sum_{m=1}^{N} \left(k_{wt} - k_{\text{model}} \right)^2 \tag{6.23}$$

where ω_1 and ω_2 are the weights used to make the units consistent and to ensure that one constraint does not dominate the objective function. $\gamma_{actual}(\mathbf{h}_l)$ and $\gamma_{\text{model}}(\mathbf{h}_l)$ are respectively the actual and the model semivariograms, while k_{wt} and k_{model} are the field and model well test permeabilities derived from pressure transient analysis. k_{model} is calculated using power averaging technique [42]. The averaging power exponent and averaging volume must be pre-determined. Deutsch [38] suggests these values can be obtained from stochastic modeling and forward well test simulations. The major drawback of the Deutsch' annealing method is that it can only be applied for a single layer reservoir.

Ouenes [72] developed an SA algorithm to simultaneously estimate relative permeability and capillary pressure curves. The experimental data obtained from standard drainage and imbibition were automatically history matched. The objective Function in this case was:

$$\begin{aligned} E = & \sum_k \omega_k^R (R_k^c - R_k^e)^2 + \sum_k \omega_k^{\Delta P} (\Delta P_k^c - \Delta P_k^e)^2 + \\ & \sum_k \omega_k^S (S_{k,i}^c - S_{k,i}^e)^2 + \omega^T (BT^c - BT^e)^2 \end{aligned} \tag{6.24}$$

where the terms with superscript *c* are computed from numerically solving the one-dimensional diffusivity equation for multiphase flow. The terms with superscript *e* are the experimental values to be matched. *R* refers to the cumulative recovery for different

times, ΔP is the pressure drop, S is the saturation and BT is the breakthrough time. The application of this method is limited to laboratory experiments due to computational effort required to solve a reservoir-scale problem. Furthermore, it does not include the semivariogram as a constraint. Therefore it can not capture the spatial relation of random variable.

Hird et al. [73] developed a conditional simulation method based on SA that allows permeability fields constrained to connectivity functions to be generated. Such functions are to some extent correlated to production performance parameters and are intended to replace numerical simulation. The least resistive paths are determined by finding the minimum distance required to move from one surface (defined as a set of adjacent blocks) to another. A resistivity index from an injector well to a given gridblock *(i,k)*is defined as:

$$RI_e(i,k) = \min\left[\sum_{Injector}^{(i,k)} \frac{\Delta l^2}{\bar{k}_a k_{rw}(i)}\right] \tag{6.25}$$

where Δl and $\bar{k}_a$ are respectively the distance and the directional absolute permeability between the center of two adjacent grid blocks, and $k_{rw}(i)$ is the relative permeability to water for the i^{th} column. This algorithm could be used to rank reservoir descriptions from the best to the worst according to secondary recovery efficiency, ultimate primary recovery, or ultimate secondary recovery. However, it has not been tested against an actual reservoir. Since the algorithm is based on a binary indicator approach, it is more suitable for discrete variables (facies) with contrasting permeability, such as sand-shale sequences.

Chapter 7

Development of a Reservoir Model for the Hall Gurney Field, Lansing Kansas City Formation

Chapter 7 provides general information about the Lansing Kansas City formation, its initial reservoir model, and the proposed model for estimating the permeability distribution. This information comes from variety sources mainly technical reports available on Tertiary Oil Recovery Project (TORP) website [74].

The feasibility of injecting miscible carbon dioxide to recover oil was studied by the Tertiary Oil Recovery Project (TORP) in the 1970's. The study involved a set of experiments to determine the minimum miscibility pressure (MMP) of lease crude oil at reservoir temperature. These experiments indicated that the MMP was about 1200-1300 psia, a pressure range that had been maintained during the waterflooding of the Hall-Gurney field. Due to lack of carbon dioxide supply further study of CO2 flooding was discontinued. The possibility of using carbon dioxide to recover oil reinvestigated in the mid-1990's when a pipeline was installed to deliver carbon dioxide to the Postle Field in the Oklahoma panhandle, a distance of about 30 miles from the southwest Kansas border. The pipeline placed a significant source of carbon dioxide within a reasonable distance to the Southwest and Central Kansas oilfields.

At the same time, Shell CO2 Company became interested in developing a market for carbon dioxide which was available in excess of demand in West Texas. A

multidisciplinary project involving the Tertiary Oil Recovery Project and Kansas Geological Survey at the University of Kansas, Shell CO2 Company and external consultants was initiated in 1998 to evaluate the feasibility of developing a pilot test of carbon dioxide miscible flooding in Central Kansas. The Hall Gurney Field, shown in Figure 7.2 was selected for detailed study because it was the largest Lansing Kansas City reservoir in Kansas with a cumulative production over 75 million barrels, had good waterflood performance and results of a pilot project could be expanded field wide if the process was successful.

This chapter describes the development of a reservoir model for the Lansing Kansas City "C" zone in the Colliver and Carter Leases in the Hall Gurney Field. This zone was selected for the initial evaluation. The reservoir model was used as the input data for a reservoir simulator. Primary and secondary oil production were simulated using this model by history matching the 50 years oil production from the Colliver and Carter Leases. After the history match, the reservoir model was used to simulate the possible oil recovery from a pilot carbon dioxide miscible test. These studies led to the submission and funding of a 10 acre carbon dioxide pilot test on a portion of the Colliver Lease as part of the U.S. Department of Energy's Class II Revisited Field Demonstration Program(DOE-AC26-00BC15124).

At the beginning of this project the reservoir modeling team recognized that reservoir and production data were limited, partially because the properties had changed hands numerous times from when the field was discovered in the 1930's. Data and

records which were referred to in some documents and reports were never found although extensive inquiries were made of all previous operators and lease holders who could be found. Therefore, the task for the reservoir modeling team was to develop an acceptable reservoir model which matched primary and secondary production history with the knowledge that limited data and production records were available.

A brief overview of the construction of the initial reservoir model is presented in this chapter. When oil production from the pilot wells did not respond as predicted, the construction of the reservoir model was revisited to determine if geostatistics could be applied to improve the geologic model of the reservoir. The challenge that the reservoir modeling team faced was how to estimate the permeability and porosity distribution at all grid points in the project area using the available, but limited reservoir, production and injection data.

7.1. Lansing Kansas City Oil Production

Lansing Kansas City reservoirs are one of the major producing intervals in the State of Kansas. Kansas reservoirs have produced nearly 6 billion barrels of oil to date, with much of the production coming from reservoirs in proximity to the Central Kansas Uplift (CKU) [75]. Reservoirs in the LKC account for nearly %19 cumulative oil production for the state (Figure 7.1). It is estimated that greater than 70% of Lansing Kansas City(LKC) production is from oomoldic limestone reservoirs, including those of the Hall-Gurney Field in Russell County (Figure 7.2).

The Lansing Kansas City (LKC) formation consists of a series of alternating deposits of marine limestone and nonmarine shale. The limestone deposits were exposed to weathering and erosion with percolating rain water dissolving the ooids. Subsequently, recrystallization of dissolved ooids resulted in cementing of the original porosity. The limestones of the LKC are oolitic grainstones and serves as the main petroleum reservoir in Kansas. The porosity is a mold of the originally present ooids. This oomoldic pore is the dominant porosity in the LKC formation deposited during Pennsylvanian series [75]. There were 11 major marine-nonmarine cycles in the LKC interval in this field, each averaging about 30 feet thickness [75]. These distinctive cycles are identified by a set of letter designations from *A* through *L* (Figure 7.3). The interval *C* was studied in this research.

The Carter-Colliver lease shows a strong west to east trending with the pay exhibiting closure in the southern portion of the lease[74]. The thickness of the gross pay interval varies from 10 to 20 feet. The structures with higher locations exhibits thicker pay in general. The porosity in the *C* and *D* zones is consistently higher than in the other zones. Therefore, these zones are considered the best pay at the CO2 Pilot area due to both thickness and areal distribution of high porosity.

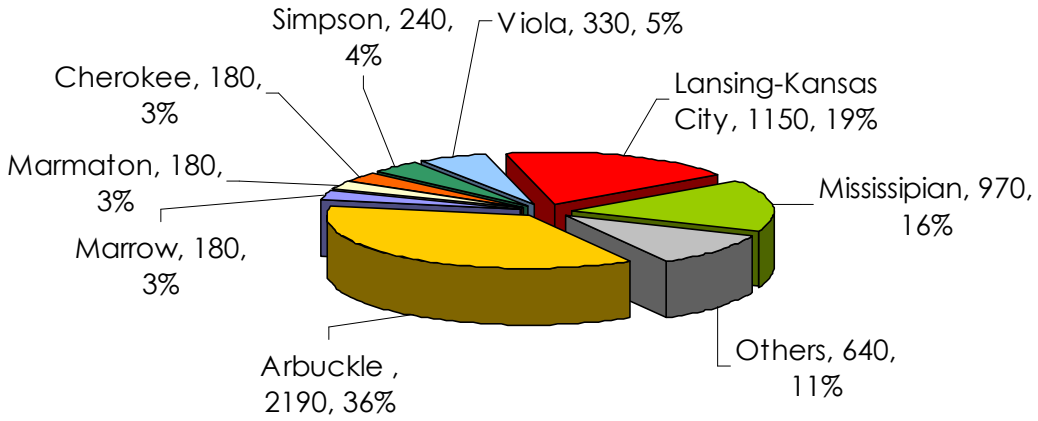

Figure 7.1. Lansing Kansas City reservoirs produced 1150 billion barrels of oil representing 19% of total Kansas oil production [74]

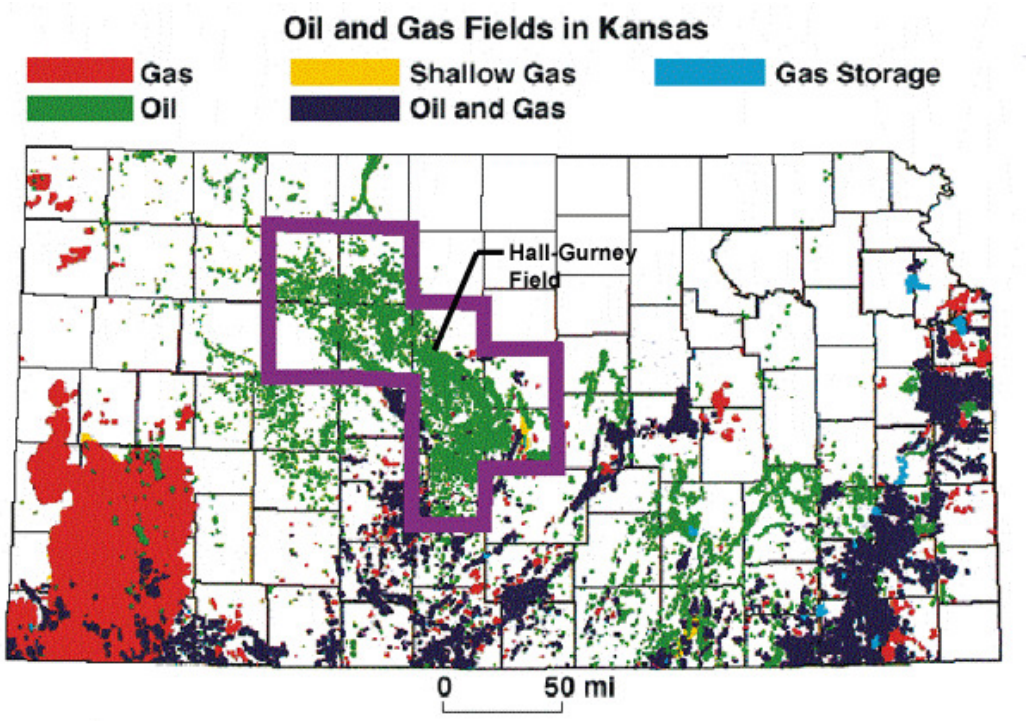

Figure 7.2. The Central Kansas Uplift in Lansing Kansas City [75]

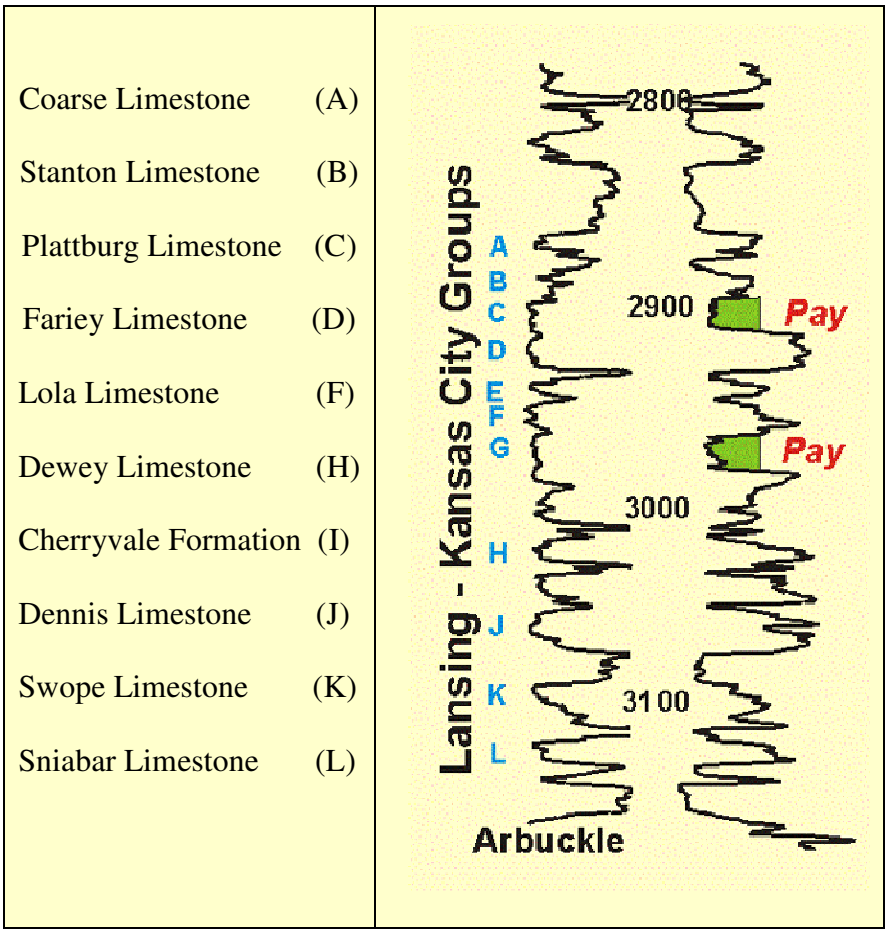

Figure 7.3. Stratigraphic Formation and latter nomenclature of the LKC Groups [75]

The Hall-Gurney Field was discovered in 1931. However, it did not have significant production until the late 1930's when over 300 wells were drilled. Peak production was attained in 1943 when nearly 6 million barrels of oil was produced [74]. Most early production as well as significant waterflood oil is from the Upper Pennsylvanian L-KC Groups. The first waterfloods were accidental "dump" floods caused by casing leaks or poor cement jobs [74]. Successful waterflood pilots in the late 1950's led to widespread L-KC waterfloods in the early 1960's most of which depleted the reservoirs by the early 1980's. Figure 7.4 displays the Hall-Gurney annual cumulative oil production.

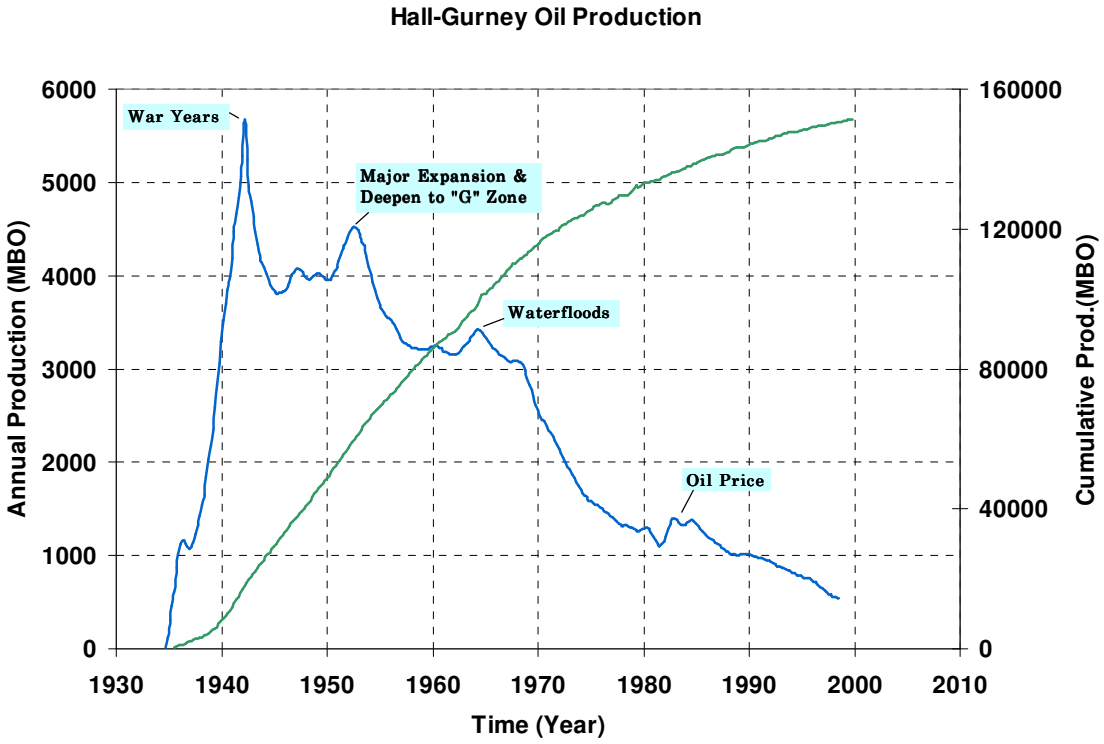

Figure 7.4. The Hall-Gurney annual cumulative oil production [74]

The Hall-Gurney produced first by solution gas and partial water drive. In many fields because of low dissolved gas content, primary recovery by solution gas drive is often modest with recovery efficiencies of less than 25%. Many of the fields on the L-KC, including the Hall-Gurney Field, were excellent waterflood candidates, however, a significant amount of residual oil remains. This residual oil in the L-KC is considered a potential target for CO_2 miscible flooding.

The initial pressure of the Colliver-Carter lease was about 1200 psia which depleted at the end of primary production down to 50-100 psia [74]. The lease was re-

pressurized by waterflood to improve oil recovery. There were two phases in waterflood. Initially, a single well (Colliver#10) was converted to a water injection well as a pilot flood. The pilot flood was successful and the waterflood program was initiated in the field scale. An agreement was reached by the owners of surrounding leases to cooperatively waterflood in order to prevent oil leak-off from the lease. The cooperative waterflood consisted of locating off-set water injectors to prevent oil from moving out of the leases [74]. The cooperative waterflood completed by 1987 with only a few wells injecting water beyond this date and oil production form the individual wells declined to single digits.

7.2. Initial Reservoir Model

This section describes the development of the initial geological models, petrophysical and PVT properties, and also history matching of primary and secondary oil recovery in the Colliver-Carter lease of the Hall-Gurney Field.

7.2.1. Geological Model

The initial geologic model was developed by the Kansas Geological Survey (KGS). The formation was characterized by analyzing the many cuttings and wireline logs. The wireline log gamma ray and unscaled neutron porosity depth logs indicated that the LKC interval in the Colliver-Carter lease basically consists of three stacked beds. These beds were later further divided into six zones for greater accuracy during numerical simulation. The initial geological model, therefore, consisted of six zones with distinct permeability and porosity [75].

The porosity around each well was estimated from gamma ray (neutron logs) that is available for 41 wells in the pilot area. The logs were unscaled neutron logs but accurate enough to give porosity values within +/-2 porosity units. The neutron response was calibrated using the linear relationship given in Eq.(7.1):

$$Log_{10}\{Porosity \ \ in\,\%\} = A * Neutron + B \tag{7.1}$$

where A is the slope of the correlation and B is the intercept. The constants A and B were obtained using a log linear straight line relationship between the following two points: 1% porosity maximum response and 40% porosity minimum response [75]. This estimated porosity values for each well in each zone was used to generate field wide contours for each zone.

A porosity-permeability transform was used to generate permeability values from porosity values. The porosity and permeabilities from cores for this field were estimated from one whole core available for Colliver-1 (Phillips Petroleum (1936)) and core chips from Colliver-12. The permeability versus porosity for the LKC is plotted in Figure 7.5. The full-diameter permeabilities measured for Colliver-1 are the highest measured in the LKC interval and are displayed as solid red crossed squares. Figure 7.5 shows two trends, with the trend line for the low porosity regime in blue and the trend line for the high porosity regime in red leveling off at higher porosity values. The equations that define the two trends are defined as follows:

$$k = \begin{cases} 28.78\Phi - 584.4 & if \quad \Phi > 21.4\% \\ 10^{0.21\Phi - 3.05} & if \quad \Phi < 21.4\% \end{cases} \tag{7.2}$$

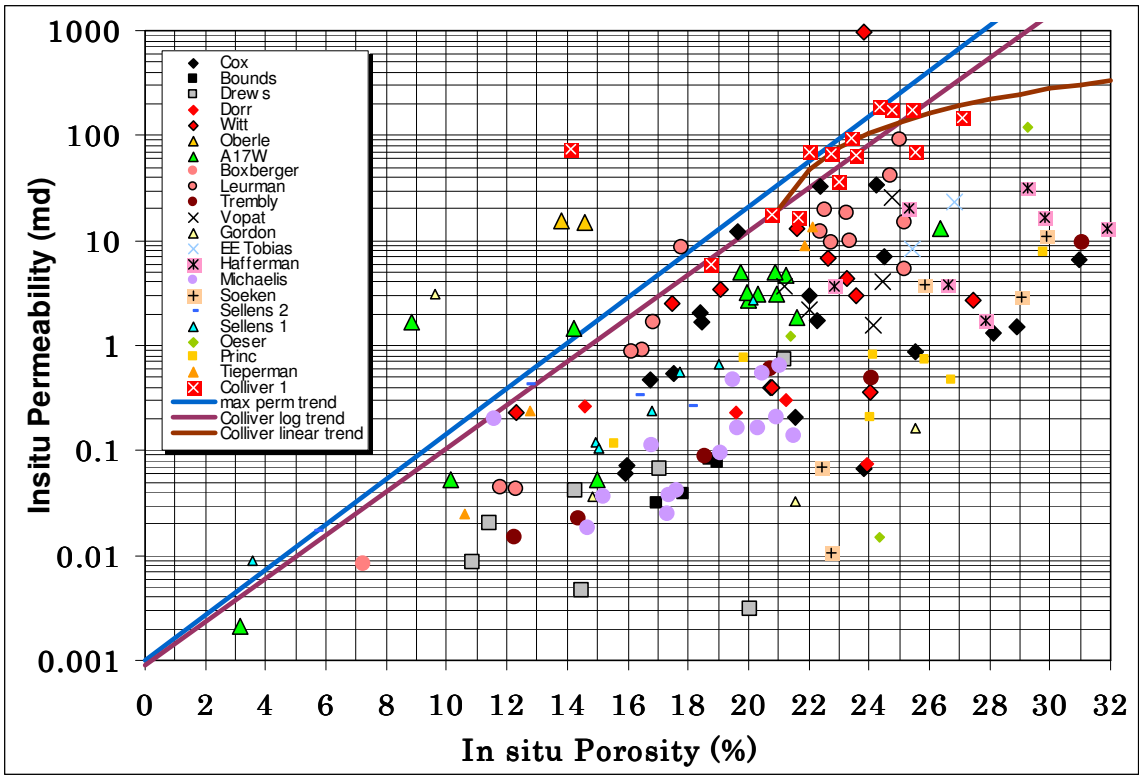

Figure 7.5. Crossplot of permeability-porosity for core samples in Hall-Gurney field [75]

where k is permeability in *md*, and Φ is porosity. The correlation between permeability with depth was not considered in Eq.(7.2). The inter-well permeability values were estimated based on the porosity values estimated from well neutron logs.

In addition, the LKC samples were subjected to air-brine pressure measurement to obtain a trend of water saturation as a function of permeability and height of oil column above free-water level. The LKC structure is about 45-50 feet above free-water level at the Colliver-Carter lease [75]. Figure 7.6 shows the variations of initial water saturation with permeability and height of oil column above free-water level. The solid trend line indicates the variation of the water saturation of the projected site with permeability. The

initial water saturation decreases as the permeability increases for the same oil column height above oil-water contact [74]. This figure established a methodology to estimate the initial water saturation from permeability values for each zone.

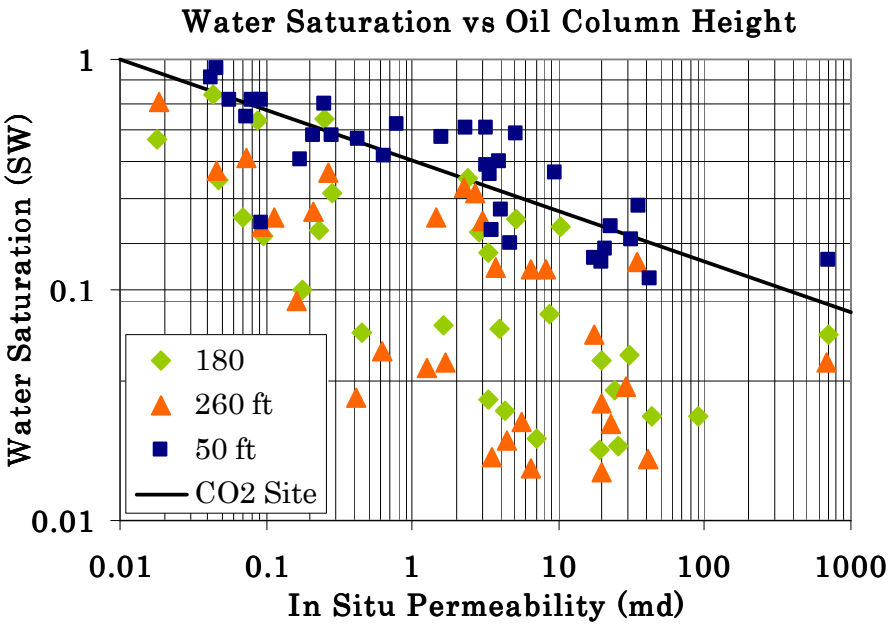

Figure 7.6. The initial water saturation decreases as the permeability increases for the same oil column height above oil-water contact [74]

Mercury capillary pressure was measured on a core chip from Colliver-12 and eight other samples obtained from other locations in the Central Kansas Uplift. The measured samples showed a wide range of porosity and permeability values that is typically common for the reservoirs in the LKC formation. Figure 7.7 displays the capillary pressure curves for different core samples. The figure displays a log-linear trend between water saturation and reservoir oil-brine capillary pressure for a range of permeability values. Comparison between samples of different permeability indicates that capillary pressures decrease with increasing permeability at any given saturation.

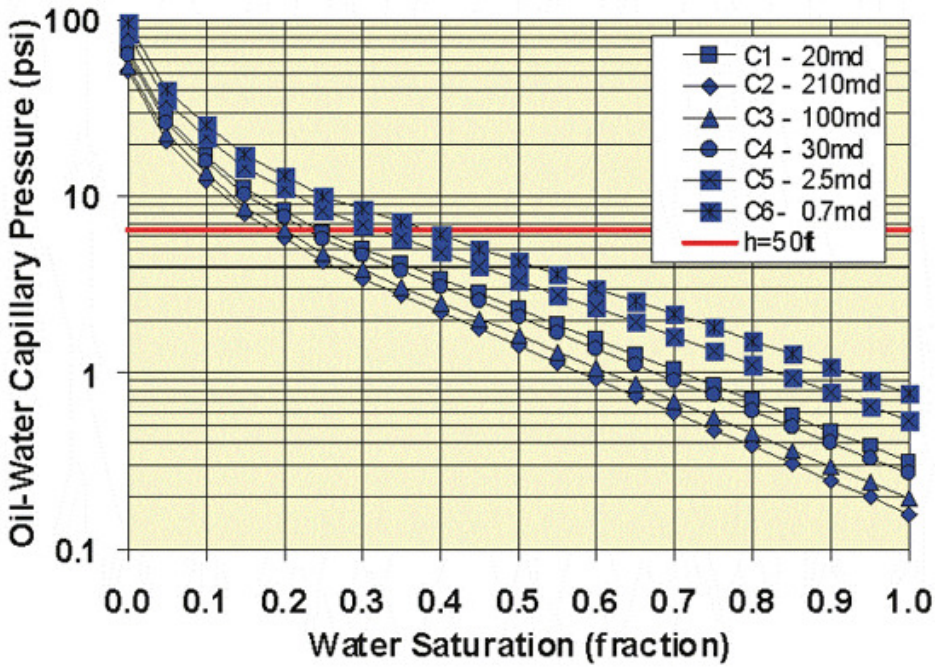

Figure 7.7. Capillary pressure curves for oomoldic limestone [75]

Analyzing the relationship between the change in capillary pressure and permeability, an equation was constructed that provides approximate capillary pressure curves for any given permeability:

$$P_C = 10^{(A.S_w+B)}(\rho_{water} - \rho_{oil}) \tag{7.3}$$

where P_c is reservoir oil-brine capillary pressure (psia), S_w is water saturation (fraction), ρ_{water} and ρ_{oil} are water and oil density (g/cc), and A and B are constants that vary with permeability. These constants are predicted as follows:

$$\begin{aligned} A &= -0.1663 * \log_{10}(k) - 1.5186 \\ B &= 0.1088 * \log_{10}(k) + 2.2476 \end{aligned} \tag{7.4}$$

where k is permeability of the rock (md).These equations provide generalized capillary pressure curves that approximate the relationships for the available samples.

Data obtained from McCoy Petroleum were used to determine the imbibition water-oil relative permeability curves [74]. These data were measured on oomoldic limestone from the Marmaton Formation, Finney County, Kansas [74]. The properties exhibited by these limestones are very similar to that of LKC formation. The initial water saturation (S_{iw}) was estimated from generalized capillary pressure curves. Single average water saturation was assigned to each zone in Colliver-Carter leases to track average fluid flow from or into each zone. Table 7.1 summarizes the average properties of each layer in the initial geological model.

Since relative permeability end point saturations change with permeability, the relative permeability curves also change with absolute permeability. Relative permeability curves for each layer were predicted using the Corey-type equations below where S_{iw} was obtained from P_c-k relations and the average absolute permeability values for each layer. Exponent m and n values were initially obtained from the measured data and were modified during simulation to reproduce lease production data.

$$\begin{aligned} k_{ro} &= a_1(1-S_{WD})^m \\ k_{rw} &= a_2 {S_{WD}}^n \\ S_{WD} &= \frac{(S_w - S_{iw})}{(1-S_{iw}-S_{orw})} \end{aligned} \tag{7.5}$$

where k_{ro} and k_{rw} are the relative permeability of oil and water respectively.

Table 7.1. The average properties of each layer in the initial geological model [75]

Layer	Thickness (ft)	Permeability (md)	Porosity (%)	Average S_{iw}
1	1.5	8	21.8	0.24
2	3.7	150	28.8	0.23
3	2.4	40	25.0	0.23
4	2.5	6	22.4	0.25
5	1.8	2	14.7	0.34
6	2.3	0.3	12.0	0.44

7.2.2. PVT Properties

There was no information on the composition and other properties of the reservoir fluids at the start of this project. Thus, PVT properties required to simulate the primary and secondary production were estimated by correlations. However, the oil obtained from a nearby lease (Letsch) in 2000 was used to generate PVT properties for the reservoir simulator (VIP Black Oil simulator) and compared against the previous correlated properties. Furthermore, a sensitivity analysis was performed to estimate the initial saturation pressure of the reservoir using the amount of gas produced at the end of primary production.

7.2.3. History Matching the Primary and Secondary Oil Production

The initial pressure of the reservoir was estimated 1200 psia which is consistent with other L-KC formation. The pressure dropped to about 50-100 psia at the end of

primary before waterflooding of the reservoir. Since the field had several operators, little well information existed about individual well production during primary and secondary phases. A lease-based production history data was developed using commingled production data. Therefore, history matching process for primary and secondary recovery of this field was carried out on a lease data basis. The initial geologic model was used as a starting point to history match the primary and secondary oil production in Colliver and Carter leases in the Hall-Gurney field. Vector Implicit Program (VIP) reservoir simulator from Landmark Graphic Corporation was used for history matching process[74]

Figures 7.8 and 7.9 show the comparison of the true oil production rate and cumulative oil production of Colliver and Carter leases and those obtained from reservoir simulator for primary and secondary oil production. These figures indicate that the cumulative oil production of the Colliver lease is acceptable with the model withdrawing the right amount of oil from the lease. However, the cumulative oil production of the Carter lease obtained from simulation results does not match with field data. The match specially worsened after start waterflooding of the lease. After reasonable history match was obtained and residual oil in place determined, a compositional model was developed and used to simulate the performance of carbon miscible flooding.

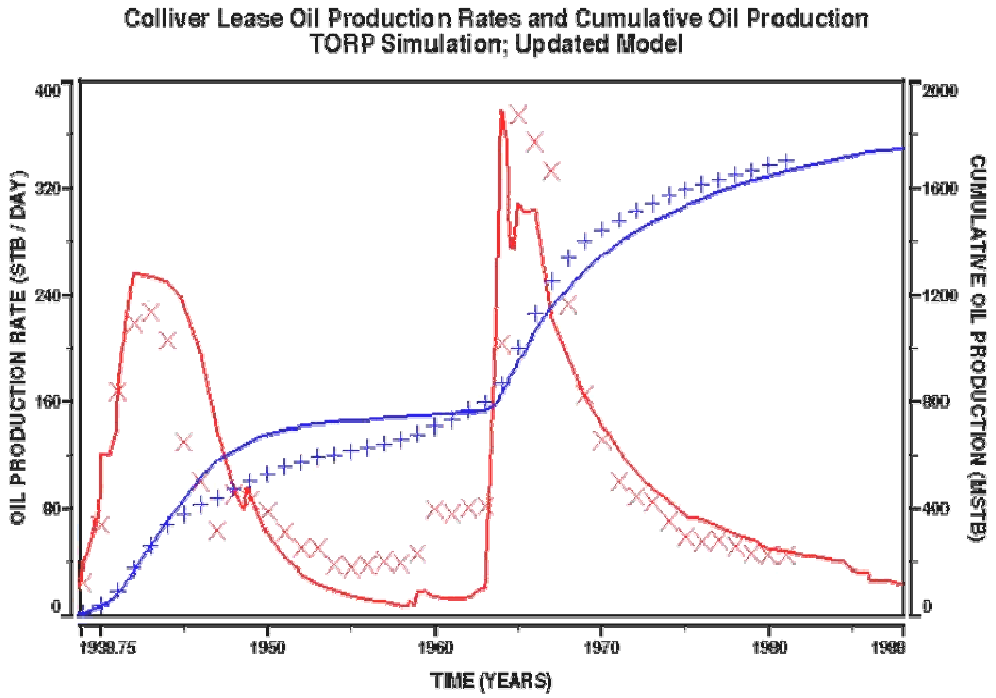

Figure 7.8. History matching of oil production for Colliver lease [74]

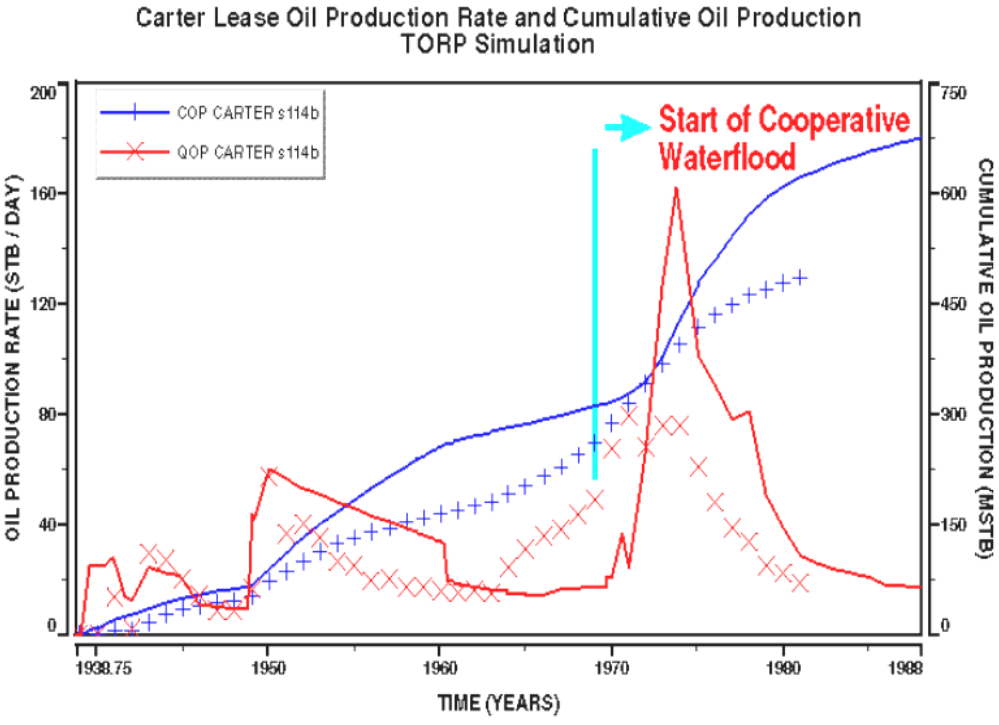

Figure 7.9. History matching of oil production for Carter lease [74]

7.3. Updated Geologic Model Based on CO2I-1 Cores

CO2-I1 was drilled on September 23, 2000 and completed on October 2, 2000 in the Hall-Gurney field. Five cores were taken including three conventional cores and two high pressure cores. Unfortunately, the high pressure cores obtained from the reservoir interval exhibited severe damage and little useful information was obtained at this interval. The core permeabilities decreased with increasing depth below the top of the *C* zone. Figure 7.10 shows the variation of permeability with depth for core plugs obtained from the new drilled well CO2I-1. There is a general trend, shown as a solid blue line, indicating a reduction in permeability as depth increases. This trend is also seen in the Colliver#1 well that was used as the basis of the initial model.

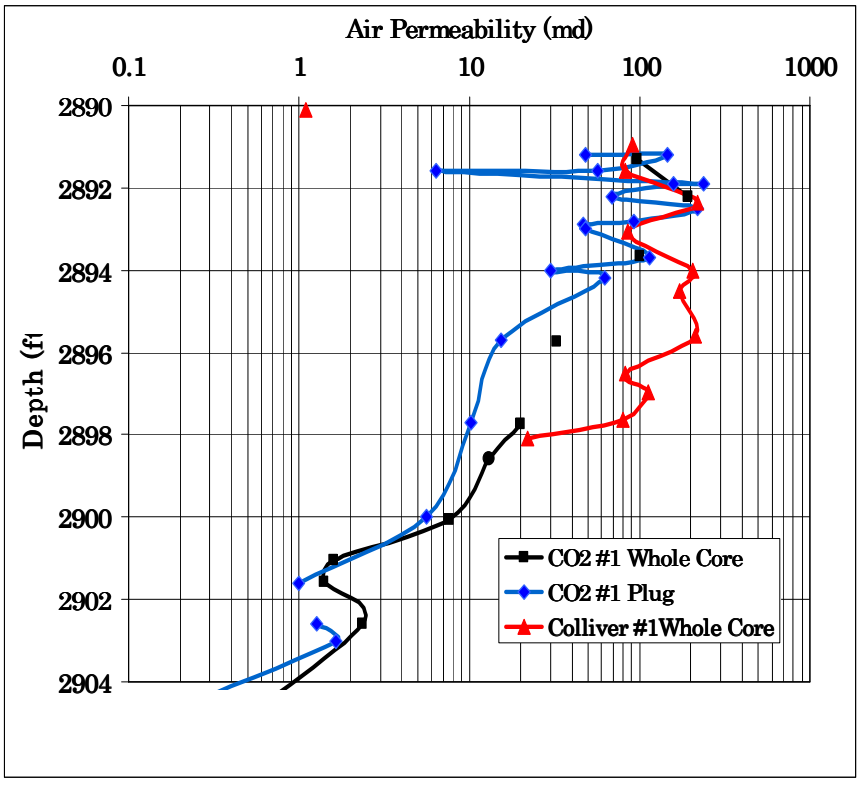

Figure 7.10. Permeability versus depth for Murfin Carter-Colliver CO2 I well and Colliver#1 well [74]

7.4. CO_2 Pilot area in the Hall-Gurney Field

The feasibility of injecting miscible carbon dioxide to recover oil was studied by the Tertiary Oil Recovery Project (TORP) in the 1970's. The study involved a set of experiments to determine the minimum miscibility pressure (MMP) of lease crude oil at reservoir temperature. These experiments indicated that the MMP was about 1200-1300 psia, a pressure range that had been maintained during the waterflooding of the Hall-Gurney field. The project gained attention in 1990's when a carbon dioxide pipeline in Oklahoma was installed [74]. This pipeline delivered carbon dioxide to the Postle Field in the panhandle area in Oklahoma. The pipeline placed a significant source of carbon dioxide within reasonable access to the Southwest and Central Kansas oilfields. Another motivating factor was the availability of excess carbon dioxide with Shell CO_2 Company and their interest in finding a market for this excess CO_2.

In order to study the feasibility of a full scale CO_2 flooding, a pilot test was planned. The objective of the plan was to demonstrate the viability of carbon dioxide miscible flooding in the Lansing-Kansas City formation on the Central Kansas Uplift and to obtain data concerning reservoir properties, flood performance, and operating costs and methods to aid operators in future floods. The 10 acre pilot area represented the oomoldic limestone reservoir in the Hall-Gurney Field (Figure 7.11). The pilot test designed to ensure the development of the miscibility (1200-1300 psi) in the pilot area in Figure 7.11. The carbon dioxide and water was injected into CO2I-1 in rate to permit completion of the flood in the project time frame.

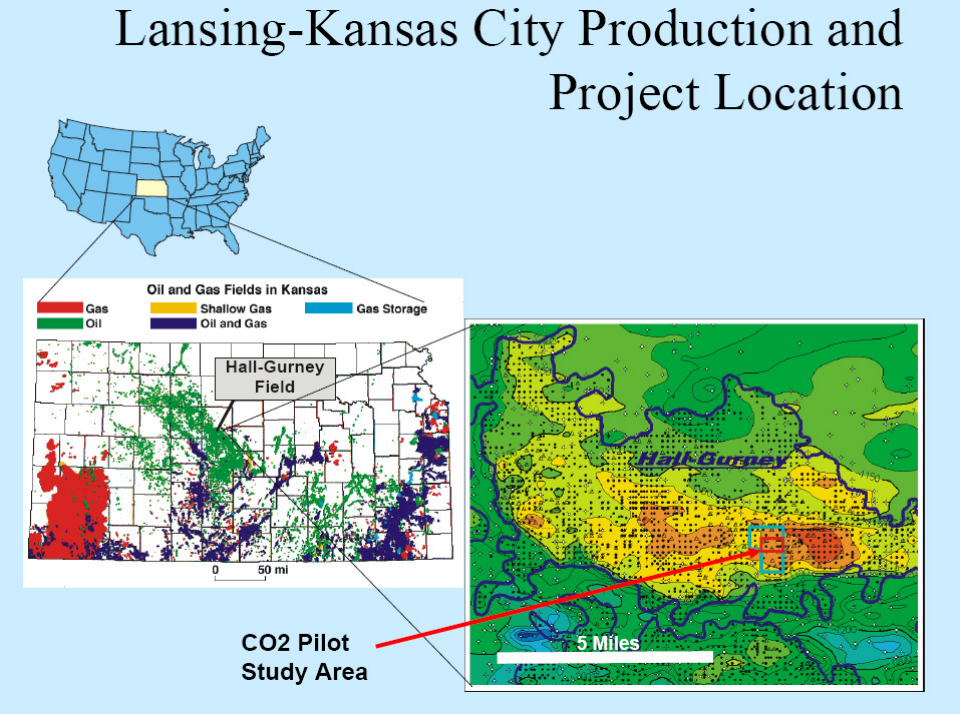

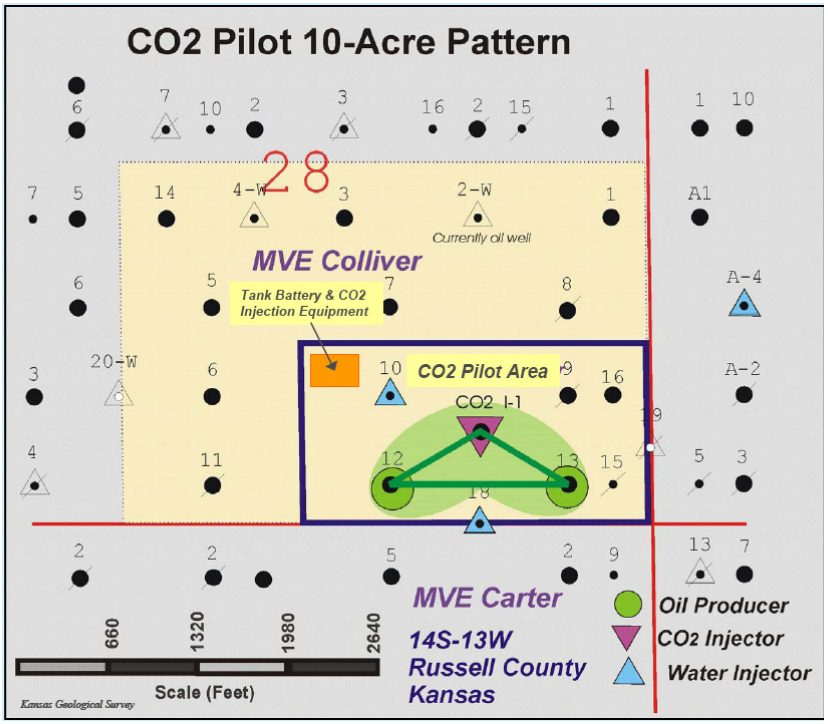

Figure 7.11. The 10-Acre CO_2 pilot area in the Hall-Gurney Field [74]

Both Colliver-10 and Colliver-18 wells in the pilot injected water to confine the carbon dioxide to the pilot area and maintain the pressure. There are also two producing wells Colliver-12 and Colliver-13 to the south of CO2I-1 in the pilot area.

7.5. Field Diagnostic Activities

Before injecting any CO2 into the pilot test area, a series of activities and analysis was performed to obtain important information about the well injectivity and connectivity between the wells in the pilot area. The most important activities are as follows:

1. Short-term well injectivity test of the CO2I-1 in February 5-6, 2003
2. Shut in Colliver-18 in March 7, 2003
3. Water injection test in CO2I-1 in April 23, 2003
4. Colliver-12 and Colliver-13 production tests in June 11, 2003 for two weeks.
5. Conductivity test between CO2I-1 and Colliver-13 in August 20, 2003
6. Start Repressurring of the pilot in September 5, 2003

7.5.1. Short-term injection test of the CO2I-1 in February 5-6, 2003

A short-term injection test was performed in CO2I-1 in February 5, 2003 for two days to verify that there is sufficient injectivity for setting up a long-term water supply and determine if further stimulation is needed. Extrapolation of the short injection rate to long-term rate indicated that the well has sufficient injectivity for the demonstration and move forward with the long term injectivity rate without additional stimulation at the present time.

7.5.2. Shut in Colliver#18

Colliver-18 was shut in March 4, 2003 to verify its connectivity with CO2I-1, Colliver-10, and Colliver-12. Bottom hole pressure (BHP) for these wells were monitored and calculated (Figure 7.12). The pressure decline of these wells indicated that the reservoir was stabilizing and all wells were in communication.

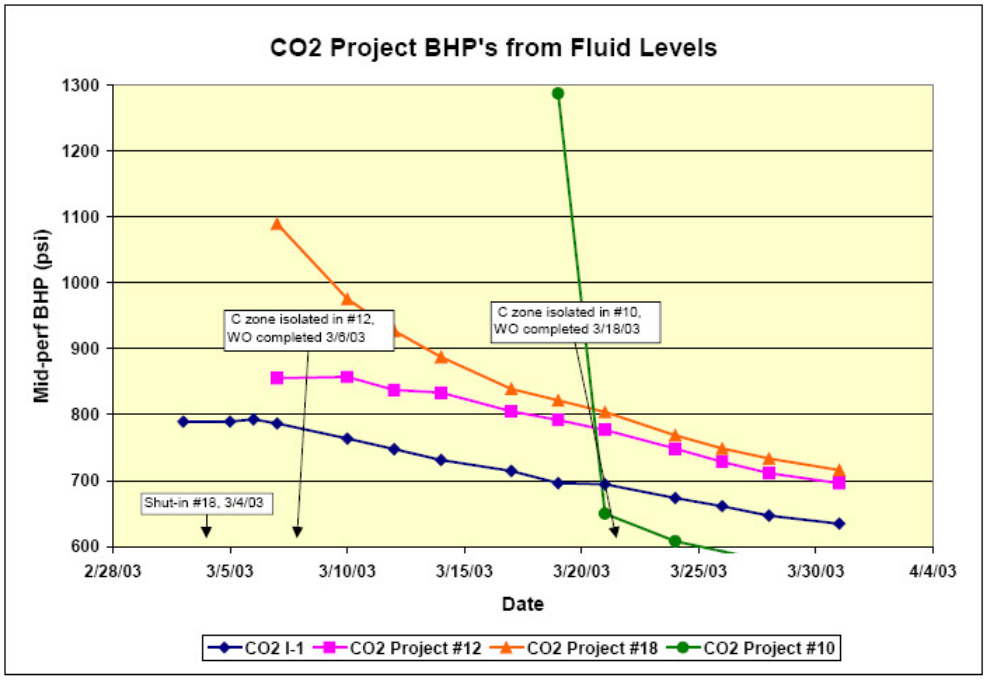

Figure 7.12. Bottom hole pressures through time showing decline of reservoir pressures following shut in Colliver-18 [74]

7.5.3. Water Injection test in CO2I-1

A long-term water injection in CO2 I-1 began on April 23, 2003 to verify communication between this well and the other wells in the 10-acre pilot. In addition, the

information obtained from this test was used to refine the reservoir model and improve prediction of CO_2 miscible flood performance. Bottom hole pressures measuered in surrounding wells are shown in Figure 7.13. The data show that there was a strong connectivity between CO2I-1 and Colliver-10, Colliver-12, and Colliver-18. However, the pressure response in the Colliver-16 did not increase as fast as what was simulated in the reservoir model.

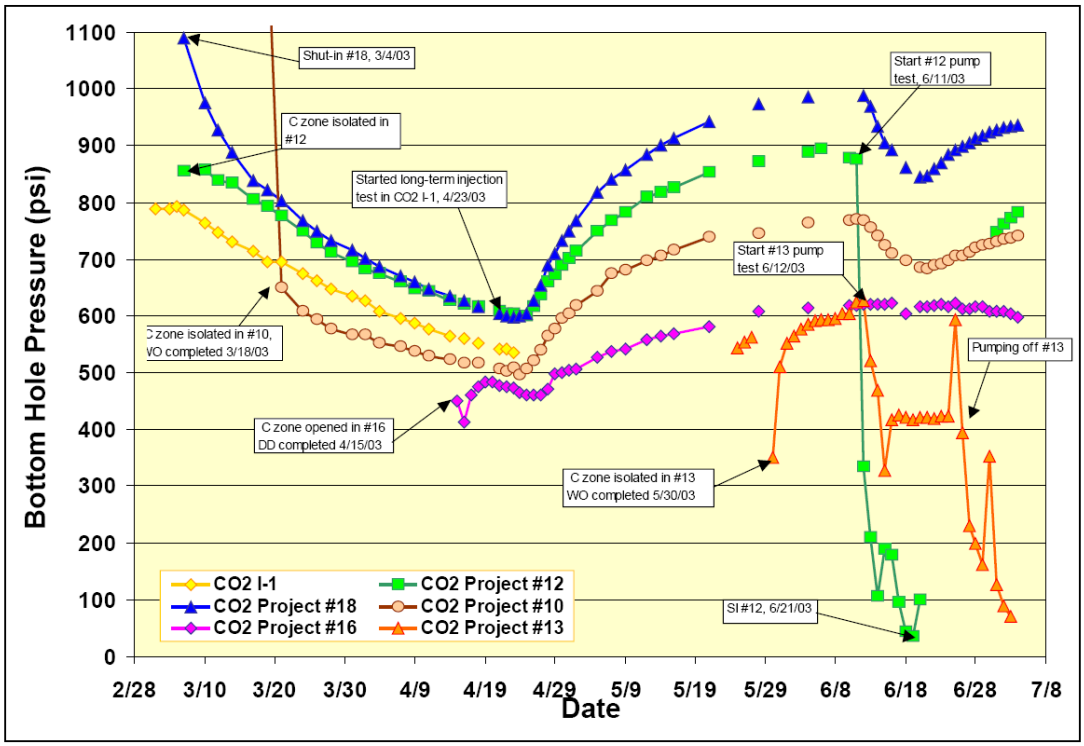

Figure 7.13. The BHP response with respect to commencement of long- term water Injection test in CO2I-1 [74]

7.5.4. Colliver-12 and Colliver-13 Production Test in June 2003

The production tests of wells Colliver-12 & Colliver 13 were conducted to determine if enough fluid could be produced by these wells to obtain sufficient displacement in the pilot pattern. The production tests consisted of individually pumping the wells in the tanks while maintaining constant injection rate into CO2I-1.

7.5.5. Conductivity test between CO2I-1 and Colliver-13 in August 2003

A conductivity test was performed in August 20, 2003 to confirm adequate conductivity between CO2I-1 and Colliver-13. The CO2I-1 injection rate was decreased from 140 BWPD to 70 BWPD in a step change while Colliver-13 was pumped off. The production rate from Colliver-13 decreased consistently with the injection rate change at CO2I-1 (Figure 7.14). The result of this test was interpreted as adequate connectivity between CO2I-1 and Colliver-13.

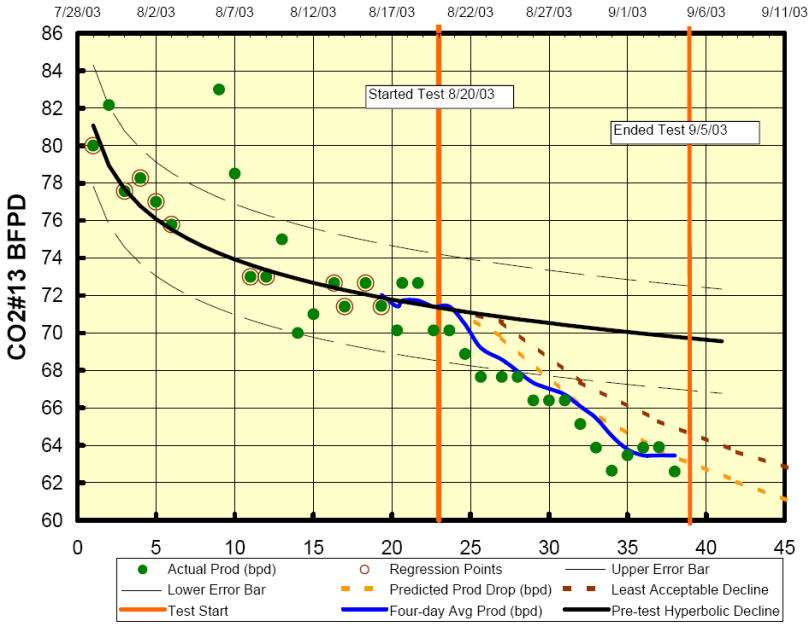

Figure 7.14. Conductivity test between CO2I-1 and Colliver-13 [74]

7.5.6. Start Repressuring of the pilot in September 5, 2003

Repressuring of the pilot began on September 5, 2003. Repressuring was done before starting CO_2 injection to make sure reaching the pressure in the pilot could reach miscible condition in the reservoir. Water injection rate in CO2I-1 was increased from 70 BWPD to 150 BWPD. Water injection began in the containment wells, Colliver10 & Colliver-18, on September 15, 2003.

7.6. CO2 Injection in the Hall-Gurney Field

Injection of carbon dioxide began on November 23, 2003. Operational problems were encountered on startup that delayed continuous injection until December 2, 2003. In the next thirteen months, 11.31 MM lbs of carbon dioxide were injected into CO2I-1. Figure 7.15 shows the monthly carbon dioxide injection rate. The injection rate declined substantially in May through June due to the excessive vent loss. Project design and management is based on controlling carbon dioxide loss to the north by maintaining the pressure around Colliver-10. This was done by maintaining adequate water injection rates into Colliver-10 & Colliver-18, and controlling the injection/withdrawal ratio in the pilot pattern.

At the beginning of the project, both production wells Colliver-12 and Colliver-13 produced 100% water. Figure 7.16 represents the liquid production rate from these production wells. By the end of December 2003, oil production averaged 1.6 STB/D, primarily from Colliver-12. Oil production averaged 2.5 STB/D for the period from March-June. The average daily oil production rate is shown in Figure 7.17. Carbon dioxide arrived at Colliver-12 on May 31, 2003, and arrived at Colliver-13 in August 2003.

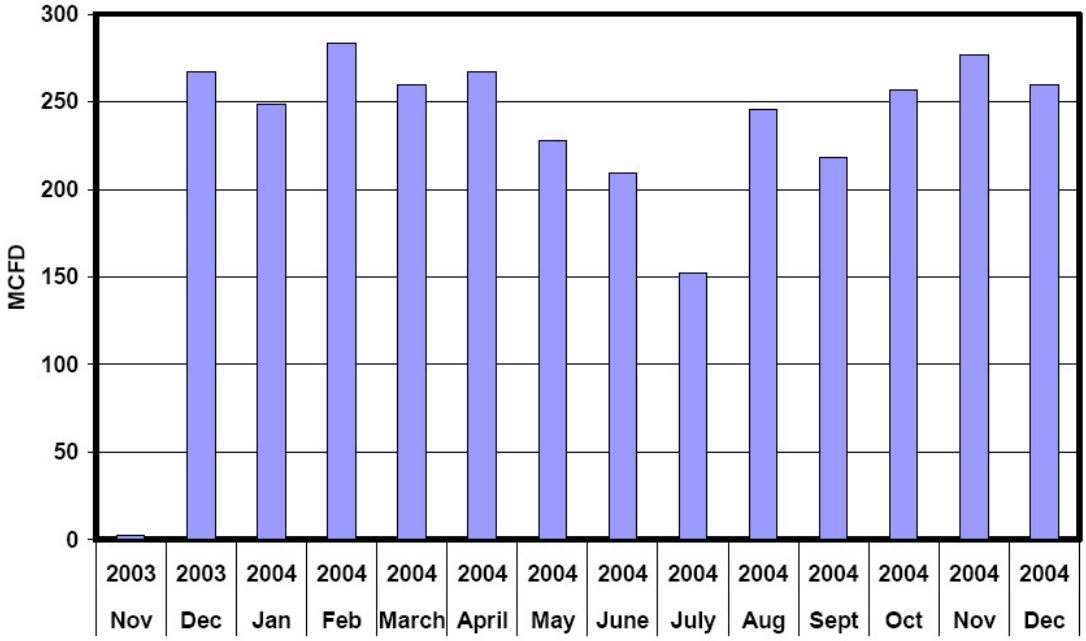

Figure 7.15. Carbon dioxide injection rate in CO2I-1 [74]

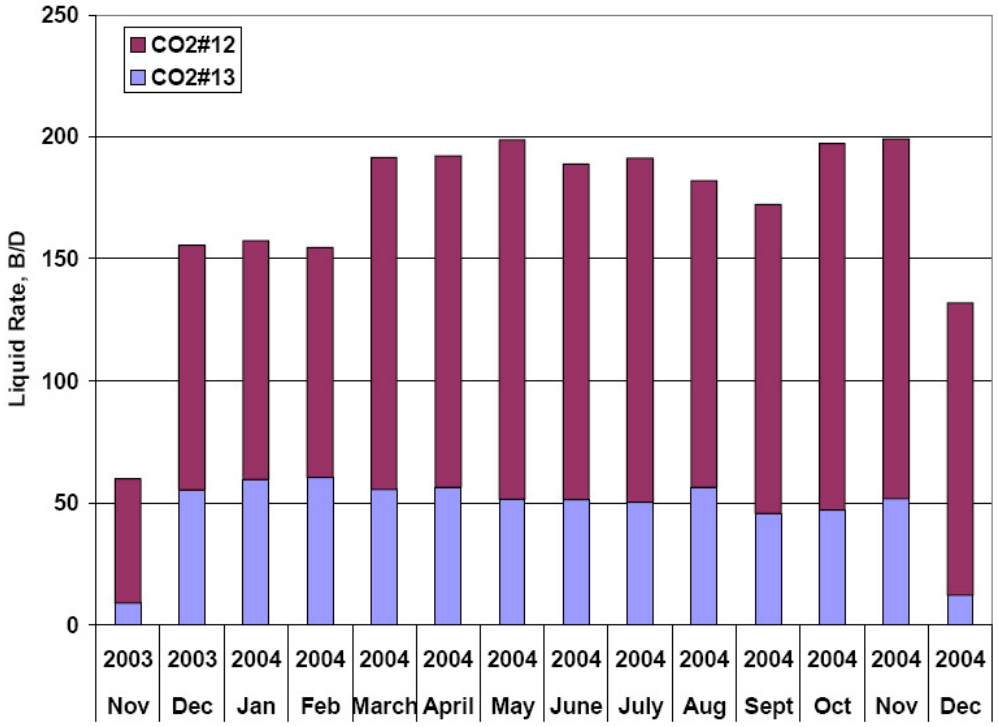

Figure 7.16. Liquid production rate from Colliver-12 and Colliver-13 [74]

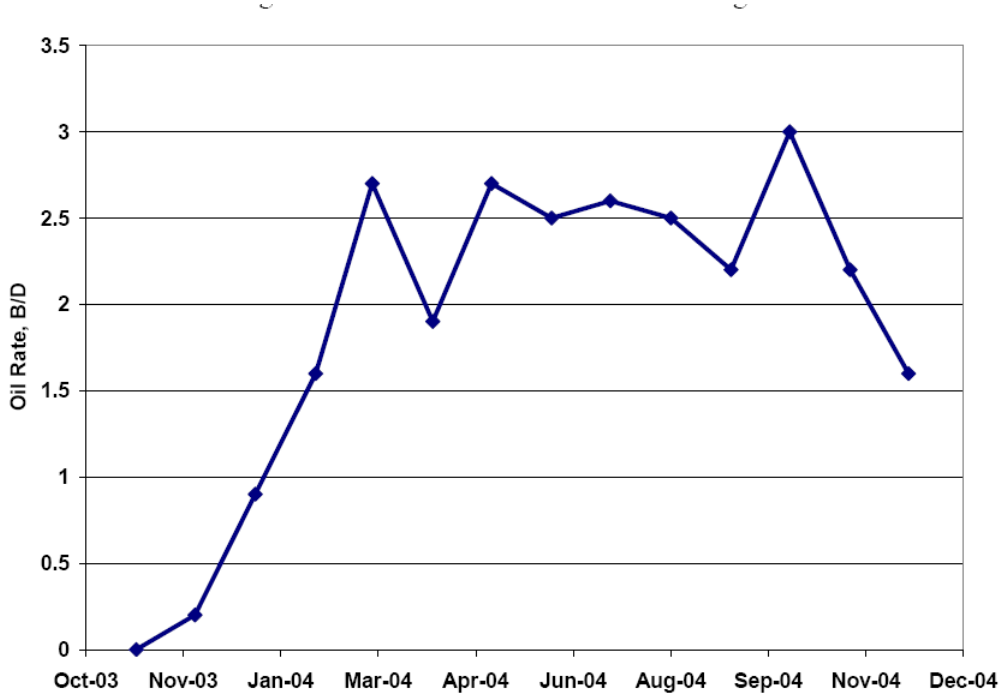

Figure 7.17. Average daily oil production rate from pilot area [74]

7.7. Modeling of Solvent (CO_2) Miscible Flooding

The Todd-Longstaff [76] model was used to model CO2 miscible flooding in this study. The Todd-Longstaff model is an empirical treatment of the effects of physical dispersion between the miscible components in the hydrocarbon phase. The model introduces an empirical parameter, ω, whose value lies between 0 and 1, to represent the size of the dispersed zone in each grid cell. The value of ω thus controls the degree of fluid mixing within each grid cell. A value of ω=1 models the case when the size of the dispersed zone is greater than a typical grid cell size and the hydrocarbon components is considered to be fully mixed in each cell. In this case the miscible components have the same value for the viscosity and density, as given by the appropriate mixing rule. A value of ω=0 models the effect of a negligibly thin dispersed zone between the gas and oil components, and the miscible components should then have the viscosity and density values of the pure components. In practical applications an intermediate value of ω would be needed to model incomplete mixing of the miscible components.

Computer Modeling Group (CMG) provides an extension of the Black Oil Model to enable modeling of reservoir recovery mechanisms in which injected fluids are miscible with the hydrocarbons in the reservoir. This solvent model enables the user to model gas injection projects without going through the complexity and expense of using an alternative compositional model. A value of ω=1 indicating full miscibility was assumed for this study. The other property of solvent was calculated using slim tube experiments and empirical correlations.

7.8. New Geological Structure and Petrophysical Properties

The geological model was provided by Kansas Geological Survey (KGS). The physical geologic model was constructed by defining the top of structure of layer 1 and then defining the thickness maps for each zone. Layering of the reservoir influences the performance of the CO_2 miscible flood in which cross-flow enhanced gravity segregation. As the number of layers is increased the gravity segregation is more pronounced. The primary and secondary oil production history match in the Hall-Gurney field was simulated using a 6-layer model. However, the geological model for the history match of CO_2 miscible flooding was first constructed as a 12-layer model. In fact, the 12 layers were determined according to minimum resolution of well-log data (1 ft). Later, the geological model was cut into an 8-layer model due to lack of porosity in the last four bottom layers. Figure 7.18 displays a 3-D view of the final geological model used in the simulation.

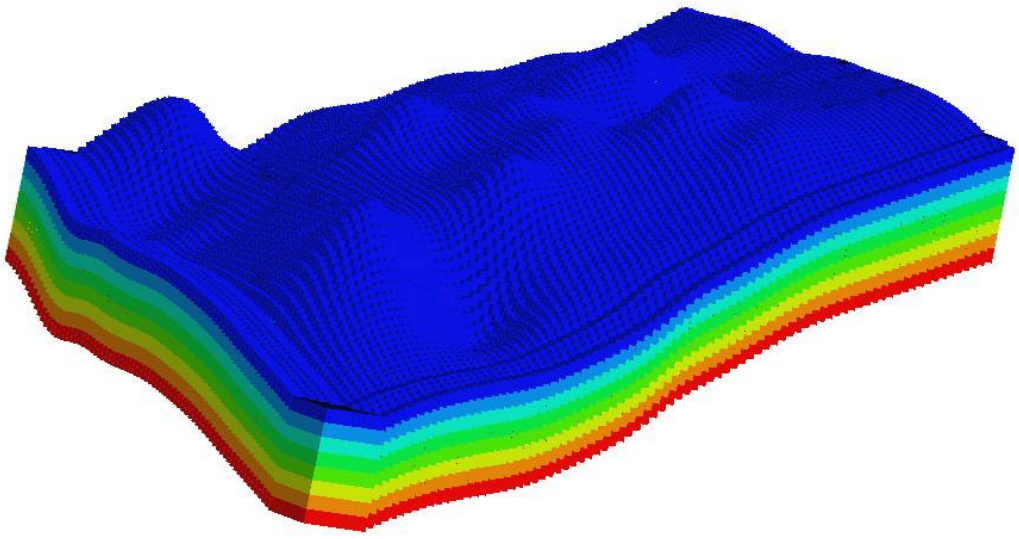

Figure 7.18. A 3D view of the 8-layer geological model used in the simulation

7.9. Porosity Distribution of the Geological Model

There were no modern or even scaled electric logs available within the field area until the Carter-Colliver CO2I-1 well was drilled. The only logs available were Gamma Ray-Neutron Logs (unscaled) in the open portion of the wells. The neutron logs were calibrated using the only available core petrophysical measurements from the Colliver-1. The porosity values of log data were estimated in 25 wells in the *C* zone of CO_2 pilot area after calibrating the well log data (Figure 7.19). Then, the porosity of all wells in each layer (one-foot thickness) of the 8-layer model was assigned using well-log data. Table 7.2 lists the porosity values of the 25 wells in the all eight layers of the geological model.

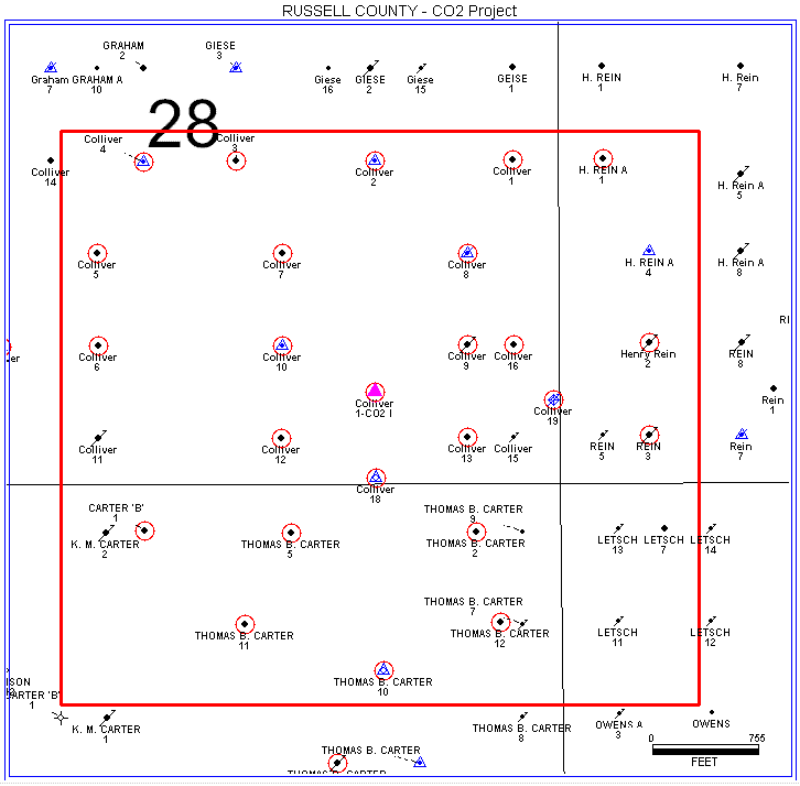

Figure 7.19. Available well Log data in the Hall-Gurney Field [75]

Table 7.2. Porosity values of wells at different layers [37]

Well Name	Layer 1	Layer 2	Layer 3	Layer 4	Layer 5	Layer 6	Layer 7	Layer 8
Carter10	0.26	0.27	0.25	0.25	0.25	0.23	0.22	0.21
Carter2	0.17	0.25	0.29	0.29	0.29	0.31	0.30	0.29
Carter5	0.22	0.24	0.26	0.25	0.28	0.28	0.28	0.25
CO2I1	0.14	0.26	0.28	0.30	0.29	0.29	0.28	0.27
Colliver1	0.24	0.26	0.26	0.27	0.26	0.24	0.21	0.20
Colliver10	0.26	0.23	0.26	0.24	0.23	0.22	0.19	0.16
Colliver12	0.23	0.29	0.30	0.30	0.28	0.27	0.26	0.25
Colliver13	0.09	0.13	0.24	0.29	0.30	0.29	0.24	0.14
Colliver16	0.22	0.28	0.28	0.27	0.26	0.25	0.24	0.21
Colliver18	0.14	0.25	0.30	0.31	0.31	0.32	0.32	0.32
Colliver6	0.21	0.20	0.19	0.16	0.16	0.18	0.19	0.18
Carter 11	0.26	0.29	0.28	0.28	0.27	0.26	0.25	0.25
Carter12	0.17	0.18	0.25	0.25	0.24	0.23	0.23	0.23
Henry 2	0.06	0.03	0.06	0.12	0.21	0.26	0.28	0.26
Colliver19	0.17	0.19	0.23	0.29	0.30	0.30	0.29	0.28
Colliver 2	0.23	0.25	0.25	0.24	0.26	0.26	0.23	0.21
Henry 1	0.24	0.25	0.27	0.27	0.26	0.27	0.26	0.25
Colliver 3	0.23	0.21	0.20	0.20	0.16	0.15	0.14	0.13
Colliver 4	0.19	0.21	0.19	0.16	0.13	0.14	0.14	0.14
Colliver 5	0.16	0.17	0.17	0.16	0.16	0.15	0.13	0.11
Colliver 7	0.12	0.10	0.11	0.13	0.15	0.17	0.16	0.15
Carter1	0.08	0.10	0.15	0.17	0.20	0.23	0.25	0.26
Colliver 8	0.19	0.18	0.21	0.26	0.29	0.28	0.27	0.25
Rein 3	0.18	0.16	0.19	0.21	0.22	0.17	0.15	0.17
Colliver 9	0.32	0.24	0.26	0.26	0.23	0.23	0.23	0.18

7.10. Verification of the Reservoir Layering Using Descriptive Statistics

The 8-layer geological model was constructed on the basis of the well-log data and one-foot thickness. The statistical ANOVA test was used to verify the reservoir layering. The ANOVA is used to test for differences among two or more independent groups based on their variances. For this study, the ANOVA test was performed for the porosity data of the eight layers in order to investigate if these data comes from the same population of porosity data. Table 7.3 presents the results of ANOVA test performed using the available toolbox in Microsoft Excel. The analysis revealed that the same

population hypothesis for the porosity data in the eight layers cannot be accepted because $F>F_{crit}$. In other words, the porosity data in all layers obtained from different population which could interpreted as different geological facies. Statistical *F-test* and *t-test* analysis was applied to check the population similarity analysis for porosity data in each pair of layers in the 8-layer model. Tables 7.4 and 7.5 represent the *t-test* for porosity samples of the layers 1 & 2 and 5 & 6 respectively. The analysis indicated that porosity of these two layers was not sampled from the same population. Tables 7.6 and 7.7 show *F-test* analysis for porosity samples of layers 1 & 2 and 5& 6 respectively. This analysis rejected that the porosity samples in these layers have the same population. In general, the results of these statistical tests indicated confirm the number of layers in the reservoir. However, it is not possible to statistically investigate if the porosity data in a layer sampled from the same population. The well-log data must be provided on the basis of less than one-foot thickness to perform such analysis.

Table 7.3. ANOVA single for all layers of the 8-layer model

Groups	*Count*	*Sum*	*Average*	*Variance*
Layer 1	25	4.7678	0.19071	0.0039
Layer 2	25	5.2389	0.20956	0.00434
Layer 3	25	5.7204	0.22882	0.00374
Layer 4	25	5.9092	0.23637	0.0033
Layer 5	25	5.9925	0.2397	0.00291
Layer 6	25	5.9766	0.23906	0.00281
Layer 7	25	5.72	0.2288	0.00292
Layer 8	25	5.3639	0.21456	0.00304

Source of Variation	*SS*	*df*	*MS*	*F*	*P-value*	F_{crit}
Between Groups	0.0519	7	0.00741	2.20063	0.035889	2.057533
Within Groups	0.6469	192	0.00337	NA	NA	NA
Total	0.6988	199	NA	NA	NA	NA

$F > F_{crit} \rightarrow Hypothesis\ rejected$

Table 7.4. *t-test* for porosity samples in layers 5 & 6

Statistics	*Layer 5*	*Layer 6*
Mean	0.2397	0.239064
Variance	0.00290637	0.00280555
Observations	25	25
Pearson Correlation	0.99096514	NA
Hypothesized Mean Difference	0	NA
df	24	NA
t Stat	0.43893089	NA
P(T<=t) two-tail	0.6646379	NA
t Critical two-tail	0.33621573	NA

$t > t_{crit} \rightarrow Hypothesis\ rejected$

Table 7.5. *t-test* for porosity samples in layers 1 & 2

Statistics	*Layer 1*	*Layer 2*
Mean	0.190712	0.209556
Variance	0.003896	0.00433891
Observations	25	25
Pearson Correlation	0.96974606	
Hypothesized Mean Difference	0	
df	24	
t Stat	-5.83545348	
P(T<=t) two-tail	5.1135E-06	
t Critical two-tail	2.06389814	

$t > t_{crit} \rightarrow Hypothesis\ rejected$

Table 7.6. *F-test* for porosity samples in layers 1 & 2

Statistics	*Layer 1*	*Layer 2*
Mean	0.190712	0.209556
Variance	0.003895998	0.00433891
Observations	25	25
df	24	24
F	0.897920321	NA
P(F<=f) one-tail	0.397064925	NA
F Critical one-tail	0.504092768	NA

$F > F_{crit} \rightarrow Hypothesis\ rejected$

Table 7.7. *F-test* for porosity samples in layers 5 & 6

Statistics	*Layer 1*	*Layer 2*
Mean	0.2397	0.239064
Variance	0.002906372	0.00280555
Observations	25	25
df	24	24
F	2.035936236	NA
P(F<=f) one-tail	0.465899121	NA
F Critical one-tail	1.983757159	NA

$F > F_{crit} \rightarrow Hypothesis\ rejected$

7.11. Geostatistical Approach for Porosity Estimation

The experimental semivariogram of porosity for each layer was calculated using the 25 porosity samples. GSLIB program *gamv* was used to calculate the experimental semivariogram for each layer. Then, the experimental semivariogram data for each layer were fit to the basic mathematical semivariogram models. Figure 7.20 and Figure 7.21 present the analytical model fitted to the semivariogram of porosity samples in the layers 1 and 7 of the 8-layer model. No nugget effect was considered in modeling the experimental semivariograms. The range of the semivariograms for layers 1-8 vary in the range of 900-1600 ft. Porosity values at unsampled locations for the eight layers of the CO_2 pilot area was generated by ordinary kriging implemented in the GSLIB program kb2d. The search radius of 5000 ft was estimated from the distribution of well locations in the location maps in Figure 7.19. The radius was chosen in a manner to encompass the minimum number of data points (3) at any unsampled grids. Using a smaller radius (smaller than 5000 ft) would result in search failures at some of the unsampled grid

nodes. This is reasonable because it prevents the procedure extrapolating too far from the well control. The minimum and maximum number of points used in the estimation procedure was three and ten respectively. Data set in Table 7.2 set aside as hard control data for estimating the porosity values at unsampled grids of the eight-layer model. Figure 7.22 and Figure 7.23 show the porosity maps for the layers 1 and 7 of the 8-layer model.

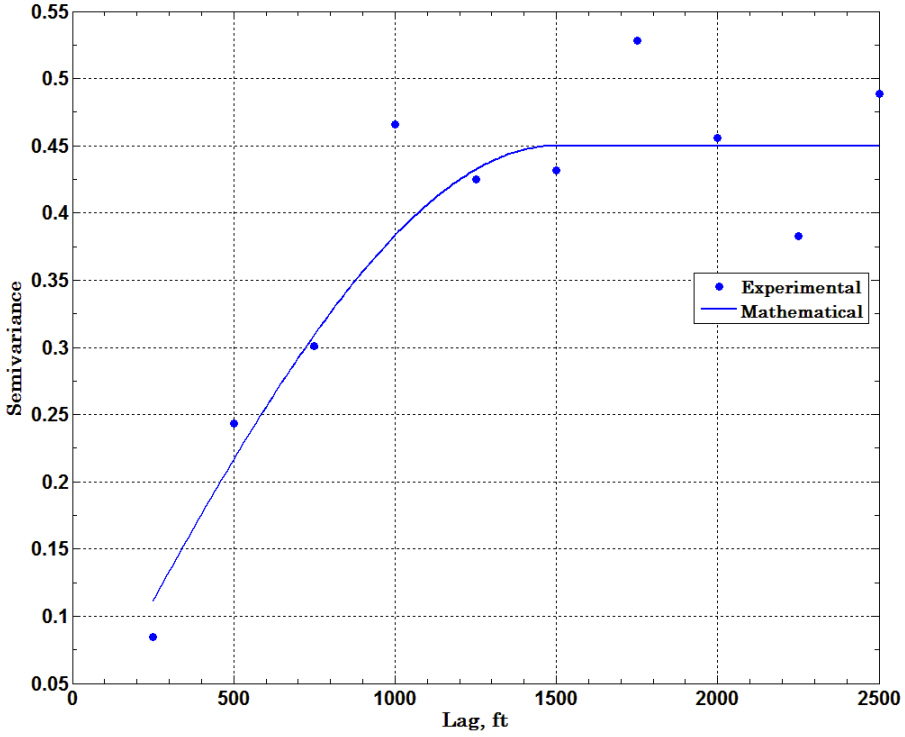

Figure 7.20. Experimental and Analytical semivariograms of the layer 1

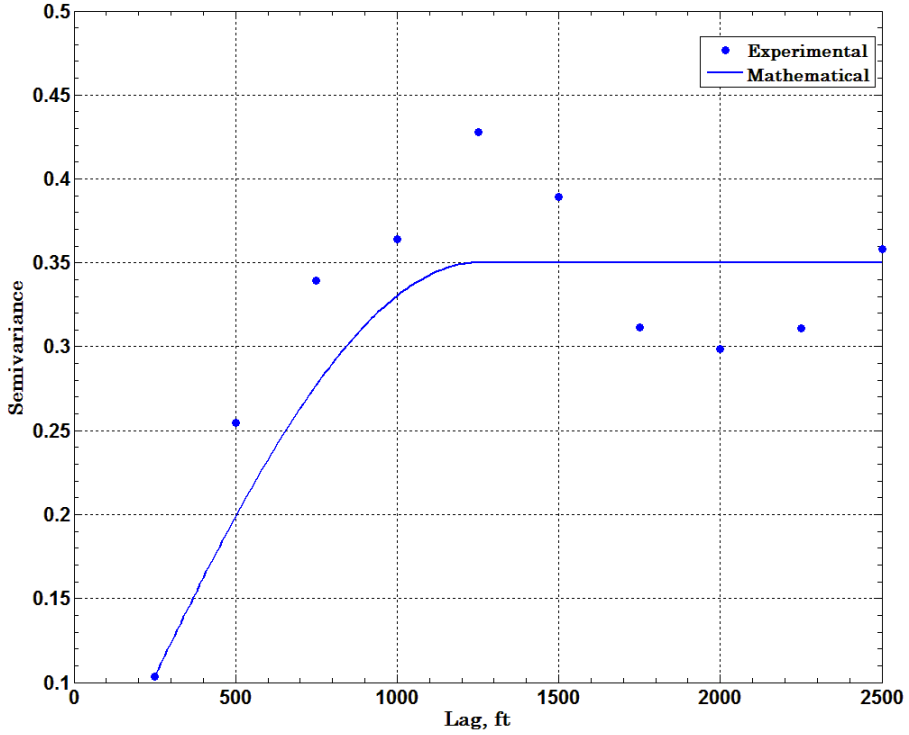

Figure 7.21. Experimental and Analytical semivariograms of the layer 7

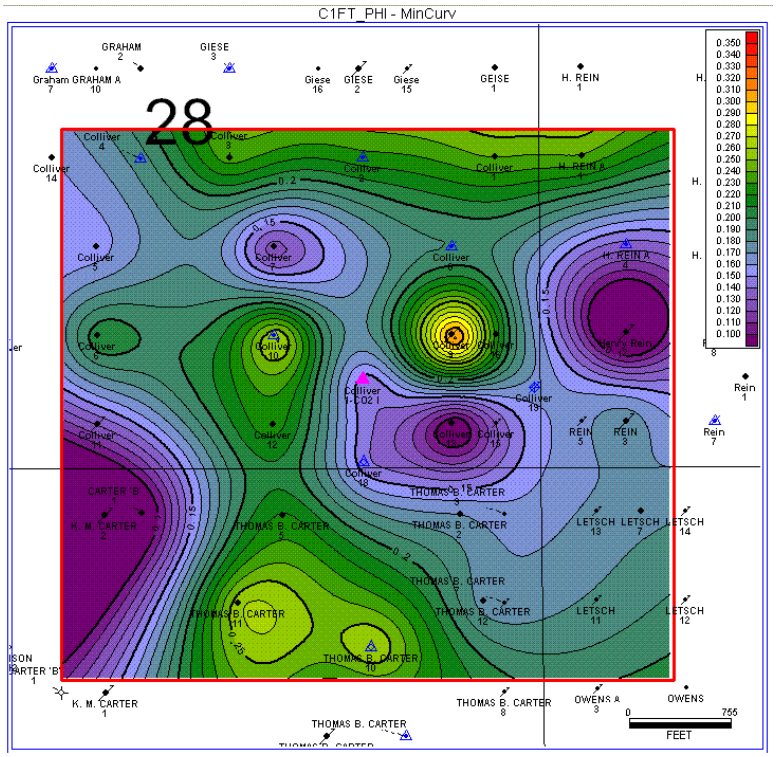

Figure 7.22. Porosity distribution of Layer-1 [37]

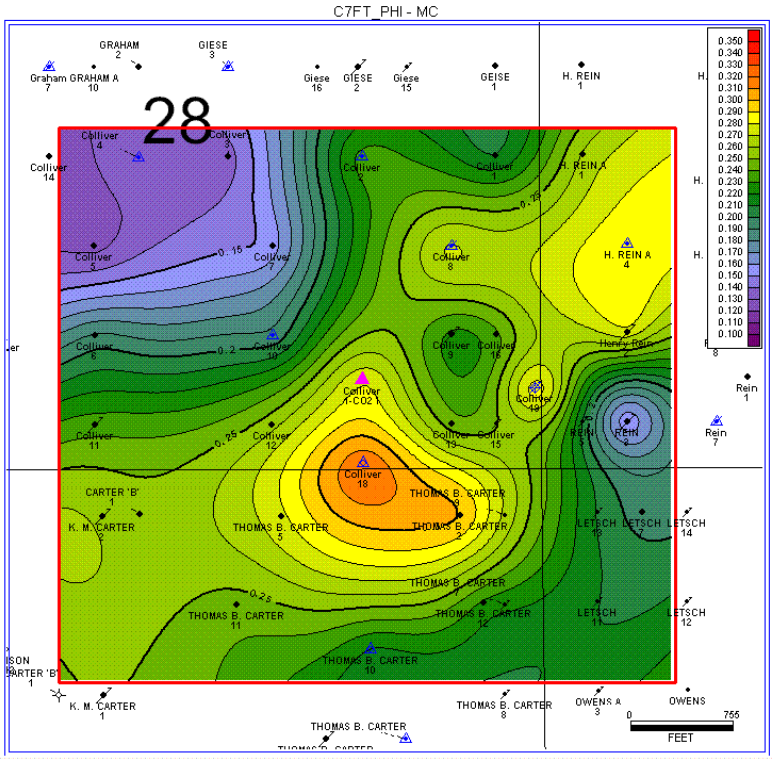

Figure 7.23. Porosity distribution of Layer-7 [37]

7.12. Permeability Distribution

The extreme petrophysical heterogeneity found in carbonate reservoirs is clearly demonstrated by the wide variability observed in porosity-permeability crossplots of core analysis data. In this type of reservoirs, porosity and permeability have little spatial correlation and are widely variable at scale of inches and feet within a rock-fabric facies. [77]. Permeability, in particular, can vary by a factor of 10 or more at a small scale. The Lansing Kansas City (LKC) consisting of a series of alternating deposits of marine limestone and non-marine shale is classified as a carbonate reservoir. Figure 7.24 represents the crossplot of porosity-permeability for all cores in the LKC formation. The wide range of variation of the crossplot shown in Figure 7.24 confirms the fact that the LKC is a carbonate reservoir. It is not accurate to model this wide crossplot by an exponential model described in the previous section, and estimate the permeability at unsampled location. An alternative method for the carbonate reservoirs is to use different crossplot for different rock-fabric facies to obtain the relationship between porosity and permeability [77]. However, it is not possible to apply this method to estimate the permeability distribution in the LKC due to lack of information about the available core data in this formation. In the following section, a new methodology is proposed to find different porosity-permeability crossplots for different regions of the LKC formation, specifically, the CO_2 pilot area in the Hall-Gurney Field.

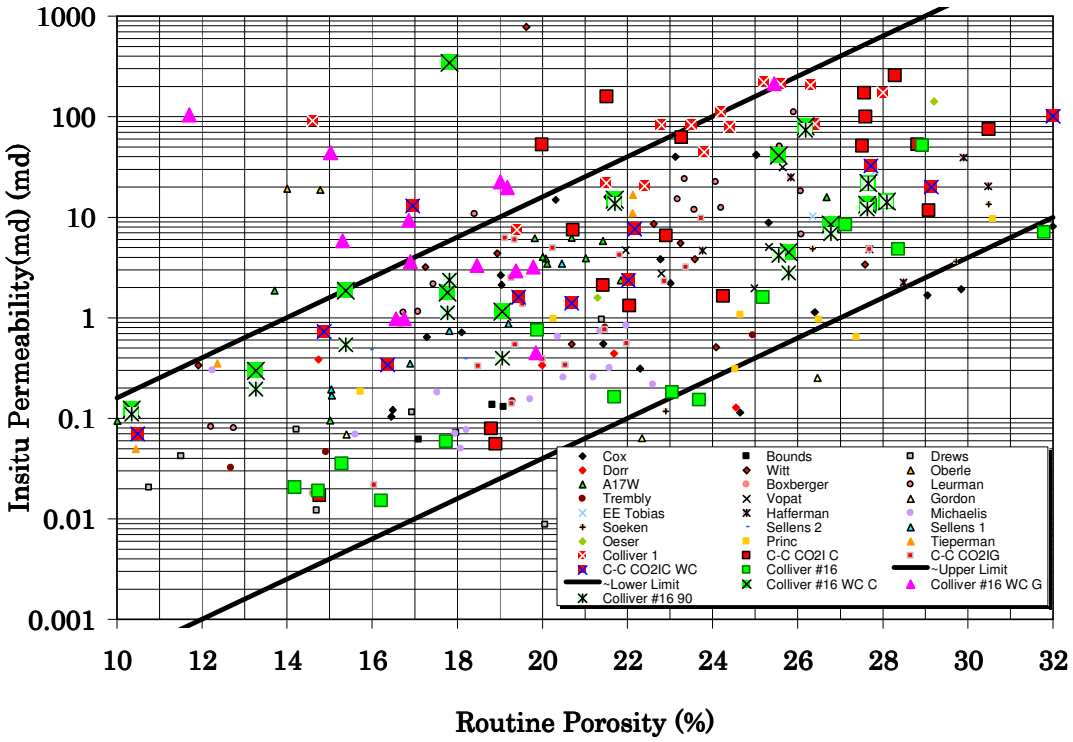

Figure 7.24. The crossplot of k-Φ for all cores in the LKC formation [75]

7.12.1. First Hypothesis: Same slope for all crossplots

The new methodology was proposed based on two hypotheses. The first hypothesis was drawn from permeability-porosity crossplot of the core samples in the LKC formation (Figure 7.24). The porosity-permeability crossplot of all core samples, shown in Figure 7.24, are bounded between two lines with approximately same slopes. However, lines do not have similar (equal) intercepts with the vertical axis. The methodology hypothesis predicts that the permeability-porosity crossplots of all core samples obtained from different facies or regions in the LKC formation have the same slope as the upper and lower boundary lines. The distinction between different crossplots

is the intercept with the vertical axis. The intercept values of crossplots can be calculated using the second hypothesis which is described in the following section

7.12.2. Second Hypothesis: Incorporation of well test data

The effective permeability calculated by a well-test analysis is based on a classical analytical solution to the diffusivity equation. The solution is based on the assumption that the reservoir is homogeneous; however, no reservoir is homogeneous. For practical purpose, the assumption is the permeability determined by a well-test analysis is an effective permeability representing some average within a radius of investigation or drainage radius influenced by production or injection well. There are some investigators in the literature trying to find an answer for what kind of average well-test derived permeability represent and over what region of the reservoir, this average is valid [35] [67] [68] [72]. The definition of effective well-test permeability becomes more complicated when dealing with multilayer heterogeneous reservoir.

Under second hypothesis, the effective or average permeability (kh_{ave}) derived from well test analysis is approximated by the average of permeability values (kh) at well locations of the different layers. Mathematically, it is defined as:

$$kh_{ave} = \sum_{i=1}^{n} (kh)_i \tag{7.6}$$

where n is the number of layers of the reservoir model.

7.12.3. Proposed Methodology

A new methodology was proposed to estimate the permeability distribution of the CO_2 pilot area. This methodology was founded based on the two hypotheses described above and porosity values at well location at different depths. From $k-\Phi$ crossplot, the relationship between porosity and permeability can be modeled as:

$$k = ae^{b\phi} \tag{7.7}$$

where *a* and *b* are the slope and intercept From $k-\Phi$ crossplot respectively. Considering the first hypothesis, the slope *a* is known for all crossplots. Using Eq.(7.7), Eq.(7.6) can be written as:

$$kh_{ave} = \sum_{i=1}^{n} [(ae^{b\phi})h]_i \tag{7.8}$$

Eq.(7.8) can be numerically solved to calculate the unknown intercept *b* of the $k-\Phi$ crossplot by knowing the porosity vs. depth at well location and the average permeability derived from well-test analysis.

The porosity data versus depth were obtained from well-log analysis for 11 wells in *C* zone of the CO_2 pilot area. Figure 7.25 displays a 3D-view of the location of these wells in the pilot area. Also, the well-test average permeability is available for Colliver-18 and CO2I-1. The average permeability of the other wells of the pilot area was assumed to be the average permeability at well locations of the previous geological model. Knowing these data and considering the same slope for the $k-\Phi$ crossplot for each well, Eq.(7.8) was solved for each well to find the unknown intercept *b* of the $k-\Phi$ crossplot. Then, the exponential model in Eq.(7.7) was used to estimate the permeability values

versus depth (Layer) for each well in the pilot area. The *Goal Seek* in in *Microsoft Excel* package was used to numerically solve Eq.(7.8).

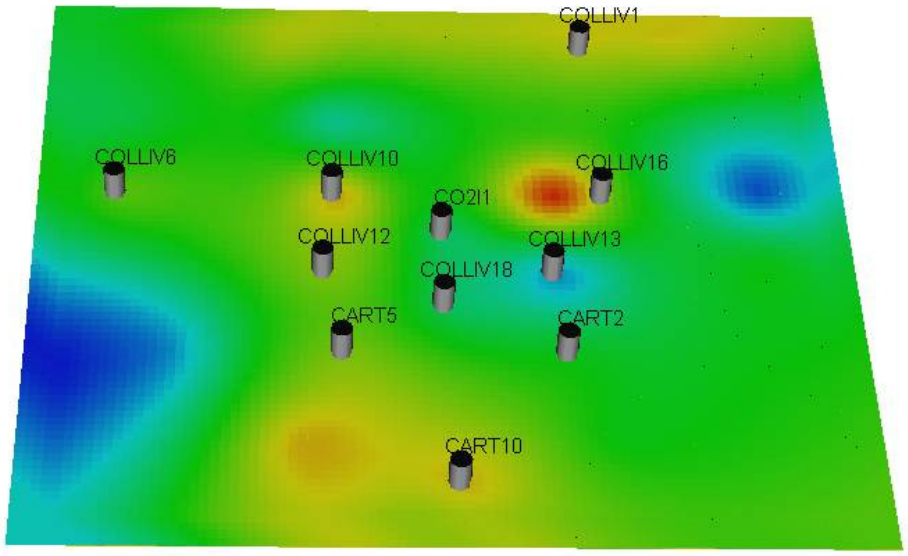

Figure 7.25. The 3D-view of the location of the wells in the CO_2 pilot area

Table 7.8 lists the intercepts of k-Φ crossplot for the eleven wells in the CO_2 pilot area. Tables 7.9 and 7.10 present the *Microsoft Excel* spreadsheet layout used to calculate the intercept and permeability versus depth for wells Colliver-18 and CO2I-1.

Table 7.8. Intercept of k-Φ crossplot

Well	Intercept
Colliver1	-3.4904
Colliver6	-2.1314
Colliver10	-3.2497
Colliver12	-4.0308
Colliver13	-3.9804
Coliiver16	-3.7524
Colliver18	-4.774
CO2I-1	-4.2596
Carter10	-3.4686
Carter5	-3.8221
Carter2	-4.3809

Table 7.9. The Excel Spreadsheet for estimating the intercept of crossplot for Colliver-18

Exponential Form $k = ae^{b\phi}$

Intercept -4.77405

Slope 0.2222

Ave. kh 995

Depth,ft (Layer)	*Φ*	*log k*	*k*	*Kh*
1	14	-1.66325	0.021715	0.021715
2	25	0.780953	6.038829	6.038829
3	30	1.891953	77.97452	77.97452
4	31	2.114153	130.0627	130.0627
5	31	2.114153	130.0627	130.0627
6	32	2.336353	216.9465	216.9465
7	32	2.336353	216.9465	216.9465
8	32	2.336353	216.9465	216.9465

$$\sum_{i=1}^{8}(kh)_i = 995$$

Table 7.10. The Excel Spreadsheet for estimating the intercept of crossplot for CO2I-1

Exponential Form $k = ae^{b\phi}$

Intercept -4.61202

Slope 0.2222

Ave. kh 442

Depth,ft (Layer)	*Φ*	*log k*	*k*	*Kh*
1	14	1.6632473	0.0217146	0.0217146
2	26	1.0031527	10.072858	10.072858
3	29	1.6697527	46.746888	46.746888
4	30	1.8919527	77.974518	77.974518
5	30	1.8919527	77.974518	77.974518
6	29	1.6697527	46.746888	46.746888
7	28	1.4475527	28.025457	28.025457
8	27	1.2253527	16.80168	16.80168

$$\sum_{i=1}^{8}(kh)_i = 442$$

Then, the experimental semivariogram of the logarithm of permeability for the all layers in the *C-zone* were calculated and fitted with mathematical models. Finally, similar to porosity estimation, ordinary kriging technique was used to estimate the permeability values of the inter-well grids. Figure 7.26 and Figure 7.27 show the permeability distribution of the layers 1 and 7 of the 8-layer models.

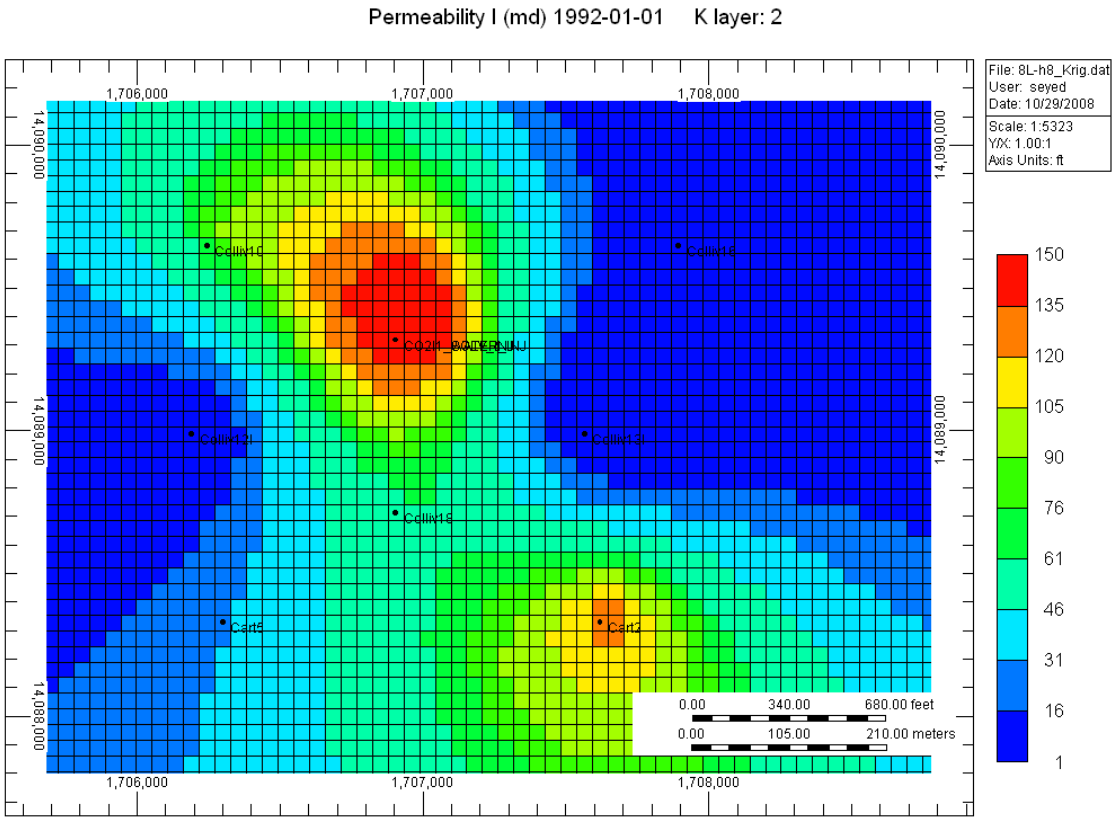

Figure 7.26. Permeability map for the Layer-1 of the 8-layer model.

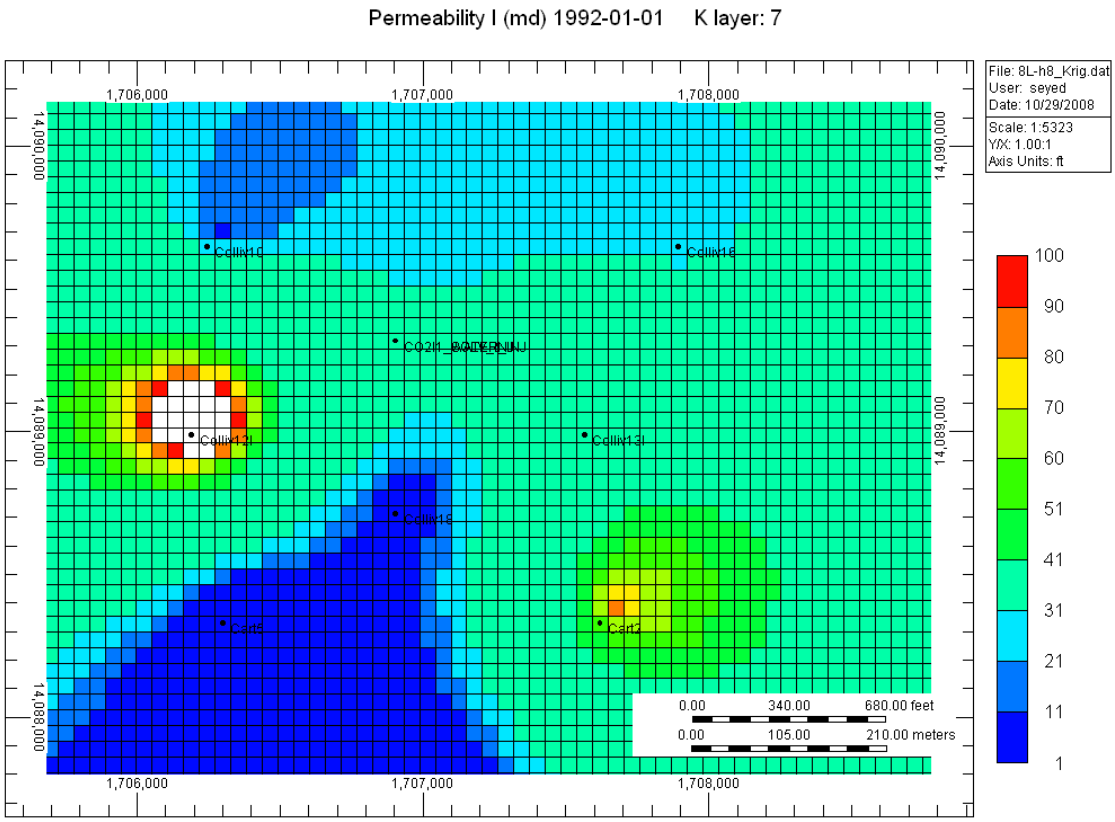

Figure 7.27. Permeability map for the Layer-7 of the 8-layer model

7.13. Discriminant Analysis for Permeability and Porosity Distribution

Discriminant analysis covers a wide range of techniques aimed at the classification of unknown samples to one of several possible groups or classes. Classical discriminant analysis has the main focus of attempting to develop a linear equation that best differentiates between two different classes. The model is established based on a set of observations for which the classes are known. These observations are called training set.

The 11 porosity and permeability samples of different layers in the CO_2 pilot area were considered as the training set. The purpose of this analysis is examination of

layering the geological model based on the porosity and permeability samples. In other word, the possibility that the different layers originated from different geological facies was examined by discriminant function analysis. The discriminant function analysis was performed for the adjacent layers (1&2, 3&4, 5&6, 7&8).

The discriminant function analysis was performed for the adjacent layers (1 and 2, 3 and 4, 5 and 6, 7 and 8) by the available tool implemented in the MATLAB package. Table 7.11 represents the results of discriminant function analysis for the layers 1 and 2 based on the porosity and permeability samples. For each sample in Table 7.11, a discriminant score was assigned based on this analysis. Also, the discriminant score index was calculated and shown at the bottom of Table 7.11. The discriminant index is a number that represent the boundary between two classes or populations.

If the discriminant scores for both classes (layers) were simultaneously plotted, the discriminant index will show the border; otherwise, the two groups under study cannot be separable. Figure 7.28 show the discriminant function analysis for layers 1&2. The blue triangle and gray square legends represent the discriminant scores for samples in the layers 1 and 2 respectively. The discriminant index score is shown by a red line. The discriminant index score in Figure 7.28 does not represent the border between the scores of the samples of the two layers. This indicated that the samples of the two layers may not be obtained from two geological facies. The same results were obtained by repeating the discriminant analysis for the other adjacent layers described above. More geological information is required to improve the accuracy of this type of analysis.

Table 7.11. Discriminant function analysis for layers 1&2

Sample No.	Φ	k(md)	Discriminant score	Layer
1	0.0597	1.5	-0.01635422	Leyer-1
2	0.0785	23.1	-0.02152559	
3	0.0874	56.2	-0.02398295	
4	0.1236	44	-0.03411338	
5	0.1435	145	-0.03988534	
6	0.1446	113	-0.04021211	
7	0.155	88	-0.04335893	
8	0.1655	32	-0.04667337	
9	0.1702	42	-0.04821717	
10	0.1748	78	-0.04977348	
11	0.1763	50	-0.05029197	
12	0.0328	2.3	-0.00897971	Layer-2
13	0.0999	5.9	-0.02745023	
14	0.1019	16	-0.02800727	
15	0.1252	38	-0.03456968	
16	0.1606	50	-0.04510606	
17	0.1686	91	-0.04768675	
18	0.1787	58	-0.051134	
19	0.184	83	-0.05305402	
20	0.1881	57	-0.05460506	
21	0.2013	64	-0.06011061	
22	0.2127	95	-0.06575389	

Discriminant Score Index=-0.039651

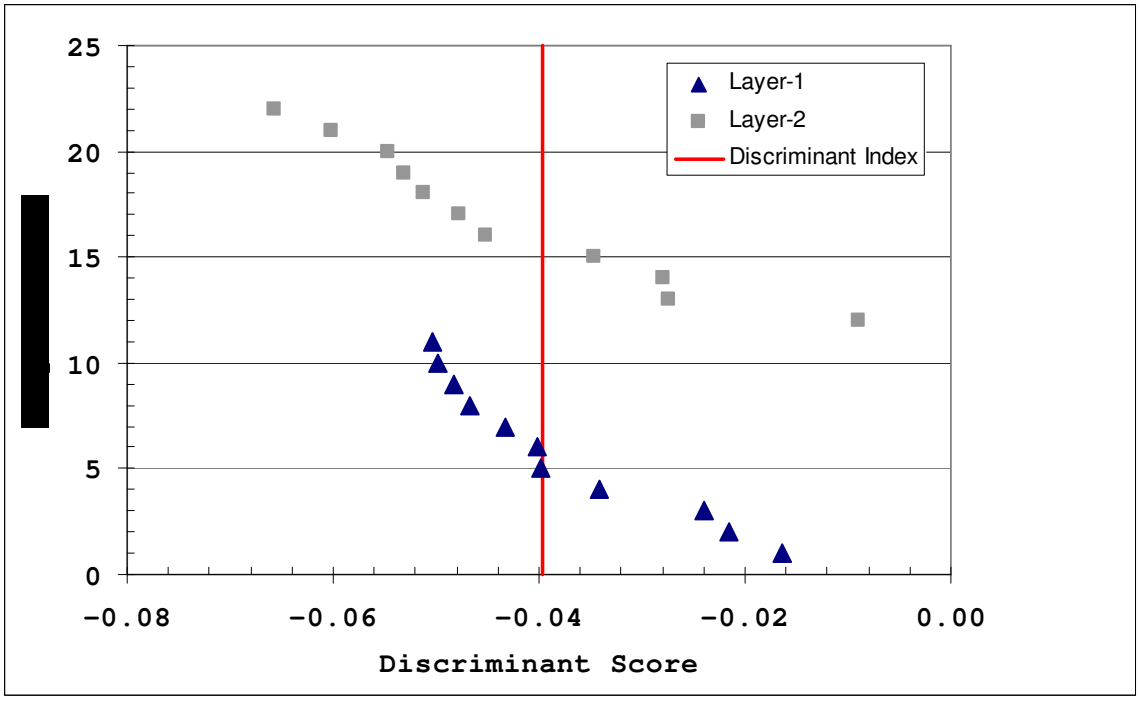

Figure 7.28. Discriminant function analysis for layers 1&2

Chapter 8

The Flow Simulation Results

The permeability and porosity distribution of that estimated in the previous sections was used as input for the flow simulation of the 8-layer model. The simulation time started on January 1, 1992 after waterflooding where the reservoir contains residual dead oil and water. Flow simulations in this research have been performed using Computer Modeling Group (CMG) reservoir simulator. The oil obtained from a nearby lease (Letsch) in 2000 was used to generate PVT properties for the reservoir simulator. The relative permeability for the oil-water system is given in Figure 8.1. Additional information pertaining to the 2-D reservoir model used for this study is given in Table 8.1. The simulation was terminated on January 31, 2006.

Figures 8.2 through Figure 8.8 show the comparison of the true bottom hole pressure (BHP) of the CO_2 pilot and those obtained from reservoir simulator for the field activities prior and during CO_2 flooding.

The match between the simulation results and field data is reasonable for Colliver 10, Colliver 18, and CO2I-1 because the BHP is constrained in these wells. Historical injection rate data for Colliver 10 were not available. . The constraint for Colliver 18, CO2I-1 in some periods switched from BHP to injection rate constraint. There is not enough injection rate data to compare with simulation results. Colliver 12 and Colliver 12 were constrained to the water production rate in the simulation model. Figure 8-2 shows BHP results for Colliver 13. The figure indicates that the simulation model under-

predicted BHP for Colliver 13 in comparison to the field data. One possible interpretation is that the permeability value at well location in the model is lower than the true value. Figure 8.3 shows that the model over-predicted BHP for Colliver 12 especially after the start of injection in CO2I-1 in 2003. The results indicate that permeability values at grid blocks surrounding Colliver 12 is higher than true values.

The match between the simulation and field data for Cart 2 and Cart 5 is shown in Figures 8.7 and 8.8. Cart 2 and Cart 5 were constrained to 10 bbl/day water production rate until both wells were shut in on January 1, 2003. Then, Cart 5 was reopened in December 28, 2004 and constrained to well BHP. The match between the simulation and field data is not acceptable. The mismatch could be explained by inspecting the permeability distribution around these wells. Figure 8.8 shows that the simulated BHP for Cart 5 is higher than the true field data indicating that permeability value of the grid blocks around this well is high. Figure 8.9 and Figure 8.10 show the comparison of the true daily oil production of the wells(Colliver 12 and 13) and those obtained from reservoir simulator during CO_2 flooding period. Both well were constrained to water production rate within this period. Simulation model under-predicted the oil production rate for both wells during the course of CO2 flooding. This indicates that connectivity between CO2I-1 and the production wells appears to be more tortuous than modeled in the simulation. In general, results indicate that the pilot area is more heterogeneous than represented in the reservoir model. The reservoir heterogeneity in the CO_2 pilot area is too high to be modeled by the proposed methodology.

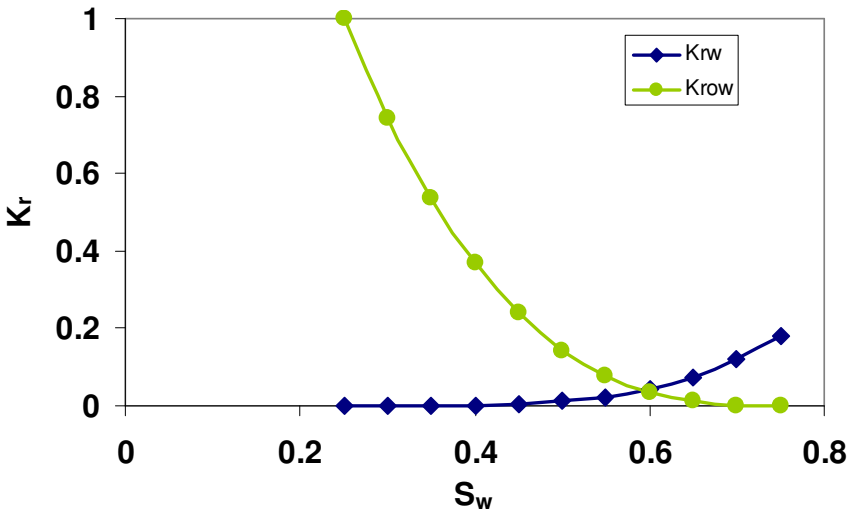

Figure 8.1. Oil-water relative permeability data set used in the flow simulator

Table 8.1. Model specifications for flow simulator

Reservoir Dimension	90 x 82
Dimension of each cell	55ft x 55 ft
Number of layers	8
Thickness of layer	1 ft
Fluid Viscosities	Water(0.7179 cp)
Water Density	69.26 lb/ft^3
Oil Density	51.26 lb/ft^3
Rock Compressibility	3.2E-6 $x10^{-6}$/psi
Equilibrium conditions	500psi@2900 ft
Constant initial water saturation	0.3
Bubble Point Pressure	6 psi

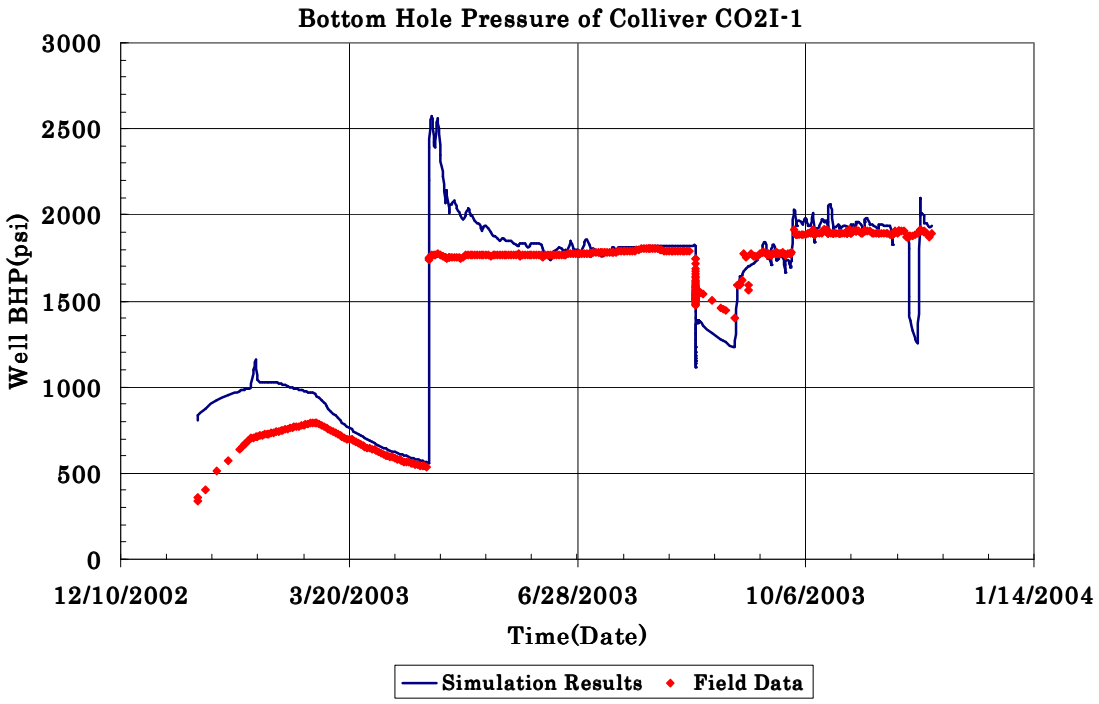

Figure 8.2. Comparison of the simulation results and field data for Colliver 13

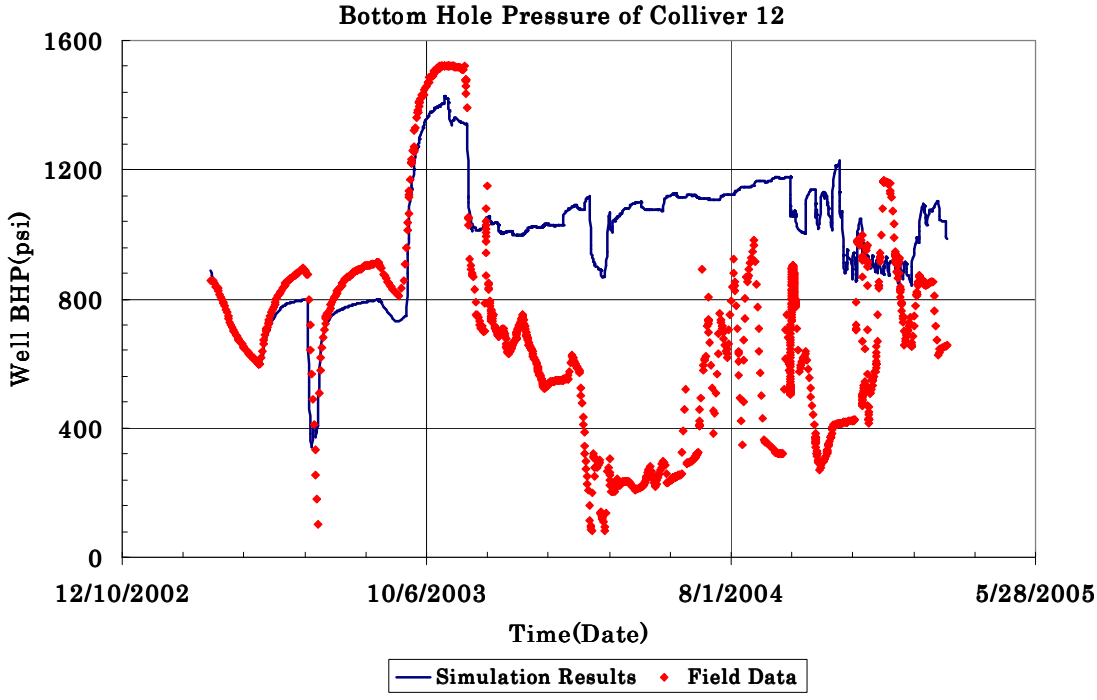

Figure 8.3. Comparison of the simulation results and field data for Colliver 12

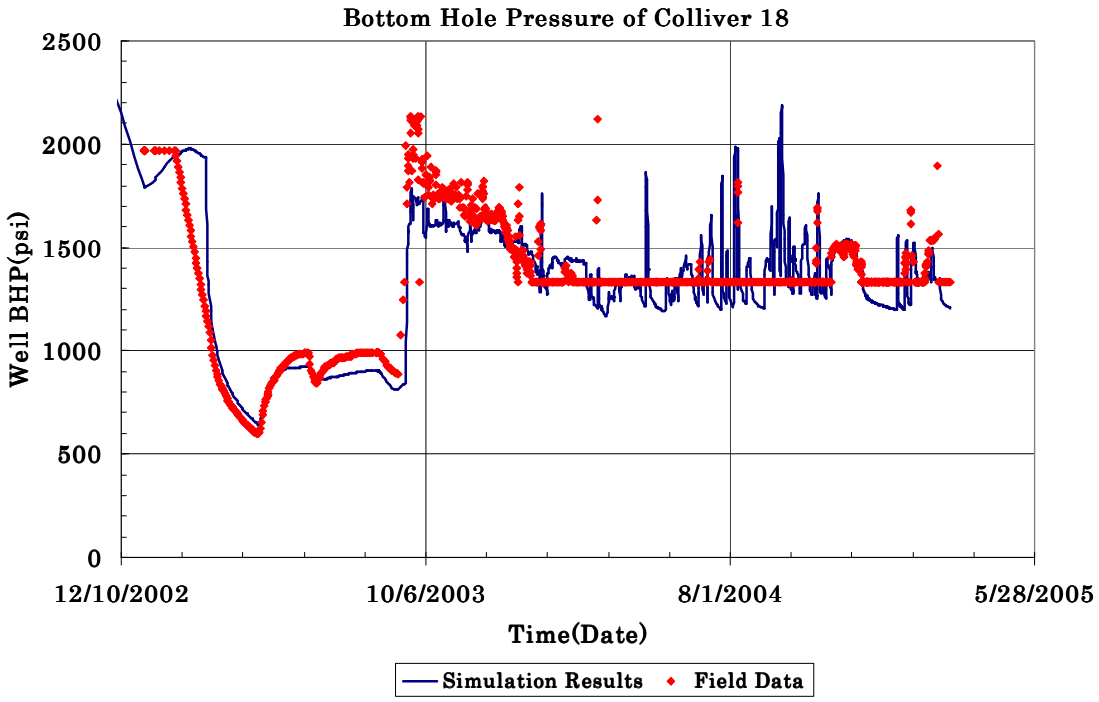

Figure 8.4. Comparison of the simulation results and field data for Colliver 18

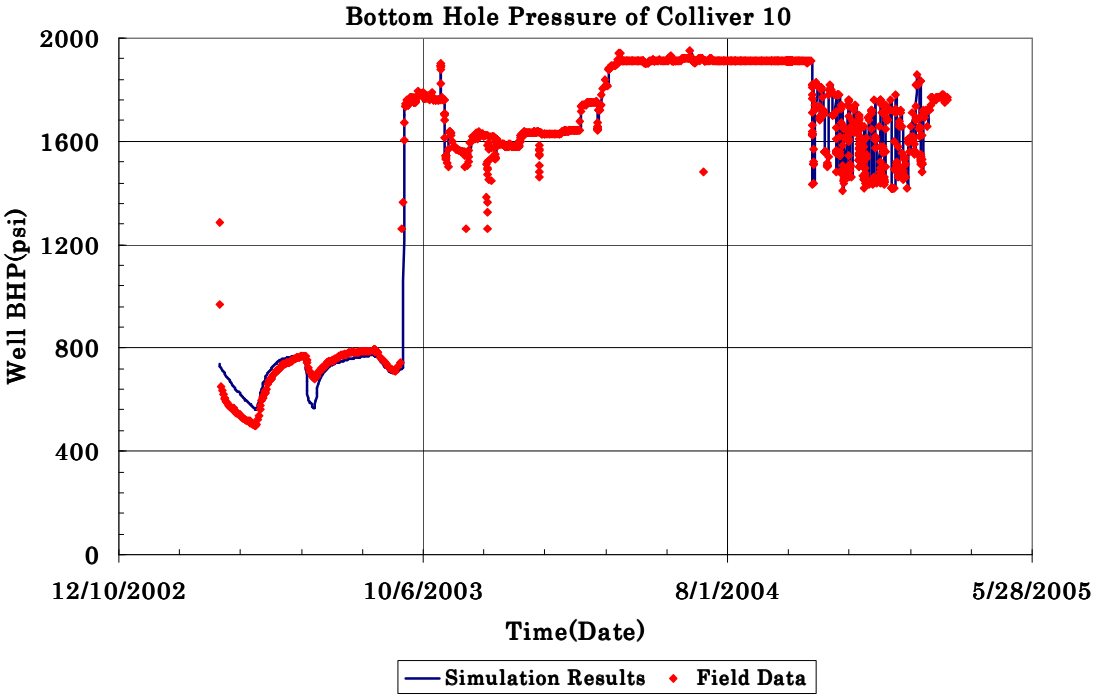

Figure 8.5. Comparison of the simulation results and field data for Colliver 10

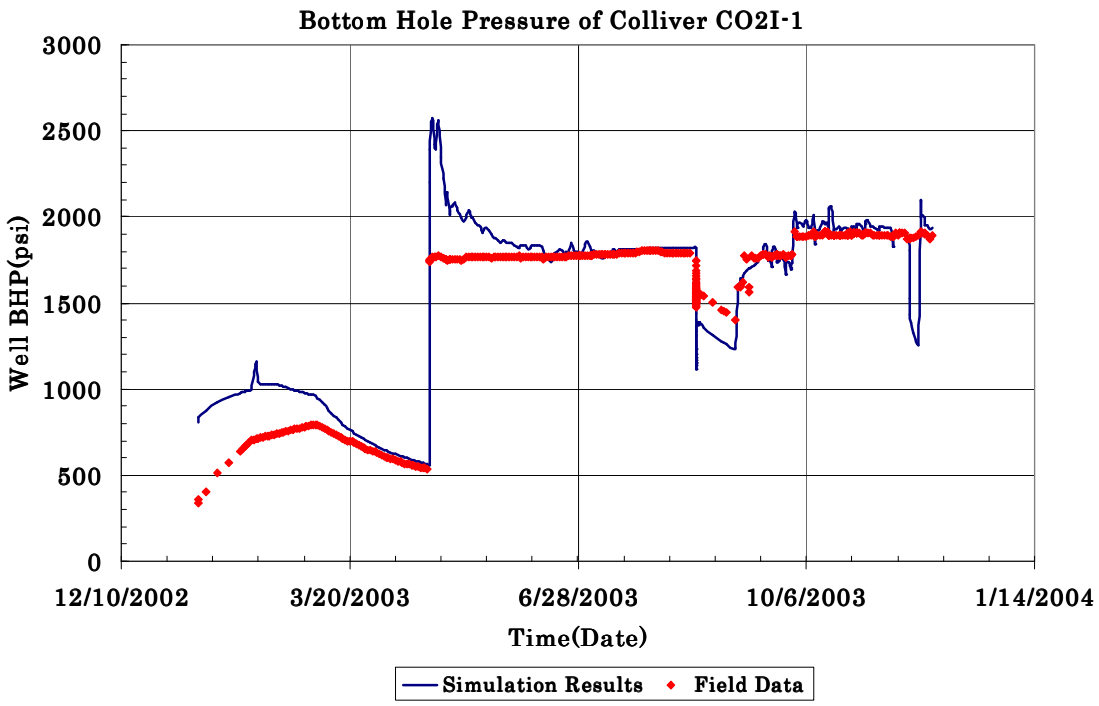

Figure 8.6. Comparison of the simulation results and field data for CO2I-1

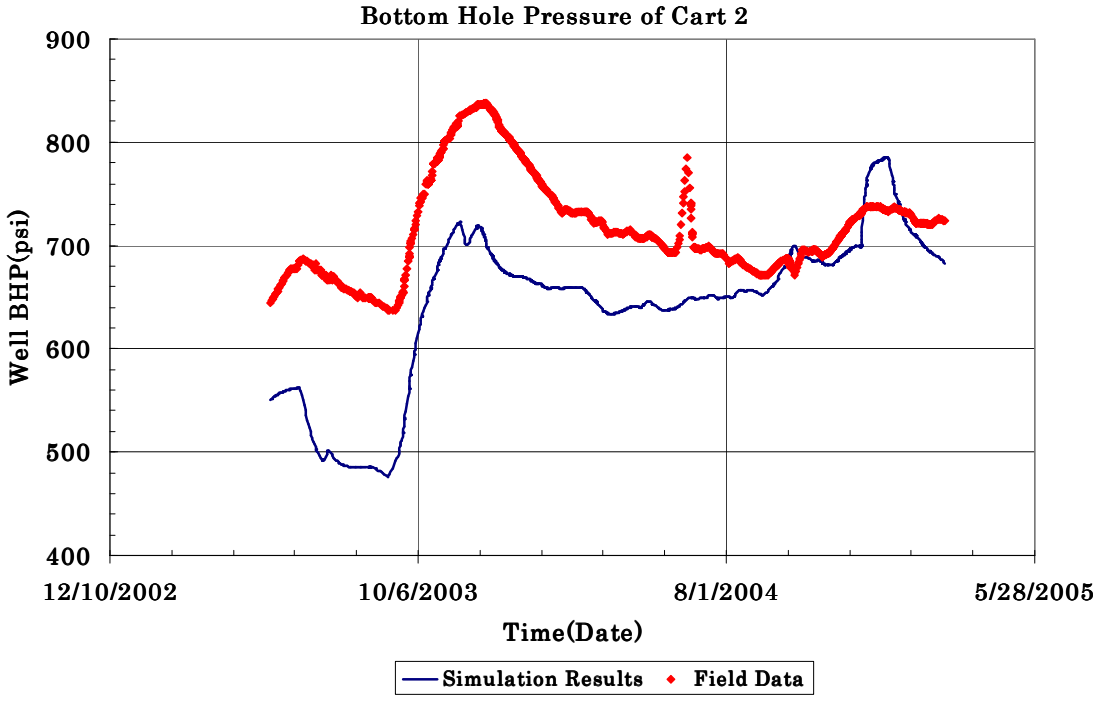

Figure 8.7. Comparison of the simulation results and field data for Cart 2

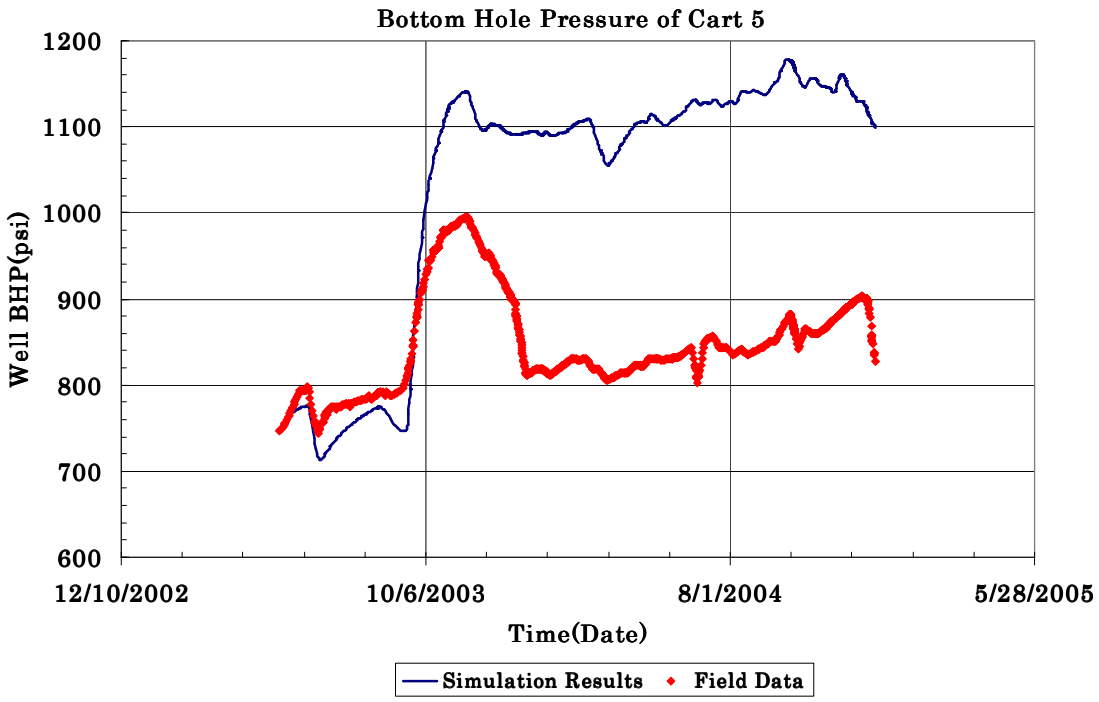

Figure 8.8. Comparison of the simulation results and field data for Cart 5

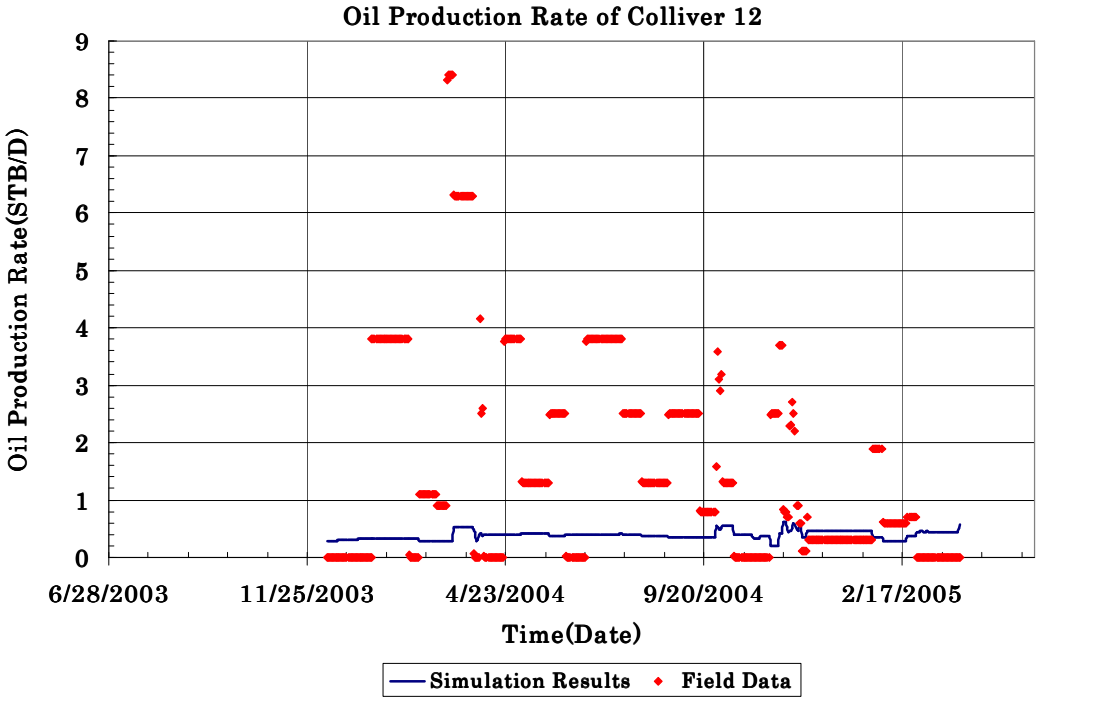

Figure 8.9. Comparison of the simulation results and field Oil Production for Colliver 12

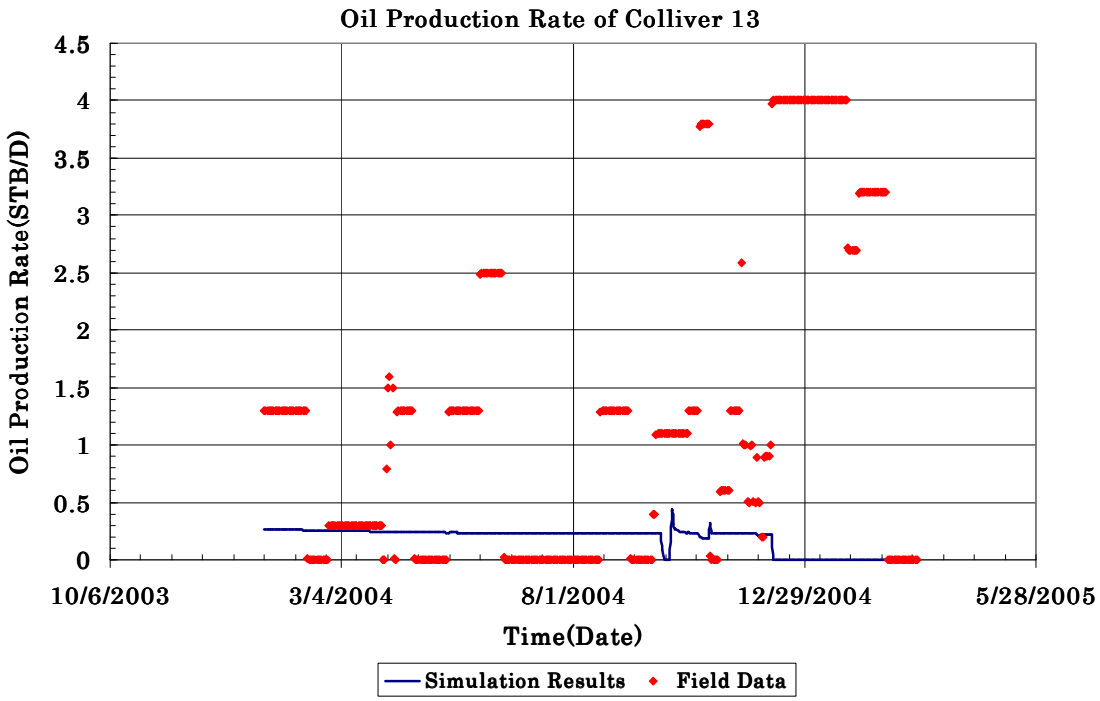

Figure 8.10. Comparison of the simulation results and field Oil Production for Colliver 13

Chapter 9

Conclusions

1. The 8-layer geological model was constructed on the basis of the well-log data and one-foot thickness for the CO_2 pilot area in the Hall-Gurney field. The statistical ANOVA, *t-test,* and *F-test* were performed for the porosity data of the eight layers in order to investigate if these data comes from the same population of porosity data. The results revealed that the porosity data in eight layers sampled from different populations. The results of these statistical tests confirmed the number of layers in the reservoir.

2. Ordinary kriging was used to estimate the porosity distribution at unsampled location in all eight layers of the CO_2 pilot area using the 25 porosity samples.

3. The new methodology was proposed for estimation of permeability distribution based on two hypotheses. The first methodology hypothesis predicts that the permeability-porosity crossplots of all core samples obtained from different facies or regions in the LKC formation have the same slope as the upper and lower boundary lines. Under second hypothesis, the effective or average permeability derived from well test analysis is approximated by the average of permeability values at well locations of the different layers.

4. Permeability values at well location in each layer of the CO_2 pilot area were estimated using porosity data versus depth at well location and the well test average permeability data. Ordinary kriging was used to calculate the horizontal permeability distribution in each layer assuming permeability is log-normally distributed.

5. The classical discriminant analysis was performed using porosity and permeability samples of each layer to investigate the layering of the geological model of the CO_2 Pilot area. The result of this analysis indicates that the porosity and permeability samples of the two different layers were obtained from the same geological population(unit). The result of this confirmed the result of the statistical ANOVA test carried out on the samples of the eight layers.

6. The permeability and porosity distribution of that estimated using proposed method was used as input for the flow simulation of the 8-layer model. The results were compared in terms of the bottom hole pressure of the wells and daily oil rate of the production wells in the CO_2 pilot area. The results of this study indicate that the pilot area is more heterogeneous than represented in the proposed model.

Part III

Chapter 10

Introduction

Flow in a reservoir is mostly controlled by the connectivity of extreme permeabilities (both high and low values). These extreme values linked with geological patterns that create preferential flow paths such as high permeability sand channels. Such structures often have a major influence on the flow behavior of a reservoir. The traditional geostatistics approach for property modeling is based on sequential simulation of facies and petrophysical properties. Practical software implementations of sequential Gaussian simulation (SGSIM) and sequential indicator simulation (SISIM) are widely used for stochastic reservoir modeling. The aim of sequential simulation, as it was originally proposed, is to reproduce the histogram and spatial covariance of the attributes being simulated through the sequential drawing from conditional distributions (ccdfs). A random path sequentially visits each mode of the model and simulated values are drawn from the conditional distribution of the value at that node given the neighboring subsurface data and previously simulated values.

However, these traditional sequential simulation algorithms are limited to reproduction of two-point statistics such as a semivariogram model. These algorithms cannot reproduce complex geological structure. Identification of two-point statistics, even if possible, is not sufficient to allow characterization and reproduction of complex structures such as meandering channels. Consider for example the three images of Figure 10-1 which may correspond to alternative geological representation of a 2D horizontal

section of a fluvial system. These three images have the same proportion of black pixels (28 %). The first image was generated using the two-point indicator simulation algorithm (SISIM) which is limited to the sole reproduction of an input covariance model. The second and third images were generated using object based algorithms (**ellipsim [5] and fluvsim [6]**). Figures 10-2 and 10-3 show the indicator semivariograms of the black facies in the horizontal and vertical directions. Although these images show completely different structures, they have similar indicator semivariograms along the horizontal and vertical directions. Thus, modeling of these complex structures requires multiple-scale, multiple-point correlations beyond the reach of the two-point correlation provided by a semivariogram model.

Srivastava [12] and Guardiano and Srivastava [11] introduced the concept of training image as a replacement of the variogram within an extended sequential simulation framework. This concept of training image led to development of multiple-point simulation (MPS) and geostatistics. Multiple-point geostatistics considers the training image as the random function model directly providing a quantification of the heterogeneities that the geologist believes to exist in the reservoir. Training images as used by MPS reflect a prior geological concept. They are not required to be conditioned to any local data. The introduction of MPS has improved the ability of geostatistical modeling to better reproduce the complex heterogeneity of a geological deposition.

An alternative approach in multiple-point simulation is to redefine the problem as a direct image construction. In this approach direct construction of image patterns is used

instead of inferred training image conditional probabilities. The image construction relies on the concept of similarity of available data and the patterns of a training image. Similarity distance function is used to find the most consistent and similar pattern for the existing data. This part of the dissertation presents a mathematical improvement to the existing similarity function used in a sequential simulation algorithm (SIMPAT, SIMulation with PATerns [1]).

Chapter 11 reviews the relevant literature and the original MPS idea. Also, this chapter introduces the image construction approach as the basis of the reservoir modeling approach proposed in this dissertation.

Chapter 12 presents the details of the SIMPAT algorithm. First, the single-grid unconditional algorithm is reviewed using a simple, binary (sand/non-sand) training image. Fundamental concepts such as patterns, data events, and similarity are discussed and a formal notation to represent these concepts is introduced. Chapter 13 introduces the proposed similarity distance, the Normalized Cross Correlations (NCC), for modification of the SIMPAT algorithm. The results of application of the proposed techniques are demonstrated by case studies in Chapter 14. The last chapter covers the conclusion of the investigation.

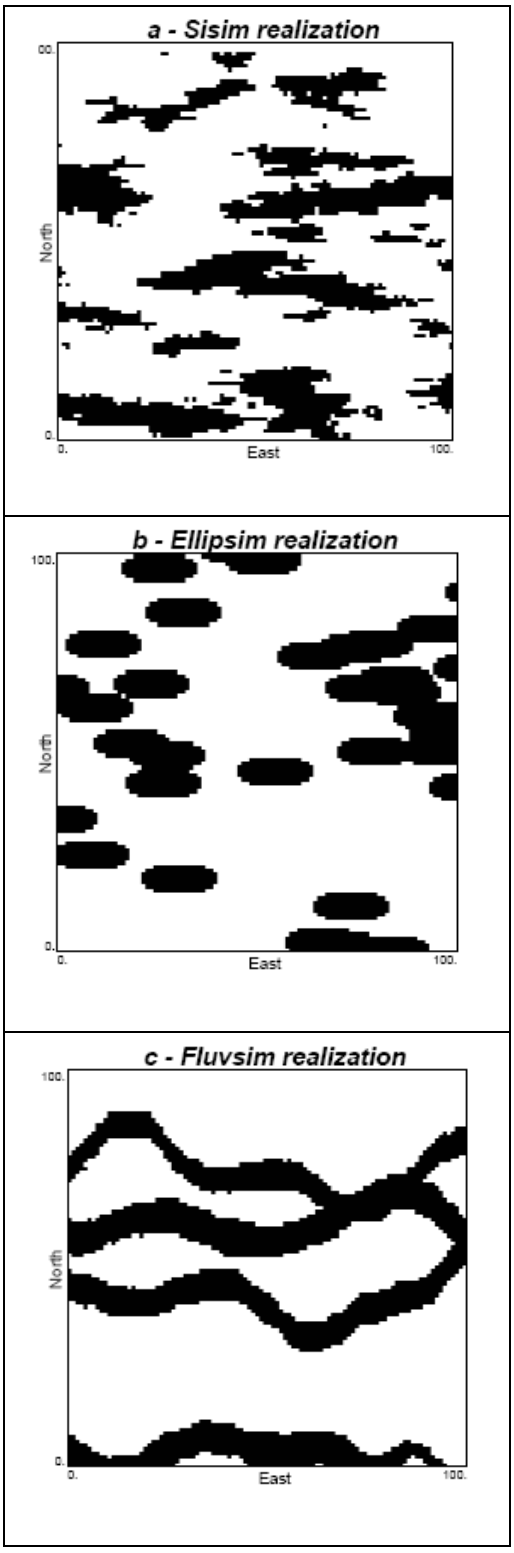

Figure 10-1. Stochastic realizations with same proportions of black pixels (28 %) [17]

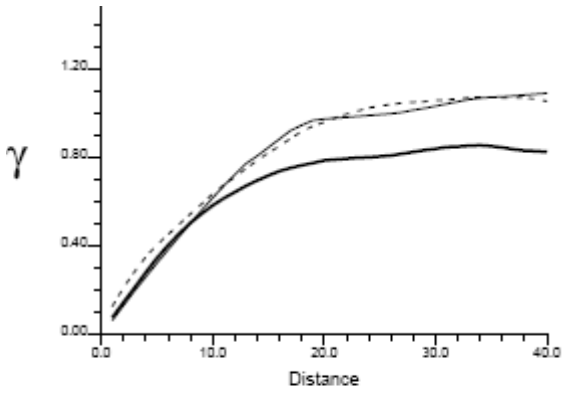

Figure 10-2. Semivariograms in horizontal direction for **sisim**(dashed line), **elipsim**(thin line), and **fluvsim**(thick line) realizations [17]

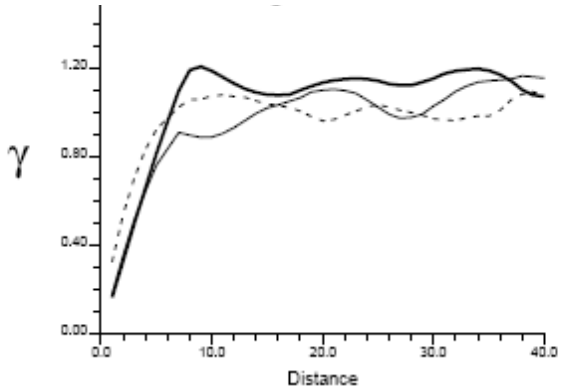

Figure 10-3. Semivariograms in vertical direction for **sisim**(dashed line), **elipsim**(thin line), and **fluvsim**(thick line) realizations [17]

Chapter 11

Background on Multiple-point (MP) Geostatistics

11.1. Background

This section briefly reviews the fundamentals of multi-point geostatistics that are essential in understanding this study. For the deeper understanding of subject matter and the mathematics behind it, however, readers are referred to the existing literature.

11.1.1. Multi-point (MP) Statistics and Connectivity Function

Most practical applications of the theory of random functions do not consider multiple-point commutative distribution function (cdf) beyond the two-point cdf. The principal reason is that inference of the multiple-point cdfs is usually not practical. Random function models have not been developed that explicitly account for multiple-point (MP) statistics. Some terminology needs to be introduced in order to define MP statistics.

Consider an attribute S such as permeability taking K possible states $\{s_k, k = 1,..., K\}$. S can be a categorical variable or a continuous variable with its interval of variability discretized into K classes by *(K-1)* threshold values. The indicator transform of the categorical variable S at location $\mathbf{u}$ is defined as:

$$I(\mathbf{u}, k) = \begin{cases} 1 \;\; if \;\; S(\mathbf{u}) = s_k \\ 0 \;\; if \;\; not \end{cases} \qquad (11\text{-}1)$$

Similarly, for a continuous variable discretizing into *K-1* threshold, indicator transforms for each threshold is defined as:

$$I(\mathbf{u},k)=\begin{cases}1 \;\; if \;\; S(\mathbf{u}) \le s_k \\ 0 \;\; if \;\; S(\mathbf{u}) > s_k\end{cases} \tag{11-2}$$

The probability that two values separated by a vector **h** are jointly in the state s_k is defined as:

$$\Phi(\mathbf{h};k)=E\{I(\mathbf{u};k).I(\mathbf{u}+\mathbf{h};k)\} \tag{11-3}$$

$\Phi(\mathbf{h};k)$ is called a two-point non-centered indicator covariance. This quantity is usually modeled to perform traditional indicator kriging/ simulation.

Consider now a data template τ_n defined by *n* separation vectors $\mathbf{h}_1,\ldots,\mathbf{h}_n$. Figure 11-1 shows examples of 1, 2, 3, 4, and 9-point configurations. The probability that the *n* values $s(\mathbf{u}+\mathbf{h_1}),\ldots, s(\mathbf{u}+\mathbf{h_n})$ are jointly in the state s_k is defined as

$$\Phi(\mathbf{h}_1,...,\mathbf{h}_n;k)=E\{\prod_{\alpha=1}^{n} I(\mathbf{u}+\mathbf{h}_\alpha;k)\} \tag{11-4}$$

where $\Phi(\mathbf{h}_1,...,\mathbf{h}_n;k)$ is the multiple-point non-centered indicator covariance or connectivity function defined by *n* lag separation vectors $\mathbf{h}_1,\ldots,\mathbf{h}_n$. According to this definition, MP statistics moment or connectivity function is the mean of product of the *n* indicator variables at different locations of the template τ_n.

The probability that the *n* values $s(\mathbf{u}+\mathbf{h_1}),\ldots, s(\mathbf{u}+\mathbf{h_n})$ are jointly in the respective states $s_{k_1},...s_{k_n}$ is called multiple-point non-centered indicator cross-covariance and is defined as:

$$\Phi(\mathbf{h}_1,...,\mathbf{h}_n;k_1,...,k_n) = E\{\prod_{\alpha=1}^{n} I(\mathbf{u}+\mathbf{h}_\alpha;k_\alpha)\} \tag{11-5}$$

The collection of all direct and cross non-centered indicator covariances identifies the MP statistics. These statistics could be estimated using training images that will be explained in the following section.

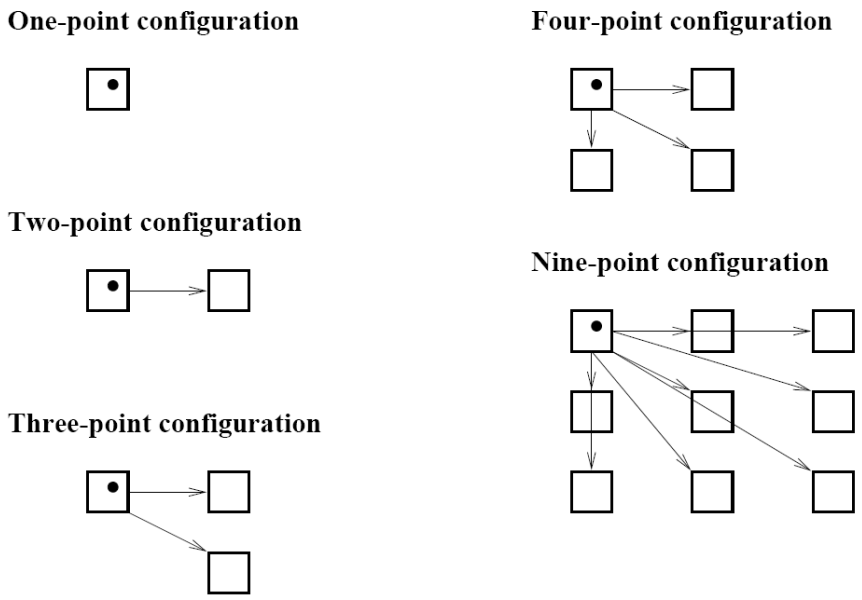

Figure 11-1. Examples of 1, 2, 3, 4, and 9-point configurations [1]

11.1.2. Training Images

The multiple-point correlation models required by multiple-point geostatistics methods are typically generated using a training image. The training image specially refers to images that depict in 3D or in a series of 2D sections and are believed to be the geological continuity of the reservoir. Training images depict the type of heterogeneities that geologist expect to be present in actual subsurface reservoir. They are required to carry any locally accurate information on the actual reservoir. Training images merely are based on an assumed realization that reflects prior geological and structural concepts. Rewrite-this does not make sense. Thus, a training image could be an unconditional realizations generated by an object-based algorithm, or a simulated realizations of a reservoir analogue, or simply a geologist's sketch processed with CAD algorithms and properly digitized. In current practices, training images are almost generated using conditional object-based [6] [7] [8] [9] or processed-based simulations [10].Some training images examples are shown in Figure 11-2.

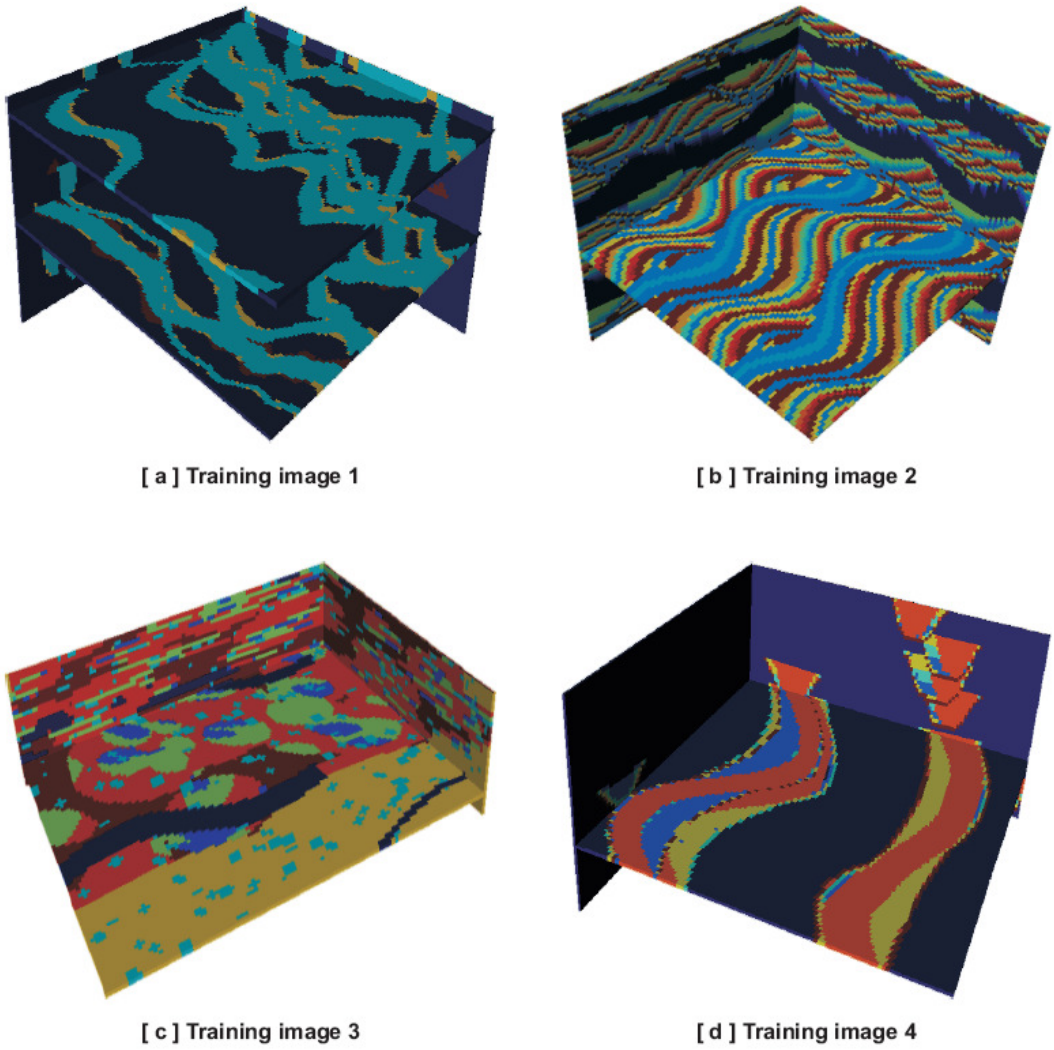

Figure 11-2. Examples of training images. All images generated using unconditional object-based or processed-based modeling tools [1]

11.1.3. Literature Review

Farmer [13] used simulated annealing technique to reproduce a few specific multiple-point statistics previously modeled from a training image. In this approach, higher order, multiple-point statistics are used as explicit constraints that each realization must honor through an objective function. The drawback of simulated annealing is that very few statistics can be simultaneously considered as such constraints. Simulated annealing, also, suffers from convergence problems due to difficulty of choosing the correct set of annealing parameters such as an efficient cooling schedule.

Guardiano and Srinavasa [11] proposed a novel algorithm that uses training images for introducing multiple-statistics into stochastic simulation. The approach follows the extended sequential simulation framework and has a remarkably simple underlying idea. At each unsampled grid, the local conditional probability is inferred by scanning the training image for replicates of the data event. The node is then simulated using this ccdf and considered as conditioning data for the rest of simulation process. Since the conditioning data configuration is allowed to vary, the simulation is direct and avoids the convergence issues of iterative algorithms.

Tjelmeland [14] proposed a new method based on Markov random field to obtain MP statistics. Although this technique was theoretically established, it is iterative and extremely CPU demanding, and may not converge satisfactorily, and, thus far has not been proved to be practical for 3D applications. Caers and Journel [15] and Caers et al. [16] applied artificial neural networks (ANN) to model multiple-point statistics inferred

from a training image. This algorithm produced good results. However, it is iterative in nature and CPU-demanding. Furthermore, issues related to the neural network architecture make it difficult to tune.

Strebelle [17] proposed Single Normal Equation Simulation (SNESIM). The name of this algorithm implies that it utilizes only a single normal equation when modeling the probability of a facies at a particular grid node. In fact, the single normal equation is the Bayes relation defining a conditional probability. This idea was first originated by Journel [18] who showed the connection between multiple-geostatistics and the extended evaluation of probabilities an extended system of normal (kriging) equations. Strebelle [17] obtained the multiple-point probability using experimental proportions read from the training image instead of modeling the multiple-point statistics from some lower order statistics. Hence, the method eliminates the need to solve a full kriging system; instead, it derives the probability directly from a single normal equation equivalent to the identification of the attribute proportion.

SNESIM scans the training image using a pre-defined data template to extract training image events. For every data event, SNESIM searches for replicates of that event, and then retrieves the corresponding histogram of the central value. For example, in a binary (sand/non-sand) training image, if a data event is found 10 times with 3 out of these 10 replicates yielding a sand central node, SNESIM evaluates the sand conditional probability as 0.3. Once data events and their associated central values are retrieved from the training image, SNESIM stores them in a dynamic data structure called a search tree

[19]. This is opposite to Srivastava's original proposal which called for rescanning the training image for each new data event that is the set of hard and previously simulated values found in the scanning template [12]. The SNESIM algorithm, then, follows the flowchart of a typical sequential simulation algorithm, visiting unsampled nodes using a random path and simulating these nodes conditional on available original data and previously simulated values.

An alternative approach to the sampling strategy of Srivastava [12] and Strebelle [17] is to redefine the problem as a direct image construction problem instead of construction of higher order statistics. The aim is not to explicitly reproduce MP statistics of a training image but to directly reproduce multiple-scale training image patterns in a stochastic manner. Such an image construction task was commonly investigated in computer vision and image processing especially in the field of texture synthesis [21] [22] [23] [24] [25] [4].The image construction approach has one potential advantage. The advantage is that it is less limited by the requirement that is common to all probabilistic methods. This is achieved by completely abandoning the explicit use of probabilities. Image construction algorithms, instead, typically rely on the concept of similarity. Such algorithm construct the final image (realization) based on the similarity of individual data events to training image patterns rather than building form a probability calculated conditional to the data event.

Another advantage of the image construction approach is the ability to capture pattern to pattern relations of a training image. This is opposed to variogram-based

algorithms that capture only point-point correlations. Using pattern to pattern relations (simulating a whole vector of values at a time instead of a single value) is especially important when conditioning to high quality seismic information. Such high quality data typically relate best to patterns in realizations, for example, small piece of a meandering channel.

Arpat [1] investigated the applicability of the image construction approach to reservoir modeling. He developed a practical algorithm (SIMPAT) based on the several image processing concepts such as image similarities. The Manhattan similarity distance is used in the SIMPAT algorithm to assign the most similar and matched pattern in the database to the grid at unsampled location. Modification of the SIMPAT algorithm is the main focus of this part of the dissertation. The following chapter introduces step-by-step an image construction algorithm (SIMAPT) that uses the similarity concept and pattern to pattern relations.

Chapter 12

SIMPAT Algorithm

The SIMPAT algorithm was proposed by Arpat [1]. This algorithm utilizes a stochastic simulation framework that reproduces realizations from a training image. The realization is generated based on the similarity distance criterion. This chapter presents the details of SIMPAT algorithm.

12.1. **SIMPAT Algorithm**

The unconditional SIMPAT algorithm is broken down into the following steps as:

1. The training image is scanned using an arbitrary template **T** to acquire all patterns **ti** in the x and y Cartesian coordinate direction. The template size is smaller than the training image size.

2. The patterns are collected and stored in a database. They are denoted as Pat_T^k, where k represents the pattern number, and **T** represents the pattern size (template size), Figure 12-1 represents the preprocessing and scanning of a binary (sand/non-sand) training image.

3. For all unknown nodes are visited randomly, a data event $dev_T(\mathbf{u})$ is defined as the set of hard and previously simulated values found in the template **T**. It is

centered at visited location **u** where **T** is the same size template used to scan the training image.

4. The $dev_T(\mathbf{u})$ is compared to all available patterns in the database using a predefined similarity distance measure criterion. A simple single-point similarity function called Manhattan similarity function is used to find the most similar pattern with respect to the data event. Mathematically, it is defined:

$$d\left\langle dev_T(\mathbf{u}), pat_T^k \right\rangle = \sum_{\alpha=0}^{n_T} \left| dev_T(\mathbf{u}+\mathbf{h}_\alpha) - pat_T^k(\mathbf{h}_\alpha) \right| \qquad (12\text{-}1)$$

where $\mathbf{h}_\alpha$ are the vectors defining the geometry of the n_T nodes of the template **T** and $d\langle x, y\rangle$ describes similarity through a dissimilarity or distance function. In practice, $d\langle x, y\rangle = 0$ indicates complete similarity. Figure 12-2 shows the application of Manhattan distance when applied to sample binary (sand/non-sand) pattern.

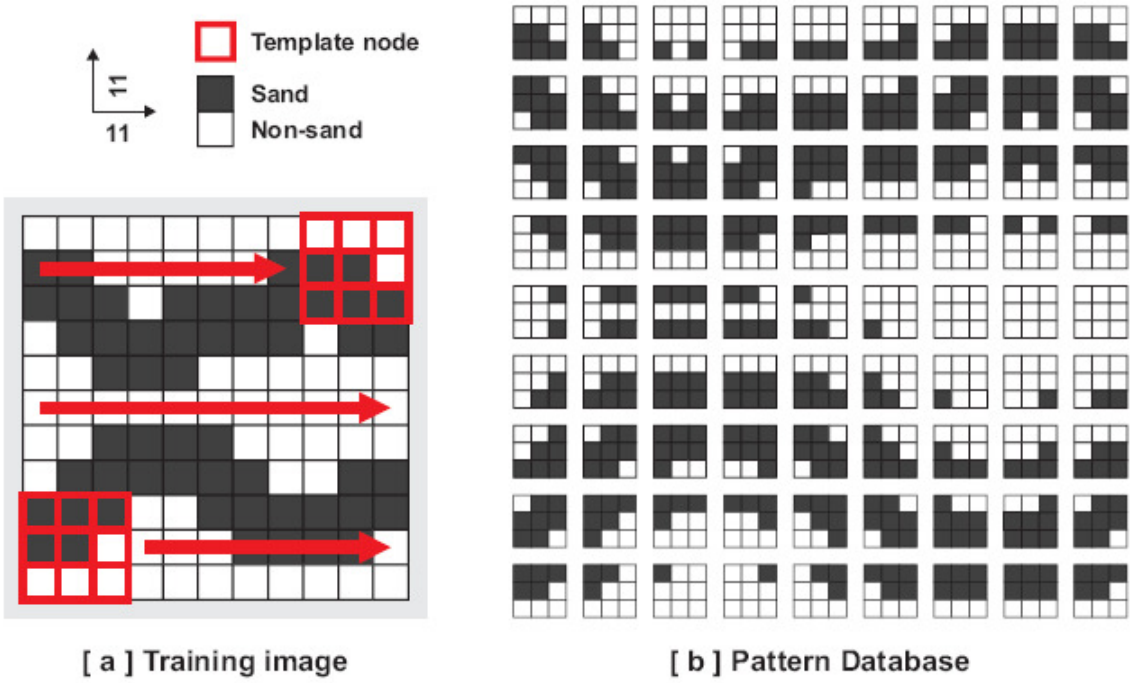

Figure 12-1. Preprocessing of the training image to obtain the pattern database using a 3x3 2D template [1]

5. Once the most similar pattern Pat_T^* is found in the pattern database, then the data event $dev_T(\mathbf{u})$ is replaced by Pat_T^* i.e. the values of Pat_T^* are pasted on to the simulation grid at the current node **u**.

Figure 12-3 and Figure 12-4 represent the steps 1 to 5 of the SIMPAT algorithm when it was utilized to generate an unconditional 11x11 realization using the training image and pattern database in Figure 12-1. The detail of the SIMPAT algorithm is in the Reference 1. This study follows the SIMPAT algorithm terminologies and notations.

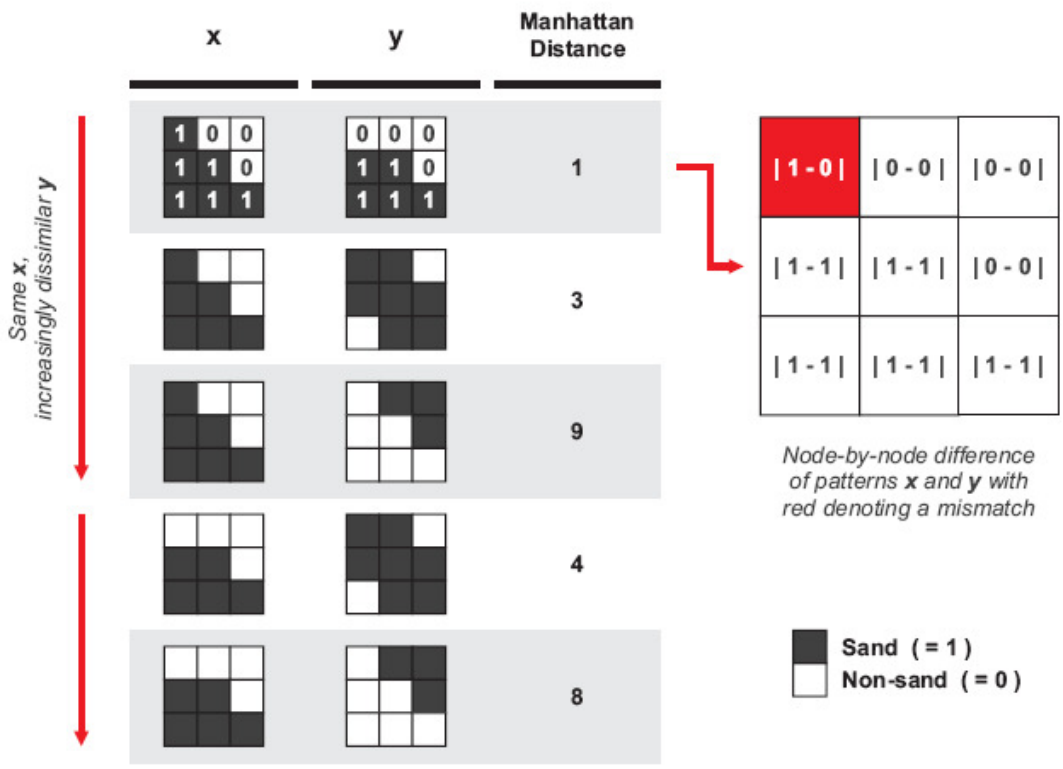

Figure 12-2. Application of Manhattan distance when applied to sample binary (sand/non-sand) pattern [1]

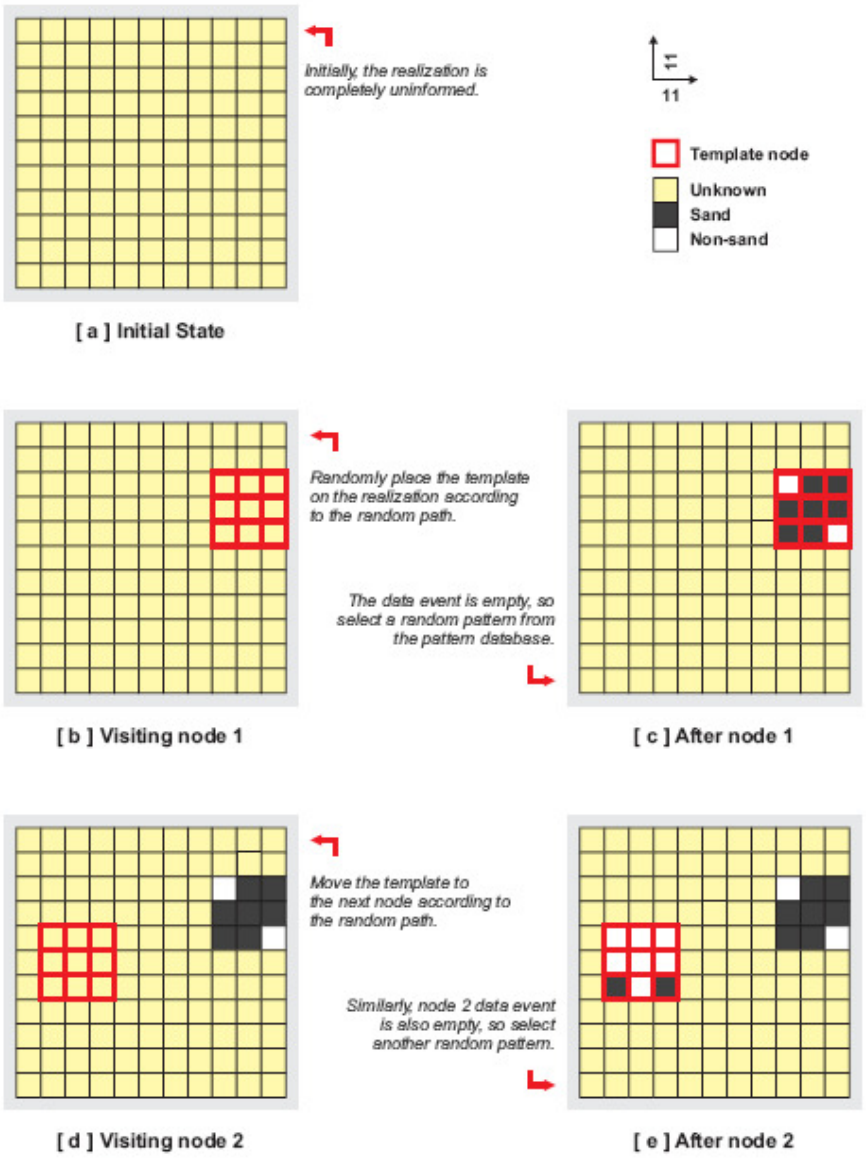

Figure 12-3. Internal steps of SIMPAT algorithm when applied to a 11x11 realization using the training image and pattern database in Figure 12-1 and a 3x3 template. The Figure continues on the next page as Figure 12-4 [1].

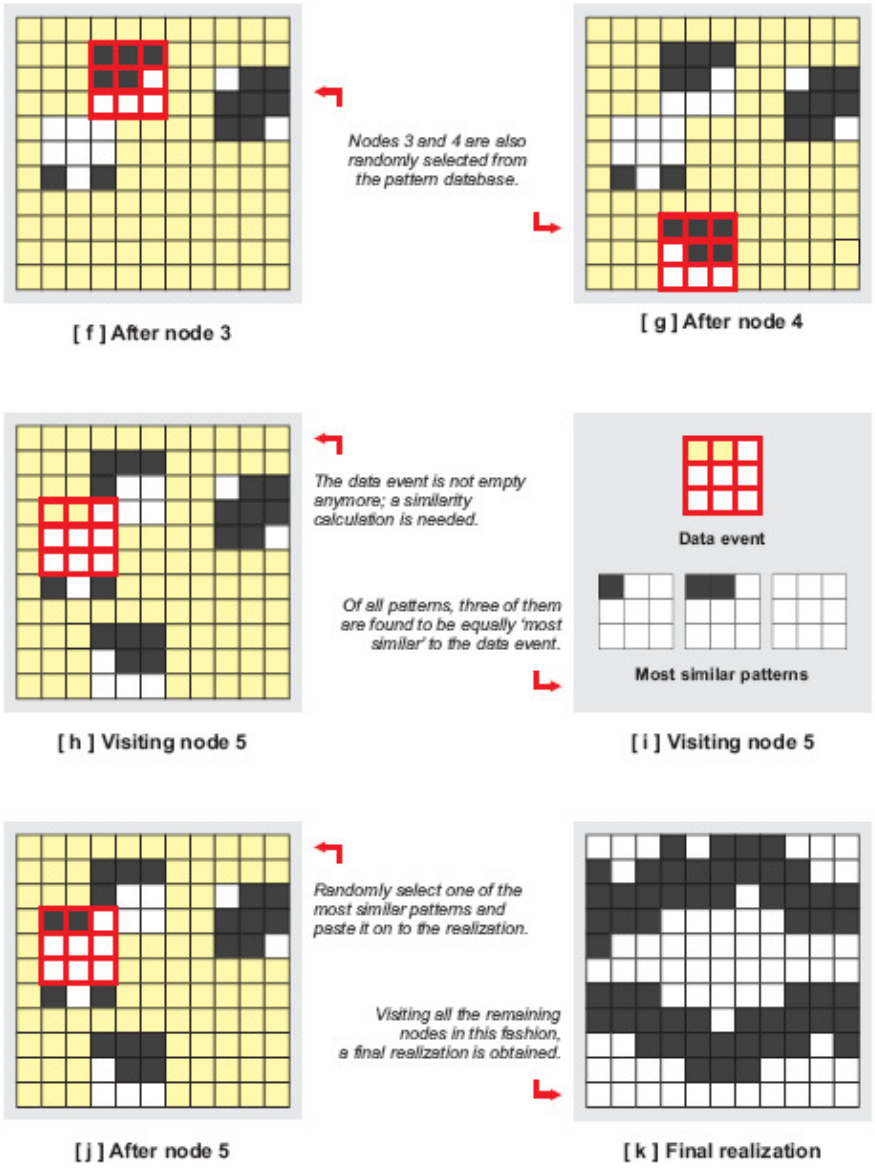

Figure 12.4. Continuation of Figure 12.3 showing different steps of SIMPAT [1]

12.2. Limitations of the Manhattan Distance

Manhattan distance used in the SIMPAT has some limitations. For example Consider the 5x5 binary data event in which a fracture is assigned to five black grid blocks (Figure 12-5). Nine patterns shown in Figure 12-5b were extracted from a training image depicting slanted fracture. The goal of this simulation is to find the most similar and consistent pattern to the data event in Figure 12-5a. Manhattan similarity distance was employed for this purpose. The selected pattern by Manhattan distance criteria is marked by red in Figure 1b.The selected pattern is geologically inconsistent to the data event in Figure 1a because it represents a disconnected fracture piece. As Arpat [1] stated "In general, whenever the global proportion of particular category is significantly less than that of any other category in the training image, the Manhattan distance is likely to prefer patterns containing this low proportion category".

Although Arpat [1] utilized specific mechanisms to enforce the global proportions of the training image categories on the generated realizations, a better similarity measure is needed to generate representative realizations. An alternative similarity distance method known as Normalized Cross Correlation (NCC) is introduced in SIMPAT algorithm to calculate the similarity between a data event and collected patterns. The following section will explain in details the mathematical formulation of NCC.

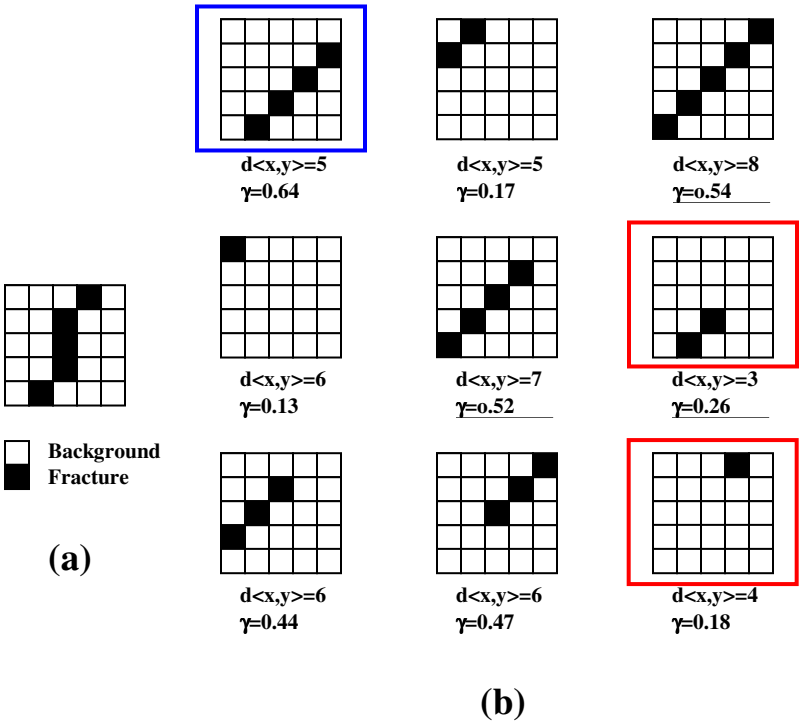

Figure 12.5. Comparison of similarity measure distance by Manhattan and NCC techniques for a data event on the left and candidate patterns on the right. $d<x,y>$ denotes the Manhattan dissimilarity distance, and γdenotes NCC measure distance [1]

Chapter 13

Modified SIMPAT Algorithm

13.1. Normalized Cross Correlations (NCC)

NCC has been extensively used to evaluate the degree of similarity between two compared images [26] [27] [28] [29]. NCC originated from the mathematical definition of cross correlation [30]. The cross correlation is a squared Euclidian distance that measures the similarity distance between two images as follows:

$$c\left\langle dev_T(u), Pat_T^k \right\rangle = \sum_{\alpha=0}^{n_T-1} dev_T(u+h_\alpha)\, Pat_T^k(h_\alpha) \tag{13.1}$$

where $c\left\langle dev_T(u), Pat_T^k \right\rangle$ represents the cross correlation similarity measure between a data event and a training image pattern.

NCC coefficient is defined to normalize Eq. (13.1). It has a unit length yielding a cosine-like correlation coefficient as follows:

$$\gamma\left\langle dev_T(u), Pat_T^k \right\rangle = \frac{\sum_{\alpha=0}^{n_T-1}\left[\left[dev_T(u+h_\alpha) - \overline{dev_T(u+h_\alpha)}\right]\left[Pat_T^k(h_\alpha) - \overline{Pat_T^k(h_\alpha)}\right]\right]}{\left\{\sum_{\alpha=0}^{n_T-1}\left[\left[dev_T(u+h_\alpha) - \overline{dev_T(u+h_\alpha)}\right]^2 \sum_{\alpha=0}^{n_T-1}\left[Pat_T^k(h_\alpha) - \overline{Pat_T^k(h_\alpha)}\right]^2\right\}^{0.5}} \tag{13.2}$$

where $\gamma\left\langle dev_T(u), Pat_T^k \right\rangle$ shows the NCC coefficient which is always between -1 and 1. $\overline{dev_T(u+h_\alpha)}$ and $\overline{Pat_T^k(h_\alpha)}$ represent the mean of the continuous or categorical variable in the data event and realization respectively within the template T. In practice, the larger NCC shows the more similarity between a data event and a training image pattern. $\gamma\left\langle dev_T(u), Pat_T^k \right\rangle = 1$ indicates complete similarity.

13.2. Modified SIMPAT Algorithm

The section introduces a modification of SIMPAT algorithm**.** This method is called Modified SIMPAT which employs the NCC similarity distance instead of Manhattan similarity distance. In general using NCC similarity distance in the SIMPAT algorithm has clear advantages. First it improves the accuracy of selecting the most similar and consistent pattern in the training image pattern database; in situation where the Manhattan similarity distance fails. The 5x5 binary data event in Figure 12.5a was revisited to show the NCC pattern selection advantage. The NCC similarity distance was applied to find the most similar pattern to the data event shown in Figure 12.5a. NCC was calculated for each pattern in this Figure. The results of this calculation are denoted by γ at the bottom of each pattern in the Figure 12.5b. The pattern with the largest γ is the most similar pattern in the Figure 12.5a. This pattern is marked by blue line in Figure 12.5b. It is geologically consistent with the data event shown in the Figure 12.5a. The continuity and direction of the fracture of the selected pattern in Figure 12.5b is identical to that of the data event Figure 12.5a.

For both Manhattan and NCC similarity distances, the difference between the grid block values of the data events and patterns is the most important factor in Equations 4 and 7 in the previous section. However, the small and large value differences between data events and patterns in Eq.(12.1) are treated to have the same effect in the similarity calculation for Manhattan distance. In other words, large differences have the same weight in the calculation as the small differences. It is more appropriate to penalize larger

differences with larger weights and smaller differences with smaller weights in the similarity calculation.

One possible solution is to multiply each term in the similarity calculation by itself so that small differences have smaller weights and large differences have larger weights. This form of penalizing the difference is achieved by squaring the difference term in Eq.(13.2) used for NCC calculation. Thus, compared to Manhattan distance, the NCC (Euclidean distance) magnifies the larger differences between data events and patters and results in a better similarity measure.

13.3. Case Studies

Three training images were studied to investigate the validity of the Modified SIMPAT algorithm. These training images were also used to compare the performance of both original and Modified SIMPAT to generate the realizations honoring the same patterns and facies distribution observed in a training image. These training images (Figures shown in 13.1 through 13-3) represent different types of petroleum reservoir showing specific discrete facies distribution. The following section presents the details of these case studies.

Case Study 1 represents a horizontal 2D section of a fluvial reservoir. A fluvial reservoir is characterized by the presence of sinuous sand-filled channels with a background of mudstone. For this case, three types of facies are considered. Facies 1 is channel sands which correspond to the best reservoir rock. Facies 2 displays Levee sand which has

intermediate reservoir quality. Facies 3 represents floodplain background which is usually considered as non-reservoir rocks.

Case Study 2 has two facies and consists of diagonal elliptical bodies of facies 1 on the background facies 2. The elliptical bodies are considered as high permeability zones in a real reservoir.

Case Study 3 has four facies in a diagonal direction. Facies 1, 2, and 3 with different reservoir qualities are distributed on floodplain background. A Southwest-Northeast trend is considered in cases 1 and 3 to investigate the capability of the method to reproduce any existing spatial trend in a training image.

The training images shown in Figures 13.1 to 13.3 are 100x100 unconditional realizations generated using the object-based program in PETREL [31]. Several features of the object-based modeling were utilized to generate these cases with desired facies distribution. A computer was written in MATLAB to implement Modified SIMPAT and original SIMPAT algorithms.

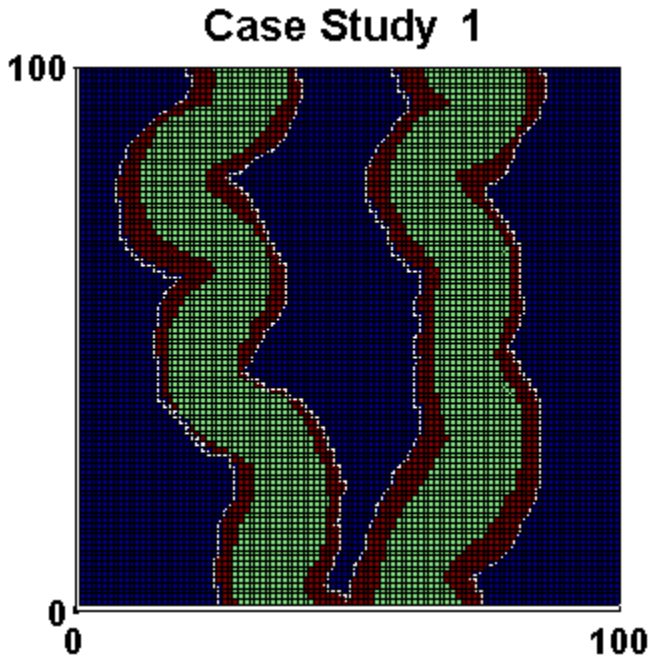

Figure 13-1. Training image representing a fluvial reservoir

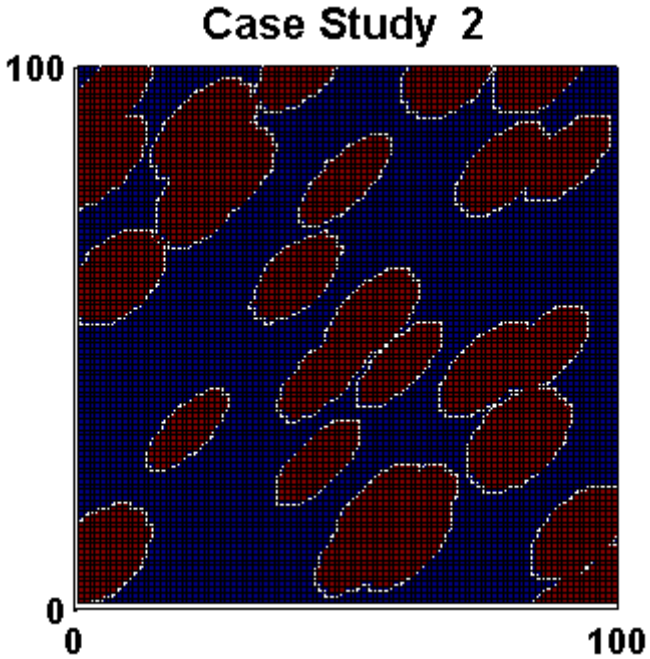

Figure 13.2. Diagonal elliptical bodies in the training image

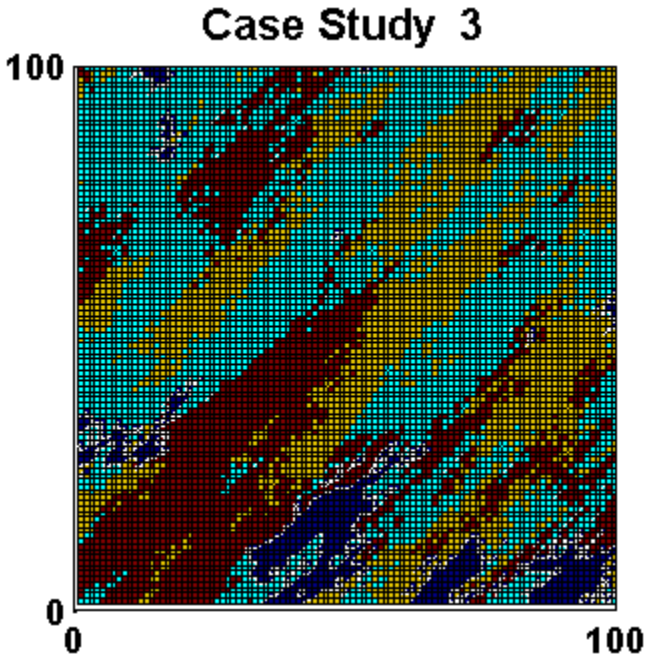

Figure 13.3 Training image shows four facies in the Southwest-Northeast direction

Chapter 14

Results and Discussion

A predefined 30x30 template was used to scan the training images. Then, modified SIMPAT and SIMPAT algorithms were employed to generate fifty unconditional realizations for each training image. Figures 14.1 through 14.3 show the comparison between realizations generated by both algorithms and the corresponding reference training image. The figures demonstrate that the Modified SIMPAT realizations reproduce the available patterns of the training images in comparison to that of SIMPAT algorithm.

The performance of stochastic methods to generate realizations can be examined by multiple-point connectivity function. The MP connectivity function is a statistical function representing the joint variability or connectivity of an object in a realization at more that two location at time. The mathematical formulation of this function detailed in section 11.1.1. Channels and ellipses in Figure 14.1 & Figure 14.2, and red objects in Figure 14.3 are denoted by Facies 1. The connectivity function was calculated for facies 1 in the realization shown in Figures 14.1 through 14.3 and the corresponding training images.

Figures 14.4 through 14.6 represent the comparison of the connectivity function of facies 1 in realization of the Figures 14.1 through 14.3. The results obtained from the Modified SIMPAT realization, shown as red circle in these figures, is closer to the

training image connectivity function shown as a solid line. This confirms that the Modified SIMPAT realizations better capture facies connectivity and direction in comparison to the SIMPAT realizations. This advantage is very important in the reservoir modeling. The accurate connectivity of high and low permeability zones in a very important factor for modeling fluid flow in porous media.

14.1. The Effect of Template Size

The CPU time needed for pattern matching process in the SIMPAT algorithm is a function of template size. Smaller template size considerably reduces the CPU time. When using small template, the algorithm successfully reproduces all the small-scale details of the training image. However, the large scale of the training image is not replicated. Using larger template size results in better replication of overall structure, but increases the total runtime of the algorithm. Original SIMPAT algorithm shows sensitivity to the template size. Realizations generated using Modified SIMPAT on the other hand is less sensitive to the template size. The sensitivity of both algorithms to the template size were compared using four different template sizes to generate realizations. The connectivity function for facies 1 in all training images was used for this comparison. Figures 14.7 through 14.9 represent that the realizations replicated by both algorithms depend on the template size. However, the connectivity of facies 1 in the realization generated by the Modified SIMPAT is less variable to the template size. This confirms that the Modified SIMPAT algorithm is less dependent on the template size, thus indirectly reducing CPU time.

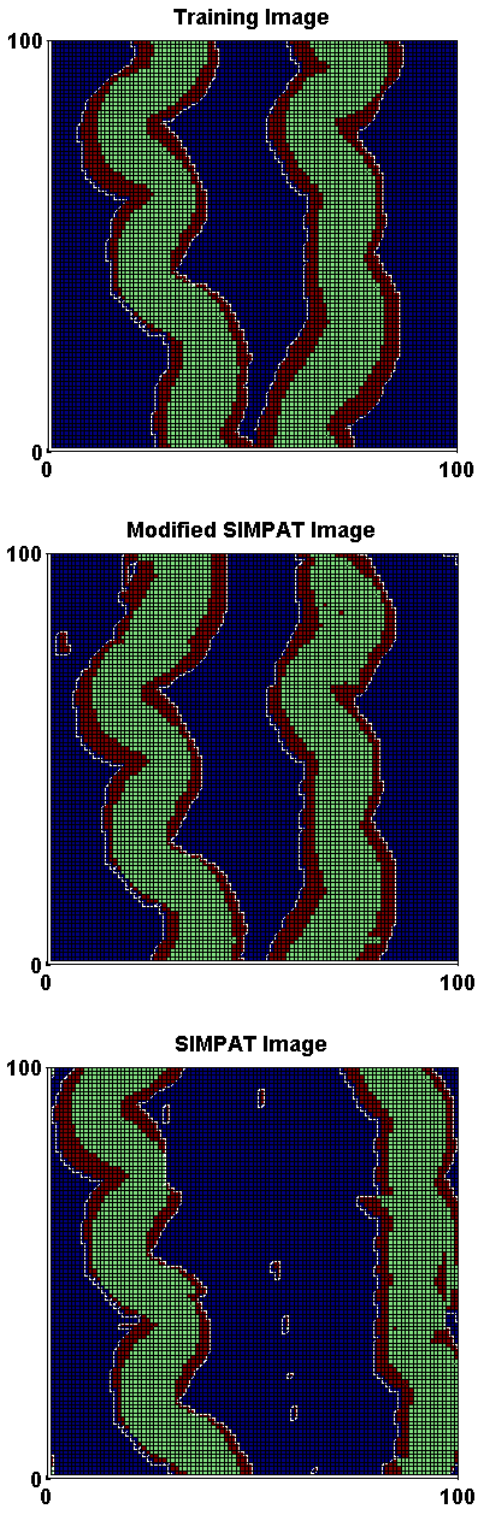

Figure 14.1. Comparison between training image 1 and simulated realizations

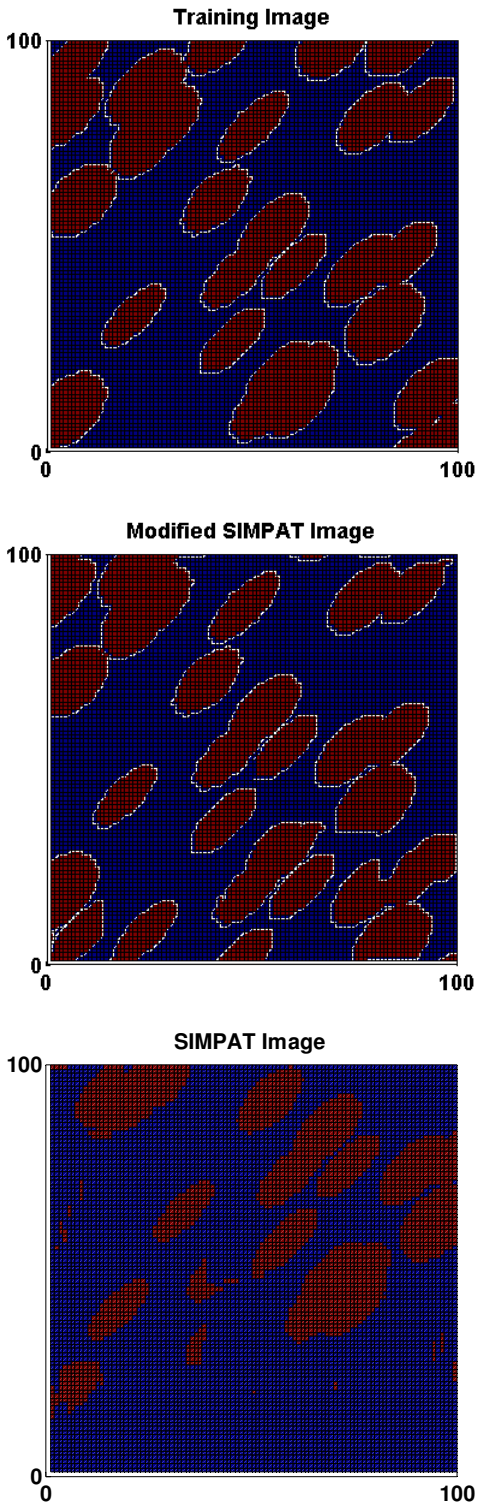

Figure 14.2. Comparison between training image 2 and simulated realizations

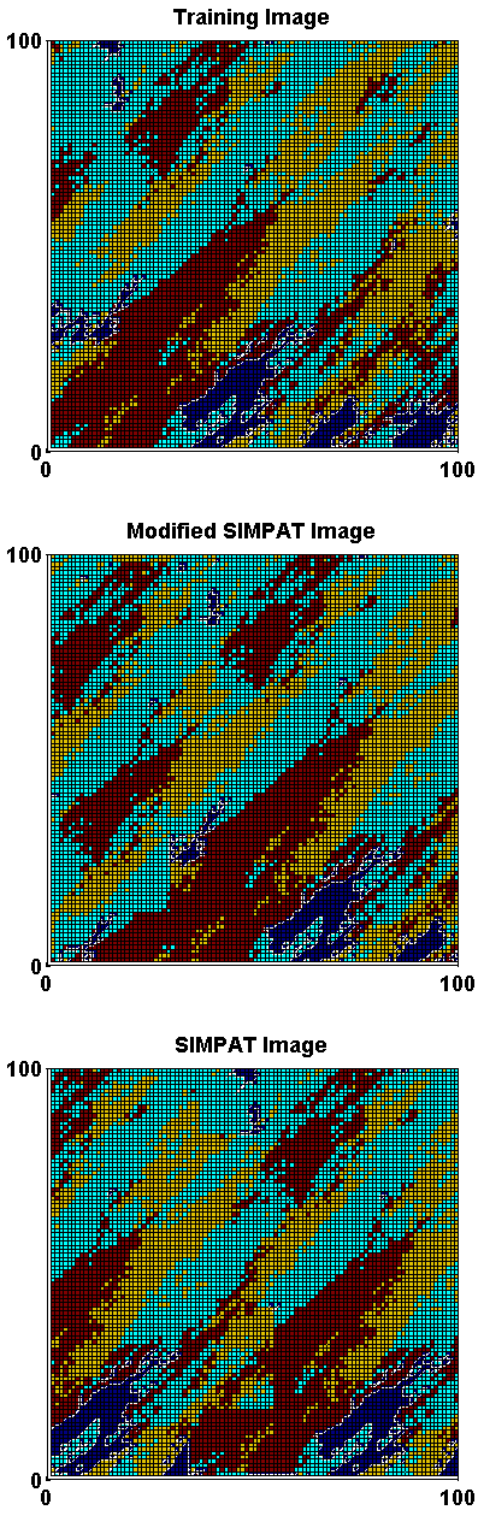

Figure 14.3. Comparison between training image 3 and simulated realizations

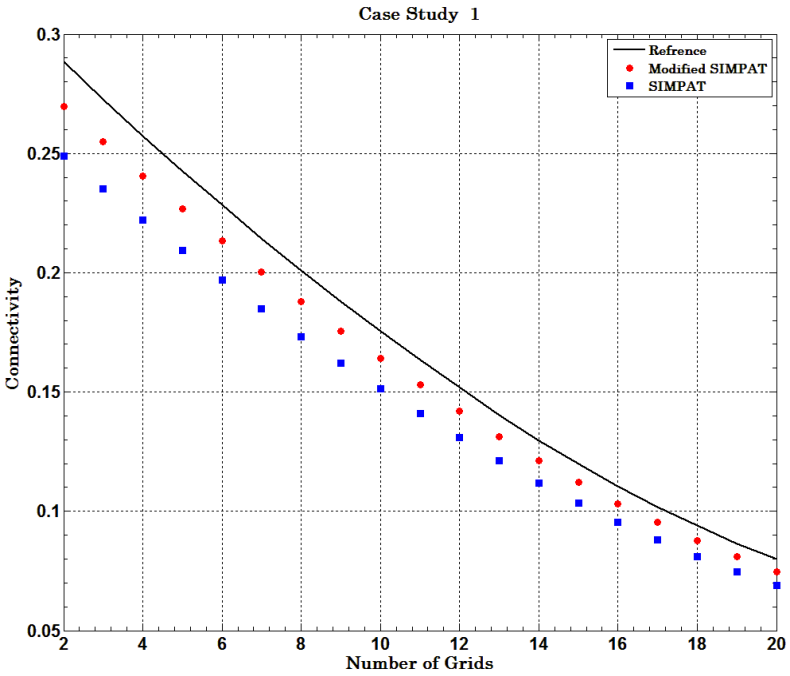

Figure 14.4. Connectivity function of facies 1 of realizations simulated with a 30x30 template and the training image 1

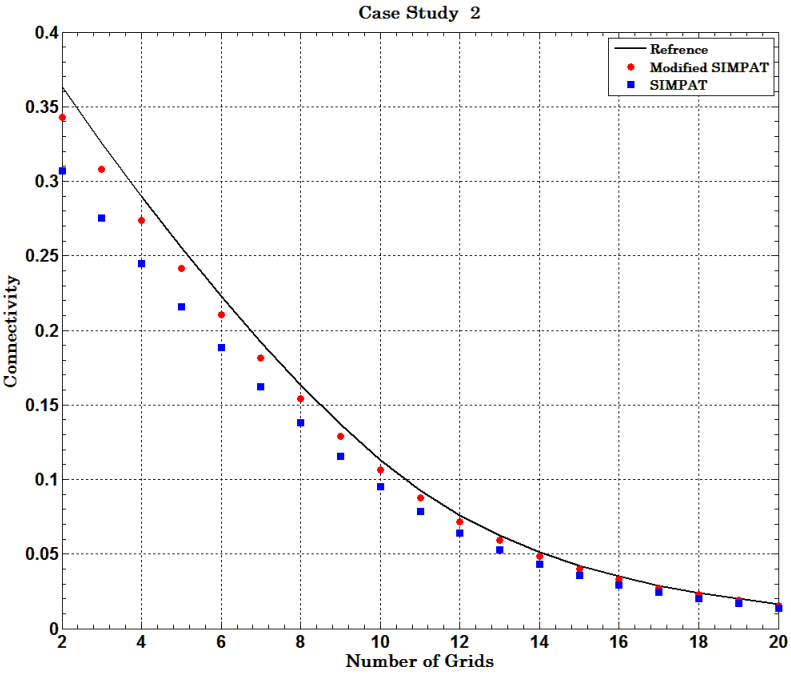

Figure 14.5. Connectivity function of facies 1 of realizations simulated with a 30x30 template and the training image 2

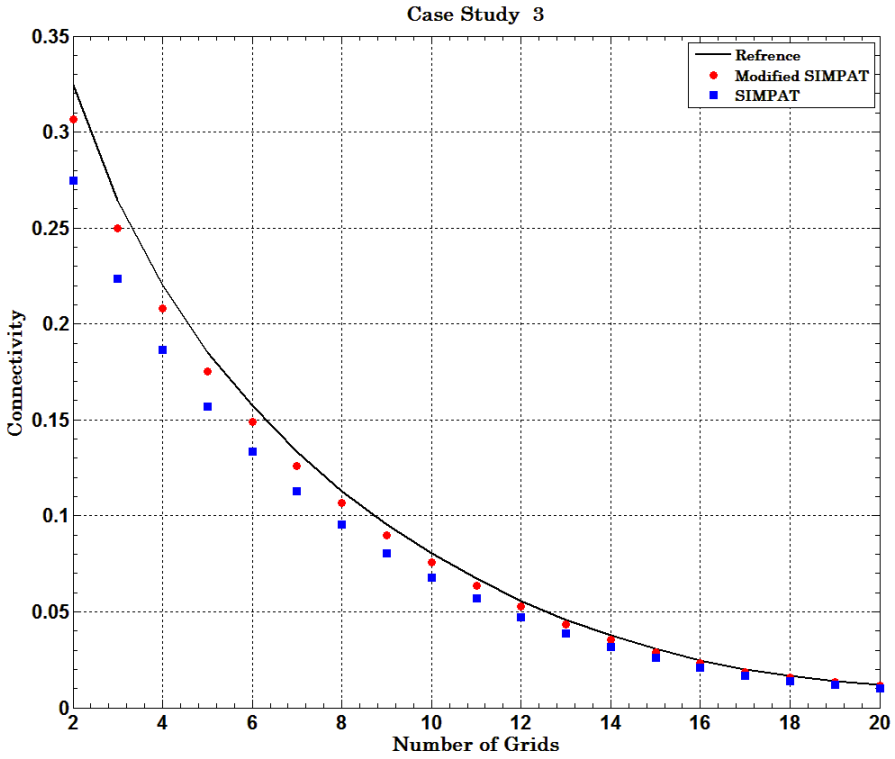

Figure 14.6. Connectivity function of facies 1 of realizations simulated with a 30x30 template and the training image 3

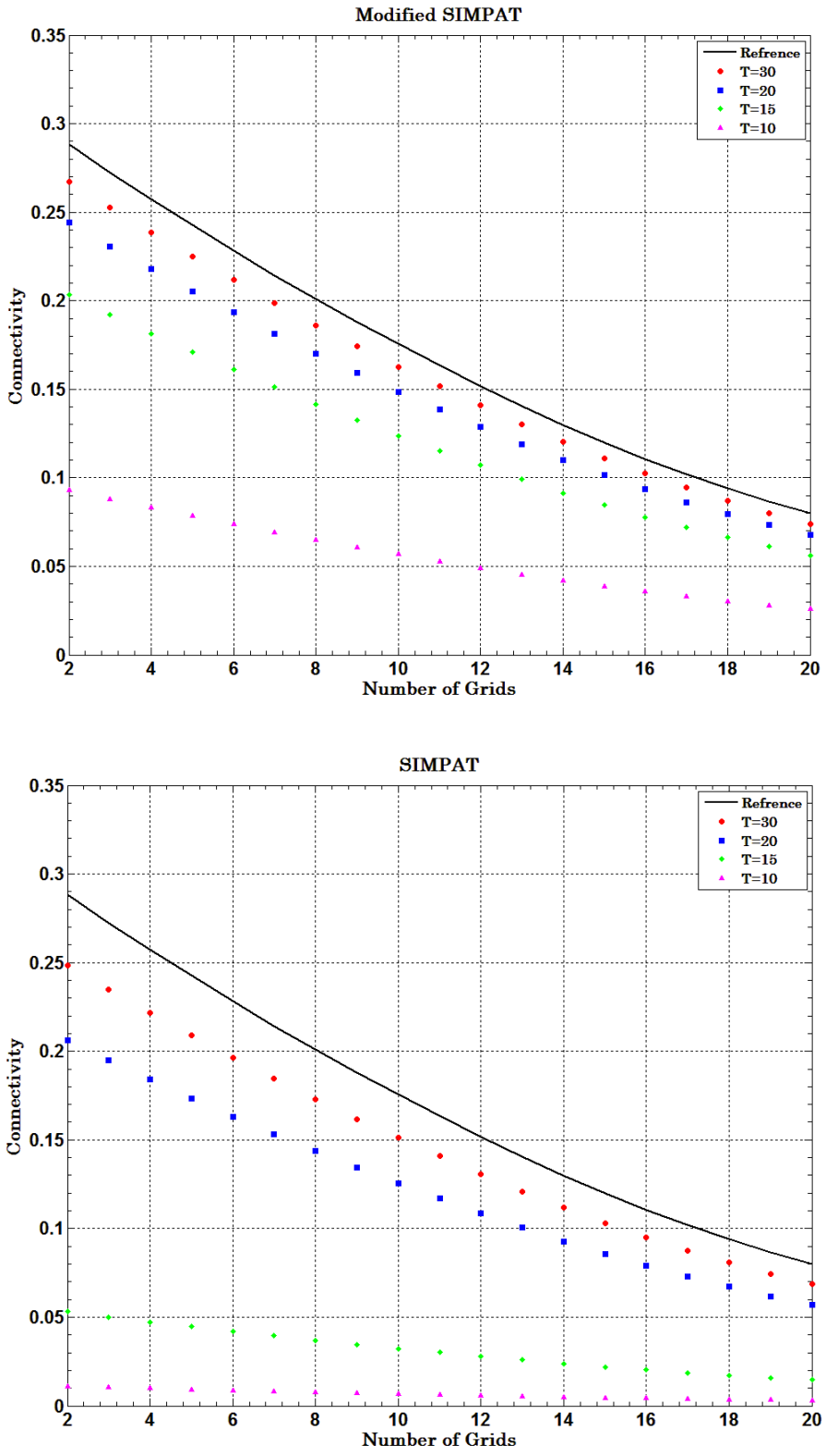

Figure 14.7. Connectivity function of facies 1 when different template sizes used in original and Modified SIMPAT algorithms used to generate realizations for case study 1

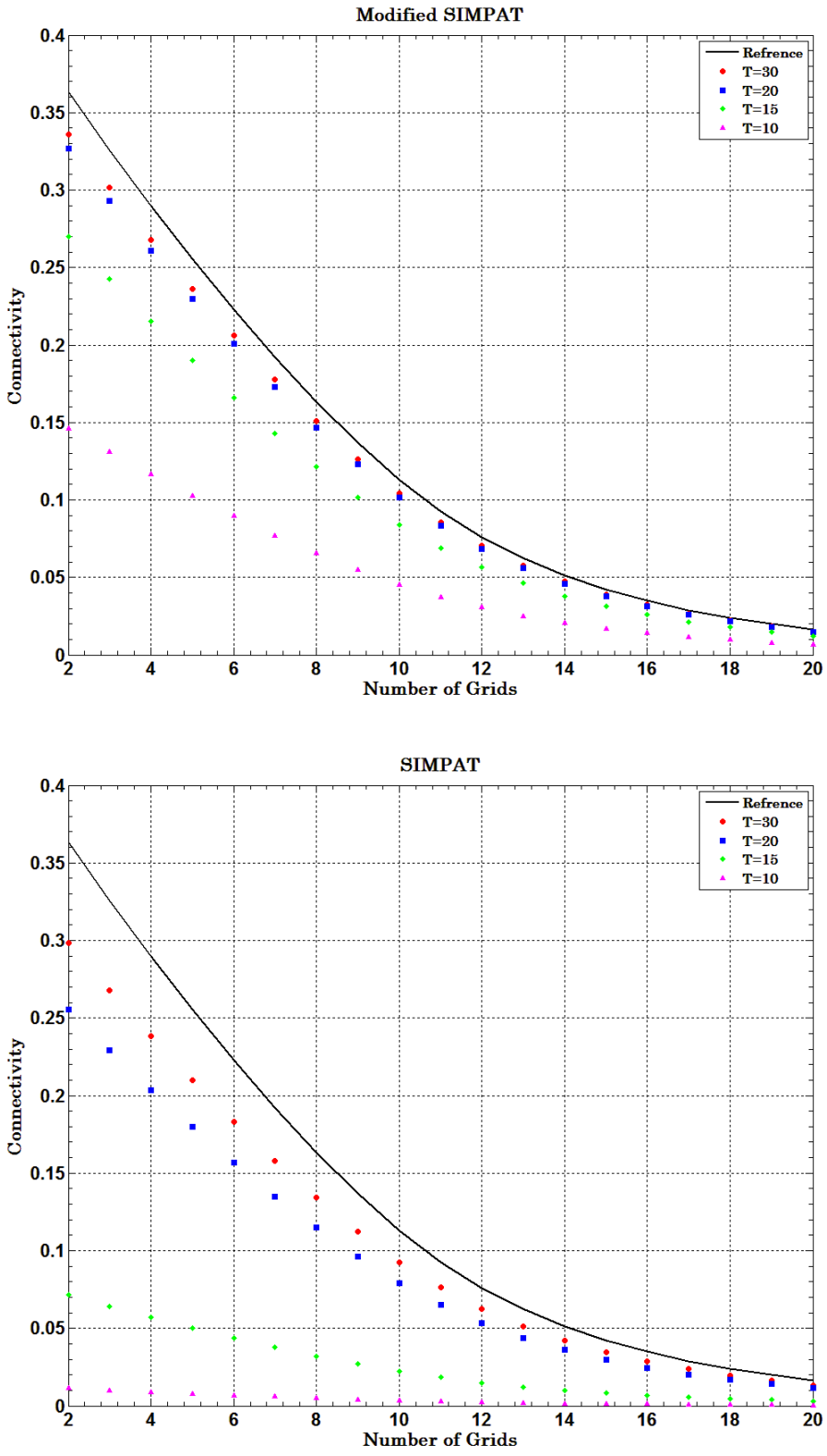

Figure 14.8. Connectivity function of facies 1 when different template sizes used in original and Modified SIMPAT algorithms used to generate realizations for case study 2

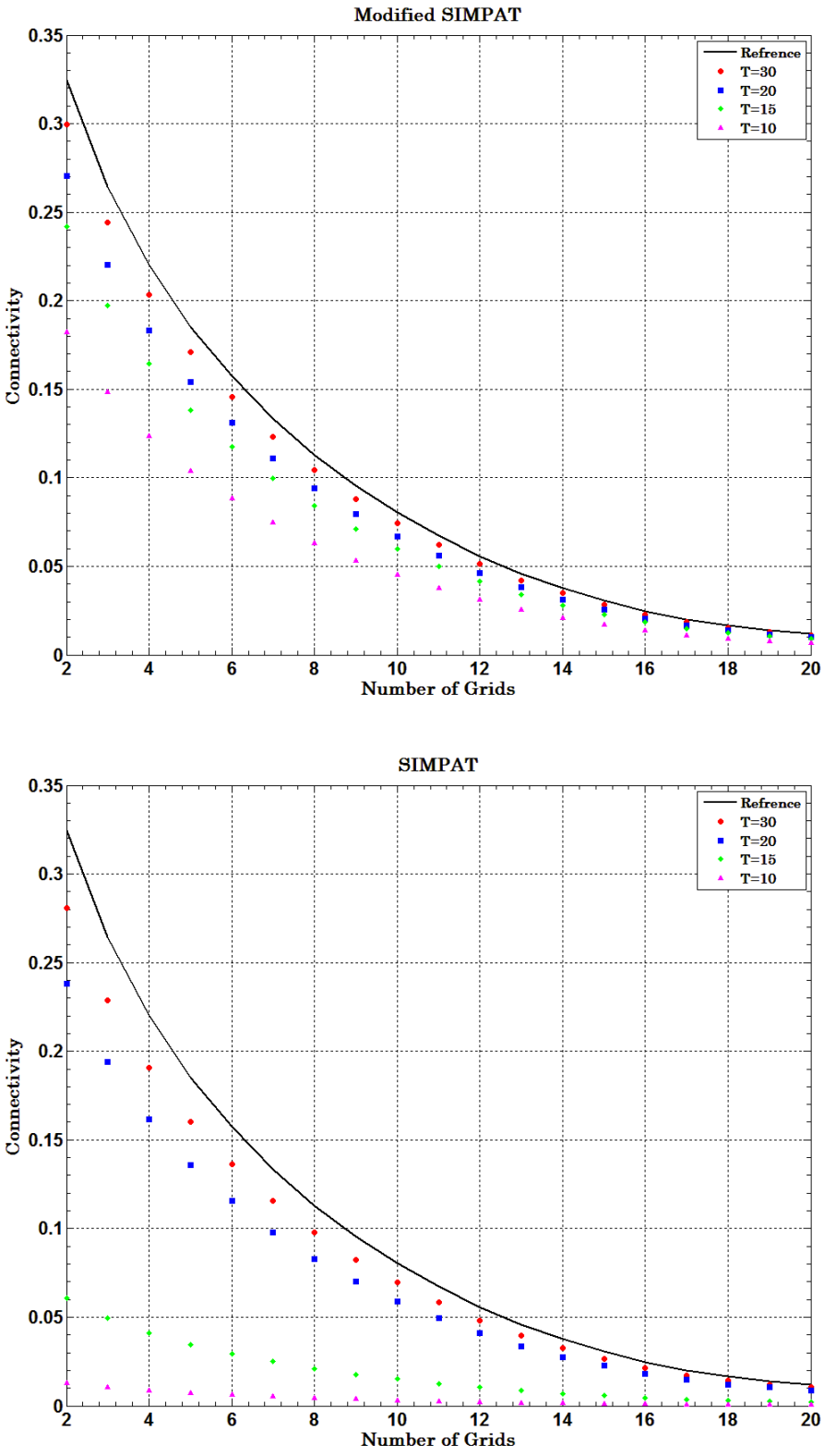

Figure 14.9. Connectivity function of facies 1 when different template sizes used in original and Modified SIMPAT algorithms used to generate realizations for case study 3

14.2. Application Example for History Matching Process

The final outcomes of any stochastic simulation method are realizations that are considered to represent the actual variable distribution. In petroleum engineering, these realizations are used as input data in flow simulations. For example, porosity and permeability are considered random variables whose realizations are reproduced by stochastic simulation methods. Therefore, the accuracy of the realizations directly affects the results of flow simulations, and the accuracy of the realizations in turn depends on the algorithm used to generate those realizations. The algorithms considered in this study to generate realizations are SIMPAT and Modified SIMPAT. The accuracy and precision of these two algorithms are compared in terms of results obtained by flow simulator case studies.

A flow simulation was carried out using a reference permeability distribution. Then, fifty realizations of permeability distribution were generated using Modified SIMPAT and SIMPAT methods, respectively. Flow simulations were performed using permeability realizations generated by both methods and the reference permeability distribution. The results obtained from these simulations were compared.

The reference permeability distribution for the flow simulation is a synthetic reservoir which has 50 grid blocks in X and Y directions (Figure 14.10). The Dykstra-Parson coefficient was used to represent the felid heterogeneity. The Dykstra-Parson coefficient of 0.75 indicates a heterogeneous permeability distribution. The petrophysical properties and required input parameters were maintained the same for the different

simulations. Table 14.1 lists the input parameters except permeability used in flow simulations. Figure 14.11 shows oil-water relative permeability data set used in the flow simulation.

The flow simulator used in this study was ECLIPSE, a commercial reservoir simulator [32]. A black-oil model was applied. The performance of the five-spot pattern shown in Figure 14.10 was simulated. Well I in the center of the five-spot injected water at a rate of 400 bbl/day. The production wells at the corners produced oil at a rate of 100 STB/day. The flow simulation was terminated when all production wells reached a water-cut of 30%. . Results obtained from the simulations for the fifty realizations were compared against the reference case in terms of water-cut and bottom-hole pressure (BHP) at the four production wells for both methods.

Figures 14.12 and 14.13 show the BHP (solid blue line) obtained using the fifty realizations generated by Modified SIMPAT and SIMPAT, respectively, compared against the reference case (filled black circle).The BHP's from the realizations include the reference case indicating acceptable accuracy for all the four wells for both methods. The results in Figure 14.12 and 14.13 show better precision because the results lie in a narrower band indicating Modified SIMPAT is better in comparison to the SIMAPAT algorithm. Later in the discussion this precision will be quantified. Figures 14.14 and 14.15 show the water-cut results generated using the two algorithms compared against the reference case (shown as filled black circle) both the cases indicate acceptable accuracy. The precision of the Modified SIMPAT algorithm is again evident.

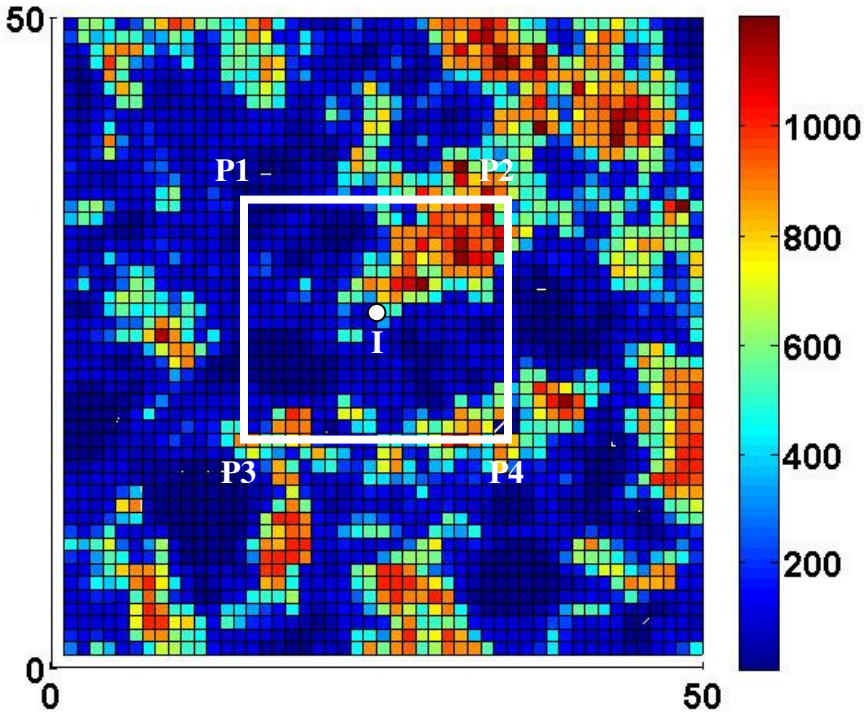

Figure 14.10. The reference permeability distribution for flow simulations

Table 14.1. List of parameters used in flow simulator

Reservoir Dimensions (Number of Grids)	50x50
Dimensions of each grid	50 ft x 50 ft
Reservoir Thickness	10 ft
Uniform porosity	0.25
Equilibrium Conditions	2000 psi@ 4500 ft
Water density	69.3 lb/ft^3
Water viscosity	0.74 cp
Oil formation volume factor	1.2
Oil density	51.3 lb/ft^3
Oil Viscosity	0.7 cp
Total compressibility	3e-5 1/psi
Constant initial water saturation	0.2
Initial Pressure	2000 psi
Bubble point Pressure	14.7 psi

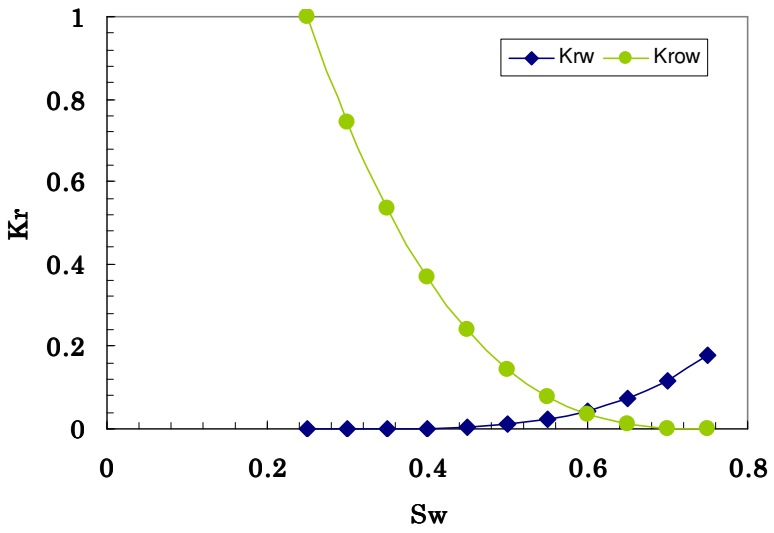

Figure 14.11. Oil-water relative permeability data set used in the flow simulator

The time required for injected water to breakthrough at the production wells and the time for the water-cut to reach 30% in each well were the two parameters used to compare the two methods. Water breakthrough is defined as when the injected water reaches the production wells. The following analysis was performed for the production wells.

Comparison the simulation results was done by creating histograms of breakthrough time and time for 30% water-cut frequency for the fifty realizations generated by the two respective methods. The true values obtained from simulation are shown in the histograms as black solid circles.

Figures 14.16 through 14.19 show the histograms of water breakthrough time for both methods. The mean of frequency distribution for the Modified SIMPAT method is closer to the true value when compared against the mean value obtained using SIMPAT

method. The lower standard deviation of the Modified SIMPAT distribution indicates better precision. The standard deviation of the distribution generated by the SIMPAT method, on the other hand, is higher indicating higher variability. Figure 14.20 represents the histograms of time for 30% water-cut for both methods for production well P4. In Figure 14.20**,** again the Modified SIMPAT method exhibits better precision in comparison to the SIMPAT method. This confirms better reliability of the Modified SIMPAT over the SIMAPT method to generate random variable realizations.

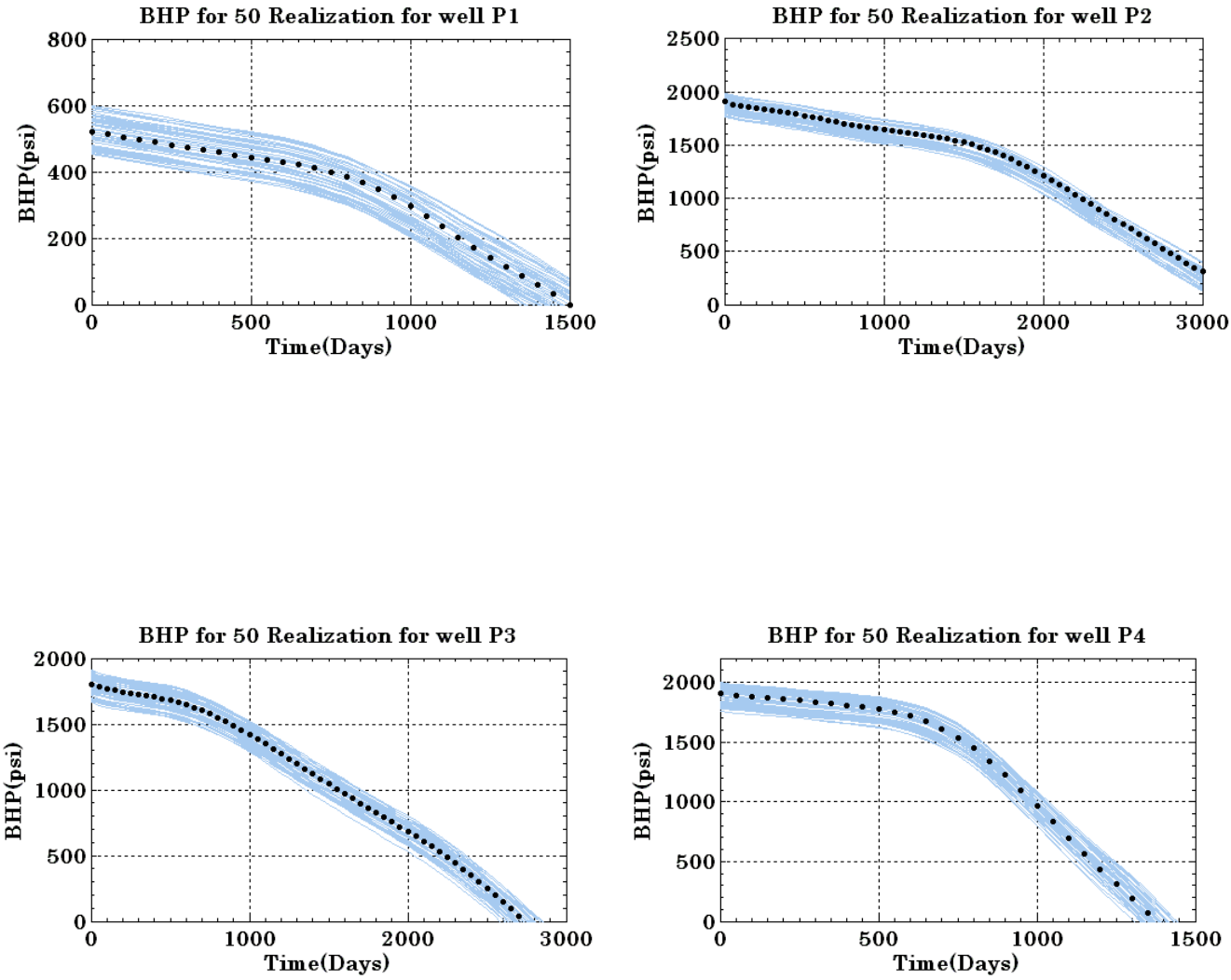

Figure 14.12. BHP's of the four production wells obtained using fifty realizations generated by Modified SIMPAT algorithm and the reference image

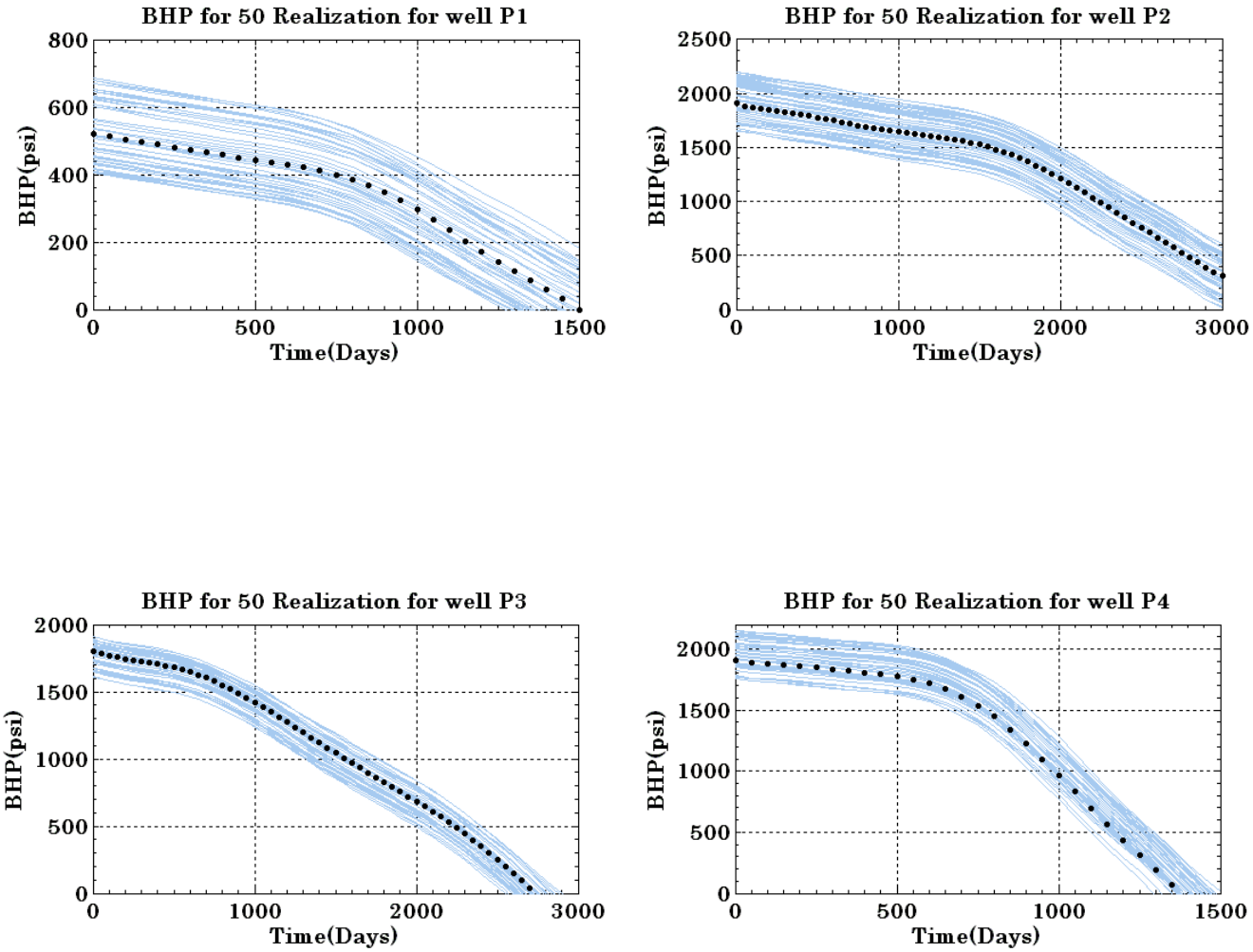

Figure 14.13. BHP's of the four production wells obtained using fifty realizations generated by SIMPAT algorithm and the reference image.

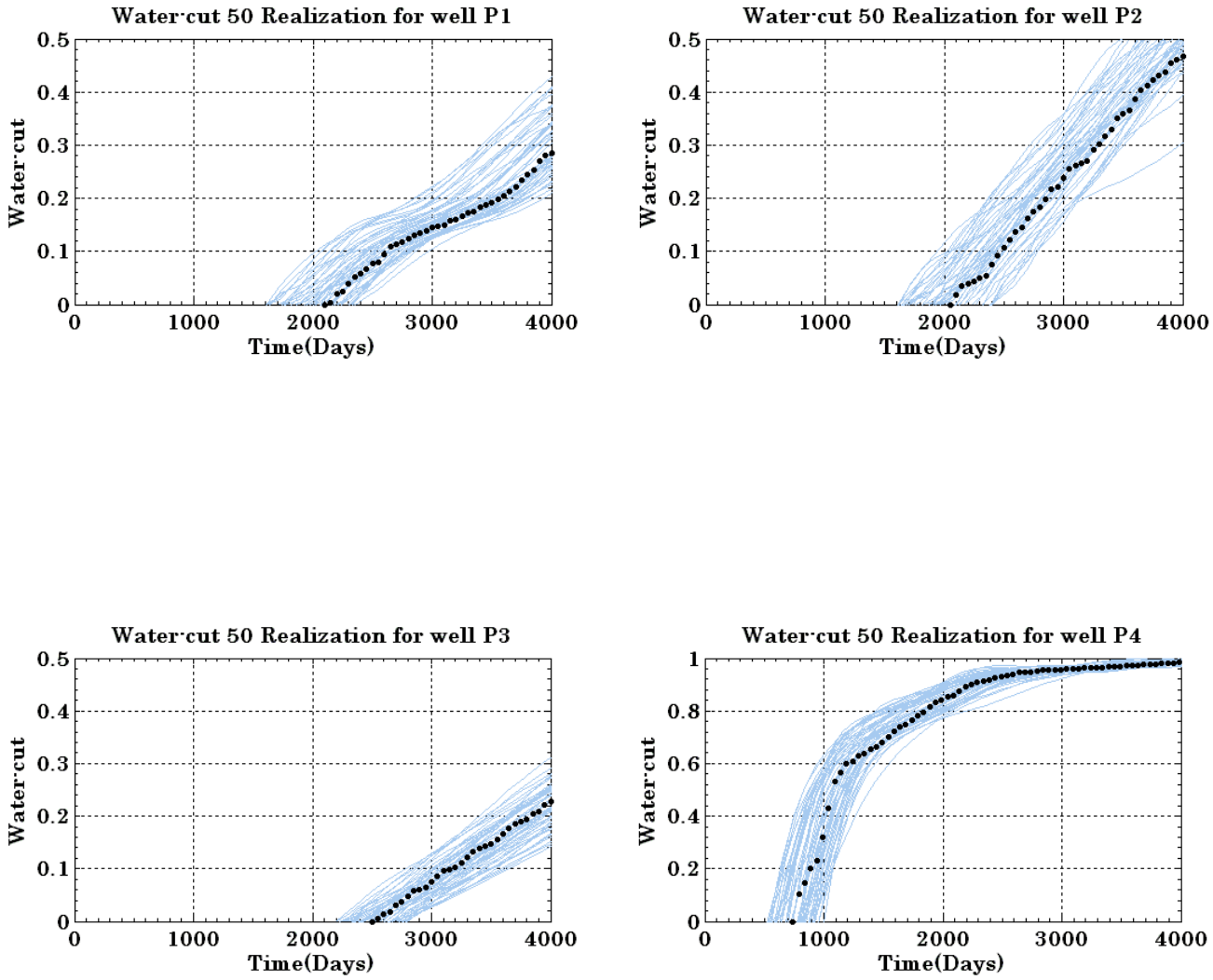

Figure 14.14. Water-cut of the four production wells obtained using fifty realizations generated by Modified SIMPAT algorithm and the reference image

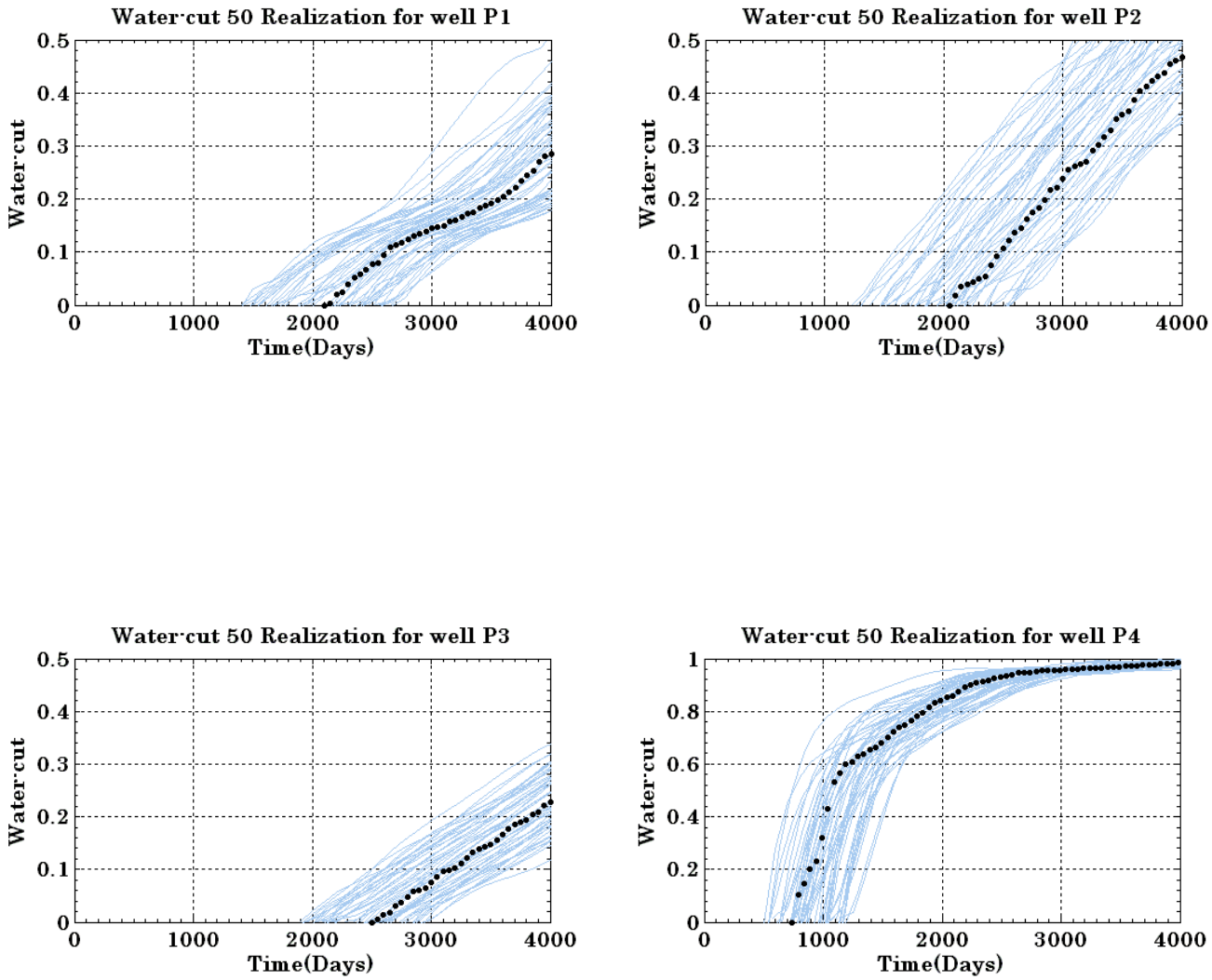

Figure 14.15. Water-cutof the four production wells obtained using fifty realizations generated by SIMPAT algorithm and the reference image

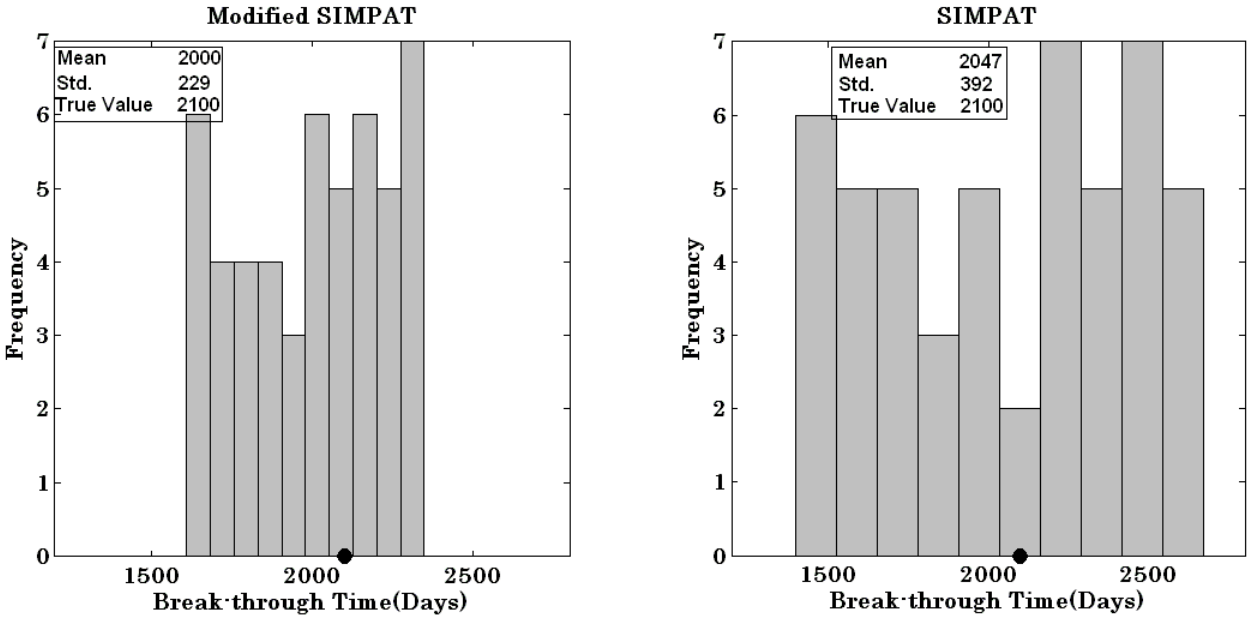

Figure 14.16. Histogram of water breakthrough time at production well P1 obtained from the flow simulation of fifty realizations using both algorithms

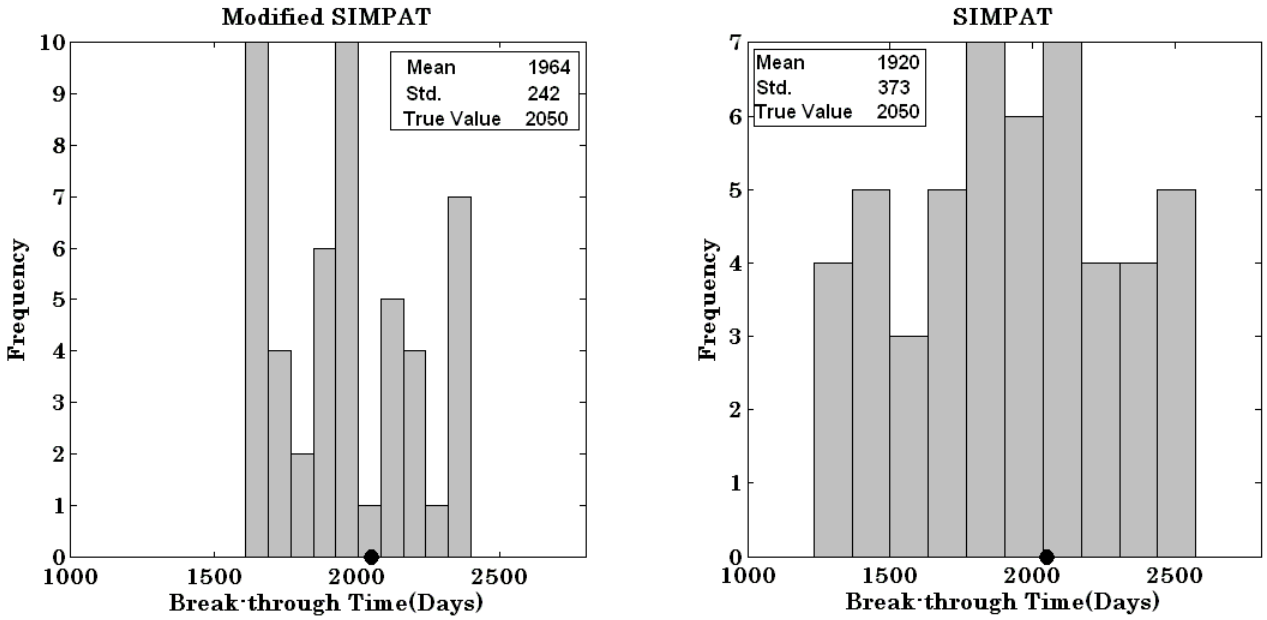

Figure 14.17. Histogram of water breakthrough time at production well P2 obtained from the flow simulation of fifty realizations using both algorithms

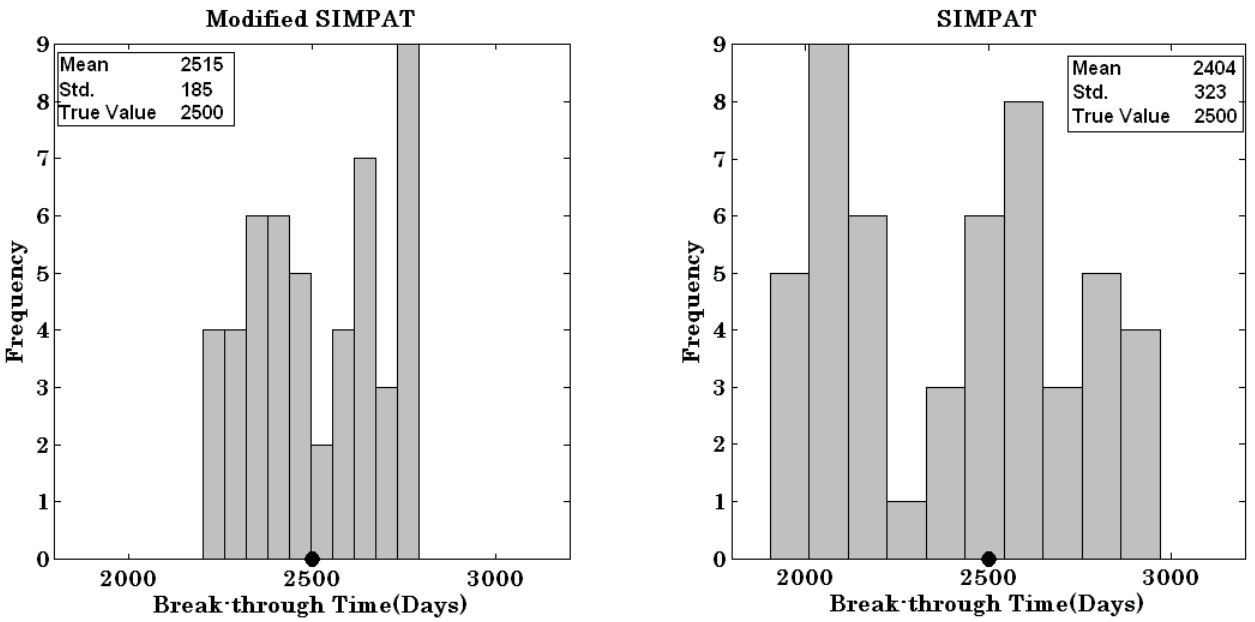

Figure 14.18. Histogram of water breakthrough time at production well P3 obtained from the flow simulation of fifty realizations using both algorithms

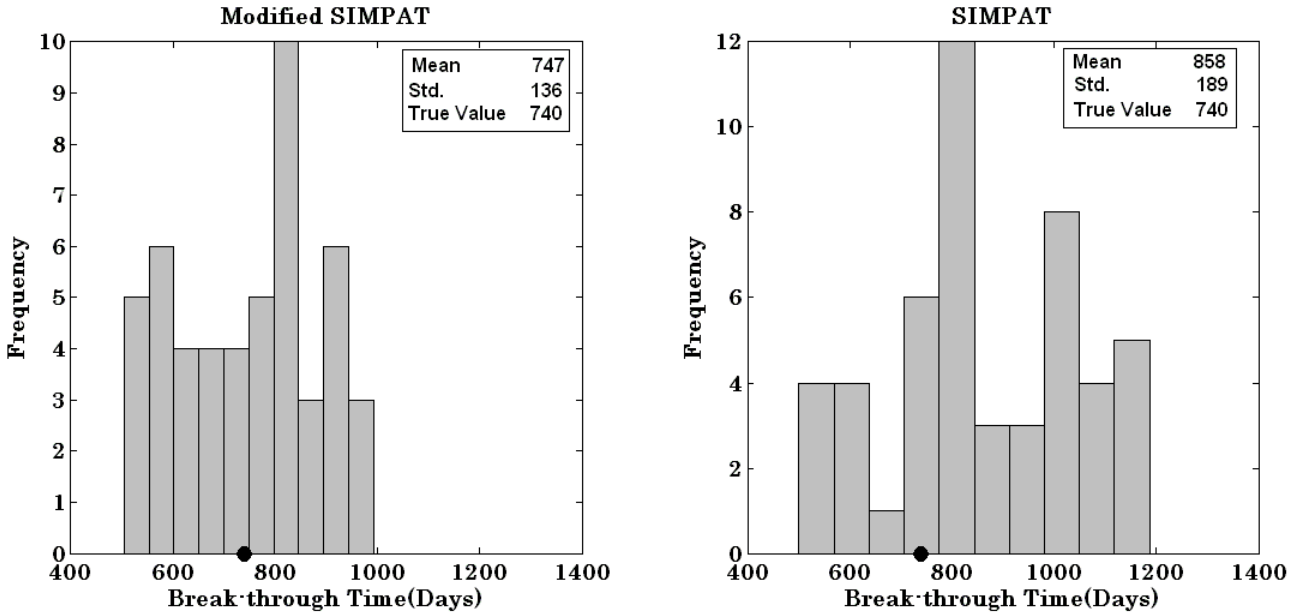

Figure 14.19. Histogram of water breakthrough time at production well P4 obtained from the flow simulation of fifty realizations using both algorithms

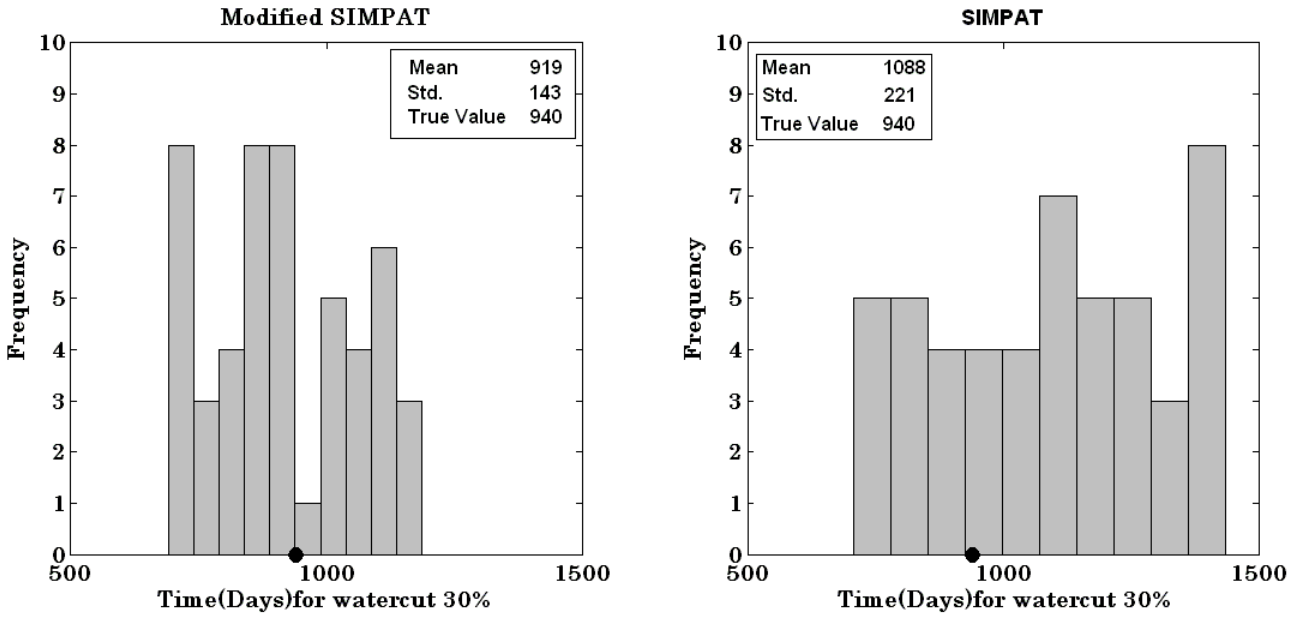

Figure 14.20. Histogram of 30% water-cut time at a production well obtained from the flow simulation of fifty realizations using both algorithms

Chapter 15

Conclusions

1. Normalized Cross Correlation (NCC) was introduced as a better technique for similarity distance measurement. The results shows that NCC similarity distance improves the accuracy of selecting the most similar and consistent pattern in the training image pattern database.

2. The stochastic SIMPAT algorithm was modified with introducing the NCC similarity distance instead of Manhattan distance. The performance of both Modified and original SIMPAT algorithm to generate realizations were investigated and compared using three types of training images. The results indicate that the Modified SIMPAT algorithm is more robust to replicate the patterns of training image.

3. The sensitivity of both Modified and original SIMPAT algorithms with respect to template sizes was investigated using connectivity function. The results of this study show the connectivity function of facies in the realizations generated with Modified SIMPAT is less sensitive to the template size.

4. The performance of both algorithms was compared using BHP and water cut from simulation results. Permeability realizations generated with Modified and original SIMPAT were used as input data in a flow simulator. The results of this study

indicate acceptable accuracy for both algorithms. However, the Modified SIMPAT realizations results more precise dynamic data when used as an input in the flow simulation.

References

[1] - G. B. Arpat, "Sequential Simulation with Patterns", Ph. D thesis, Stanford University, 2005.

[2] - J. S. D. Bonet, "Multi-resolution sampling procedure for Analysis and Synthesis of Texture Images", In Computer Graphics, 1997, pg. 361-368.

[3] - O. Duda, P. Hart, D. Stork, " Pattern Classification", John Willey & Sons Inc., 2nd ed., 2001.

[4] - A. Efros, W. Freeman, "Image Quilting for Texture Synthesis and Transfer", In SIGGRAPH Proceeding, Los Angeles, CA, Aug. 2001.

[5] - C.V. Deutsch, A. G. Journel, "GSLIB: Geostatistical software library and user's guide", 2nd ed., Oxford University Press, New York, 368 pages, 1998.

[6] - C.V. Deutsch, L. Wang, "Hierarchical object-based stochastic modeling of fluvial reservoirs", Mathematical Geology, 28(7), 1996, pg. 857-880.

[7] - H. Haldorsen, E. Damsleth, "Stochastic Modeling", JPT (SPE 20321), April 1990, pg. 404–412.

[8] - L. Holden, R. Hauge, O. Skare, and A. Skorstad, "Modeling of Fluvial Reservoirs with Object Models", Mathematical Geology, 24(5), July 1998, pg.473–496.

[9] - S. Viseur, "Stochastic Boolean Simulation of Fluvial Deposits: A New Approach Combining Accuracy with Efficiency", In SPE ATCE Proceedings, Vol. 2, October 1992.

[10] - R. Wen, A. Martinius, A. Nass, and P. Ringrose, "Three-Dimensional Simulation of Small-Scale Heterogeneity in Tidal Deposits - a Process-Based Stochastic Simulation Method", In IAMG Proceedings, International Association for Mathematical Geology, 1998.

[11] - F. Guardiano, R. M. Srivastava, "Multivariate geostatistics: Beyond bivariate moments", Kluwer Academic, Dordrecht, 1993, pg. 133-144.

[12] - M. Srivastava, "Iterative methods for spatial simulation", Stanford Center for Reservoir Forecasting, Rep. No. 5, 24 pages, 1992.

[13] - C. Farmer, "Numerical rocks. In P. King, editor, The Mathematical Generation of Reservoir Geology", Clarendon Press, Oxford, 1990, pg.22-33.

[14] - H. Tjelmeland, “Stochastic Models in Reservoir Characterization and Markov Random Fields for Compact Objects”, PhD thesis, Norwegian University of Science and Technology, Trondheim, Norway, 1996.

[15] - J. Caers, A. Journel, “Stochastic Reservoir Simulation using Neural Networks Trained on Outcrop Data”, In SPE ATCE Proceedings, SPE 49026, September 1998.

[16] - J. Caers, S. Srinivasan, and A. Journel, “Geostatistical Quantification of Geological Information for a Fluvial-Type North Sea Reservoir” In SPE ATCE Proceedings, SPE 56655October 1999.

[17] - S. Strebelle, "Sequential Simulation Drawing Structures from Training Images”, Ph.D. Thesis, Stanford University, 2000.

[18] - A. Journel, “Geostatistics: Roadblocks and Challenges”, Kluwer Academic Publications, Dordrecht, 1992, pg.213–224.

[19] - D. Knuth, “Art of Computer Programming” Addison-Wesley Pub. Co., 3rd edition, 1997.

[20] - S. Palmer, “Vision Science: Photons to Phenomenology”, MIT Press, Massachusetts, 1999.

[21] - J. S. D. Bonet, “Multiresolution Sampling Procedure for Analysis and Synthesis of Texture Images”, In Computer Graphics, ACM SIGGRAPH, 1997, pg. 361–368.

[22] - Z. Bar-Joseph, “Statistical Learning of Multi-Dimensional Textures”, Master’s thesis, The Hebrew University of Jerusalem, Jerusalem, Israel, June 1999.

[23] - J. Portilla and E. P. Simoncelli, “A Parametric Texture Model Based on Joint Statistics of Complex Wavelet Coefficients” Int’l Journal of Computer Vision, 40(1), October 2000, pg.49-71.

[24] - L. Wei, “Texture Synthesis by Fixed Neighborhood Searching, PhD Thesis, Stanford University, Stanford, CA, USA, 2001.

[25] - R. Paget and I. D. Longstaff, “Texture Synthesis via a Noncausal Nonparametric Multiscale Markov Random Field”, IEEE Transactions on Image Processing, 7(6), June 1998, pg. 925–931,

[26] - J. H. Kim, H. S. Cho, and S. Kim, “Pattern Classification of Solder Joint Iimages using a Correlation Neural Network”, Eng. Appl. Artif. Intell, 9, 1996, pg. 665-669.

[27] - T. Wakahara, Y. Kimura, A. Tomono, “Affine-Invariant Recognition of Gray-Scale Characters using Global Affine Transformation Correlation”, IEEE Trans. Pattern Anal. Machine Intell., 23, 2001, pg. 384-395.

[28] - J. M. Gallegos, J. R. Villalobos, G. Carrilo, and S. D. Gabrera, “Reduced-Dimension and Wavelet Processing of SMD Images for Real-Time Inspection”, In: Proceedings of the IEEE Southwest Symposium on Image Analysis and Interpretation, San Antonio, Texas, 1996, pg. 30-36.

[29] - D. M. Tsai, C. H. Chiang, “Rotation-Invariant Pattern Mmatching using Wavelet Decomposition”, Pattern Recognition Lett., 23, 2002, pg. 191-201.

[30] - J. P. Lewis, “Fast Template Matching”, Vision Interface, 1995, pg. 120-123.

[31] - Petrel Schlumberger, www.slb.com

[32] - ECLIPSE Schlumberger, www.slb.com

[33] - P. Goovaerts, “Geostatistics for Natural Resources Evaluation”, Oxford University Press, 1997.

[34] - M. Kelkar, G. Perez, “ Applied Geostatistics for Reservoir Characterization”, Society of Petroleum Engineering Inc. , United States, 264 pages, 2002.

[35] - C. V. Deutsch, “Geostatistical Reservoir Modeling”, Oxford University Press. Inc, Unites States, 376 pages, 2002.

[36] - J. Caers, “ Petroleum Geostatistics”, Society of Petroleum Engineering Inc. , United States, 88 pages, 2005.

[37] - A. Journel, C. J. Huijbregts, “Mining Geostatistics”, Academic Press, New York, 600 pages, 1978.

[38] - C. V. Deutsch, “Annealing Techniques Applied to Reservoir Modeling and the Integration of Geological and Engineering (Well Test) Data”, PhD thesis, Stanford University, Stanford, CA, 1992.

[39] - A. Journel, “Non-Parametric Estimation of Spatial Distributions”, Math Geology, 15(3), 1983, pg.445–468.

[40] - H. Xiao, “A Description of the Behavior of Indicator Variograms for a Bivariate Normal Distribution”, Master’s thesis, Stanford University, Stanford, CA, 1985.

[41] - E. Isaaks and R. Srivastava, “An Introduction to Applied Geostatistics”, Oxford University Press, New York, NY, 1989.

[42] - F. Alabert and G. J.Massonnat, “Heterogeneity in a Complex Turbiditic Reservoir: Stochastic Modeling of Facies and Petrophysical Variability”, In 65th Annual Technical Conference and Exhibition, SPE 20604, September 1990, pg.775–790.

[43] - P. Scholle, D. Spearing, “Sandstone Depositional Environments”, The American Association of Petroleum Geologists, Tulsa, Oklahoma, 1992.

[44] - P., Jacquard, C. Jain, “Permeability Distribution from Field Pressure Data”, SPE 1307, October 11, 1965.

[45] - P. E. Gill, W. Murray, M. H. Wright, “Practical Optimization”, Academic Press Limited, UK, 1981.

[46] - J. E. Killough, Y. Sharma, A. Dupuy and R. Bissell, “A Multiple Right Hand Side Iterative Solver for History Matching”, SPE 29119, Presented at SPE symposium on Reservoir Simulation, San Antonio, 12- 15 February 1995.

[47] - F. Anterion, R. Eymard, and B. Karcher, “Use of Parameter Gradients for Reservoir History Matching ", Presented at SPE Symposium on Reservoir Simulation, Houston, Texas, SPE 18433, 6-8 February 1989.

[48] - W. Yeh, “Review of Parameter Identification Procedures in Groundwater Hydrology: The Inverse Problem”, Water Resources Research, Vo1.22 No.2, February 1986, pg. 95-108.

[49] - J. L. Landa, M. M. Kamal, C. D. Jenkins, and R. N. Home, “Reservoir Characterization Constrained to Well-Test Data: A Field Example”, Presented at the SPE Annual Technical Conference, Denver, Colorado, SPE 36511, 6-9 October 1996.

[50] - Z. Wu, A. C. Reynolds, D. S. Oliver, “Conditioning Geostatistical Models to Two Phase Production Data”, SPE Annual Technical Conference, SPE 56885, 27-30 September 1998.

[51] - G. Xue, A. Datta-Gupta, “Structure Preserving Inversion: An Efficient Approach to Conditioning Stochastic Reservoir Models to Dynamic Data”, Presented at SPE Annual Technical Conference, San Antonio, Texas, SPE-38727, 5-8 October 1997.

[52] - B. S. RamaRao, A. M. LaVenue, G. de Marsily, L. Marietta, “Pilot Point Methodology for Automated Calibration of an Ensemble of Conditionally Simulated Transmissivity Fields, 1. Theory and Computational Experiments”, Water Resources Research, Vol. 31, No. 3, March 1995, pg. 475-493.

[53] - G. de Marsily, A. M. La Venue, B. S. RamaRao, M. G. Marietta, “Pilot Point Methodology for Automated Calibration of an Ensemble of Conditionally Simulated Transmissivity Fields: 2. Application”, Water Resources Research, Vol. 31, No. 3, March 1995, pg. 495-516.

[54] - R. C. Bissell, O. Dubmle, P. Lamy, P. Swaby, and O. Lepine, “Combining Geostatistical Modeling with Gradient Information for History Matching: The Pilot Point Method”, Presented at SPE Annual Technical Conference, San Antonio, Texas, SPE 8370, 5-8 October 1997.

[55] - J. J. Gomez-Hernandez, J. E. Capilla, A. Sahuquillo, “Stochastic Simulation of Transmissivity Fields Conditional to Both Transmissivity and Piezometric Head Data - II. Demonstration on a Synthetic Aquifer”, Journal of Hydrology, Vol. 203, 1997, pg. 175-188.

[56] - T. T. Tran, X. H. Wen, R. A. Behrens, “Efficient Conditioning of 3D Fine-scale Reservoir Model to Multiphase Production Data using Streamline-based Coarse Scale Inversion and Geostatistical Downscaling”, Presented at SPE Annual Technical Conference, Houston, Texas, SPE 56518, 3-6 October 1999.

[57] - X. H. Wen, C. V. Deutsch, A. S. Cullick, “High resolution reservoir models integrating multiple-well production data”, Presented at SPE Annual Technical Conference, San Antonio, Texas, SPE 38728, 5-8 October 1997.

[58] - X. H. Wen, T.T. Tran, R. A. Behrens, J. J. Gomez-Hernandez, “Production data integration in sand/shale reservoirs using sequential self-calibration and geomorphing: A comparison”, Presented at SPE Annual Technical Conference, Dallas, Texas, SPE 63063, 1-4 October 2000.

[59] - H. Omre. H. Tjelmeland, “Petroleum Geostatistics”, Kluwer Academic Publishers, Volume 1, 41 -52, 1997.

[60] - S. N. Lee, A. Malallah, A. Datta-Gupta, “Multiscale Data Integration using Markov Random Fields”, Presented at SPE Annual Technical Conference, Dallas, Texas, SPE 63066, 1-4 October 2000.

[61] - L. Bonet-Cunha, D. S. Oliver, R. A. Render, A. C. Reynolds, “Markov Chain Monte carlo methods for conditioning a permeability held to pressure data”, Mathematical Geology, V.29,N. 1, 1991, pg. 61-91.

[62] - R. Goodman, “Introduction to Stochastic Models”, the Benjamin / Cummins Publishing Company, 1999.

[63] - W. M. Hastings, “Monte Carlo sampling methods using Markov chains and their Applications”, Biometrika, Vol. 57, No. 1, 1970, pg. 97-109.

[64] - M. Mezghani, F. Roggero, “Combining gradual deformation and upscaling techniques for direct conditioning of fine scale reservoir models to dynamic data”, Presented at SPE Annual Technical Conference, New Orleans, Louisiana, SPE 71334, 30 September-3 October 2001

[65] - F. Roggero, L. Y. Hu. and Helios Reservoir Group, “Gradual deformation of continuous geostatistical models for history matching”, Presented at SPE Annual Technical Conference, New Orleans, Louisiana, SPE 49004, 27-30 September 1998.

[66] - S. Srinivasan, J. Cares, “Conditioning reservoir models to dynamic data – A forward modeling perspective”, Presented at SPE Annual Technical Conference, Dallas, Texas, SPE 62941, 1-4 October 2000.

[67] - C. E. Shannon, “Bell System Technology Journal”, 27 (379), 1948.

[68] - P. Siarry, G. Dreyfus, “ An Application of Physical Methods on the Computer Aided Design of Electronic Circuits”, Journal de physique, Letters, 45, L39, 1984.

[69] - N. Metropolis, A. W. Rosenbluth, M. N. Teller, “"Equations of State Calculations by Fast Computing Machines” J. Chem. Phys., 21, 1087, 1953.

[70] - S. Kirkpatrick, Jr. Gelatt, C. D. Vechi, “Optimization by Simulated Annealing”, Science 220(67), 1983, pg. 147-164.

[71] - A. Ouenes, “Application of Simulated Annealing to Reservoir Characterization and Petrophysics Inverse Problems”, PhD thesis, New Mexico Institute of Mining and Technology, Socorro, NM, 1992.

[72] - G. Perez, “Stochastic Conditional Simulation for Description of Reservoir Properties”, PhD Thesis, the University of Tulsa, 1991.

[73] - K. B. Hird, M. Kelkar, “"Conditional Simulation for Reservoir Description Using Spatial and Well Performance Constraints”, Presented at the SPE Annual Technical Conference and Exhibition, Houston, TX, 4-7 October, 1993.

[74] - Tertiary Oil Recovery Project (TOPR), www. torp. ku.edu

[75] - M. K. Dubios, A. P. Byrnes, W. L. Watney, “Field Development and Renewed Reservoir Characterization for CO2 Flooding of the Hall-Gurney Field, Central Kansas”, Presented at the Annual AAPG Convention in Denver, Colorado, 2001.

[76] - M. R. Todd, W. J. Longstaff, “he Development Testing and Application of a Numerical Simulator for Predicting Miscible Flood Performance”, JPT, July 1972.

[77] - F. J. Lucia, “Carbonate Reservoir Characterization”, New York, Springer-Verlag, 226 pages, 1999.